Martin Sebastian Meier
Trinity College, University of Oxford

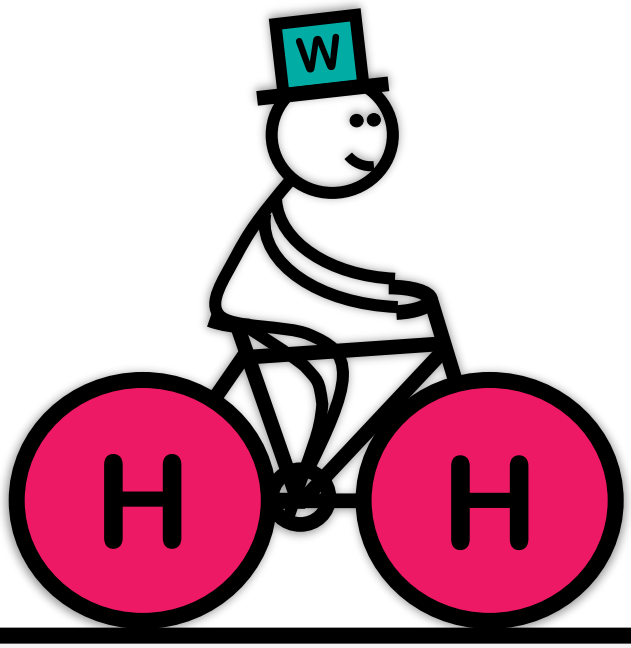

All Things Hydrogen

Hydrogen Imaging in Atom Probe Tomography and its Application to Tungsten

A thesis submitted for the degree of
Doctor of Philosophy, Materials Science

Trinity Term, 2023

Abstract

This thesis investigates the fundamental behaviour of contaminant hydrogen in Atom Probe Tomography (APT), develops an APT imaging method for sample hydrogen, applies it to deuterium implanted tungsten, and describes a large-scale APT data analysis and its application to hydrogen.

Rate cycling experiments are introduced, where the evaporation rate or frequency is repeatedly changed during experiments. Contaminant hydrogen is, other than sample hydrogen, rate dependent, therefore this allows estimating the true amount of sample hydrogen. By undertaking APT experiments below the evaporation threshold, it could then be investigated how the electric field influences the contaminant signal on tungsten. Beyond a critical field strength, the contaminants are found to evaporate with a detectable energy deficit. This allows differentiation between contaminant and sample hydrogen, which evaporates without any energy deficit, enabling development of a method for direct hydrogen imaging using pulsed laser APT.

The technique is applied to image deuterium in self-ion irradiated, deuterium implanted tungsten. The deuterium is retained with a characteristic depth distribution, which is imaged by APT with high spatial resolution. The highest deuterium concentrations are found in a layer directly under the material surface (up to 20 nm deep), corresponding to the depth reached by the deuterium during implantation, and in a deeper layer (ca 120 to 170 nm below) due to radiation damage. The scatter of measured concentrations across samples is large, and potentially requires further study.

Finally, a large-scale data analysis, covering 848 archival datasets from the Oxford APT group is presented. It is shown that many APT spectra can be regarded as a point cloud, in which a similarity metric based on the city block distance is well suited to search spectra by similarity. The point cloud contains clusters, mostly due to chemical composition of the underlying APT specimens. The dependence of contaminant hydrogen behaviour on material, voltage and electric field strength is studied.

Special Thanks

I would very much like to express my gratitude to Alfred Cerezo, Andy London, Anke Wohlers, Anthony Hollingsworth, Ben Jenkins, Christina Hofer, Dan Haley, David Armstrong, Duc Nguyen, Eugene Zayachuk, George Smith, Hazel Gardner, Jack Haley, James Douglas, Jaspreet Singh, Meg Jones, Megan Carter, Michael Moody, Paul Bagot, Peter Felfer, Sam Waters, Sophia Ungermann, Ty Prosa and the Oxford Raptors for support with my research, helpful discussions and supervision. I would also like to thank Cameca Instruments Inc for funding of my Dphil project, and the National Nuclear User Facility (NNUF) for funding my experiments on tritiated tungsten samples.

Published Work

Some of the research presented in this thesis has already been published in papers or conference presentations. These are:

Journal Papers

M. S. Meier, M. E. Jones, P. J. Felfer, M. P. Moody, and D. Haley, "Extending Estimating Hydrogen Content in Atom Probe Tomography Experiments Where H2 Molecule Formation Occurs," Microscopy & Microanalysis, pp. 1-14, 2021, doi: 10.1017/S1431927621012332.

M. S. Meier, P. A. J. Bagot, M. P. Moody, and D. Haley, "Large-Scale Atom Probe Tomography Data Mining: Methods and Application to Inform Hydrogen Behavior," Microscopy & Microanalysis, p. 1-11, 2023, doi: 10.1093/micmic/ozad027.

Conference Presentations

M. S. Meier, M. P. Moody, T. J. Prosa, and D. Haley, “Extrapolating Hydrogen content in Steel”, Mini Presentation at the APT&M Conference 2020, Oxford, UK, 2020. Recording available online: https://youtu.be/i_omBpKZY_U.

M. S. Meier, and D. Haley, “Upgrading a Reaction Cell for Controlled Gas Phase Treatment of AT specimen”, Mini Presentation at the APT&M Conference 2020, Oxford, UK, 2020. Recording available online: https://youtu.be/ZMG4Jhki43U.

M. S. Meier, P. A. J. Bagot, M. P. Moody, and D. Haley, "Inter-Experiment Machine Learning on APT experiments: New Insights from Meta-Analysis," Microscopy & Microanalysis, vol. 27, no. S1, pp. 182-183, 2021, presented at the M&M Conference 2022, doi: 10.1017/S1431927621001264.

M. S. Meier, P. A. J. Bagot, A. Hollingsworth, A. Wohlers, M. P. Moody, and D. Haley, "3D Nanoscale Analysis of Implanted Deuterium in Tungsten using Atom Probe Tomography," Microscopy & Microanalysis, vol. 28, no. S1, pp. 2102-2104, 2022, presented at the M&M Conference 2022, doi: 10.1017/S1431927622008133.

M. S. Meier, P. A. J. Bagot, M. P. Moody, and D. Haley, "Solving Peak Tail Overlaps in Atom Probe Tomography using Convolutional Networks," Microscopy & Microanalysis, vol. 28, no. S1, pp. 698-700, 2022, presented at the M&M Conference 2022, doi: 10.1017/S1431927622003269.

M. S. Meier, M. E. Jones, P. J. Felfer, P. A. J. Bagot, M. P. Moody, and D. Haley, "Exploiting Adsorption Dynamics in Atom Probe Tomography for accurate Measurements of Hydrogen Concentrations," Microscopy & Microanalysis, vol. 28, no. S1, pp. 1650-1652, 2022, presented at the M&M Conference 2022, Portland, USA, doi: 10.1017/S1431927622006572.

M. S. Meier, M. P. Moody, P. A. J. Bagot, and D. Haley, "Using Advanced Database Analysis Techniques to Guide New Experimental Approaches and Gain New Insights into Hydrogen Behaviour in Atom Probe Tomography Data," presented at the APT&M Conference 2022, Nanjing, China, 2022. Recording available online: https://www.youtube.com/watch?v=Kq99MStPAw4.

In addition, I have contributed to further publications during my Dphil, which are not directly focus of my work and where I am not the main author. These works are:

M. Stückler *et al.*, "Oxide-stabilized microstructure of severe plastically deformed CuCo alloys," *Journal of Alloys and Compounds,* vol. 901, p. 163616, Apr 25 2022, doi: 10.1016/j.jallcom.2022.163616.

Y. Shi *et al.*, "Towards accurate atom scale characterisation of hydrogen passivation of interfaces in TOPCon architectures," *Solar Energy Materials and Solar Cells,* vol. 246, p. 111915, Oct 1 2022, doi: 10.1016/j.solmat.2022.111915.

B. M. Jenkins *et al.*, "Preliminary Atom Probe Tomography Evidence for Hydrogen Trapping at a β-Nb Second Phase Particle in a Neutron-irradiated Zirconium Alloy," *Microscopy & Microanalysis,* vol. 28, no. S1, pp. 1658-1659, 2022, presented at the M&M Conference 2022, Portland, USA, doi: 10.1017/S1431927622006596.

0. Contents

1. Literature Review: Fusion Energy and Tungsten

1.1. Principle of Fusion

Fusion reactors are one potential future sustainable and safe energy source. Research into fusion reactors for energy production has been going on for over 70 years, with a multitude of reactors proposed and constructed [1, 2]. To date, the technology is not mature, and no power plant that is able to release net energy has yet been constructed.

All fusion reactors aim to produce energy through a fusion reaction where two light nuclei fuse into a heavier nucleus. Nuclei self-repel through the electrostatic force, but are attracted by the nuclear force which holds the protons and neutrons together in nuclei. The electrostatic force is more long-range and dominates the attractive nuclear force unless the nuclei are brought into close contact. This competition of forces leads to the so-called Coulomb barrier. If two nuclei are brought sufficiently close together, tunnelling through this energy barrier can occur, resulting in the formation of a larger nucleus from two smaller ones [3].

In theory, a net energy production through fusion is possible through any nuclei lighter than iron-56 as these reactions are exothermic [4]. Research however is mainly centred around the deuterium-tritium reaction, as it is easiest to produce [5]:

$$ {}^{2}_{1}D + {}^{3}_{1}T \rightarrow {}^{4}_{2}He + {}^{1}_{0}n $$

Equation 1

The reaction is highly exothermic (17.6 MeV per reaction [5]) and produces intense energy fluxes, which must be contained to sustain the reaction. The high temperatures and intense neutron fluxes are challenging from a materials perspective, and any containment vessel must withstand these conditions during the reactor operation. Maximising the lifespan, meeting regulatory limits and minimising the chance of failure for reactor components exposed to hydrogen plasmas are actively under research.

1.1.1. Tokamak Reactors and Divertors

Tokamak reactors are the leading candidate for future power plant fusion reactors. ITER (International Thermonuclear Experimental Reactor), currently under construction in France, is the world-leading fusion reactor programme, seeking to generate a long-standing fusion reaction with net energy output [6]. It is envisioned in the community that ITER will be followed by another reactor, DEMO, which will be the first grid connected, electric energy producing fusion power plant [7].

In tokamaks, fusion occurs in a plasma of several million degrees Celsius circulating in a toroidal chamber (Figure 1A). Magnets confine the plasma in the chamber, but this containment is imperfect and some losses into the containment walls occur [8, 9]. Current tokamaks typically work in a pulsed mode where the conditions for fusion to occur are only maintained for at most a few seconds at a time. The construction and operation of reactors with continuously fusing plasma (“steady state plasma”) is, however, possible [8].

Of particular engineering interest is the divertor, as it is exposed to the highest damage rates within the reactor. This structure in the fusion chamber is used for the removal of fusion products (the helium that is generated, the “ash”) and other waste via a pumping duct at the divertor base. Figure 1B shows a cross-

section of a tokamak with a divertor and the outermost surface of magnetic plasma confinement (the Separatrix). Outside of the Separatrix lies the scrape-off layer, from which material is guided towards a target area in the divertor [10-12].

The divertor typically consists of baffles, a dome, liner and target. The points in the divertor where the Separatrix crosses the target are called strike points [10]. The areas around the strike points are in direct contact with plasma, and are therefore subjected to the most intense heat- and particle fluxes of all plasma-facing surfaces in the reactor [10].

In ITER, the divertor is not a single piece but consists of several cassettes in a circular arrangement at the bottom of the reactor (Figure 2). On both the inner and outer side, baffles and targets are combined into one element each [13, 14], and made from tungsten monoblocks which are lined up on CuCrZr tubes for water cooling [15, 16]. Dome and reflector plates are composed of flat tungsten tiles, which are also water cooled [17]. Table 1 lists expected fluxes and particle energies on the plasma facing components in ITER under normal operation [10].

Table 1: Overview over expected heat and particle loads in ITER. Unless otherwise stated, reference is [10]

	Heat Flux / MW/m^2	Particle flux / DT/m^2s	Particle energy / eV
First Wall	0.5	10^{19} … 10^{20}	100 … 500
Divertor Target area	10 (continuous), 20 (few seconds) [16]	$\leq 10^{24}$ [10, 16]	1…30
Divertor Side Wall – not target area	3	10^{20} … 10^{22}	>30
Divertor Dome	3	10^{21} … 10^{22}	>30

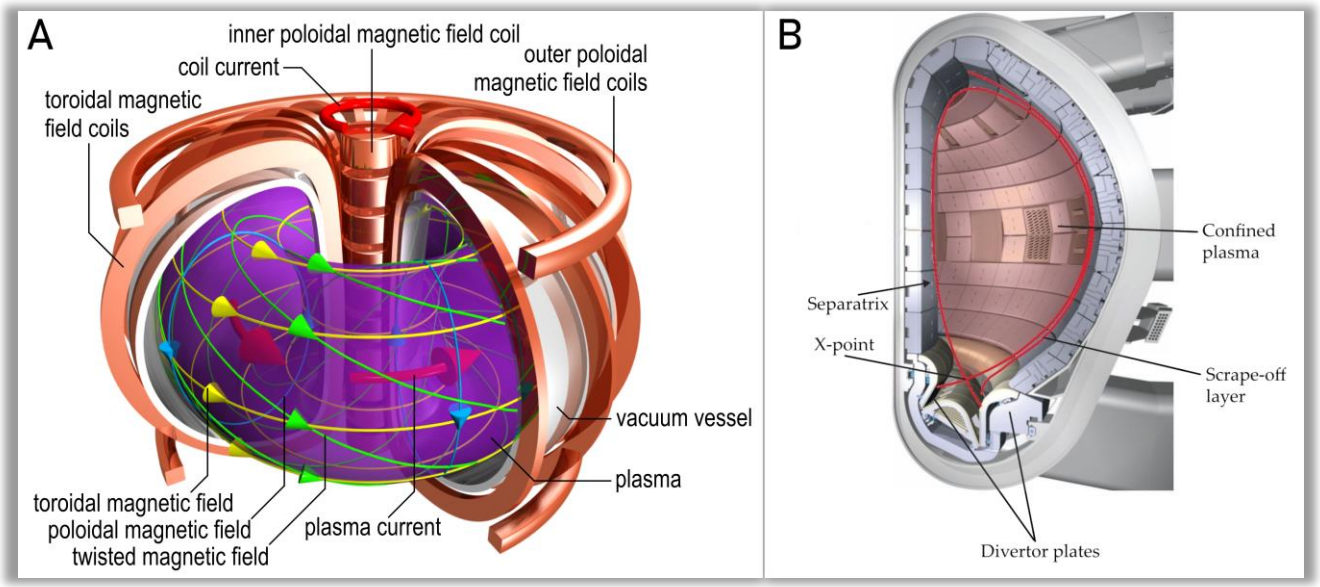

Figure 1: A) General structure of a tokamak sector. The plasma is confined in the chamber by magnets. Image by C. Brandt, IPP Greifswald. B) Cross-section through tokamak reactor with separatrix. Adapted, taken from [18]*. Copyright by C. Brandt (A) and ITER Organization (B), re-used with permission.*

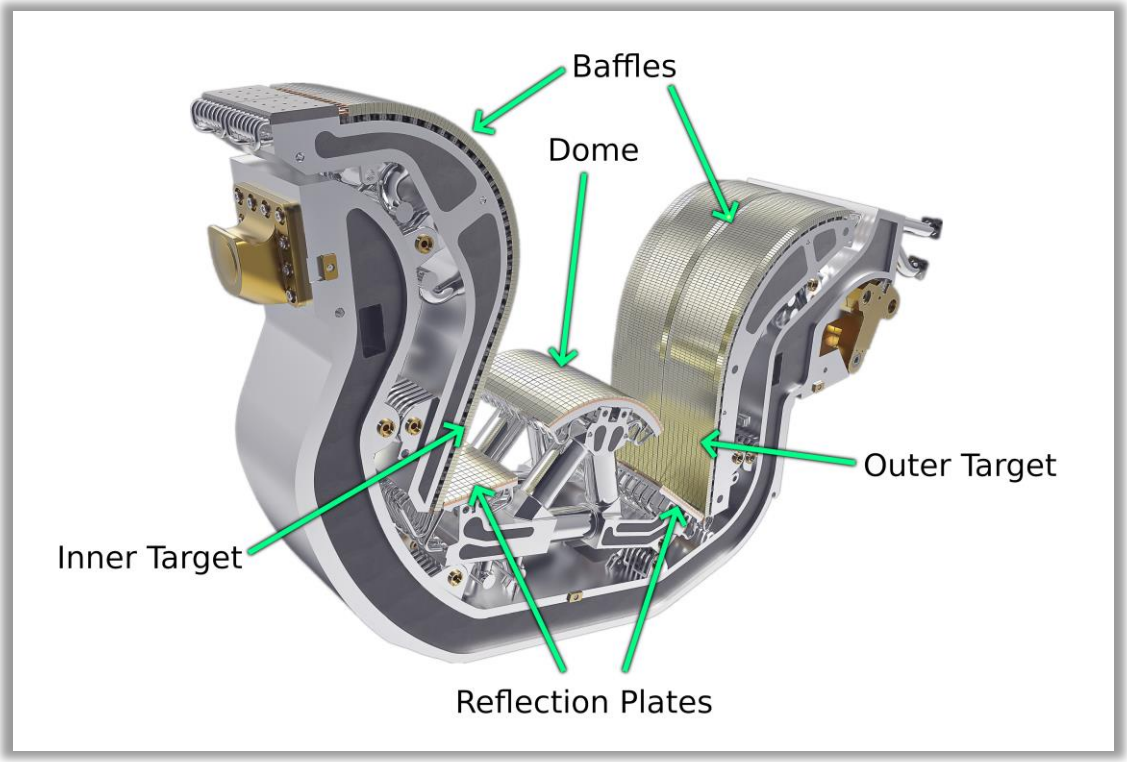

Figure 2: Divertor cassette as planned for ITER. Inner and outer baffles and targets are combined into two walls from tungsten monoblocks, dome and reflection plates are flat tungsten tiles. Adapted, taken from [19]. Copyright by ITER Organization, re-used with permission.

1.2. Tungsten for Fusion Rectors

Tungsten has been chosen as the material for the plasma-facing parts of the divertor on ITER, and is – eventually alloyed with other elements – the primary candidate for all plasma facing surfaces in a future DEMO reactor [20, 21]. Tungsten is a d-group metal with a body-centred cubic structure and particularly high melting and boiling points, 3695 K and 5828 K respectively [22]. The recrystallisation temperature, dependent on sample condition and testing method, ranges from 1773 to 2523 K [23-26].

The advantages of tungsten are a high sputtering threshold (200 eV, deuterium sputtering [25]), minimising plasma contaminations with tungsten atoms. Additionally, its high melting point and low vapour pressure, along with a high thermal conductivity, makes it attractive for actively cooled, high temperature applications [25]. Unlike a prior alternative for the ITER divertor target, carbon, tungsten does not form hydrogen-rich co-deposits with deuterium and tritium from the reactor fuel [27]. Concerns about high tritium inventory were the main rationale for ultimately selecting tungsten over carbon [20]. Building ITER with a carbon divertor for an initial campaign with pure deuterium fuel, but switching to a tungsten divertor before operation with tritium-containing fuel was considered as well, but this was ultimately scrapped due to too high costs [20]. At the time, production of only one divertor from tungsten is planned for ITER [20].

Key disadvantages of tungsten are its transmutation to rhenium and toxic osmium under neutron irradiation [28], and a high ductile-to brittle transition temperature ranging from 423 to 523 K, leading to brittle behaviour at room temperature [29, 30]. Tungsten contaminations in the plasma core will lead to plasma cooling which can result in reduced energy production or even a complete halt of the fusion reaction [31, 32]. Tungsten will not sublimate, but could melt if the maximum heat flux is exceeded during accidents [20].

1.2.1. Thermal Loads

During reactor operation, energy from the plasma is directed into the plasma facing materials, leading to strong heating. Importantly, so-called Edge Localised Modes (ELMs) frequently occur and lead to an expulsion of up to 15% of the energy in the plasma into the scrape-off layer, from which the energy is transported into the divertor [10]. The ELM frequency is usually ~1Hz during operation, though ELMs at lower intensities in ITER may be triggered deliberately at up to ~30 Hz to preclude more intense ELMs [33, 34]. This will superimpose cyclic, quick heating ("thermoshocks") above the base temperature on the tungsten in the divertor.

Apart from these normal loads, plasma disruptions (and vertical displacement events (VDE) which are also disruptions [10]) lead to extremely strong surface heating within short timeframes. During disruptions, the plasma is fully quenched, and the energy rapidly deposited on the reactor walls and the divertor [10]. Figure 3 provides an overview of the heat fluxes that are expected to occur in ITER. It is expected that the target surface in the divertor of ITER will reach 1273-1633 K during normal operation and up to 3393 K during disruptions [16].

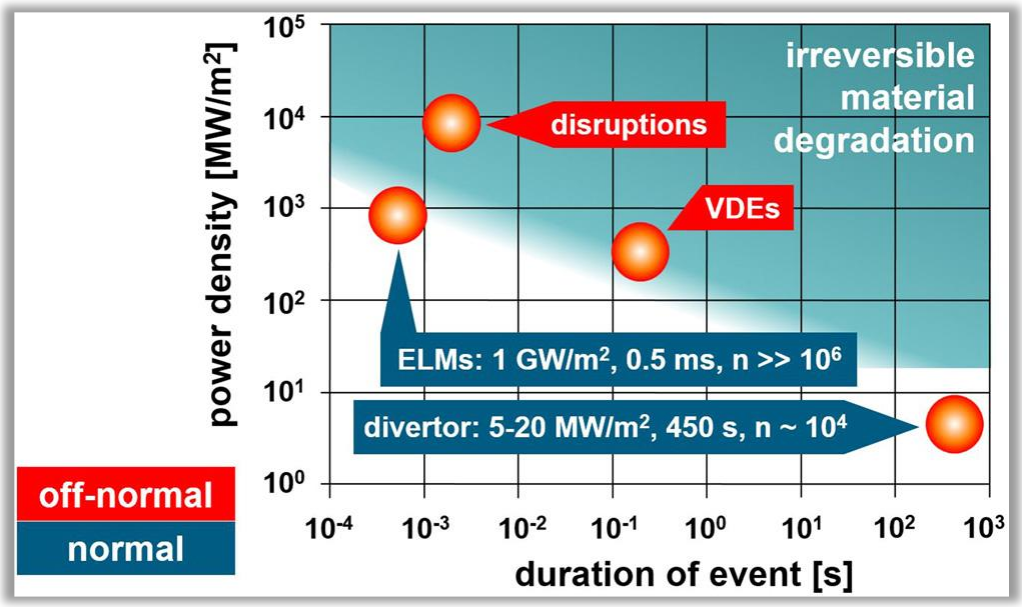

Figure 3: Expected Heat loads on the divertor in ITER. During operation, the operator will be loaded with a baseline heat flux above which ELMs impose rapid, repeated additional heating. Disruptions (and vertical displacement events, VDEs) lead to rapid deposition of high thermal loads which is expected to result in irreversible material alternations. Taken from [35]. *Image by J Linke and J Du, licensed under CC-BY*, re-used with permission.

Effect on Tungsten

Heating of the material leads to stresses from thermal expansion. Subsequently, plastic deformation and cracking upon cooling down can occur [36], typically along grain boundaries (Figure 4A). Single crystal tungsten and tungsten with grains parallel to the temperature loaded surface are less prone to cracking [37-39], and the latter has been chosen as the material for ITER [40]. However, such a grain orientation leads to increased cracking parallel to the surface, partially or fully undercutting parts of the material (Figure 4B). This can result in to reduced thermal conductivity, increased temperatures or material loss [41].

Besides cracking, surface roughening is observed in thermal shock experiments, potentially leading to increased erosion [38]. As the cracking behaviour is directly related to the mechanical properties of the material, any damaging influences from the fusion plasma which alter the mechanical properties of tungsten (e.g. hydrogen implantation, and neutron irradiation) also affect the susceptibility to thermal cracking [42]. It is therefore important not to regard thermal cracking as an isolated issue, but also in the context of other damage mechanisms [43]. Hydrogen, which is implanted into tungsten, can lead to hydrogen embrittlement and eventually increased cracking (see Section 1.2.3) [44]. To research the possible effects of the thermal loads on plasma-facing tungsten, electron- or ion beams, plasma accelerators/guns, or lasers are used to simulate the conditions experienced within fusion reactors [36].

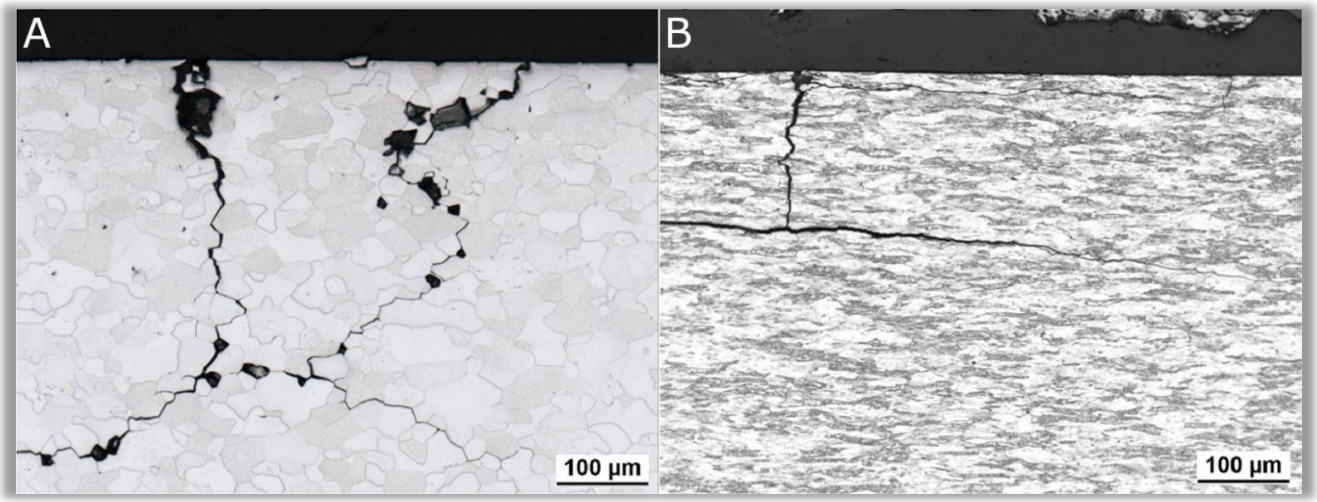

Figure 4: Scanning Electron Microscopy (SEM) images of cross-sections through cracks in W-5%Ta material after 100 thermoshocks, A) intergranular cracks in a sample that was recrystallized before thermal loading (no preferred grain orientation), B) undercutting of material in a sample with grains parallel to the surface. Taken from [41]*. Images by M Wirtz, licensed under CC-BY-NC-ND, re-used with permission.*

If parts of the divertor in ITER are misaligned, temperatures significantly in excess of the expected 1273-1633 K will occur and lead to the repeated formation of thin molten layers on the surface [16, 45]. This possibility therefore imposes stringent manufacturing tolerances [16]. In addition, disruptions may lead to melting, and eventually evaporation of tungsten. This could result in significant material transport and losses [46]. In the worst case, changes in the geometry due to melting could lead to uncontrolled heat deposition which might ultimately result in severe damages to the monoblocks in ITER and the underlying cooling pipes [31].

1.2.2. Neutron Damage

In addition to macroscopic damage, irradiation is a key problem. As seen in Equation 1, fusion of deuterium and tritium leads to the ejection of neutrons. These neutrons have high energies (14 MeV in the D-T reaction) and impinge on the plasma-facing components. This leads to two types of interactions: displacement of tungsten from lattice positions and transmutation [47]. Radiation damage is usually quantified in displacements per atom (dpa).

Displacement Damage

The high energy of the neutrons is sufficient to cause large collision cascades in tungsten, or the displacement of several atoms from their lattice positions. This produces self-interstitial atoms and

vacancies, of which a large fraction recombine quickly [48]. A fraction will however remain in the material and eventually form dislocation loops [49]. Under sufficient irradiation, void formation, and in some cases even regular void lattices occur [49]. It is important to note that these microstructural alterations greatly increase the ability of tungsten to retain hydrogen and therefore potentially affect the damaging influence of this element, this is further discussed in Section 1.2.3. If the irradiation is conducted at elevated temperatures, less damage formation is observed due to a competing annealing effect [49].

No neutron source which can accurately mimic the neutron fluxes in ITER or a potential DEMO reactor currently exists. As proxy, neutron displacement damage for materials research is typically simulated using either fission reactors [50] or ion irradiation [51, 52]. Fission reactors have the drawback of producing significantly different neutron energy spectra [50], whilst ion irradiation leads to strong gradients in the displacement damage as a function of distance from the irradiated surface. This is because the penetration depth of ions is much lower than that of neutrons [53]. Macroscopically, neutron and ion irradiation leads to hardening of the material [51, 53-55].

Transmutation

Transmutation is the conversion of atoms from one isotope into another [56]. In plasma-facing tungsten, this can be triggered upon the capture of a neutron, which may be followed by radioactive decay if the newly formed nucleus is unstable [28]. This leads to gradual changes to the chemical composition of the material and production of additional atoms in the lattice [28]. The rates of transmutation for the various isotopes in the material are highly dependent on the neutron energy spectrum [36, 57]. For this reason, transmutation in fusion environments cannot be simulated accurately in fission reactors. As such, simulations are currently established ways of investigating the composition evolution.

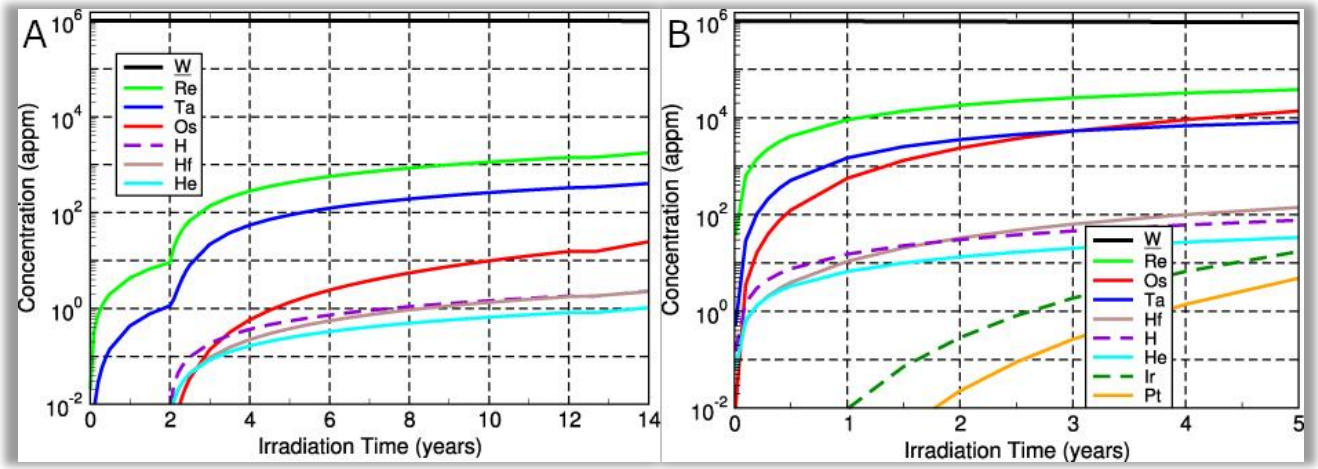

Figure 5: Expected concentrations of transmutation products in A) ITER during the first 14 years and B) a potential DEMO reactor design during 5 years. Taken from [28]*. Copyright by IAEA, re-used with permission.*

The most important transmutation reactions for tungsten are to rhenium and tantalum, and the subsequent transmutation of rhenium to osmium [58]. Figure 5 shows the evolution of rhenium, tantalum and osmium contents in plasma facing tungsten components in ITER and a possible DEMO reactor design [28], where a much higher degree of transmutation is expected than in ITER. Self-shielding of the neutrons by the irradiated material leads to different evolutions of the composition depending on the depth from the exposure surface, resulting in complex chemistry profiles [59].

The maximum quantity of transmutation-produced hydrogen in ITER (around 10 atom-ppm) is insignificant when compared to the concentrations that are reached due to implantation in the surface-near regions (up to around 1%, see Section 1.2.3).

1.2.3. Hydrogen in Tungsten

Deuterium or tritium are implanted into the reactor walls and divertor in tokamak reactors. Notably, tritium is a radioactive beta-emitter (half-life: 12.3 years [60]) and therefore a potential safety risk. It necessitates remote handling and repair of parts in the reactor if the radiation exceeds certain limits, and potentially poses hazards if released into the environment during accidents. Tritium is therefore subject to legal restrictions [61, 62]. For ITER, the authorised limits at the time are 4 kg of tritium on-site [10, 62], and 700 g as inventory in in-vessel components [63].

Tritium also is a particularly scarce resource as it needs to be bred using neutron sources, and loss due to implantation should therefore be minimised [10]. Future fusion reactors will feature breeder blankets producing tritium via transmutation reactions to solve the scarcity problem, reaching "tritium self-sufficiency". ITER however will only feature experimental test breeding modules, not producing enough tritium for reactor operation [64].

It is noted that in the ITER design, the amount of retained tritium in the vessel might not be governed by the divertor, but the beryllium walls or Be/H co-deposits, which could account for more than a magnitude more of retained hydrogen than the divertor [63, 65]. Nonetheless, hydrogen can negatively affect the performance of the divertor in several ways, as will be laid out in the following sections.

Hydrogen behaviour in tungsten

Tungsten is an endothermic hydrogen absorber with an enthalpy of solution of approximately 1 eV [66]. Thus, the equilibrium concentration of lattice hydrogen under standard conditions is negligibly low [67]. Diffusion of (interstitial) hydrogen in a tungsten lattice occurs quickly, with an activation energy of approximately 0.4 eV [66] and a diffusivity of $4.1*10^{-7}$ m^2s^{-1} [27, 66]. The interaction between interstitial hydrogen atoms in a lattice is, depending on distance, repulsive or a negligibly weak attraction (0.01 eV) [68], meaning there is no relevant driving force for hydrogen to cluster by itself in an otherwise defect-free tungsten lattice [68, 69].

Table 2: Trapping energies of hydrogen at various defects in tungsten

Defect	Energy / Trapped H	Reference
Vacancy (1 to 6 Hydrogen atoms trapped)	ca. 1.25 eV … 0.4 eV for 1…6 Hydrogen	[67, 69-72]
Vacancy Cluster	ca. 1 … 2.15 eV for 1…5 Vacancies	[71, 73]
Screw Dislocation	0.53 eV	[69]
Edge Dislocation	0.89 eV	[69]
Dislocation jog	1.4 eV for 1...3 Hydrogen	[74, 75]
Grain boundary	1.11 eV	[76]

Defects in the lattice that trap hydrogen have a significant influence on the hydrogen diffusivity and concentration in the material. The most important intrinsic trapping sites are grain boundaries, dislocations and vacancies. Typical trapping energies for hydrogen at the various defects from the literature are listed in Table 2, and an diagram of typical traps and energies is shown in Figure 6.

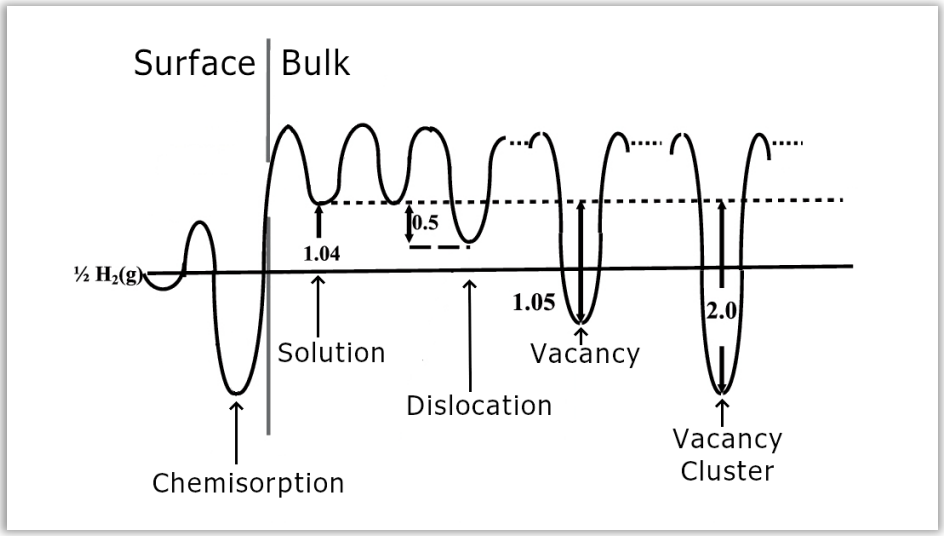

Figure 6: Energy diagram, showing chemisorption, enthalpy of solution and typical traps and trapping energies for hydrogen in tungsten. All energy values are in eV. Adapted from [71] with the permission of AIP Publishing.

Common trap densities in polycrystalline tungsten lie at around 10^{-3} atomic-% (measured in W annealed at 1673 K for 1 h) [77], but radiation can increase this density up to approximately 1% [78-81]. Given sufficient hydrogen supply, these traps are mostly occupied at temperatures below 500 K, which is why the trap concentration is a guide for the expected hydrogen retention at such temperatures [77, 78].

It is noted that in future reactors, tungsten-based alloys rather than pure tungsten may be used, and this is an area currently under research [82, 83]. The presence of alloying elements (which may also be due to transmutation) such as rhenium could potentially lead to additional traps in the lattice [84-90]. This however is not part of the research presented here, and is therefore not discussed in further detail.

Hydrogen related material damage

The energy and doses of hydrogen implanted into the divertor strongly vary with reactor, position in the chamber and operation mode. Within the ITER tungsten divertor, hydrogen arrives at energies of up to approximately 30 eV. This is considerably below the energy threshold at which implanted hydrogen can cause direct material damage by displacement, which is 940 eV for deuterium in tungsten [27, 91]. The response of tungsten to hydrogen implantation is temperature dependant. Depending on the location on the divertor surface, this ranges from approximately 400 to 1600 K (though higher temperatures, esp. during disruptions are possible, see Section 1.2.1) [16, 43]. Fluxes between 10^{20} and 10^{24} atoms * $m^{-2}s^{-1}$ are expected in the ITER divertor (Table 1) [10].

The effects of hydrogen plasma exposure are frequently studied using linear plasma devices. These can expose samples to plasmas at ITER-like compositions, fluences and incident ion energies (up to approximately 300 eV) [92]. Similarly, neutral hydrogen beams, which operate in the much higher incident

atom energy range from approximately 10 to 100 keV [92], and magnetron plasma devices [93] have been used.

When hydrogen is implanted into the tungsten lattice, at a rate higher than the rate of diffusion back to the surface and release, a supersaturation will build up in the material. This results in mechanical stresses in the implantation layer. In recrystallised tungsten samples (i.e. with low defect concentrations), intragranular cracks arise near the surface, leading to blister-like surface structures observed after deuterium implantation at 400 – 500 K, with the damage pattern dependent on dose and flux (Figure 7) [94]. When the implantation occurs in a temperature range from 500 to 600 K, the damage pattern changes to cavity formation at the grain boundaries. This reflects the brittle-to-ductile transformation of tungsten [94]. The blisters can eventually coalesce and breach the surface, releasing trapped gas [95].

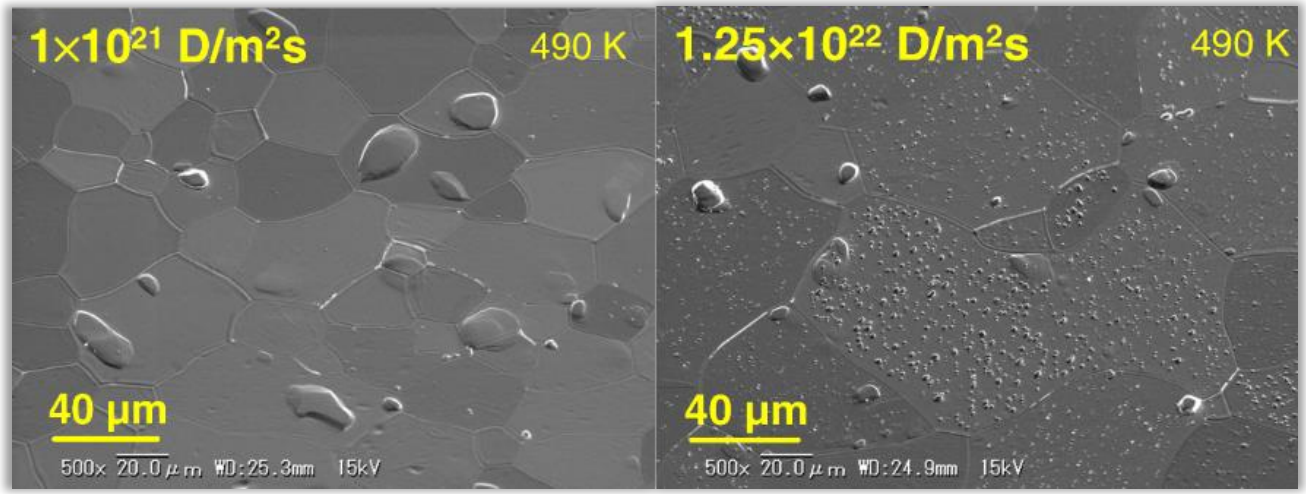

Figure 7: SEM images of blisters in tungsten after deuterium implantation to a dose of 10^{26} D/m^2, using different fluxes. Different blister structures are observed, depending on flux. Taken from [94]. © IOP Publishing. Reproduced with permission. All rights reserved.

Limited blistering is observed in implantation experiments with fluxes below 10^{22} $m^{-2}s^{-1}$ and temperatures above 700 K, which might be due to a faster diffusion away from the implantation zone and therefore lower (super-) saturations [45, 94, 96, 97]. It was also pointed out that annealing could occur at these temperatures, decreasing the defect density [98]. However, at higher fluxes, as expected at the strike points in ITER (10^{24} $m^{-2}s^{-1}$), blistering and nanostructuring of the surface is observed in experiments at temperatures up to 1273 K [43, 99-102].

"Technical" tungsten surfaces (i.e., surfaces which are processed through grinding rather than chemical etching and/or annealing and which therefore are comparably defect-rich) tend to have a lower tendency to blister [103, 104]. One possible explanation to this is a faster escape of hydrogen through surface-connected defects, such as surface-near dislocation networks or microcracks and grain boundaries [94, 103, 104]. There are further and complicating contributions to this, nevertheless, because such surfaces are also rougher, therefore by virtue of their increased surface area favour to release implanted hydrogen more, and growing bubbles are more likely to break through the surface and stop growing at an early (small) stage [103].

Like most other metals, tungsten is susceptible to hydrogen embrittlement [105-107], which might ultimately result in increased thermal shock cracking in fusion reactors [44] (also see Section 1.2.1). Hydrogen embrittlement is a complex phenomenon where many possible mechanisms can lead to an observed

degradation of mechanical properties [108]. Dislocation pinning and increased dislocation nucleation in the presence of hydrogen have been suggested to explain the embrittlement of tungsten [105, 107], though there is no current certainty as to which mechanisms are most relevant to tungsten in fusion environments.

1.2.4. Helium in Tungsten

For completeness, it is noted that helium implantation into tungsten is another relevant damage mechanism which needs to be considered in tokamak reactors. Like hydrogen, helium has low solubility in tungsten [109], high mobility [110-112], and can be trapped at defects [113, 114]. Unlike hydrogen however, helium interstitials in a tungsten lattice are not self-repellent but attracted to each other [68], leading to the formation of clusters [115]. Self-trapping or "trap-mutation" of helium clusters is possible, where the helium cluster can cause the ejection of a tungsten atom from its lattice position (creating a Frenkel Pair) [115]. The vacancy created can act as a trapping site, which in turn attracts more helium from the lattice, leading to the ejection of further lattice atoms and eventual creation of large vacancy complexes and bubbles [115, 116].

On the macroscopic level, bubbles [11, 117, 118], open voids [45, 117, 119] and development of highly porous layers (occasionally referred to as "fuzz") [43, 120-124] have been observed in helium implantation experiments on tungsten, depending on the exposure parameters. Synergistic effects with hydrogen [52, 125-129], radiation damage [130, 131] and temperature [132-134] are investigated. My work however is only focused on imaging of hydrogen in radiation damaged tungsten, therefore helium related effects shall not be discussed any further.

1.2.5. Conclusion and Engineering Challenge

Plasma-facing tungsten in fusion reactors is subject to a multitude of damaging influences, high temperatures and thermal shocks, hydrogen-and helium implantation and neutron irradiation. Thermoshocks lead to cracking, and overheating from disruptions or misaligned plasma-facing parts result in melting and consequently material loss and deformation. Implanted hydrogen can lead to blistering and embrittlement, and implanted tritium will make the material radioactive. Helium is effective in forming vacancies and voids when implanted and gives rise to dense microbubble films and fuzz. Neutrons damage material directly through knock-on as well as causing transmutation, gradually changing the composition of the material and leading to radioactive activation.

This means that a range of material science problems needs to be solved before fusion for large-scale energy production becomes feasible. It needs to be known if, and under what conditions the tungsten divertor in ITER and other future reactors can work, and how they should be designed. Since the interplay of the various damaging factors is highly complex, there is uncertainty about how tungsten will behave in ITER. Also, currently, the number of experimental fusion reactors is low, and data from actual fusion experiments is scarce. Simulated materials are therefore often used as proxy (e.g. ion radiation damage instead of neutron radiation from a fusing plasma), but it is not always clear how accurately such samples can model material from ITER.

The hydrogen retention and behaviour in fusion tungsten is highly dependent on the number and nature of trapping sites which themselves can be the product of a multitude of influences. Synergistic effects between hydrogen and other influences from the plasma need to be considered. While depth profiled retention

measurements in radiation damaged samples have been made to investigate macroscopic retention [80, 135], little research has been conducted on the behaviour of hydrogen in tungsten on the microscopic scale. More research around the microscopic behaviour of hydrogen in tungsten and its alloys is needed. Improvement of microscopy techniques for investigating the underlying mechanisms on the nanostructural level is an important target for the progression of fusion reactors.

Fittingly, experimental protocols for Atom Probe Tomography (APT) on hydrogen loaded materials have been well explored in the past decade, and have advanced to a point where methods for examining hydrogen in fusion relevant tungsten samples can be developed. APT and its application to hydrogen imaging will be discussed in the next part of the literature review.

2. Literature Review: Hydrogen in APT

Atom Probe Tomography (APT) is a microscopy technique which produces three dimensional datasets with near-atomic resolution. The sample is a sharp needle (less than 50 nm tip radius) which is placed in a vacuum chamber opposite a counter electrode. A strong electric field, with either superimposed voltage or laser pulses is applied, such that atoms from the sample field evaporate and accelerate towards a position-sensitive detector. From this, time-of flight measurements can be made to determine the mass-to-charge state ratio of the evaporating atoms. This allows for the reconstruction of 3D datasets with the approximate positions of the atoms prior to evaporation [136, 137]. A schematic drawing of an APT experiment is shown in Figure 8.

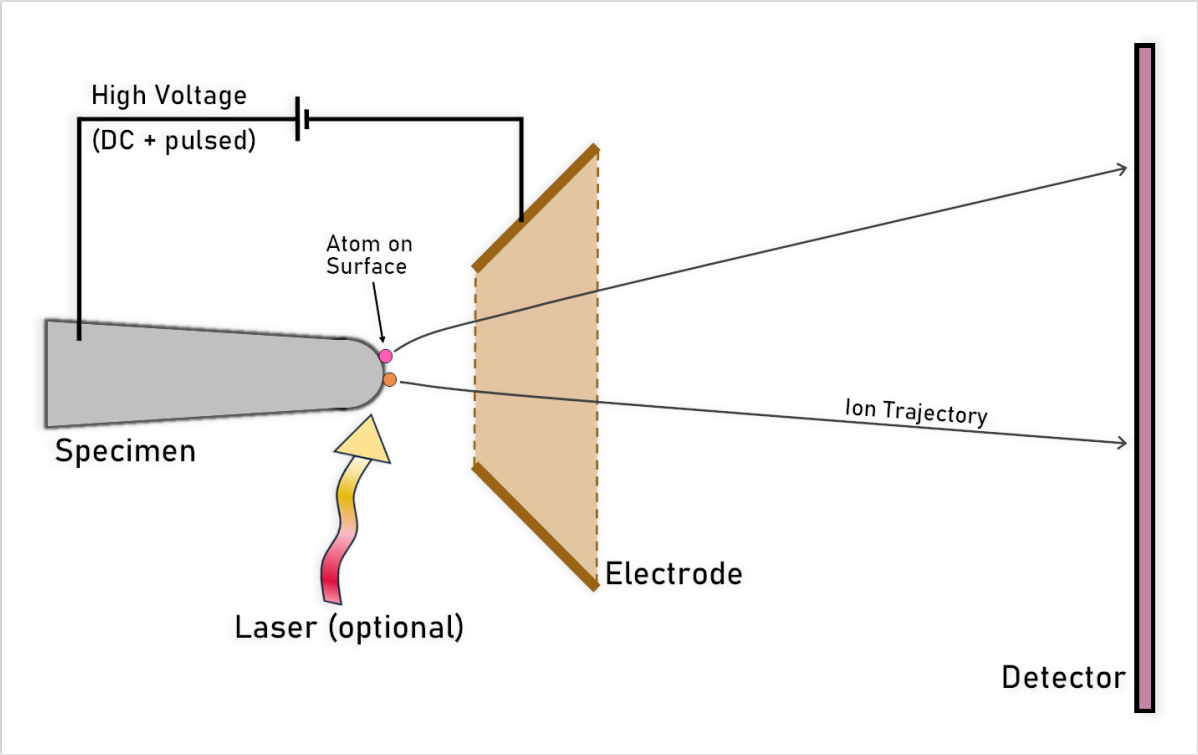

Figure 8: Schematic drawing of an APT experiment. Dimensions of components are not to scale.

In theory, APT has the same chemical sensitivity to all elements. Hydrogen is an exception to this, as this element is also present as a contaminant in virtually every APT experiment [138-140]. It is known that the contaminant is continuously supplied whilst the APT experiment is running, so the contamination occurs throughout the experiment [141-146]. From the detector signal alone, it is not possible to differentiate between hydrogen originating from the sample and the contaminant type of hydrogen, making analysis of hydrogen a challenge for current APT research.

A range of different terms has been used throughout the literature to refer to the different hydrogen signals present in APT, for example “true” or “intrinsic”, and “parasitic”, “background” or “artefact” hydrogen. I use the terms “sample” and “contaminant” hydrogen. ‘Sample hydrogen’ is any hydrogen that is contained in the APT specimen at the time of the experiment, even if it has been added as contaminant during an earlier state of the sample preparation routine (e.g. accidental introduction of hydride phases in Zr or Ti during FIB sharpening of APT tips [139, 147]). ‘Contaminant hydrogen’ in this thesis is defined as the spurious hydrogen signal from hydrogen that arrives at the evaporating surface whilst the APT experiment is running, so this type of hydrogen that is never part of the APT specimen.

I also avoid using the term “background” when discussing hydrogen in APT, because it could be confused with time-of-flight-constant (TOF-constant) noise that is part of APT spectra, but the latter comes from a range of sources and is usually not related to hydrogen at all. Instead, I try to use “TOF constant noise floor” to describe the flat background signal in APT. Peak tails in APT spectra can extend far away from the actual peaks and – especially in the context of peak fitting [148-150] – are in the literature sometimes considered a “background signal” too, however my definition of “noise floor” does not include peak tails (though it may in practice not always be possible to clearly distinguish TOF-constant noise and long peak tails).

2.1. Hydrogen Field Evaporation

2.1.1. Field-free Hydrogen

Hydrogen in field-free, undisturbed environments appears as a nonpolar dimer molecule H_2. On metal surfaces, it can typically be found in two different states: physisorbed and chemisorbed. In the physisorbed state, hydrogen molecules are weakly bound on metal surfaces (3…5 kJ/mol [151], approx. 0.03…0.05 eV/molecule) through van-der-Waals forces (or London dispersion forces). This binding state is due to its low energy mostly relevant at low temperatures near the boiling point of hydrogen gas [152], which is 20.4 Kelvin [22].

In the chemisorbed state, the hydrogen dimers are dissociated and the hydrogen atoms bond to the surface individually[1]. Typical energies range from 2 to 3 eV/atom [156, 157]. Depending on the material and crystallographic surface, dissociative chemisorption can occur spontaneously or upon supply of an activation energy, and incorporation into sub-surface sites and modification of the metal surface (“reconstruction”) may be observed [152, 158].

2.1.2. Field Adsorbed Hydrogen

In strong electric fields as encountered in APT or FIM (Field Ion Microscopy) experiments, dipoles are induced into normally nonpolar species such as H_2. This allows these molecules to interact much more strongly than just through London dispersion forces with the surface, becoming field adsorbed [142, 159-162]. To estimate the adsorption energy of field-adsorbed hydrogen dimers on molybdenum, Kellogg et al [138] first applied a formula by Tsong et al. [159] for noble gases and obtained increasing binding energies in the range of 0.08 to 0.6 eV for increasing electric fields from 20 to 40 V/nm. Drachsel et al. measured the binding energy using a surface coverage approach, obtaining slightly lower values of 0.08 to 0.13 eV for 20 to 30 V/nm on a tungsten tip [163]. It is noted that that the underlying mechanisms of field desorption of nobles gases have been discussed in more detail by Forbes and others [160-162], but the refined models have not yet been extended to hydrogen.

2.2. Hydrogen Detection in APT

In APT experiments, hydrogen can typically be detected as single atom ion H^+ and diatomic ion H_2^+, and occasionally as triatomic ion H_3^+ or more complex hydride ion with other elements e.g. FeH^+, CuH^+. A common observation are water-like ions OH^+, $H_2O^+$and H_3O^+. The relative abundances of the hydrogen containing ions are strongly dependant on the sample chemistry and experimental parameters, and can vary significantly throughout an experiment.

[1] In some specific instances, non-dissociative chemisorption can exist as well, though this is rare [153-155]

2.2.1. H_2^+ and H^+ in APT/FIM

The most frequently observed and obvious appearances of contaminant hydrogen in APT spectra are H^+ and H_2^+, which appear in the very beginning of the spectra at m/n=1,2. Despite their ubiquity, the binding states in which these species exist at the surface and the relevant evaporation mechanisms are not yet fully understood.

In early research by Kellogg et al. [164], the H_2^+ molecule was discovered first in the first pulsed laser APT experiments. It was proposed that adsorbed H_2 is present on the sample, and thermal evaporation followed by subsequent field ionisation leads to the emission of H_2^+ ions [138, 165]. In further experiments, an energy deficit of H_2^+ ions was observed, which was attributed to an away-from-surface ionisation mechanism [166, 167].

Doubt however has been cast over the neutral thermal evaporation theory in more recent work. Sundell et al. [142] show that, at least in modern APT instrument designs, the laser is unlikely to supply sufficient energy to cause thermal evaporation of H_2 species, which are expected to be field adsorbed at the high electric fields on the specimen. Instead, it was proposed that H_2^+ is the product for regular field evaporation from the surface [142]. I would add that the observation of H_2^+ by Kellogg et al. in laser APT was the first observation of such ions in APT at all, which likely prompted the assumption that a thermal laser pulse was in some way fundamental to the evaporation of H_2^+. However, in modern APT, H_2^+ is readily observed in pulsed voltage experiments where no sample heating occurs [140, 142, 143, 168] (likely this was not detected in earlier APT due to lower sensitivity). So, in potential conflict with the thermal evaporation theory, detection of contaminant H_2^+ is now known to not require thermal pulses.

Tsong et al. conducted isotope-tracing in FIM-like experiments on a Ni tip, where a mixture of light and heavy hydrogen gas was added (H_2 and D_2, but not HD), and evaporation was triggered using laser pulses [169]. Intermixing between the atoms of the supplied H_2 and D_2 to form HD^+ molecules was observed at field strengths below approx. 30 V/nm, with the extent of intermixing seen increasing with decreasing field strength. This means that at least a fraction of hydrogen which evaporates as H_2^+ ions apparently does at some point undergo dissociation and recombination, or another process leading to an exchange of hydrogen atoms between molecules (e.g. intermittent formation of H_3 molecules). At approximately 20 V/nm, the amount of H_2^+ ions that have gone though a mixing process was observed to be in the range of 25% [169]. Unfortunately, this type of experiment has not been followed up in later research, especially not in the context of modern APT, such that the relevance of such mechanisms for current APT methods is unknown.

Potential controversy also exists around the evaporation mechanism of contaminant H^+. At least on some materials, adsorbed hydrogen on the surface can transition easily into an absorbed state, where it is present in the shape of single H species. These likely undergo “normal” field evaporation and contribute to the observed contaminant H^+ in materials where this is likely, such as Pt, Pd and Zr [140, 170-172].

Besides this, post-ionisation and dissociation of H_2^+ has been proposed as an alternative H^+ producing mechanism, which does not depend on the presence of single H species on the sample [142]. Post-ionisation is a process where shortly after evaporation, whilst the ion is at a critical distance from the sample surface, an electron tunnels from the ion into the sample, thus increasing the charge state of the ion [173]. If post-ionisation of H_2^+ occurs, the result is two protons without any potentially binding electron, so the “molecule” dissociates instantly, producing two H^+ ions [174].

Post-ionisation is more likely when electric field strengths are high, and correspondingly, shifts from H_2^+ to H^+ with increasing field strengths as reported throughout literature, which is in support of the post-ionisation mechanism [142, 165, 169, 170]. The critical field strength from which more H^+ than H_2^+ is detected in experiments was found to be in the range from 25 V/nm to 32 V/nm [165, 169, 170].

2.2.2. The H_3^+ ion in APT

Besides H^+ and H_2^+, H_3^+ is occasionally detected in APT [175]. H_3^+ is a stable, triangular molecule ion [176, 177] which has long been known to form in the gas phase through the reaction [178]

$$H_2^+ + H_2 \rightarrow H_3^+ + H$$

Equation 2

Similar reaction pathways have been proposed in early research on ionisation in FIM-like experiments, where hydrogen was supplied as imaging gas [175, 179]. Hydrogen pressures in these studies were considerably higher than in current APT experiments. Clements et al. [175] however pointed out that such a gas phase reaction was rather unlikely to be the dominant H_3^+ production mechanism in APT/FIM after observing that the occurrence of the ion is strongly associated with protruding corner atoms at a sample tip, indicating a reaction on the surface rather than in the gas phase.

It is also noted that a gas-phase reaction, even if it was occurring, likely is undetectable in APT which uses time-of-flight to determine ionic identities. The products of the above reaction need to conserve the kinetic energy of educts, so depending on where the reaction is happening between sample and detector and how much kinetic energy the H receives, the measured time-of-flight and mass-to-charge ratio for the H_3^+ could likely be anywhere above 2 Da (from H_2^+). In particular, detection of m/n=3 Da (for H_3^+) is not any more likely than any other TOF or mass-to-charge ratio. Therefore, even if this reaction is occurring in APT, the resulting H_3^+ is not detected as such. Gas-phase reactions in APT therefore can likely be ruled out [170, 175].

A range of alternative formation mechanisms has been proposed since [165, 169, 175, 180-183]. The most recently proposed mechanism is by Rigutti et al. [146]. In their research on evaporation of contaminant hydrogen from semiconductors, it was found that H_3^+ is detected in correlated evaporation events with H^+. This led to the assumption that H_3^+ likely is a product from two field-adsorbed H_2 molecules on the sample surface:

$$1\ H_2(field-adsorbed) \rightarrow H_3^+(g) + H^+(g) + 2e^-$$

Equation 3

It is not yet known if other intermediate steps in this reaction are involved [146]. However, this appears to be a sound theory and the presented evidence is convincing, at least for materials where all or most of the contaminant hydrogen is present as field-adsorbed H_2. It could however be different in materials where a significant amount of absorbed single H is present.

With the requirement that single H is available on the specimen surface, it has been proposed that H_3^+ involves a reaction between absorbed H and field-adsorbed H_2 [170, 175, 180]:

$$H_2 + H \rightarrow H_3 \rightarrow H_3^+ + e^-$$

Equation 4

It is unclear if the intermediate step of neutral H_3 exists at all, or how stable it is [180-182]. Neutral H_3 is unstable under normal conditions, however it has been argued that either the ionisation occurs immediately before it can fall apart [175], or that it could be stable under the high-field conditions at the sample surfaces in APT [165, 169, 182, 183]. I expect that the stability of neutral H_3 on a surface and the influence of the field is material dependent, so if this mechanism is relevant in APT in the first place, it could possibly explain a material-dependence of measured H_3^+ fractions seen across the literature [165, 169]. Alternatively, it has been proposed that the true mechanism does not involve a neutral H_3 step at all [180].

At this point, it is not possible to determine with certainty what the exact processes are, and what the material-dependence is.

2.2.3. Complex H-containing Ions

Complex metal hydride ions, e.g. TiH^+ or ZrH_2^+ are commonly observed in APT, and can form due to both sample or contaminant hydrogen [139, 143, 171, 184]. Their abundance is strongly dependent on the involved elements, and for some elements (e.g. tungsten) the detection of hydride ions seems impossible, presumably as these are not sufficiently stable. Dissociation of metal hydride ions is also possible, which can result in the detection of additional H_2^+ and H^+ ions with energy deficit [145, 185-187].

It has been observed that the field evaporation of a specimen is "enhanced" [188] in the presence of hydrogen, meaning that the evaporation field of a sample is lower, or the voltage at which field evaporation sets in is lower [188, 189]. Nishikawa et al. [190, 191] rationalised this through (what I would describe as) a lens-like effect, where a field-adsorbed hydrogen on the sample surface effectively enhances the field strength on the sample atom directly below it to promote evaporation [187, 190], however at least in some materials an alternative explanation could also be formation of hydrides with decreased evaporation field [145, 185].

In pulsed voltage APT experiments, this results in the observation of increased energy spreads of ions which evaporate as hydrides. Vurpillot et al. [145, 185] showed for aluminium samples that the evaporation field for AlH^+ ions is slightly lower than for Al^+. This means during pulsed voltage APT, the AlH^+ ions tend to evaporate at a slightly earlier point during the voltage pulse, rather whilst the voltage is ramping than during the pulse peak. The effective evaporation voltage and therefore kinetic energy for AlH^+ is thus lower, and if subsequent dissociation occurs, this results in detection of Al^+ and H^+ ions with energy deficits.

2.2.4. Origin of Hydrogen in APT

Several possible supply routes for the contaminant hydrogen that is detected in APT/FIM are theoretically possible and have been discussed in the past.

The residual gas in the APT vacuum chamber is believed to contain a major fraction of H_2, which may be the source of the contaminant [140, 192]. This is due to the use of stainless steel vacuum chambers: this material can dissolve and release hydrogen, therefore acts as a (virtually) infinite reservoir of the contaminant. Conversely, a near complete suppression of the contaminant is observed in a specially built atom probe where the vacuum chamber is made from titanium, with stainless steel avoided where possible [192]. However, it has also been found that baking of APT samples prior to the experiment reduces the amount of the contaminant

[193]. This could suggest that an appreciable amount of hydrogen is introduced with the sample, rather than being present in the vacuum chamber itself.

A third theoretically possible source of contaminant hydrogen is from hydrogen containing species other than H_2 in the gas phase, like H_2O or CH_4. The appearance of oxygen containing molecules in nominally oxygen free tips may indicate a certain contribution of water vapour [143]. Potential supply mechanisms involving such molecules have not been studied in detail to date.

Besides of these contaminant hydrogen sources, accidental introduction of hydrogen into specimen during preparation a frequent observation. Due to the ubiquity of hydrogen in the environment and chemicals used during sample preparation, the number of potential hydrogen sources during sample preparation is high, and pin-pointing a particular source may be challenging. Using the terminology of this thesis, this is not contaminant, but sample hydrogen. Nevertheless, the most important sources shall be briefly discussed.

Firstly, hydrogen pickup may occur from chemical agents in grinding, polishing or cleaning processes during sample manufacturing. For titanium, this was shown by Ding et al found an increased number of hydrides in samples which were prepared through polishing in colloidal silica and etching in a solution of HF and HNO_3, compared to dry ground material [194]. Arroyo et al compared various cleaning agents for steel specimen and noted a strongly increased hydrogen content in samples cleaned using a HCl-containing solution [195]. Even re-wetting of dried-in salt solution droplets on steel surfaces due to high humidity was found to result in corrosion and associated hydrogen-pickup [196]. Clearly, careful selection of chemicals and methods during sample production are vital for accurate investigations on sample hydrogen.

FIB-preparation of APT samples has been found to result in increased amounts of sample hydrogen, for example in titanium [147, 197] , zirconium [194] [198] and steel [193]. The critical step during FIB preparation appears to be the sharpening of the tip. Chang et at proposed that this may be a consequence of the ion beam continuously causing a oxide-free, reactive surface which could allow for easy hydrogen absorption [197]. Use of Cryo-FIB during the tip sharpening has been shown to effectively counter this incorporation of hydrogen, likely due to a slower diffusion of adsorbed hydrogen in the material [197, 198].

Electrochemical polishing of microscopy specimen as well can lead to accidental incorporation of hydrogen into the material, for example in titanium [199]. In the context of APT, this has for example been observed in the context of electropolished magnesium alloys [200]. Karnesky et al [201] described a possible replacement of trapped deuterium in steel samples during electrochemical polishing with hydrogen from the electrolyte, composed of perchloric and acetic acid. However, conflicting with this claim, experiments by Chen et al [202] where steel specimen which were electropolished in fully deuterated electrolytes did not show a relevant introduction of deuterium. Incorporation of hydrogen into the material during electropolishing appears material dependent, and is not necessarily problematic.

2.2.5. Supply Route of Contaminant Hydrogen in APT

Controversy exists around the potential supply route of contaminant hydrogen. Two pathways appear possible, and it is not yet clear if or for what material which mechanism is more relevant. These are direct arrival, where hydrogen arrives directly at the evaporating surface of the APT sample, and shank diffusion, where hydrogen diffuses along the specimen shank towards the tip apex. Unfortunately, no easy experiment to discriminate between the two has been thought of so far, and existing arguments involve complex and conditional reasoning.

For NiCr samples, Sundell et al. [142] measured the dependence of the hydrogen signal on the standing (DC) voltage in voltage pulsed APT, and the pulse energy dependence in laser pulsed APT. Lower DC voltages (inversely, higher pulse fractions) in pulsed voltage mode results in higher amounts of contaminant hydrogen, and higher laser energies (beyond a certain threshold) lead to lower amounts. The authors argued that if the supply route was shank diffusion driven by electric field gradients, then the opposite observation should have been made in pulsed voltage APT, and if it was shank diffusion driven by thermal diffusion, then the opposite dependence on laser energy should have been detectable. Therefore, it was concluded that direct arrival is more compatible with the observations.

Kolli et al. [143] studied the dependence of hydrogen on experimental parameters for Cu samples, including tip base temperature and laser energy. In agreement with Sundell, it was found that thermal diffusion of hydrogen on the shank is unlikely to be relevant. It also was estimated that hydrogen condensation on the sample due to cryogenic conditions is negligible at temperatures above 10K, which is significantly below the usual temperature range in APT. Since contaminant hydrogen on Cu is observable nonetheless, the conclusion is that the hydrogen more likely arrived directly at the tip apex.

A different stance was taken by Yoo et al. [144], who compared the contaminant hydrogen signal on sodium- and platinum samples. DFT (Density Functional Theory) simulations for hydrogen on the surfaces of these materials showed that hydrogen coverage and therefore supply through shank diffusion is likely for platinum, but not for sodium. This tallies up with their experimental observations where no H^+ and H_2^+ were observed on the sodium sample, and this has been interpreted as indication of surface diffusion as the potential supply mechanism.

I would add that this conclusion however hinges on two implicit assumptions: Firstly, field evaporation of hydrogen from sodium would occur to a detectable extent if it was present at the specimen surface, and secondly, chemisorbed hydrogen is the underlying cause of the contaminant hydrogen signal in APT. Concerning the first requirement, the evaporation fields of sodium and platinum are strongly different (11 vs 45 V/nm [136]), whereby the evaporation field of sodium is one of the lowest of all elements, below any commonly run material in APT [136]. It is therefore not certain if the observed difference in contaminant hydrogen might not possibly also be explicable through effects due to the electric field, for example if the strength of field adsorption of H_2 (Section 2.1.2) becomes too low at these fields, or if a critical evaporation or ionisation field of hydrogen is undercut. Regarding the second requirement, this arises because the DFT simulations cover only the case of single chemisorbed hydrogen atoms on the metal surfaces, but this does not allow for conclusions about eventual field-adsorbed H_2 species, which by other authors were seen as major contributors to the observed contaminant signal [142, 146].

The so-called Southon formula [203, 204], derived to estimate the supply rate of gas molecules to specimens in FIM-like arrangements, has been used to estimate the supply of contaminant H_2 from the gas phase to the specimen [138, 144, 205, 206]. If there is enough supply, then direct adsorption could be considered. Across the three occasions in the literature where this has been attempted, the results span a range from "the right order of magnitude, approximately 1 hydrogen molecule per second […to support the direct arrival mechanism]" [205] over a time of 13.28 hours for a full coverage of a sample with a monolayer of hydrogen [206] (which is not enough to support a direct arrival mechanism), to 1800 years [144] (which is even less). Clearly, a deeper study of this formula and its applicability, and the influence of various experimental parameters, which admittedly vary across all the instances where it has been used, could be helpful.

In earlier studies, Drachsel et al. [163] studied the hydrogen signal in a FIM environment where a pulsed laser (frequencies significantly below the ones currently used in modern APT) was fired at the tip. It was found that directly after laser pulses, the hydrogen signal intensity dropped, and only recovered after approximately 0.5 ms. This could also show that shank diffusion is a relevant supply mechanism, and the laser pulses cleared adsorbed hydrogen from the shank, disrupting the supply for a short timeframe.

Hellsing et al. [168] also made an argument about supply disruption, but towards the opposite view, in a study on voltage pulsed evaporation from tungsten tips. There, it was found that – given the evaporation field is exceeded during voltage pulses – the strength of the pulse (pulse fraction) seems to be irrelevant to the hydrogen signal. It was argued that if shank diffusion was occurring, then stronger pulses should clear a larger area of the sample from hydrogen (similar to the laser in Drachsel et al. [163]), thus moving an eventual diffusion front of hydrogen on the shank further away and weakening the signal. As this was not observed, direct adsorption was concluded to be more relevant.

2.2.6. Isotope Effects on Hydrogen in APT

Due to the high relative difference in masses of protium and deuterium (natural abundance: 0.0156% [207]), isotopic effects are more pronounced than for other elements in APT. Given identical supply of either H_2 or D_2 in the residual gas atmosphere during a FIM experiment (pressure range: 10^{-8} to 10^{-4} mbar), Drachsel et al. [163] found the rate of D^+ detection to be lower by a factor of $\sqrt{2}$ than the detection of H^+. This was ascribed to the lower impingement rate of D_2 on the sample in the gas atmosphere at unchanged temperature.

Similarly, it was observed that the dissociation rate of H_2^+ into H^+ is higher by a factor or $\sqrt{2}$ for deuterium compared to protium [163]. Conversely, the ratio of H_2^+/H^+ is higher for protium than for deuterium. This could possibly be interpreted in the light of post-ionisation [173], since the flight speed of deuterium (twice as heavy as deuterium) will be slower than protium by a factor of $\sqrt{2}$. It therefore remains for longer at a critical distance for post-ionisation and subsequent dissociation to occur, making it more likely. This phenomenon has likely also has been observed in a recent experiment, albeit the results have been interpreted differently [170].

2.2.7. Control of Detected Amount of Contaminant Hydrogen

The amount of contaminant hydrogen is strongly dependent on experimental parameters. Two recent studies investigated the dependence of the strength of the contaminant hydrogen signal in modern[2] APT, using NiCr [142] and Cu samples [143]. The findings are summarised in Table 3.

It emerges that the electric field is a major relevant factor for the behaviour of contaminant hydrogen. In modern APT, the electric field is typically not a directly controlled parameter. Instead, a feedback loop is in place to adjust the voltage to keep the detection rate constant during APT experiments, which in turn affects the electric field. Parameters which influence the field indirectly (e.g. laser energy and tip base temperature) should have at least an indirect effect on contaminant hydrogen in constant detection rate experiments.

Table 3: Influence of APT parameters on the concentration of contaminant hydrogen

Parameter	Material	Tested range	Effect on contaminant Hydrogen concentration	Reference
Laser Energy	NiCr	~0.25 nJ – 0.7 nJ (wavelength: 532 nm)	Increase up to approx. 0.4 nJ, decrease above	[142]
	Cu	40 pJ — 80 pJ (wavelength: 355 nm)	Decrease with increasing energy	[143]
Base Temperature	NiCr	40K – 240K	Increase with temperature, approx. saturation from 200K	[142]
	Cu	20K – 80 K	No clear trend, rather decrease with increasing temperature	[143]
Pulsing rate	NiCr	50kHz, 200kHz	Decrease with increasing rate, inversely proportional	[142]
	Cu	100 – 500 kHz	Decrease with increasing rate	[143]
Voltage (Laser mode)	NiCr	4kV – 9 kV	Increase until ~7.7kV, slight tail-off afterwards	[142]
Pulse fraction (Voltage mode)	NiCr	12% - 30%	approx. linear increase	[142]

A consistent observation across the existing literature is a decrease in the overall amount of detected contaminant hydrogen at high field strengths [142, 146, 208]. Three mechanisms which could lead to this negative field dependence at high fields have been proposed.

Firstly, field ionisation of hydrogen ahead of the tip could be at play [142, 208]. When the electric field is sufficiently strong, gas molecules can be ionised in front of the sample surface before arrival through tunnelling and accelerated away from the sample, similar to FIM. When the field strength during an APT experiment is sufficiently high, this should lead to the ionisation of any hydrogen molecule approaching the tip from the gas atmosphere, effectively leading to a hydrogen-free surface on the specimen [209]. This explanation, however,

[2] By “modern APT”, I refer to wide field-of-view APT using local electrodes and pulse frequencies in the multi-kHz range.

requires that a direct supply of hydrogen from the gas phase to the tip is the main supply mechanism, which is controversial (see Section 2.2.5).

Alternatively, it may be possible that hydrogen on an APT tip ionises off-pulse once a critical field strength is exceeded [146]. Interestingly, for both this and the field ionisation mechanism, the supply rate of contaminant hydrogen towards the tip is not necessarily altered at high fields, and it even is technically still present in the spectrum. Since the ionisation or evaporation occurs off-pulse however, it should appear as part of the TOF-constant noise floor in the spectrum rather than in peaks, therefore cannot be identified.

In contrast, it has also been proposed that a high electric field alters the strengths at which single hydrogen atoms are bonded to the surface. Theoretical calculations for chemisorbed hydrogen on W, Ni or Re using jellium models or DFT show that the binding strength of the H to the surface decreases with increasing field strength until chemisorption eventually becomes energetically unfavourable [168, 183, 205]. The critical values range from 50-60 V/nm (jellium model, W-110 surface) [168] to 30-35 V/nm (Rhodium, DFT) [183]. This would essentially mean that at sufficiently high field strengths, the surface must be hydrogen-free. It is important to note however that current research points towards a major role of H_2 as opposed to H in causing the contaminant signal [142, 146, 170]. Energetic considerations regarding only single absorbed H may therefore not be sufficient to explain the disappearing contaminant at high field strengths.

In previous studies, this effect has successfully been employed to suppress contaminant hydrogen on a tungsten sample [208]. It is however noted that the field strength at which the sample was found to be protected is 38 V/nm, which is above the evaporation field of most metals. Thus, this method would therefore only be applicable to a limited number of high-evaporation field materials e.g. W, Rh, Mo.

In addition to a decrease of hydrogen with increasing field strength, some existing experimental evidence could also indicate that the hydrogen-field relationship reverses from negative to positive if the field is below a critical value, such that lower electric fields lead to less contaminant hydrogen. Firstly, the observations of Sundell (NiCr specimen) [142] and Kolli (Cu specimen) [143] indicate that the use of higher laser energies (lower electric fields) result in less contaminant hydrogen. Secondly, Sundell observe a continuous increase in contaminant hydrogen in a pulsed-laser APT experiment where the electric field increases throughout, up to a threshold from which the negative relationship between field and contaminant sets in [142]. Potential reasons for these observations could be a decreased binding strength in field-adsorbed hydrogen at low fields [142, 143], a lower supply, or the undercutting of a critical field for hydrogen field evaporation or ionisation.

2.2.8. APT Detection Strategies for Hydrogen

As stated in the introduction to Chapter 2, APT in theory has the same sensitivity to all ions, and therefore can image hydrogen as any other element. The contaminant hydrogen signal however obscures hydrogen coming from the sample, such that only a sum signal of contaminant and sample hydrogen is imaged, making direct and accurate measurement impossible. Nevertheless, various methods exist to still enable use of APT for research on hydrogen [140].

Firstly, it is usually possible to reduce the contaminant hydrogen signal by choosing suitable experimental parameters. Reduction of contaminant hydrogen to 1 atomic-% or less is often possible by optimising

parameters, such as frequency and detection rate. When this is paired with a specimen containing a high amount of sample hydrogen, e.g., hydride phases, the spatial distribution of sample hydrogen above the remaining contaminant signal can be resolved [198, 206, 210, 211]. The absolute accuracy at which the concentration of sample hydrogen is measured is reduced, though may be sufficient for the intended research purposes. An early example for this is by Sepehri-Amin et al. [212] shown in Figure 9, where hydrogen-rich phases in a Nd-Fe-B powder are imaged clearly despite the presence of contaminant hydrogen. The concentration of hydrogen in the hydrogen-rich phase is approximately 60 atomic-%, while the fraction of contaminant hydrogen in this study likely is less than 1% [212].

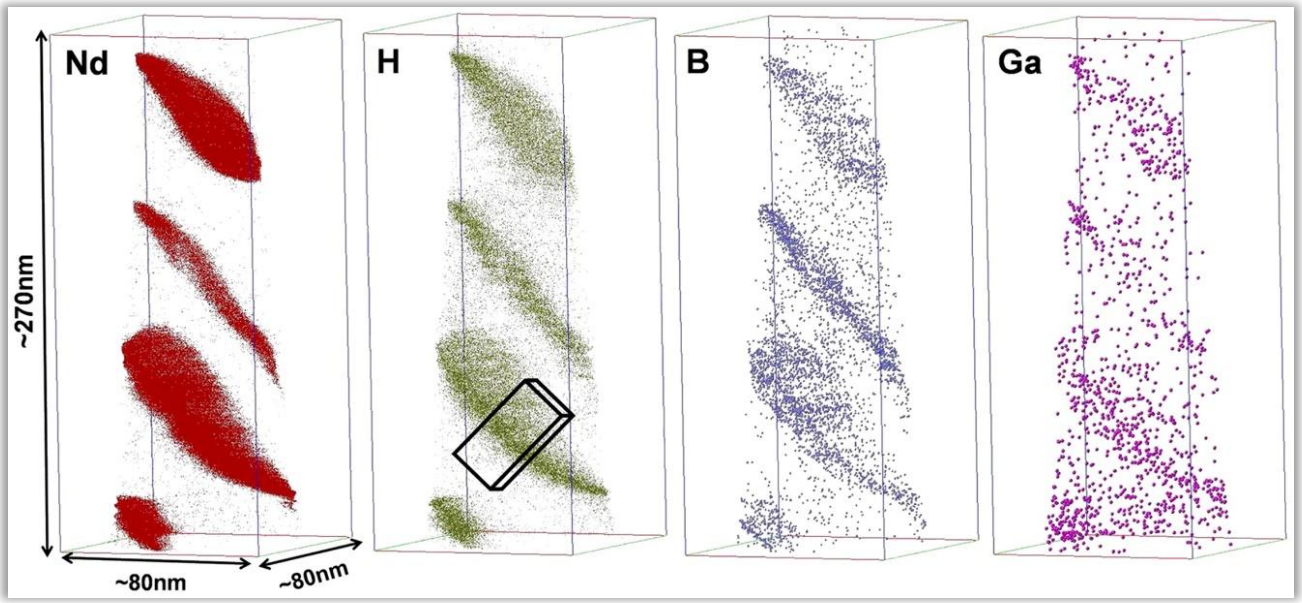

Figure 9: Reconstruction maps of Nd, H, B and Ga of a Nd-Fe-B sample. Taken from [212]. Copyright 2010 by Elsevier B.V. Re-used with permission.

Optimisation of experimental parameters for low contaminant hydrogen cannot achieve an acceptable signal-to-noise (sample-to-contaminant-hydrogen) ratio of the concentration of sample hydrogen is too low. Consequently, direct imaging of naturally abundant hydrogen (protium) becomes impossible. In these situations, deuterium tracer experiments can be used. The natural abundance of deuterium is 0.0156% [207], therefore the contribution of this isotope to the contaminant hydrogen can be neglected. Conversely, if a sample is prepared using deuterium instead of natural hydrogen, the time-of-flight spectrometry in APT can distinguish between contaminant and sample hydrogen, as shown in the example spectrum in Figure 10A.

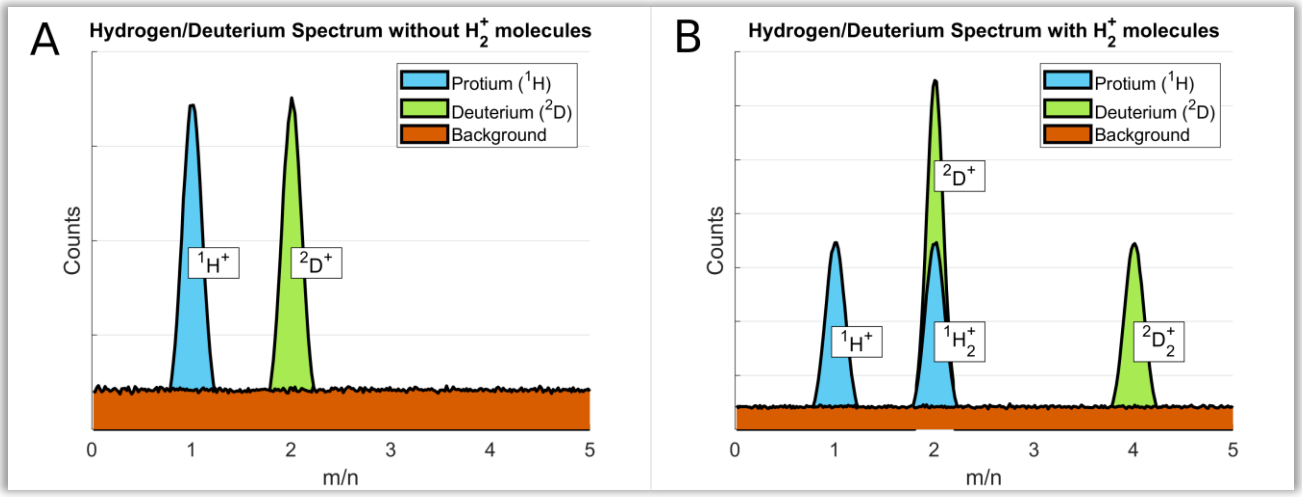

Figure 10: Schematic drawing of APT diagram showing hydrogen and deuterium without (A) and with (B) H_2^+ molecules. Also published in [141].

An additional difficulty to this however is the evaporation of H_2^+ ions. The mass-to-charge state ratio of this molecule ion (2.1057 Da [213]) is too close to the D^+ ion (2.0141 Da [213]) for APT to distinguish. This is illustrated in Figure 10B. The overlap between H_2^+ and D^+ is "rank deficient" and cannot be mathematically decomposed [214, 215], therefore accurate imaging of deuterium through the D^+ ion is only possible when the H_2^+ overlap is avoided.

The commonly-used solution to this problem, pioneered for steel samples by Takahashi et al. [214, 216], is the use of pulsed voltage evaporation to achieve high fields where only H^+, but no H_2^+ ions are detected. The signal at a mass-to-charge-state ratio of 2 can then be assumed to consist of pure deuterium (D^+), which enables deuterium detection with very high sensitivity. Imaging of trapped deuterium at carbides in steel was successful at concentrations of less than 10 deuterium atoms per carbide [214], as shown in Figure 11. The method has been successfully used in subsequent studies by different APT groups, mostly on steel [214, 216-226].

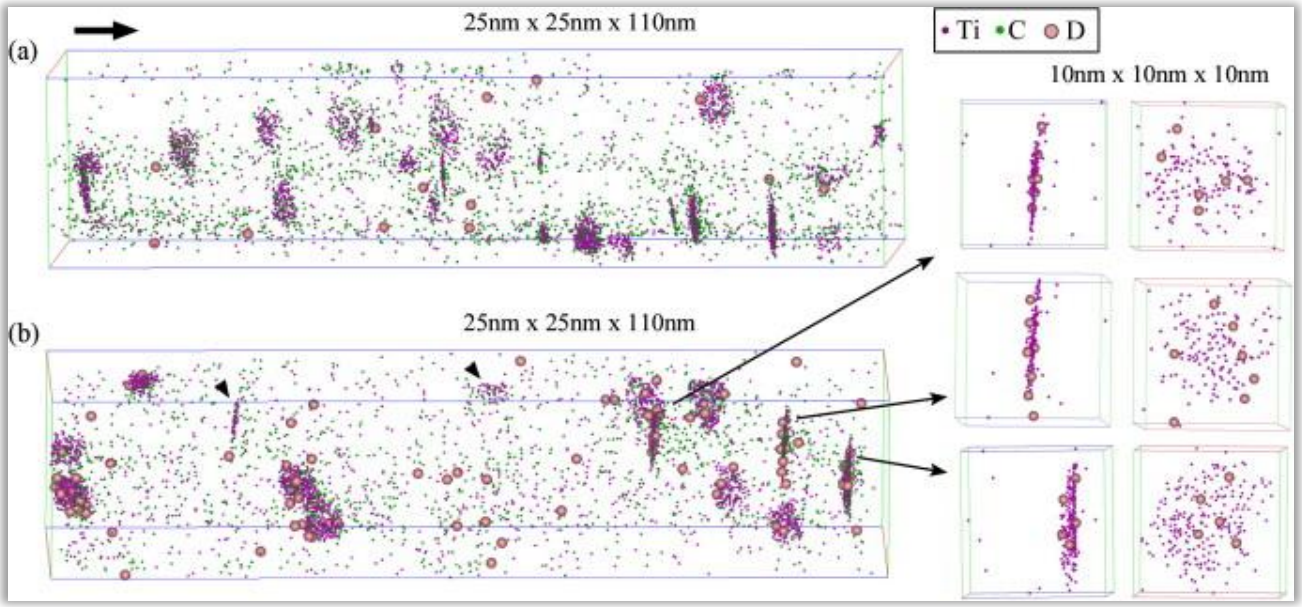

Figure 11: Deuterium imaged at titanium carbides in a steel sample. Taken from [214]. Copyright 2010 by Acta Materialia Inc. Re-used with permission.

Currently, deuteration can be seen as a "best practice" method for hydrogen imaging in APT, even when concentrations of sample hydrogen (deuterium) are not critically low [171, 172, 184, 222-225, 227, 228].

Nonetheless, there are limitations to this technique. Firstly, it requires samples to be prepared with deuterium, which is impossible in some cases such as for geological materials (because of timescales and unclear material histories) or partially transmuted material from nuclear reactors. Secondly, if pulsed voltage evaporation is used, this restricts the method to materials which can be analysed using this mode (electrically conductive samples, typically metals). Pulsed voltage mode is also associated with lower yield for most materials, making it more difficult to obtain datasets of useful size.

Alternatively, deuterium tracing has also be applied to heavier ions, e.g. D_2O^+ in catalysts [229] or SiD^+, D_2^+ in solar cells [230, 231]. Observation of such ions enables detection of deuterium in APT despite of the presence of H_2^+ molecules. However, the non-decomposable overlap of H_2^+ and D^+ persists in these experiments. The observation of deuterium under such conditions therefore is purely qualitative, but no conclusion about concentrations in the material can be drawn. In particular, as the tendency for the evaporation of molecules may vary across the APT sample, only very limited conclusions about the location of the deuterium within the sample can be drawn.

2.3. Summary and Proposed and Conducted Research

As documented in Section 1.2, plasma-facing tungsten tiles are subject to a wide range of harsh conditions. Whilst the isolated effects of all these influences on the material is at least to some extent understood, it is not well known how the combination of all these influences will affect tungsten in the ITER divertor throughout its lifetime. Hydrogen behaviour is strongly influenced by mutual damage effects [35, 232], and, subsequently, a number of experimental studies on hydrogen retention and damage in combination with irradiation, helium and/or temperature loading have been carried out.

Existing experimental studies however largely examine relatively macroscopic parameters such as total or depth-profiled retention, and (electron-) optical damage inspection, e.g. blisters and cracks [79, 80, 87, 127, 134, 135, 233, 234]. Simulation studies have examined the interaction of hydrogen with fusion-related defects, such as vacancies [84, 90, 128, 232, 235, 236], providing the theoretical base on which macroscopic phenomena can be interpreted. Nevertheless, there is a gap in the literature examining the real behaviour of hydrogen and other fusion related damages on the nanostructural level, which is needed to assess the relevance of simulation-derived interpretations and provide proper mechanistic understanding.

The most important reason for this gap is that imaging of hydrogen in metals with high resolution is particularly challenging, and no established standard technique exists. The most common analysis techniques in material research, electron beam microscopy and X-ray diffraction, are not suitable, as the interaction of hydrogen with —beams and X-rays is weak, resulting in a signal that is usually too weak for meaningful analysis, especially in settings where the hydrogen concentration is low [108].

APT is a potentially valuable method in the investigation of hydrogen in plasma-facing tungsten. It has been applied to fusion relevant tungsten samples in the past [237-243], but so far only for the investigation of precipitates and radiation damage, not for the investigation of hydrogen. However, APT is known to work for detection of trapped hydrogen in low concentrations, as publications on other materials have shown [214, 217]. FIM on a deuterium implanted grain boundary in tungsten has also been successful [244]. From the existing literature, it appears feasible to extend hydrogen imaging protocols in APT for imaging of hydrogen in tungsten.

In this thesis, I present my results on hydrogen imaging methods in APT, and their application to deuterium implanted tungsten samples. In Chapter 3, my experimental work around the fundamental behaviour of contaminant hydrogen in APT are presented. Contaminant hydrogen is unlike any other element in APT since it does not actually originate from the sample material. This makes it a very exciting phenomenon to study. Based on my findings on contaminant hydrogen, I develop a method which allows imaging of sample hydrogen in tungsten, using laser-assisted field evaporation mode.

In Chapter 4 I successfully apply this method to the imaging of deuterium implanted in irradiation damaged tungsten samples. The results from this show characteristic depth profiles of deuterium retention. APT enables hydrogen imaging in fusion tungsten samples at significantly higher magnifications and depth sensitivities than existing methods. This is significant to research on fusion reactors, and application to a wider set of deuterium implanted samples in future research is instructive and straightforward.

Finally, I present a large-scale data analysis of archival APT data – the first of its kind – in Chapter 5. To achieve this, I wrote code to automatically export data from archives, and apply statistical analyses to the datasets. A particular emphasis of this analysis rests on hydrogen, and I show that field dependence in the behaviour of contaminant hydrogen exists, observed across multiple past experiments. Use of archival data, it is shown, is of great potential for future APT research, and the scope for future extension of my work is vast.

3. Fundamental Hydrogen Imaging Methods

3.1. Rate Cycling in APT

Previous research has shown that contaminant hydrogen in APT arrives at the evaporating surface of the sample whilst the experiment is running [142, 143]. Changes of flux (evaporated ions per time) affect the relative amount of contaminant hydrogen that is observed in APT datasets, because faster APT runs (higher fluxes) leave less time for contamination to occur. This can be exploited in order to statistically estimate the amount of hydrogen in a sample: If the amount of hydrogen in an APT tip is measured at a range of evaporation rates or pulse frequencies during an experiment, the approximate amount of sample hydrogen can be estimated. The following chapter develops this technique.

3.1.1. Theory

It has been reported that the amount of detected contaminant hydrogen in APT is approximately proportional to the inverse of pulsing rate [142, 143], indicating an at least nearly time-constant supply of contaminant hydrogen. The time available for hydrogen to arrive at the tip is therefore proportional to the (mean) time between evaporation events t_E during the APT experiment. t_E is the inverse product of field evaporation rate per pulse r_{evp} (dimensionless) and pulse frequency f_{pulse} (in Hz):

$$t_E = \frac{1}{f_{pulse} * r_{evp}} = \frac{1}{f_{pulse} * r_{det} * \zeta}$$

Equation 5

($r_{det} \rightarrow$ dimensionless Detection Rate, $\zeta \rightarrow$ Detection Efficiency)

By changing the experimental conditions with time one can measure the observed hydrogen concentration H_{obs}, as a function of evaporation rate or pulse frequency. Since the contaminant hydrogen supply is limited by the time available for hydrogen arrival and the true sample hydrogen concentration can considered to be unaffected by the evaporation rate, it is possible to extrapolate the expected hydrogen concentration at zero time between evaporation events. This extrapolation corresponds to a theoretical measurement with infinitely high field evaporation rate. Assuming a smooth behaviour of hydrogen contamination, when the amount of contaminant hydrogen H_{cont} is proportional to t_E, such an extrapolation corresponds to theoretically zero contaminant hydrogen. Consequently, I propose that the extrapolated concentration can predict the true amount of hydrogen originating from the sample H_{sample}.

$$\lim_{t_E \to 0} H_{obs} = \lim_{t_E \to 0} \left(H_{sample} + H_{cont}\right) = H_{sample} + 0$$

Equation 6

Interestingly, as the evaporation rate and pulse frequency can be altered rapidly during an APT experiment, it is possible to record the amount of hydrogen for different rates and perform this extrapolation within a single experiment. Requirements for this are a) a sufficiently wide range of evaporation rates or frequencies covered during the experiment, b) acquisition of sufficient ions at each evaporation rate or frequency, c) a sufficiently fast response to set-point changes in r_{evp} or f_{pulse}, and d) a sample from which the data can be acquired that is sufficiently locally homogeneous.

The detection rate r_{det}, i.e. atoms detected per pulse, is an indirectly controlled parameter in APT, and maintained through control of the tip voltage. Thus, target and observed rates will differ. For this study, there is a key distinction between actual and target rate, as will be discussed subsequently (Section 3.1.4). The pulse frequency is a directly controlled parameter, deviations between set-point and actual frequency are expected to be negligibly small on modern machines, and changes can be made very rapidly.

3.1.2. Experimental

The sample material used for these experiments is a vanadium-carbide containing steel, identical to the material studied by Chen et al. [217]. This material has previously been used successfully for deuteration experiments in APT, demonstrating that deuterium tracing in such-prepared samples is feasible [217, 218]. The nominal composition of the material is provided in Appendix B-1.

Specimens with dimensions of approximately 10 x 0.5 x 0.5 mm profile were cut from a sheet of steel. The samples were then electropolished following the established two-stage process for APT samples [136] with rough stage polishing using 25 vol.-% perchloric acid in acetic acid between 25 and 15 V and the fine step polishing using 2 vol.-% perchloric acid in butoxyethanol at 5 to 15 V. For deuterium charging, an established electrochemical procedure as described in Appendix A is used.

In order to estimate the true amount of hydrogen of an APT sample within only one experiment, I propose an approach where the evaporation rate or frequency is repeatedly cycled between different values throughout the run. This way, the hydrogen signal in the same specimen is sampled for multiple rates or frequencies, and an extrapolation of the hydrogen signal at a theoretical, infinitely fast experiment (Equation 6) becomes possible. Theoretically, a linear extrapolation to such an infinitely fast experiment is already possible using only 2 support points, such that sampling hydrogen at only two different rates or frequencies would be sufficient for an extrapolation. However, in order gain additional insight, in particular as to whether the critical assumption of contaminant hydrogen being at least approximately proportional to t_E holds, three different rates or frequencies are sampled all rate cycling experiments.

In order to automatically change the rate or frequency during APT experiments, a UI automation script was devised, using AutoIT [245]. Once an APT experiment has been started, the script can monitor the cumulative number of detector events during the experiment, and change either detection rate or frequency as soon as a critical number of events (the “Step Size”) since start of the script or last rate/frequency change is exceeded.

To investigate the validity and optimal parameters of the proposed rate cycling approach, APT experiments were performed on steel tips, some of which are deuterated, to test various APT analysis parameters. In particular, the effect of time-based rate and step size is investigated, i.e. number of atoms detected before the rate is switched. To this end, three experiments for both evaporation rate and frequency cycling are conducted each, varying (average) evaporation rate and step size.

The list of experiments is shown in Table 4, and additional comments in Table 5. It is pointed out that, whilst the table lists both detection- and evaporation rate, they are not independent, but assumed to be directly proportional by the detection efficiency. The detection efficiencies used here when converting between

evaporation- and detection rate are 80% for the Cameca LEAP XS instrument [246], and 56% for the Cameca LEAP XR[3]. The identifiers (Run Numbers) of all extrapolation experiments are listed in Appendix B-2.

The datasets from the experiments in Table 4 were sectioned along the steps in the evaporation rate or frequency, such that each dataset yielded three derived datasets, for each (average) time between evaporation events t_E. For each derived dataset, the hydrogen content is calculated for every evaporation rate or frequency. Then, the theoretical amounts of hydrogen in infinitely fast experiments are calculated through linear extrapolation to $t_E = 0$.

Table 4 List of cycled rate experiments. Additional comments are provided in Table 5.

Name		Rate Parameters			Step Size	Deuterated	Temperature	Comment
		Detection Rate (%)	Evaporation Rate (%)	Frequency (kHz)	Number of Ions		Kelvin	
Evaporation Rate Cycling	Evp-Low-Rate	0.1, 1, 10	0.125, 1.25, 12.5	200	200000	No	40	*1
	Evp-High-Rate	3, 8, 12	3.75, 10, 15	200	200000	No	40	*1
	Evp-Few-Step	0.07, 0.7, 7	0.125, 1.25, 12.5	200	500000	No	50	*2
Frequency Cycling	Freq-Many-Step	1	1.25	125, 250, 333	150000	Yes	50	*1 *3
	Freq-Few-Step	1	1.25	125, 250, 333	500000	Yes	50	*1 *3
	Freq-High-Rate	5.6	10	125, 250, 333	500000	No	50	*2

Table 5: Additional comments for experiments in Table 4

Number	Comment
*1	Experiment was run on Cameca LEAP 5000 XS
*2	Experiment was run on Cameca LEAP 5000 XR
*3	These experiments were successively conducted on the same specimen

[3] It was necessary to use two different machines for some of the experiments due to a technical failure and associated downtime on one of the instruments.

3.1.3. Results

The extrapolations of hydrogen amount for the rate-and frequency cycled experiments are shown in Figure 12. It is seen that the relative counts at m/n=1,2,3 Da evolve highly linearly with t_E ($R^2 > 0.95$ for all experiments). The extrapolated fractions of hydrogen for the theoretical contamination time of zero are listed in Table 6. Figure 13 and Figure 14 show the evolution of evaporation rate in rate-cycled experiments or frequency in frequency cycled experiments alongside the hydrogen signals throughout the experiments, respectively.

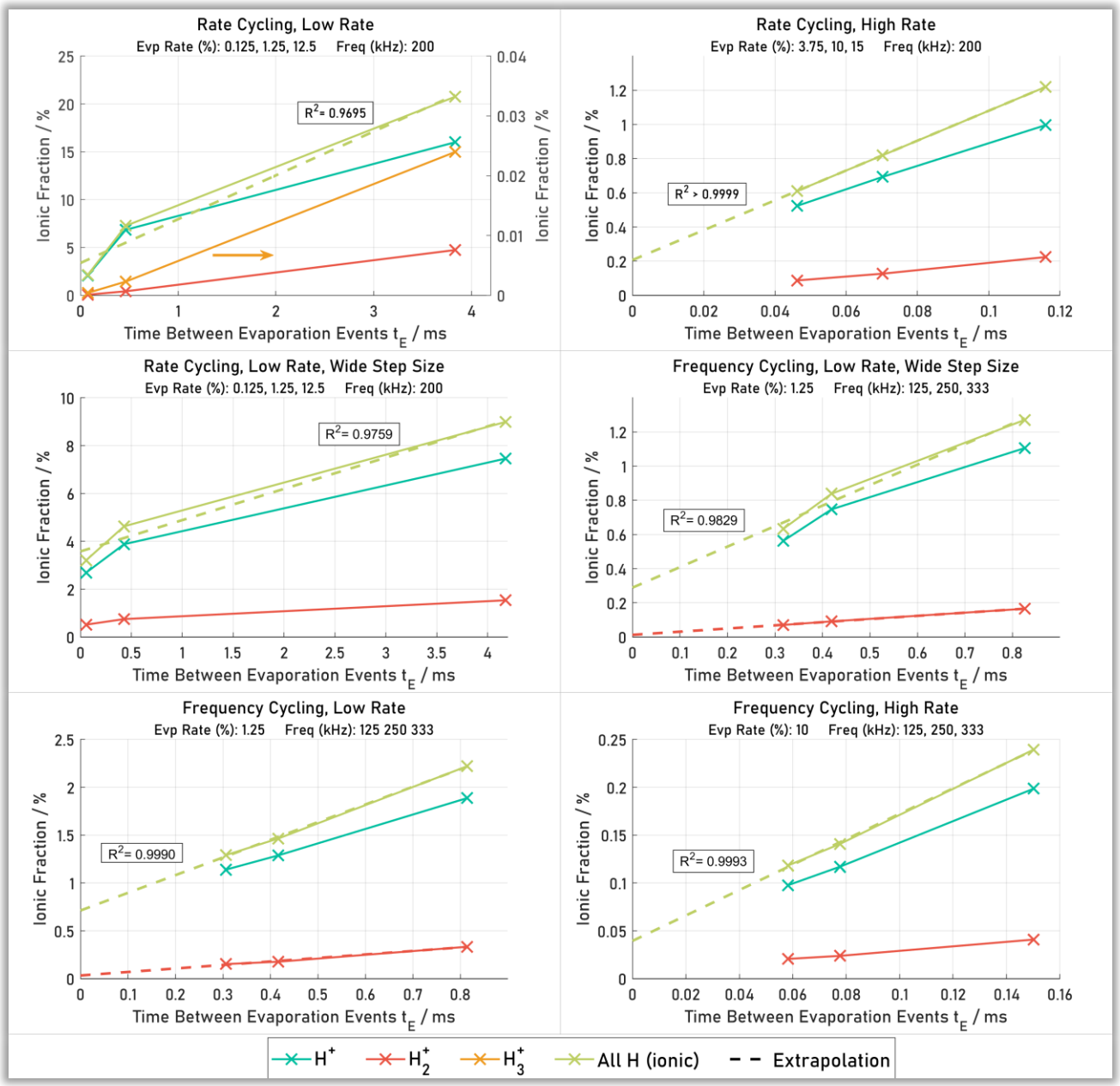

Figure 12: Extrapolation of the ionic hydrogen amounts at infinitely high evaporation rate for the cycled rate experiments. It is noted that D and E show deuterated datasets, therefore the H_2^+ fractions in these datasets are expected to also contain a certain amount of D^+

Table 6: Extrapolated amounts of hydrogen in the cycled rate experiments, predicted for $t_E = 0$

Name	Rate Cycling			Frequency Cycling		
	Evp-Low-Rate	Evp-High-Rate	Evp-Few-Step	Freq-Many-Step	Freq-Few-Step	Freq-High-Rate
Extrapolated sum, ionic-%	3.378	0.207	3.577	0.712	0.289	0.039

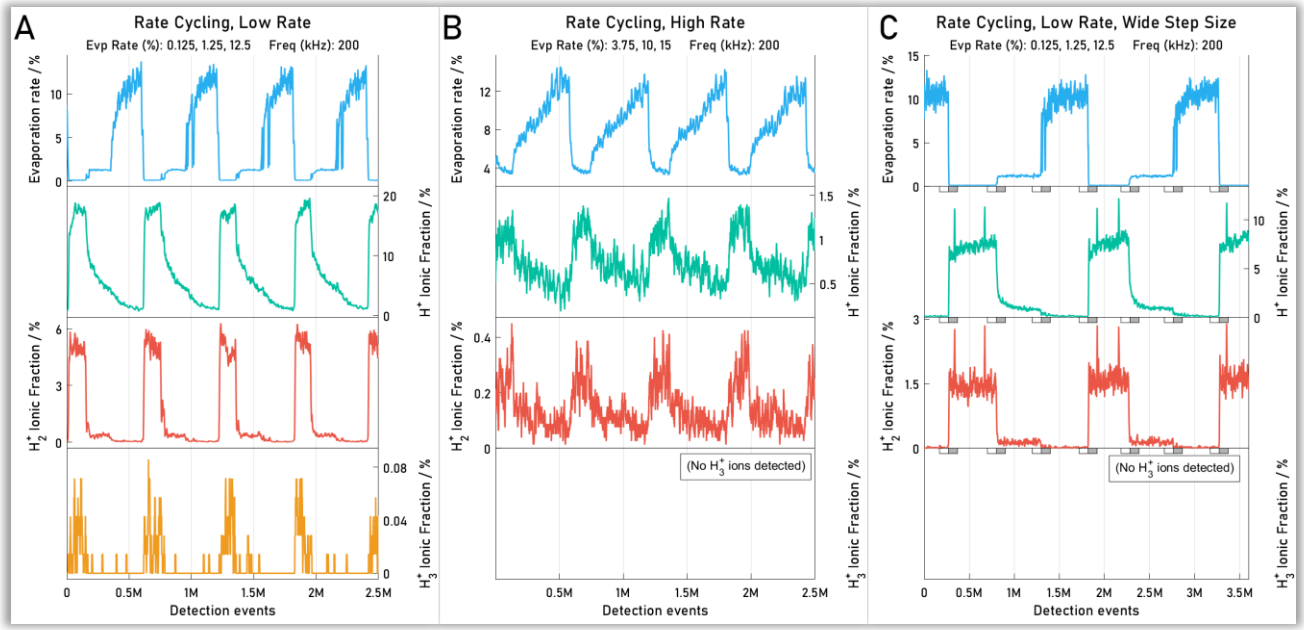

Figure 13: Evolution of evaporation rate and hydrogen fraction throughout the cycled rate experiments. The grey blocks at the x-axes in C indicate the parts of the run that were used for extrapolation based on ions directly before or after rate changes (Figure 16)

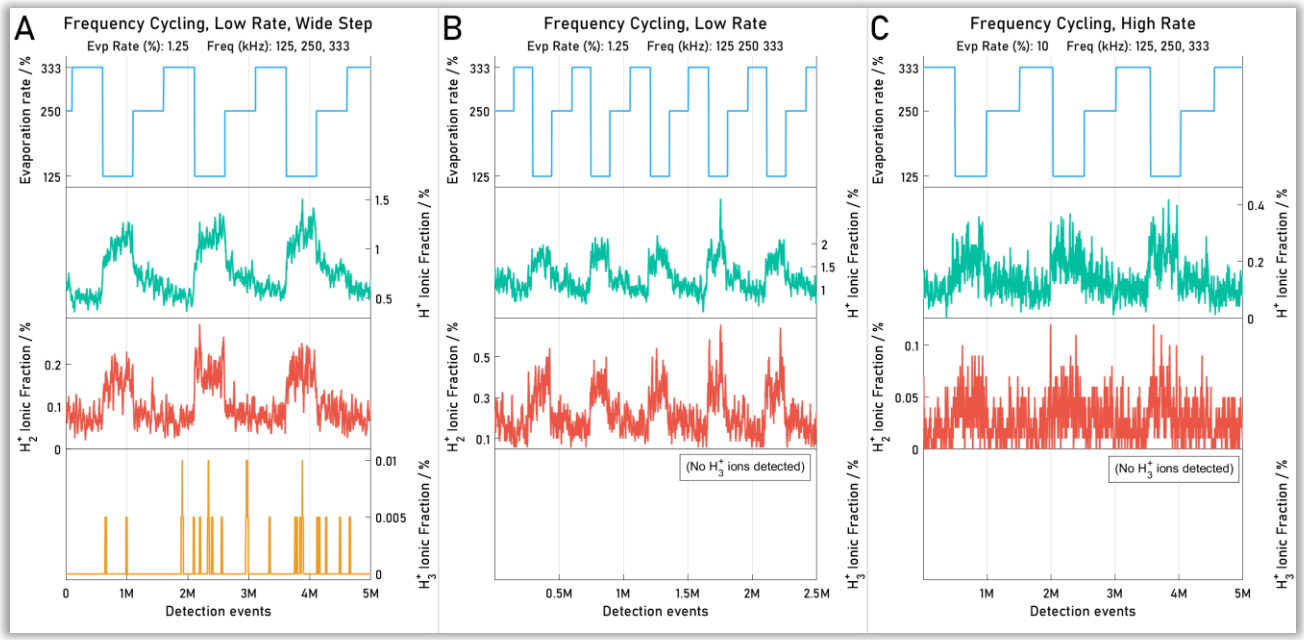

Figure 14: Evolution of evaporation rate and hydrogen fraction throughout the cycled frequency experiments

3.1.4. Discussion

Rate cycling

In all rate- and frequency cycled experiments (Figure 12) the detected hydrogen contents scale linearly with t_E, as supported by the consistently high R^2 values for these extrapolations. It is however also observed that there is a relatively high variance in the extrapolated amounts of hydrogen, from 0.039 ionic-% to 3.577 ionic-% (Table 6), which requires further discussion.

Amongst the rate-cycled experiments, only the high-rate extrapolation run (Evp-High-Rate) yielded an extrapolated hydrogen amount close to the expected values of around 0 (0.2 ionic-%), while the runs at low rate (Evp-Low-Rate and Evp-Few-Step) resulted in approximately 3.4 or 3.6 ionic-% combined H^+, H_2^+ and H_3^+. It seems unlikely that these values reflect correctly measured hydrogen contents, as they are far above hydrogen contents that are typically reached in steels [221, 247]. Figure 12A and C reveal that this is due to the H^+ ions in both experiments, which do not follow the linear trend as closely as the other species, resulting in an estimation error.

A possible factor that contributes to this nonlinear behaviour can be found in the evolution of the hydrogen content in the experiments at low rate (Figure 13). It is seen in Figure 13 that in the low-rate extrapolation runs (Evp-Low-Rate, Figure 13A and Evp-Few-Step, Figure 13C), the evaporation rate is stable when the target evaporation rate is set to 0.125%. When the target rate is switched to the higher levels 1.25% or 12.5%, the evaporation rate quickly stabilises at certain higher levels after a ramp.

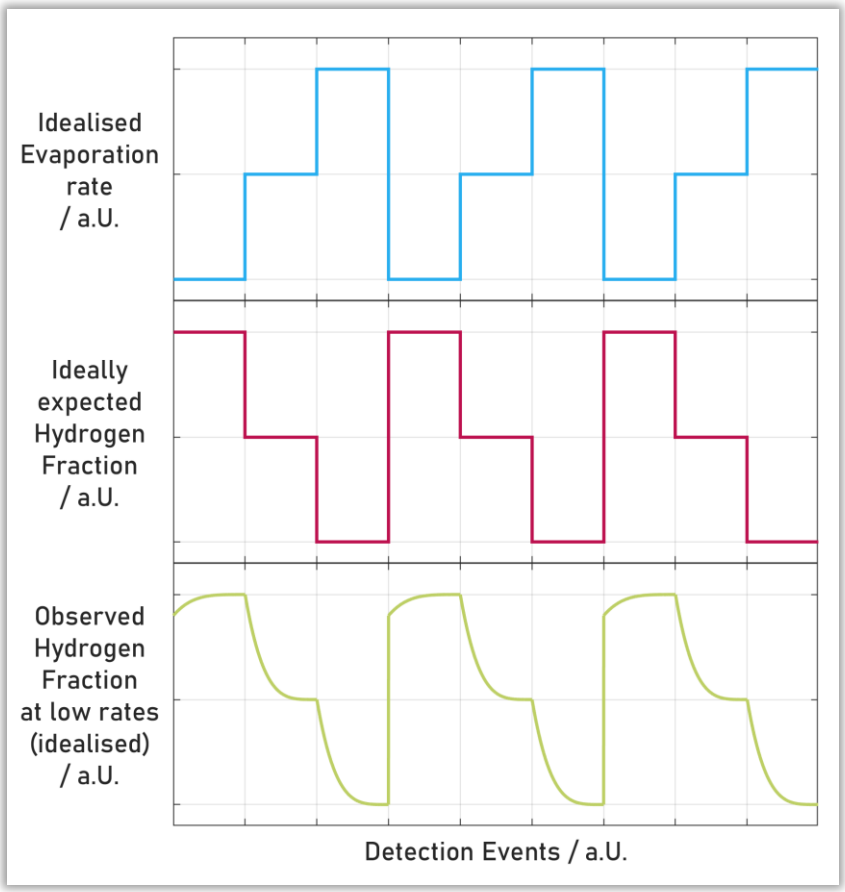

Figure 15: Idealised schematic drawings of evaporation rate and expected hydrogen fraction and observed behaviour of detected hydrogen at low rates. The data in this diagram is computer-generated for demonstration purposes, not experimental data.

However, this is not the case for the H^+rate in these experiments, which seems to react way more 'sluggish' to rate changes. This is particularly evident in the low-rate run with small step size (step size 200000, Evp-Low-Rate, Figure 13A) where the H^+rate does not stabilise at all when the target evaporation rate is set to 1.25% or 12.5%. Instead, it only gradually tails off during these phases, not reaching equilibrium before the next rate change. A schematic of this behaviour is shown in Figure 15. For clarification, these curves in Figure 15 show idealised computer-generated data for demonstration purposes, no experimental data.

In order to further investigate the effect of the slow response of H^+ to evaporation rate changes on hydrogen extrapolations, two additional extrapolations on Evp-Few-Step are conducted. In this experiment, the effect of slow "boil-off" is clearly seen (Figure 12C), but the step size is sufficient such that the detected amount of H^+ equilibrates in between rate steps. This means, it is possible to conduct extrapolation based on subsets of the data, taking only parts of the run with "stable" (after reaching equilibrium) or "transitionary" behaviour (directly after rate changes) into account. For this work, the subsets of "stable" and "transitionary" are taken as the subsets of either the last 100000 ions before or the first 100000 ions after rate changes. The light and dark rectangles in Figure 13C highlight these sections in the dataset.

The results are shown in Figure 16, with extrapolation based on the stable region in Figure 16A, and the transitionary region in Figure 16B. The much-increased linearity of stable region extrapolation, compared to transitionary becomes immediately clear. Nevertheless, even the extrapolation on the stable region in Figure 16A leads to a hydrogen content of 2.2%, which is still too high for steel. This means that transition effects in these low-rate experiments indeed add errors to the hydrogen extrapolation, however removing the affected part of the dataset is not enough to counter the effect.

On the other hand, the extrapolation result is significantly lower (0.2 ionic-%) and thereby closer to the expected range in the high-rate experiment (Evp-High-Rate, Figure 12B, Table 6). This indicates that use of high rates is likely beneficial to the extrapolation of hydrogen amounts. In my opinion, it could be that at the very low minimum evaporation rates (0.125%) which are achieved in the Extrap-low-rate experiments, the amount of contaminant hydrogen no longer scales linearly with t_E, but saturates.

It is noted that, as seen in Figure 13B, the evaporation rate never reaches equilibrium when set to one of the higher target rates in the high-rate experiment (10% or 15%), but rather is continuously ramping, not reaching the target rate before the next target rate change. This is attributed to the voltage control algorithm used by the Instrument, which seems to ramp voltages conservatively slowly if the observed detection rate is below target, but drops the voltage much faster in the opposite case. It is therefore not entirely clear from only this experiment whether the sluggish response of H^+ to rate changes actually is no longer present at the high rates in Extrap-High-Rate, or whether the observation of such a tail-off is only impeded by the continuously changing rate.

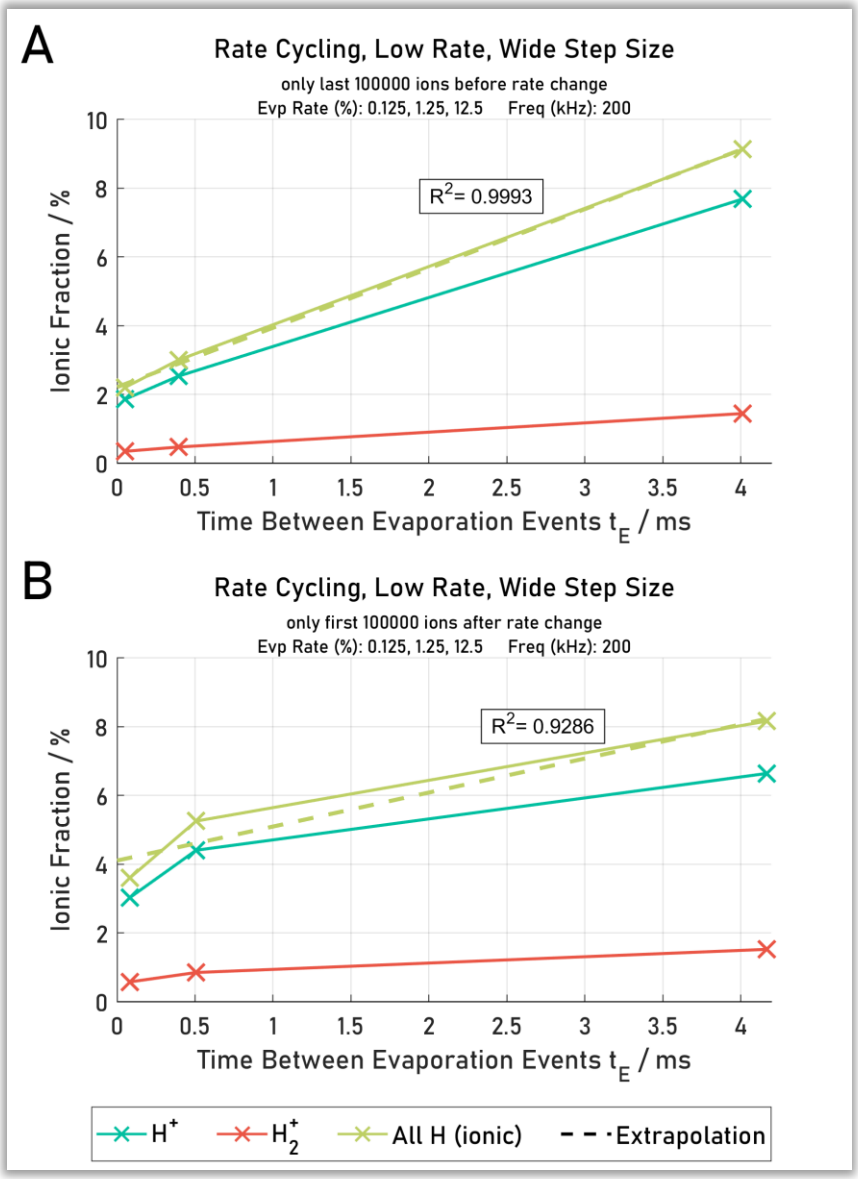

Figure 16: Extrapolation of hydrogen content in Evp-Few-Step, using the entire dataset (A), only the last 100000 ions before rate changes (B), and only the first 100000 ions after rate changes

Frequency cycling

Overall, the observations on frequency cycled experiments (Figure 12D-F) are similar to those on the rate cycled experiments. The dependency of contaminant hydrogen on time between evaporation events t_E in general follows a high degree of linearity, however the experiments with low rates (Freq-Few-Step, Freq-Many-Step) are connected to a sluggish behaviour of H^+ and an overestimation of the hydrogen content (Figure 14). It is noted that, amongst these two low-rate experiments which use identical experimental parameters except from step size (150000 vs 500000), the hydrogen response to frequency changes in Figure 12 appears more linear.

This higher linearity may possibly be interpreted as the low step size mitigating the slow boil-off effect of contaminant hydrogen, thus leading to a more accurate hydrogen extrapolation. However, an analysis of the H^+ evolution throughout the experiments, as shown in Figure 14, rather suggests a different interpretation. Changing the frequency at a high rate (after every 150000 ions in Evp-Many-Step / Figure 12A, as opposed to after every 500000 ions in Evp-Few-Step / Figure 12B) smears out the slow tail-off of H^+ across the different frequencies at which hydrogen is sampled. In other words, the response of contaminant hydrogen fraction to

frequency changes is not correctly recorded because the frequency changes too fast for the hydrogen concentration to settle. This yields an artefact in the recorded hydrogen response, whereby the extrapolation necessarily becomes more linear (and constant). I would therefore conclude that the low step size most likely does not fundamentally change the slow boil-off effect, but only obscures it in the extrapolation diagrams. On the other hand, avoiding low rates in frequency cycling experiments (Freq-High-Rate, Figure 12C) indeed seems to successfully counter slow boil-off effects. This is in agreement with the observations on the rate-cycled experiments.

In contrast to the experiments with stepped evaporation rate and Freq-High-Rate, the data in Freq-Few-Step and Freq-Many-Step was collected on a deuterated tip. The extrapolated amounts of the m/n = 2 Da peaks, which in these samples contain D^+ as well as contaminant H_2^+, extrapolate to 0.015% (Freq-Few-Step) and 0.036% (Freq-Many-Step). This is above the extrapolated amount of H_2^+ in the non-deuterated Freq-High-Rate (0.0071%). It could indicate that deuterium was successfully measured in these experiments. However, there is uncertainty about this, as no repetitions of the experiments were conducted and sources of error like potential reservoirs of contaminant hydrogen might exist.

Comparison of Rate and Frequency Cycling

When comparing rate- and frequency cycling, it is clearly seen that changes in target detection rate (Figure 13) in rate cycling experiments require a certain time and number of evaporation events until being reflected in actual detection rate, as is to be expected in such a feedback controlled system. This complicates interpretation and analysis of cycled rate experiments, as actual rate and target rate may differ significantly. The frequency changes on the other hand are instantaneous and without ramp time or delay (Figure 14), offering a higher degree of control. This is a clear advantage of frequency- over rate cycling.

One additional difference between frequency- and rate cycling, and potential source of error, that needs to be considered is the influence of the electric field. It has been shown [138, 142] that changes in the electric field during an experiment influence the amount of detected contaminant hydrogen (indeed, this is also observed in the sub-evaporation threshold experiments in Section 3.2). In the detection rate cycled APT experiments, changes in the evaporation rate are achieved through adjustments of the DC voltage [248]. Thus, if the electric field is systematically different during phases with different evaporation rates, a systematic error is possible. Frequency changes do not involve changes in field strength, therefore should not be affected by this potential artefact.

To investigate systematic differences in field strength, the Charge State Ratio (CSR) of Fe-56 ions can be used as a measure for the electric field in the steel specimen used in this study. This is shown in Appendix B-3. In Evp-Low-Rate, the CSR for the three evaporation rates are indeed very distinct, indicating different electric fields. This is different in the Evp-High-Rate experiments, where the CSRs between the evaporation rates are much more similar, indicating minimal change, and thus influence of the electric field on the contaminant hydrogen. Therefore, whilst field dependent errors are possible in rate cycling, this is unlikely in frequency cycling. This further cements the advantages of a frequency based approach.

Potential Depth-Profiling using Cycled Rates

The cycled evaporation rate technique can be applied in a localised way, such that extrapolation is not conducted across an entire dataset (which averages across the entire volume of the APT tip), but per sub-volume. This enables depth profiling and fully 3D spatial imaging of hydrogen concentrations in APT samples. To explore this further, two different methods for conducting localised hydrogen extrapolation are applied, layer-based for depth estimation and voxel-based for 3D estimation.

For the layer-based method, the datasets were sliced along the changes in either evaporation rate or frequency, resulting in curved layers in reconstruction space. Extrapolation is conducted for each layer using values obtained from the neighbouring layers and the current layer itself, i.e. a sliding window method. The detected amounts of hydrogen for each layer are shown in Appendix B-4, and the extrapolated amounts are shown in Figure 17. While the amounts of detected hydrogen - both H^+ and H_2^+ - increase throughout all experiments with increasing depth, the extrapolated amounts, in particular H_2^+, show a more varied behaviour. It is notable that the amount of extrapolated H^+ at least slightly increases with increasing depth in all of the experiments.

More research is needed to explain this increase, which may either be real or an artefact. It is noted that the electric fields in these experiments are relatively depth-independent (CSR curves in Appendix B-3, Exception: Evp-High-Rate in Figure 17B), meaning that field-related effects may not be able to directly explain these observations. In Freq-High-Rate (Figure 17D), the amount of extrapolated contaminant hydrogen for all layers is below 0.08%. This indicates that, with a careful selection of parameters, depth profiling could be feasible if the hydrogen concentration difference exceeds approximately 0.1% under optimal circumstances.

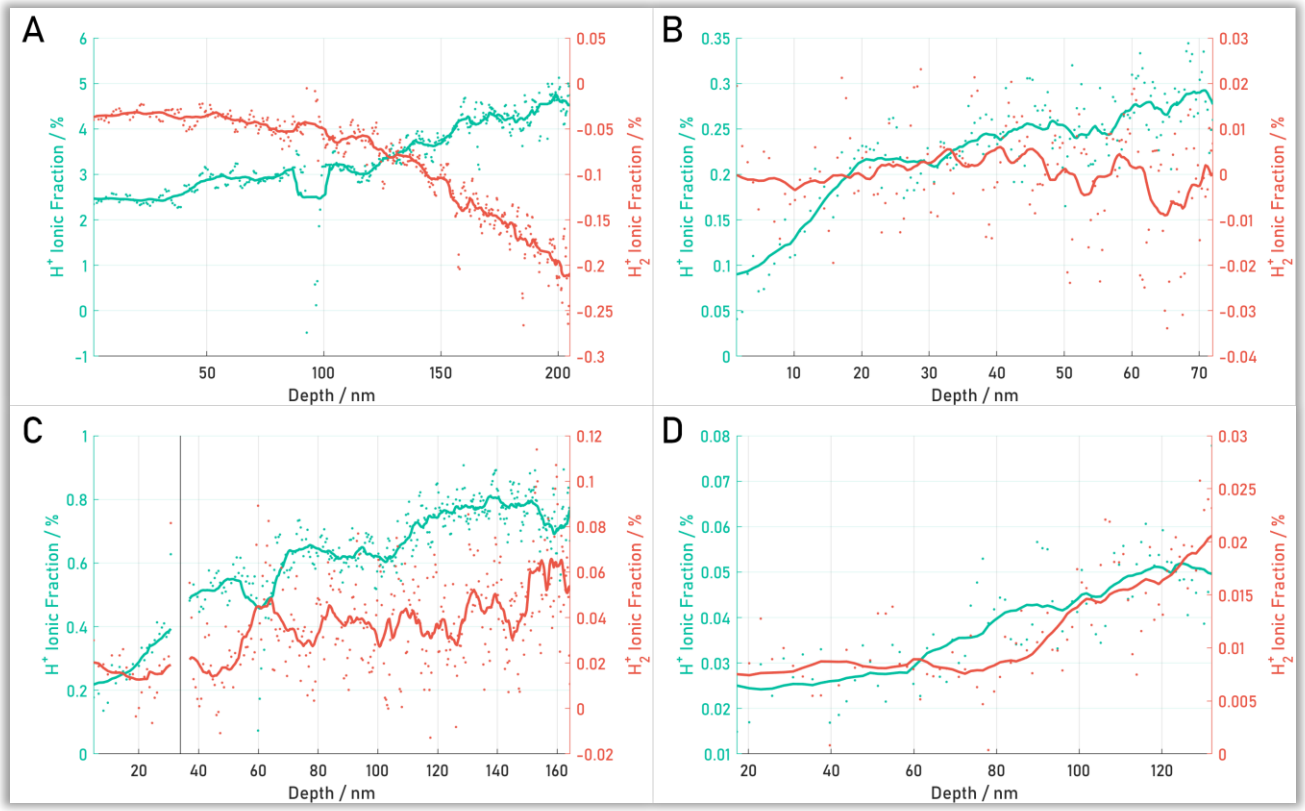

Figure 17: Depth profiles of extrapolated hydrogen in Evp-Low-Rate (A), Evp-High-Rate (B), Freq-Few-Step and Freq-Many-Step (C) and Freq-High-Rate (D). Freq-Few-Step and Freq-Many-Step in C were subsequently run on the same APT specimen (see Table 4), therefore are combined into one diagram. The dots in the diagrams correspond to extrapolated values for each layer, and the lines show moving averages across the layers.

Finally, a voxel-based extrapolation method is demonstrated as a potential method of extrapolating hydrogen with a full 3D resolution. For this method, the dataset is sliced into voxels, and a highly localised evaporation rate and concentration for every hydrogen detection event is calculated based on detection events before and after every incidence of hydrogen detection within that voxel. Extrapolation is then conducted for every voxel using the hydrogen ions contained within.

Figure 18 shows the voxels, and corresponding extrapolated amounts of hydrogen, in the Freq-High-Rate experiment. Slices parallel and perpendicular to the tip direction are shown. Once more, it can be seen that the extrapolated amount slightly increases throughout the run, in line with Figure 17D. However, no clear co-segregation of the extrapolated hydrogen with the carbides in the sample is seen, likely as concentrations are too low to permit full 3D analysis. This specimen is not deuterium-charged and only contains trapped hydrogen as contained in the as-received material, the concentration of which is unknown.

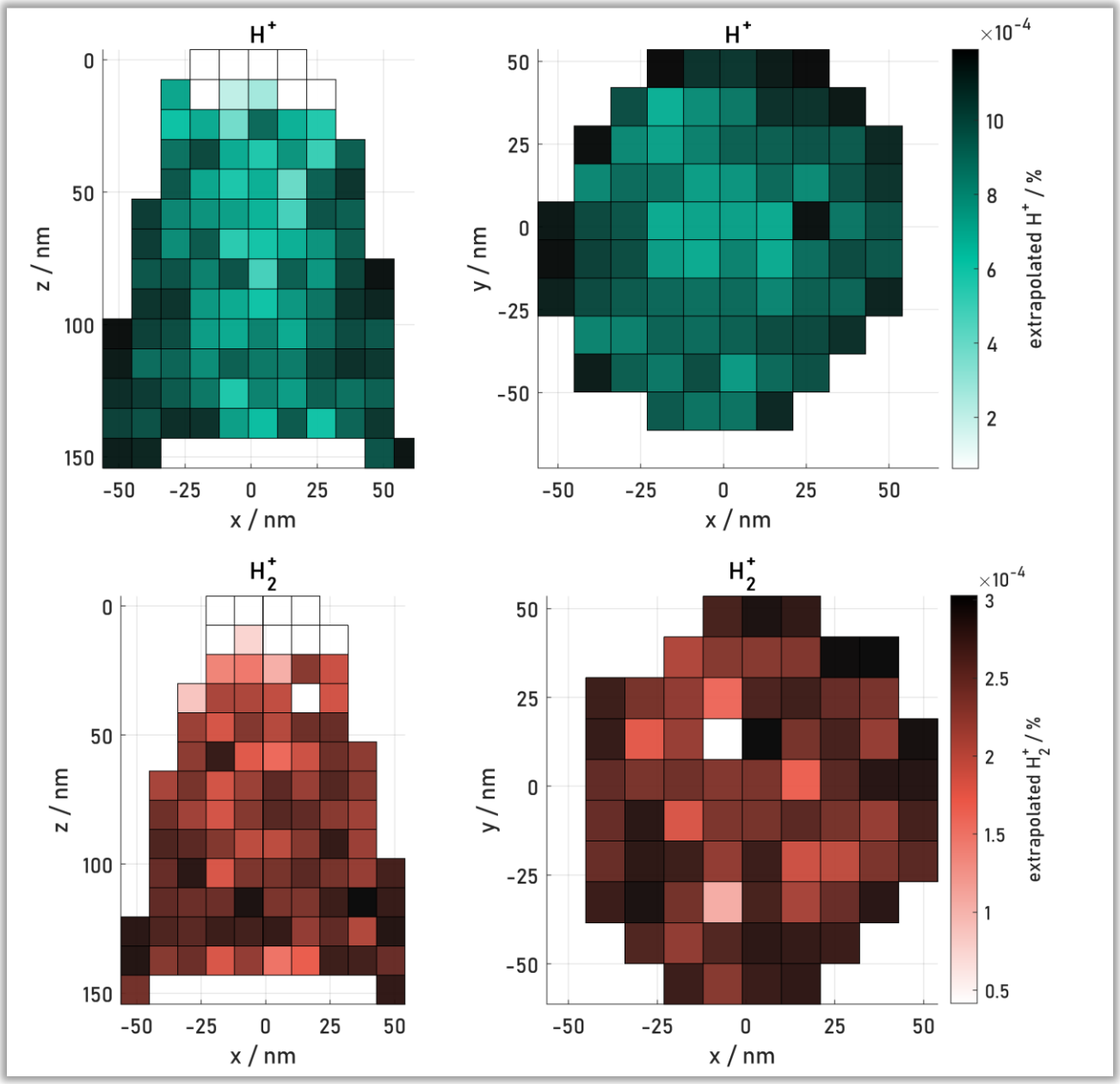

Figure 18: Voxel-based extrapolation of H^+ and H_2^+ in Freq-High-Rate. The colour bar scales are clipped, i.e. voxels with extrapolated hydrogen fractions above or below the ranges of the colour bars appear fully white or black.

3.1.5. Conclusion

Using the fact that hydrogen contamination is time-dependent, an extrapolative approach was developed to estimate contamination levels. Cycling the frequency or evaporation rate during an experiment is a new method to estimate hydrogen content from within samples, which does not require deuteration of the material. Localised extrapolation allows for spatial localisation of the hydrogen in the material, but scatter and artefacts are problematic, especially if the relative concentration of hydrogen that is to be analysed is low. A good application for the technique appears to be investigation of which ions or peaks in a spectrum likely carry contaminant hydrogen, as these will be rate dependent.

The experiments indicate parameters which are favourable to the accuracy of the method. Firstly, high fluxes (i.e. high rates and frequencies) should be preferred: this appears to prevent the build-up of hydrogen reservoirs at the tip and generally leads to lower concentrations of contaminant hydrogen, improving the signal-to-noise ratio of imaging of sample hydrogen. Secondly, frequency cycling should be preferred over rate cycling, since frequency changes are – other than rate changes – instantaneous, and do not require changes in voltage or field. Thirdly, it is advisable to monitor the CSRs and avoid strong swings in electric field throughout the experiment to avoid potential field-related errors in estimated hydrogen content.

3.2. Field Dependence of Hydrogen

It is already known that the voltage (or electric field) during APT experiments has some influence of the appearance of the contaminant hydrogen spectrum [142, 146, 165, 169, 170, 187]. However, the exact relationship between field and contaminant hydrogen over a wide range of field strengths has not yet been determined. More knowledge about this relationship will help select appropriate parameters in APT studies on (sample) hydrogen, as experimental parameters can be chosen to minimise potential confusion between contaminant and sample signal. In this chapter, the contaminant hydrogen spectrum is researched using a method which involves APT experiments on tungsten specimen below the evaporation threshold. It is found that at high electric field in pulsed laser APT, contaminant hydrogen is detected at a higher-than-expected mass-to-charge ratio. The behaviours of contaminant hydrogen in pulsed voltage- and laser mode APT are strongly different.

3.2.1. Theory

Tungsten specimen in APT can be held stably at electric field strengths which would cause evaporation of most other materials [136]. Since contaminant hydrogen arrives at the APT samples during the experiments (as also demonstrated by the experiments in Chapter 3.1) [141], it can be detected to field-evaporate from tungsten samples even under conditions where no base material evaporates, below the evaporation field of tungsten. Such APT experiments can apply different parameters to the same tungsten tip and collect the contaminant hydrogen signal without consuming the actual sample. By carefully setting the voltages such that the field evaporation threshold is never exceeded, it is possible to investigate the hydrogen spectrum at a wide range of analysis conditions on only one tungsten specimen that never changes geometry. This can be used to analyse the effect of the electric field on contaminant hydrogen while eliminating any artefacts due to sample geometry changes, as would be observed if this data was collected in “normal” APT experiments which involve evaporation of sample material.

Since the evaporation in APT is dependent on the electric field rather than the voltage, knowing the field at the emitter is critical to the interpretation of any observation in such sub-evaporation threshold experiments. Commonly, the electric field in APT is calculated from charge state ratios (CSRs), using Kingham curves [173, 249]. In the absence of any field evaporation (other than contaminants), no CSRs and thus field strengths can be obtained directly. However, an indirect approach is feasible: before starting to sample hydrogen at sub-evaporation fields, the specimen is run in “standard” APT analysis mode such that tungsten ions evaporate. This allows for a CSR and hence field strength to be calculated at a particular voltage. The established formula for the electric field strength [136]

$$F = \frac{V}{k_f R}$$

Equation 7

($F \rightarrow$ electric field, $V \rightarrow$ voltage, $k_f \rightarrow$ field factor, $R \rightarrow$ tip radius) indicates that for an unchanged geometry (constant k_f and R), applied voltage and field strength are proportional. Therefore, the field at any voltage below the evaporation voltage can be calculated through linear interpolation from the voltage and field at the onset of evaporation.

3.2.2. Experimental

The experiments in this chapter are conducted on a nominally hydrogen-free tungsten needle, electropolished in 2% NaOH solution at 2-10 V AC [210]. The solubility of hydrogen in tungsten at room conditions is extremely low, such that the accumulation of any significant amount of hydrogen in the sample appears unlikely [72]. The sample is evaporated in pulsed voltage mode (30% pulse fraction, 200 kHz pulse frequency, 50 K specimen base temperature) until the run stabilises, surface contaminants are no longer detected, and a pole figure in the desorption map becomes visible. Then, the voltage is decreased until evaporation of tungsten completely halts. This provides a clean tip that serves for all subsequent experiments.

APT experiments are conducted at constant voltage, as opposed to the common practice in APT of continuously adjusting the voltage to achieve a target detection rate via feedback-loop. The voltage is systematically adjusted to investigate the correlation of the electric field to the contaminant hydrogen spectrum. All applied voltages are below the evaporation threshold for tungsten, such that the actual sample never evaporates. Instead, only contaminants which evaporate below the evaporation threshold for tungsten are detected.

This experiment is repeated for pulsed voltage- and laser assisted evaporation at different frequencies and laser energies, listed in Table 7. All experiments were conducted using the same specimen, and as sample evaporation is never triggered, all experiments are conducted on the same, unchanged tip with (apart from machine drift) unchanged geometry. Due to insufficient signal for automated laser targeting during the laser experiments, manual laser positioning was performed. It is noted that the control software of the atom probe instrument, which likely does not foresee a constant-voltage use case, crashed multiple times during these experiments and had to be restarted. This does not affect the results, however data across several separate APT 'runs' had to be merged. A list of APT experiment ID numbers ("run numbers") is provided in Appendix C-1.

Table 7: List of Sub-Evaporation Threshold Noise Sampling Experiments

Experiment type	Pulse Frequency kHz	Laser Energy pJ	Voltages sampled V
Pulsed Voltage	200	-	646 – 2896 in steps of 250, 3046, 3146
Pulsed Voltage	500	-	646 – 2896 in steps of 250
Pulsed Voltage	25	-	646 – 2896 in steps of 250
Pulsed Laser	200, 1000, switching every 2500 detector events	2	896 – 2896 in steps of 250, 3296, 3546
Pulsed Laser	200	10	646 – 2396 in steps in 250

3.2.3. Results

For all sub-evaporation threshold experiments, Figure 19A shows the amount of H_2^+ relative to the sum of $H^+$and H_2^+ over voltage, and Figure 19B shows the total (ionic) amount of hydrogen per time. The values in Figure 19 are noise corrected, assuming a TOF-constant noise floor [148]. It is important to keep in mind that in the pulsed voltage experiments, evaporation does not occur at the standing field, but during the considerably higher pulsed field. The terms “DC field” and “pulsed field” are used to distinguish between those. The full hydrogen spectra at all tested voltages and a conversion table for DC voltages and fields and their corresponding pulsed voltages and fields are given in Appendix C-2 and Appendix C-3, respectively.

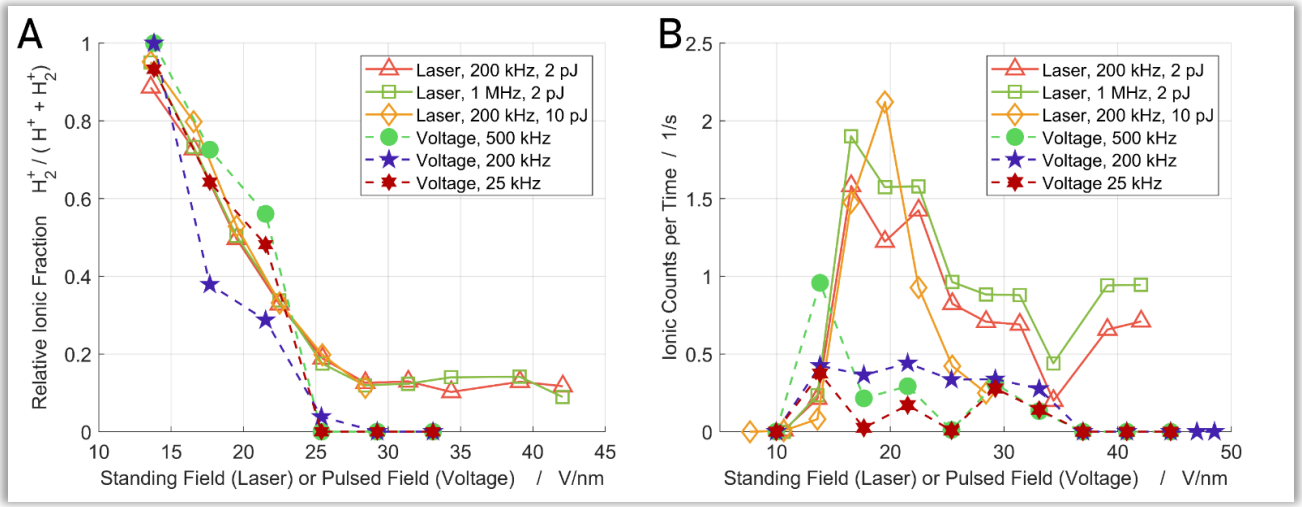

Figure 19: Ratio of H_2^+ to the sum of H_2^+ and H^+ (A) and total amount (B) of atomic hydrogen per time as detected in the various sub-evaporation threshold noise sampling experiments. The $H_2^+/(H^+ + H_2^+)$ ratio for all laser experiments – regardless of frequency and energy – is very similar and saturates at high fields at approximately 0.1. In pulsed-voltage experiments, this value drops to 0. The ionic counts of contaminant hydrogen over time (B) are higher in pulsed laser- than in pulsed voltage experiments.

It is observed in all experiments that the relative heights of the hydrogen peaks are strongly field dependent. Hydrogen peaks are first observed at 13.6 V/nm in laser mode and 13.8 V/nm (DC field: 10.6 V/nm) in voltage mode (Figure 19B). At the onset of hydrogen evaporation, the amount of H^+ is much lower than H_2^+ and H_3^+, however this changes with increasing field, such that H^+ is the dominant hydrogen species at 22.5 V/nm and above.

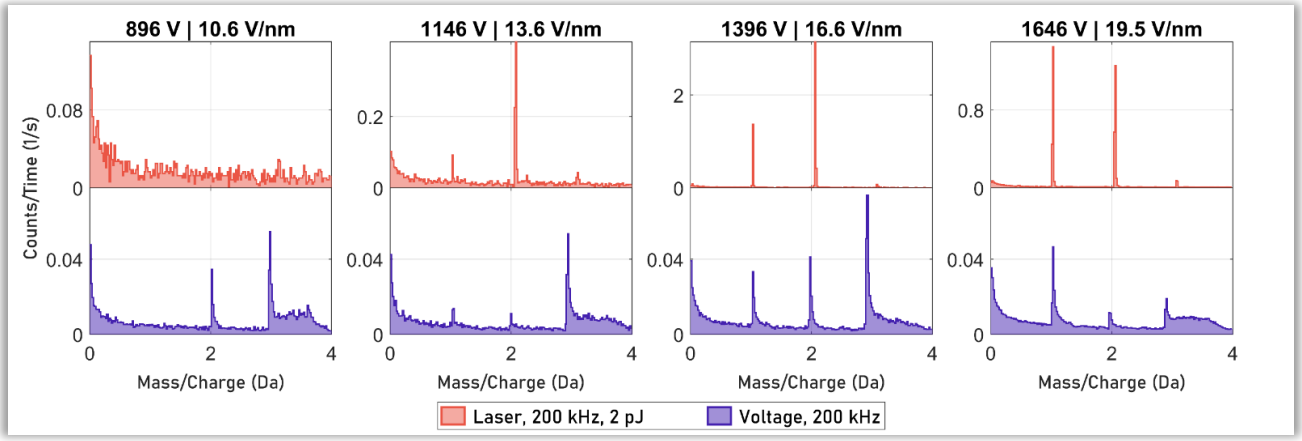

Figure 20: Evolution of the hydrogen spectra from 10.6 to 19.5 V/nm in 200 kHz / 2 pJ pulsed laser mode (red) and 200 kHz pulsed voltage mode (blue). The DC field strengths are given in the diagram headings. It is seen that with increasing field strength, the amount of H^+ relative to H_2^+ increases. H_3^+ is considerably more dominant in voltage than in laser mode.

H_3^+ is observed in similar ranges of the field in both voltage- and laser mode (13.6 V/nm to 19.5 V/nm DC in laser mode, 13.8 to 25.4 V/nm pulsed field in voltage mode), however it is considerably more dominant in voltage- compared to laser mode. This is illustrated in Figure 20, where the spectra from 10.6 to 19.5 V/nm DC field for the 200 kHz voltage- and 200 kHz / 2 pJ laser mode experiments are shown. It is also noted that the H_3^+ peak in voltage mode incorporates a relatively pronounced peak tail, which is not observed for other peaks in voltage- or laser mode. H_3^+ in voltage mode appears frequency dependent, with the high frequency of 500 kHz leading to reduced relative amounts of H_3^+ (Appendix C-3).

In pulsed voltage mode, hydrogen becomes undetectable from 28.4 V/nm DC field (37 V/nm pulsed field). Such an observation is not made in laser mode, where hydrogen continues to be detected, even at DC fields (42.1 V/nm) exceeding the pulsed field at which hydrogen disappears in voltage mode (37 V/nm, Figure 19B). However, a curious observation is made in laser mode: from the DC field where hydrogen disappears in the pulsed voltage experiment (28.4 V/nm), the H_2^+ and H^+ peaks change shape and location in the spectrum, transforming into a less sharp peak with a higher-than expected mass-to-charge ratio. In the following, the sharp peaks at the expected locations are referred to as “peaks”, whereas the term “hump” is used to describe the less sharp peaks which are observed at unusually high mass-to-charge ratios.

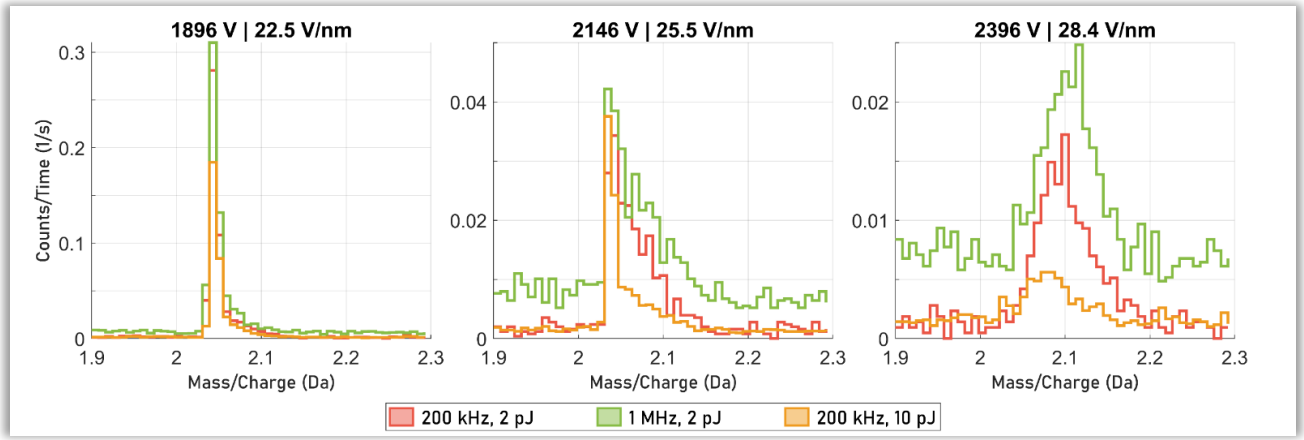

Figure 21: Field-dependent transition of the m/n=2 Da peak to hump in the pulsed laser sub-evaporation threshold experiments

For the H_2^+ peak, this is shown in detail in Figure 21, where the transition of the m/n=2 peak at 22.5V /nm (clearly a well-defined, narrow peak), 25.5 V/nm (intermediate peak-hump) and 28.4 V/nm (broader hump) in the three pulsed laser experiments is seen. Appendix C-4 contains the equivalent diagrams for the H^+ peak, showing the same behaviour. After the transition from peak to hump, the relative heights of the H_2^+ and H^+ peaks are no longer changing with increasing field, but stay constant (Figure 19A). As will be evidenced in Section 3.2 through comparison with reflectron APT data, the higher-than-expected mass-to-charge ratios are due to energy deficits of the underlying ions.

Overall, the total amount of hydrogen that is detected in laser mode is significantly (factor of approximately 3 around 20 V/nm) higher than in voltage mode (Figure 19B). It appears that the laser induced heating leads to increased detection of contaminant hydrogen. On the other hand, the influence of laser energy and pulse frequency at unchanged field strength seems small.

3.2.4. Discussion

It is clear that both field and choice of APT mode (pulsed voltage or pulsed laser) strongly impact the amount and peak height ratio of contaminant hydrogen. The current experiments show that through appropriate selection of parameters, characteristic behaviours of contaminant hydrogen can be achieved in an APT experiment: minimised amount of H^+ (low field), minimised amount of H_2^+ (high field), minimised amount of total H (voltage mode, high field), and contaminant hydrogen with energy deficit (laser mode, high field). This is of high relevance to future APT experiments aiming to image sample hydrogen, where parameters need to be tuned to avoid potential confusion between sample- and contaminant hydrogen.

Regarding the underlying mechanisms of this, the results point towards a complex behaviour of contaminant hydrogen, likely governed by multiple reactions. These shall be discussed extensively in the following. From Figure 19A, it appears that critical changes in behaviour of contaminant hydrogen are observed between approximately 25 and 30 V/nm. Therefore, the field ranges above and below the range of this threshold for change will be treated separately.

Low field strength

First, the behaviour of contaminant hydrogen up to approx. 25 V/nm shall be discussed. In this regime, the hydrogen spectrum is not empty in voltage mode, and no energy deficits are observed yet in laser mode.

In recent research on contaminant hydrogen, it has often been assumed that H_2 molecules and not single H species primarily cause the contaminant hydrogen signal. This notion appears in good agreement with the observation of decreasing H_2^+/H^+ ratios observed in the laser mode experiments presented in this study: the main evaporating hydrogen species at low voltages is H_2^+, and post-ionisation and dissociation into H^+ could be a fitting explanation for the shift from H_2^+ to H^+ at high fields. Post-ionisation is only dependent on the field, not on laser pulse frequency or -energy, therefore the relative heights of those peaks in the sub-evaporation threshold pulsed laser experiments (Figure 19A) agree very well[4].

Theoretically, correlative ion analysis [250] should be able to provide further insight into this, because H^+ would be expected to almost exclusively appear in multi-hit detector events. Unfortunately, however, the delay-line detectors currently used in APT suffer from so-called 'pile-up' effects, which strongly reduce the capability to detect ions which arrive at nearly identical time and position [251, 252]. The true number of instances of two H^+ arriving at the detector at the same time is therefore not accurately measurable.

On the other hand, due to the high amount of H_3^+ in some of the pulsed voltage experiments, it is not immediately clear whether contaminant hydrogen in this mode also originates primarily from H_2, or rather from a reservoir of H_3 on the surface (Figure 20). H_3 is not a form in which hydrogen occurs under normal conditions, therefore is considered a reaction product that forms during the experiment. Recent research by Rigutti et al. [146] on multiple hit events in semiconductors has shown that H_3^+ (and another H^+) on this material can be the product of a reaction involving two H_2 molecules [146], pointing towards H_3^+ not originating from a H_3 reservoir.

[4] I would like to point out that this trend is also observed in archival data, as shown in Chapter 5

A relevant factor to understanding the phenomenon of H_3^+ could be the pulse frequency, as amounts of H_3^+ appear reduced relative to H^+ and H_2^+ at 500 kHz (Figures in Appendix C-3). If H_2 is the dominant form in which hydrogen resides at the surface, I would expect the amount of H_3^+ to be strongly dependent on the concentration of H_2 on the surface: reactions involving two H_2 molecules in a short timeframe during or before evaporation are only likely if the population of H_2 is high. At time-constant supply of contaminant hydrogen, higher pulsing frequencies should lead to shorter average residence times for contaminant H_2 at the evaporating surface, meaning that the surface is depleted in H_2 at higher pulsing frequencies, and hence formation of H_3^+ is less likely.

High field strength

It is evident that in pulsed voltage evaporation, there is a critical field strength beyond which no contaminant hydrogen peaks are observed, which was found to be at 28.4 V/nm DC field. This is fairly close to a value of 30 V/nm that was estimated by Sundell et al. for NiCr samples, using extrapolation [142]. It has been assumed that at such high fields, the DC electric field is strong enough to ionise any contaminant hydrogen that arrives at the sample from the vacuum chamber (implying that this is the dominant supply mechanism), such that hydrogen never reaches the specimen apex and the surface is free of any hydrogen [208] – essentially, a FIM on residual gas is running in parallel to the APT experiment.

In the laser experiments however, contaminant hydrogen is detected – in the form of humps rather than peaks – at any field strength, even up to 42.1 V/nm. From the constant peak height ratio and the energy deficit of these ions, I conclude that this type of contaminant hydrogen likely ionises at a certain distance away from the sample surface.

This observation naturally leads to questions about the binding state of this hydrogen and the relevant ionisation mechanism, for which I shall outline my current thinking and hypothesis. One possible explanation might be that this hydrogen is not bound to the sample at all, but originates from residual gas that is ionised ahead of the tip during laser pulses. However, such a mechanism will – like FIM – rely on the tunnelling effect to ionise the gas, which in itself is not directly temperature dependent [253]. It is therefore unclear how laser-induced heating could trigger ionisation. An alternative explanation would be evaporation of neutral H_2 from the sample surface by the laser, which subsequently ionises and possibly post-ionises and dissociates. Such a mechanism has been proposed before [165, 167], but has proven difficult to observe and prove [142, 163]. It would also require that in pulsed-laser evaporation mode, there still is adsorbed hydrogen present at the sample surface, even at field strengths that would cause off-pulse ionisation in voltage mode.

Therefore, a possible explanation might be a combination of above processes: the laser leads to evaporation of neutral, weakly bound H_2 on the specimen shank. This H_2 then turns into a FIM-like imaging gas, and travels towards the apex very quickly, polarised and attracted by the electric field. The hydrogen may either re-adsorb closer to the tip apex, or ionise in the DC field. DC field evaporation itself is not correlated with the pulse, however as the evaporation of neutrals is, ionisation appears still sufficiently correlated with the laser pulses such that a hump in the mass-to-charge spectra occurs. If re-adsorption of such neutrals occurs, it might provide a faster track of contaminant hydrogen along the shaft towards the apex, possibly explaining the heightened amount of contaminant hydrogen in pulsed laser experiments. The amount of hydrogen that reaches the tip

through this route is limited by the amount of hydrogen that is available on the tip shaft, explaining the surprisingly low effect of laser frequency and -energy on the total amount of detected hydrogen. If this shaft hydrogen is supplied by the residual gas, this could explain the time-constant nature of contaminant hydrogen.

If the contaminant hydrogen is indeed predominantly supplied from the tip shaft, then one additional conclusion is that evaporation of hydrogen from the specimen likely still takes place at high electric fields, but outside the field of view on the shank of the specimen. At these positions, the electric field is lower than on the tip apex, but may still be sufficient to evaporate hydrogen – the detector just cannot “see” it. Fittingly however, a new ultra-high field-of-view type of APT experiment has been introduced recently (The Cameca Invizo 6000), which might possibly just be capable of providing more insight into what happens outside the field of view currently accessible to APT, and whether contaminant hydrogen evaporation indeed gradually retracts from the apex down to the tip shank as the electric field increases.

3.2.5. Conclusion

The research highlights the critical influence of the electric field on the behaviour of contaminant hydrogen, informing parameter selection in hydrogen imaging APT experiments. Three important observations are made:

- The H_2^+/H^+ ratio decreases as the electric field increases. This could be well explained by H_2 being the primary form in which the contaminant is present, and field-dependent post-ionisation and dissociation into two H^+, agreeing with existing literature [142, 163, 165]. Due to the unknown impact of detector pile-up on the detection efficiency for H^+-H^+ multiples, it is unfortunately not possible to further verify this using correlative ion analysis.
- In pulsed laser mode, the total amount of contaminant hydrogen per unit time is higher than in voltage mode. This is in line with existing literature [142, 193]. However, given the same sample geometry and field strength, higher laser energies or frequencies (within the ranges tested) do not to lead to the detection of more hydrogen.
- In pulsed voltage evaporation, contaminant hydrogen can be fully suppressed using sufficiently high fields. This could possibly be a viable strategy for countering contaminant hydrogen in APT on materials where the evaporation field is high enough. In pulsed laser experiments, a second type of contaminant hydrogen with energy deficit continues to be present, even at fields where contaminant hydrogen is fully suppressed in voltage mode. This type of hydrogen has an energy deficit and constant H_2^+/H^+ peak height ratio, possibly indicating that it ionises away from the sample surface.

More research will be needed to fully understand the relevant mechanisms that lead to the supply and evaporation of contaminant hydrogen in APT. From the current work, it becomes very apparent that contaminant hydrogen in APT is a complex phenomenon that can only be explained by the interplay of several processes, which are dependent on applied field and other experiment parameters. It appears that improvements to detectors to either increase detection efficiency for multi-events, or introduction of energy-sensitive detectors [254-256] which could discriminate single and double H^+ events by energy could greatly advance understanding and capabilities to image contaminant hydrogen. More sub-evaporation threshold APT experiments, for example on different materials, could also offer an interesting way for studying the behaviour of contaminants on APT samples.

3.3. High-field Deuterium Imaging in Pulsed Laser APT

It has been shown (Section 3.2) that contaminant hydrogen on tungsten in pulsed laser APT is detected with a higher-than expected mass-to-charge ratio (and thus an energy deficit), provided that a critical field strength is exceeded. This opens a route for accurate imaging of deuterium in tungsten using laser mode, by exploiting the energy deficit to distinguish between contaminant and sample hydrogen. By use of the rate cycling technique (Section 3.1) and by comparison of nominally hydrogen-free and deuterated tungsten spectra, the validity of this approach is demonstrated in this chapter.

3.3.1. Theory

Sample hydrogen in APT can be imaged successfully if it can be distinguished from the contaminant signal. Usually, this is achieved by using deuterated specimen, and selecting experimental conditions such that no H_2^+ is detected [214, 217]. This allows for an unambiguous observation of sample deuterium as D^+ ions in a peak at m/n=2. However, H_2^+ is normally only fully suppressed at the high electric fields which are achieved in pulsed voltage APT experiments (as has also been shown in Section 3.2), and such conditions are typically associated with low ion yield per specimen.

The energy deficit observed in Section 3.2 may possibly enable distinguishing between sample and contaminant signal for deuterated tungsten samples in an alternative way. If it is possible to produce experimental conditions where contaminant H_2^+, but not sample D^+ evaporate with energy deficit, their peaks could appear at separate locations in the mass-to-charge-state ratio spectrum, enabling differentiation between sample and contaminant hydrogen. The particular advantage of this method is that it would no longer require high-field pulsed voltage mode.

In Section 3.2 it was found that an energy deficit of H_2^+ is detected in laser-mode APT from approximately 28.4 V/nm. Experimental conditions therefore need to be set such that this field strength is exceeded. The charge state ratio of ions (CSR) is a proxy measure for the electric field strength, followingly high field strengths throughout the experiment can be ensured by running the samples in constant CSR mode. In this mode, the laser energy during the experiment is continuously adjusted, such that the CSR of one species in the mass-to-charge spectrum stays (approximately) constant.

To investigate whether such constant-CSR runs are indeed a valid strategy for hydrogen imaging, two APT experiments using this experimental condition can be conducted using two tungsten samples, one of which is nominally hydrogen free and one of which is deuterated. It needs to be shown that 1) the energy deficit of contaminant H_2^+ is reproducible in APT experiments where sample material evaporates, and 2) only the contaminant H_2^+, but no sample D^+ is affected by the energy deficit. To evidence 1), it is sufficient to demonstrate a successful constant-CSR APT run on the hydrogen free tip where H_2^+ evaporates only with energy deficit, i.e., no peak is observed at m/n = 2 Da in the mass-to-charge spectrum, but only a respective peak at higher-than expected mass-to-charge ratio.

To demonstrate 2), a cycled rate experiment (as introduced in Section 3.1) can be conducted on the deuterated sample. The contaminant H_2^+ is, other than sample deuterium, rate dependent. This means that by monitoring the response of relative peak heights to changes in pulse frequency, it can be investigated if and to what extent the various peaks in the spectrum carry deuterium. The differentiation between sample deuterium and

contaminant hydrogen is complete if the deuterium evaporates in peaks that are clearly separate from contaminant hydrogen peaks, which would amount to the presence of fully rate-independent peaks.

For further verification, it also is possible to insert an additional negative-experiment. So far, it has been assumed that the mechanism leading to the observed higher-than-expected mass-to-charge ratio is an energy deficit of the underlying ions. As consequence the higher-than-expected mass-to-charge ratio should not be observed in reflectron APT experiments, and reproduction of such an observation on a reflectron-fitted instrument must fail. This can be confirmed by repeating the non-deuterated experiment on an according instrument and confirming the non-presence of higher-than-expected mass-to-charge ratios.

3.3.2. Experimental

For the nominally hydrogen-free APT experiments, tungsten needles were electropolished in 2% NaOH solution at 2-10 V AC (same as in Section 3.2) [136]. The deuterated tungsten specimen was prepared by FIB lift-out from tungsten that had been radiation damaged (2 MeV self-irradiation) and subsequently deuterium implanted (deuterium beam energy 800 eV) (same as in Chapter 4). The radiation introduces trapping sites into the sample where the implanted deuterium can reside [257]. Mobility of hydrogen in tungsten is high, such that the implanted deuterium diffuses into the radiation-induced trapping sites [66].

The hydrogen-free (electropolished) and deuterated (fib-liftout) tungsten specimens were analysed in a Cameca LEAP 5000XS (straight-flight-path), and an additional hydrogen-free specimen was run in a Cameca LEAP 5000XR (reflectron). Pulsed laser mode was used, and the laser energies were set such that the amount of W^{3+} in the spectra is always higher than W^{2+}, following Kingham curves this corresponds to field strengths of at least 30.9 V/nm. To determine which ions carry sample- and contaminant hydrogen in the deuterated specimen, the frequency cycling technique as described in Section 3.1 is used, with frequencies of 200, 333 and 500 kHz, target evaporation rate 5%, and collection windows of 300,000 ions. As has been shown in this chapter, accuracy of estimated hydrogen amounts in cycled rate experiments benefits from high fluxes, therefore these parameters have been selected to achieve a high number of evaporated ions per time.

3.3.3. Results

Figure 22 shows the spectra obtained using the different samples and instrument types. In the nominally hydrogen-free specimen in straight-flight path APT (Figure 22A), the m/n=1 peak is split into a leading part that is at the expected position for H^+, and a second component that forms a much wider peak. No peak for H_2^+ is present at m/n=2, but only a wider peak at m/n=2.2. When a deuterated sample is used (Figure 22B), an additional peak at m/n=2 Da, presumably due to D^+ is observed, while the peak at m/n=2.2 (presumably contaminant H_2^+) persists. No split peaks, but only H^+ and H_2^+ at the expected positions of m/n=1,2 are observed in the experiment on the reflectron-fitted machine (Figure 22C).

Figure 22D shows the hydrogen amounts per (average) time between evaporation events t_E, as obtained through rate cycling on the deuterated specimen. In contrast to all contaminant peaks in the hydrogen spectrum, the m/n=2 peak, which is believed due to sample deuterium, is unaffected by t_E. No clear conclusion on the rate dependency of the m/n=4 peak (D_2^+) is possible due to its low abundance.

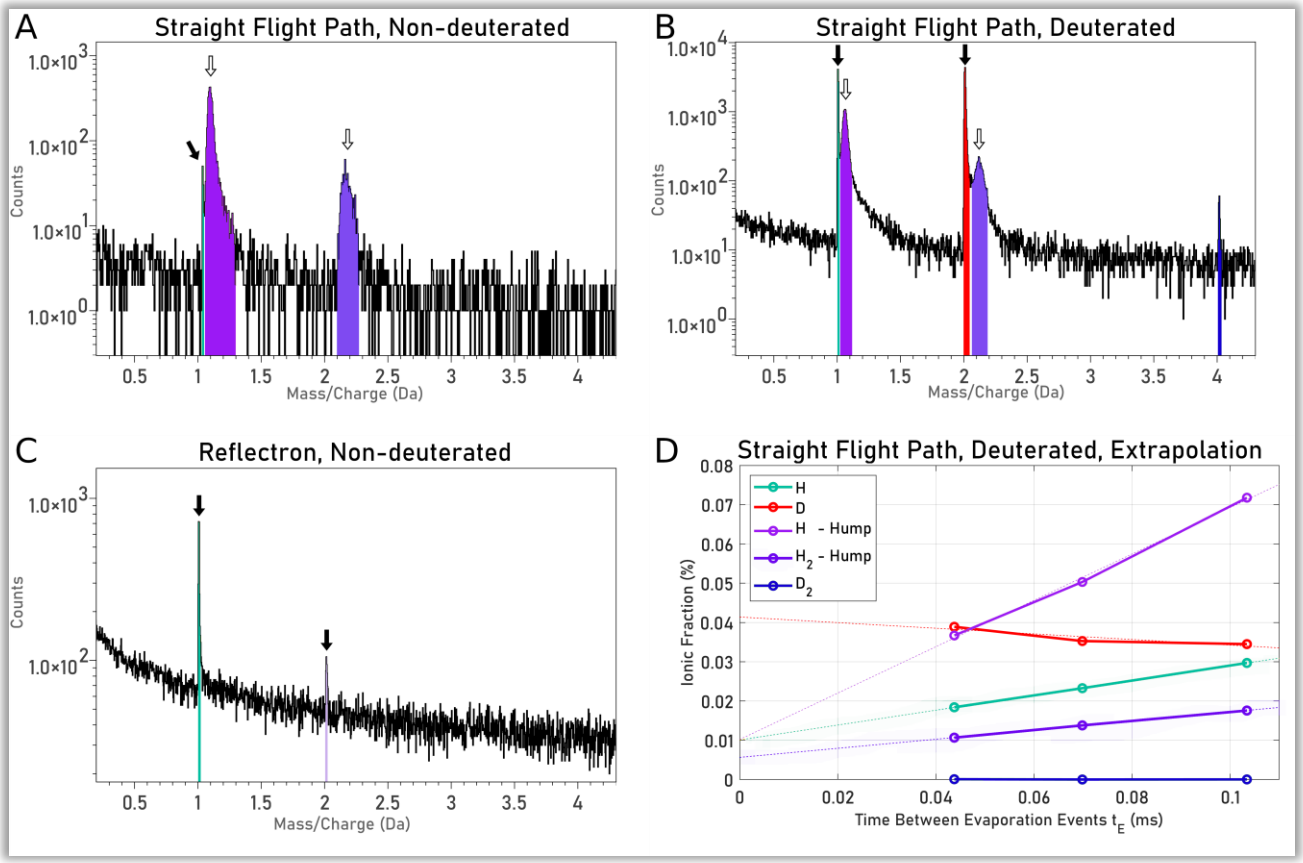

Figure 22: A-C: Spectra for hydrogen in tungsten in laser-assisted evaporation: Nominally hydrogen-free tungsten in a straight-flight-path machine (A), deuterated tungsten in a straight flight path machine (B), nominally hydrogen-free tungsten in a reflectron-fitted machine (C). Filled arrows indicate 'peaks' of H^+ and H_2^+, and empty arrows indicate 'humps' with energy deficit. D: ionic fractions of the different hydrogen peaks as function of time between evaporation events for the deuterated sample (B).

3.3.4. Discussion

The experiments clearly show that the energy deficits of contaminant hydrogen, as observed below evaporation threshold (Section 3.2), can be reproduced in pulsed laser APT runs on tungsten. The deuterated experiment (Figure 22B) shows that the energy deficit is exclusive to contaminant hydrogen and enables a differentiation between contaminant hydrogen and sample deuterium. Therefore, selecting experimental parameters to achieve an energy deficit for contaminant hydrogen, and using the m/n=2 peak to detect deuterium is a valid method for deuterium imaging in tungsten.

Further weight to this conclusion is added through the observations from the rate-cycling (Figure 22D). Whilst contaminant hydrogen is arriving at the tip during the experiment, the measured concentration of sample hydrogen (deuterium) is fixed, and should not change when the time that is available for hydrogen to arrive at the tip changes (proportional to inverse pulse frequency). As seen in Figure 22D, the m/n=2 peak, which is not observed in the deuterium-free sample is time-independent, whereas all other ions are. Therefore, only the m/n=2 peak (and m/n=4) likely carries deuterium in this experiment.

Fundamentally, two causes for higher-than-expected observed mass-to-charge ratios are possible in APT: delayed evaporation, where species leave the sample surface later than expected, and energy deficits, where ions fly slower towards the detector than expected. In the previous chapters, it has so far been assumed

without evidence that the latter mechanism is at play. Comparison of the spectra in straight flight path instrument (Figure 22A and B) and reflectron instrument (Figure 22C), however, can now provide proof. The fact that the split peaks or higher-than-expected mass-to-charge ratios are not observed in the experiment with reflectron strongly indicates that the underlying cause are energy deficits of contaminant hydrogen. Using the current technique, imaging of sample hydrogen in laser-mode APT is therefore not possible on energy compensated instruments.

3.3.5. Conclusion

In this chapter, the methods of rate cycling (Section 3.1) and the findings about the behaviour of contaminant hydrogen (Section 3.2) could successfully be combined to introduce and prove a new, alternative method for imaging hydrogen in APT, based on energy deficits. It was confirmed that in pulsed-laser APT at high electric fields, sample deuterium and contaminant hydrogen appear in separate peaks and therefore can be distinguished. Unlike the established deuterium tracer method for hydrogen imaging in APT, the current technique works in laser mode. Consequently, it appears to be more suited for long APT runs with high ion yield, and will consequently be used for the deuterium imaging experiments in Chapter 4.

Since no experiments on materials other than tungsten were conducted, the applicability of this method to other material systems remains unknown and left for future research. Formation of complex hydride ions (e.g., ZrH^+ [139, 171]) – an issue by which tungsten fortunately appears unaffected - will be a complicating factor in material systems where these are observed. A deeper understanding of the molecular-level mechanisms during field-evaporation of contaminant hydrogen, as already discussed in Section 3.2 will likely enable further advancement of hydrogen imaging techniques in pulsed laser APT.

4. Imaging of Implanted Deuterium in Tungsten

In this chapter, a self-ion irradiation damaged tungsten sample that has been implanted with deuterium is analysed by means of APT. This material is intended to emulate the behaviour of implanted hydrogen in radiation damaged tungsten, a required field of research for the progression of fusion energy (see Section 1.2.5.). The sample contains clusters of carbon, nitrogen and oxygen which are examined in depth, and the deuterium content/distribution in the material is investigated using the laser-mode APT hydrogen imaging methods introduced in Chapter 3.

4.1. Materials and Methods

The sample for these experiments is a 10x5x1 mm chip of tungsten (Plansee, 99.95% purity) which has been polished and vacuum annealed for 10 hours at 1500 ° Celsius. Then, the material was radiation damaged with a raster-scanned beam of W^{2+} ions at 2 MeV to a fluence of $1*10^{14}$ ions/cm^2 at the Accelerator Laboratory at the University of Helsinki, Finland. This introduces depth-dependent defects into the material which act as trapping sites for hydrogen [257, 258].

After W irradiation, deuterium was implanted into the material using the Delphi Implantation Device (formerly Tricem) at the MRF (Materials Research Facility) in Culham, UK. The implantation energy was 800 eV and the main ion produced by the instrument is D_3^+, correspondingly the energy per deuterium atom is approximately 267 eV. All implantation parameters are listed in Table 8. Previous research by Zayachuk et al. has shown that for this machine and conditions, the total fraction of deuterium atoms expected to be retained in the sample is approximately 1% [259].

Preparation of the bulk sample and deuterium implantation was conducted by the staff at the MRF. I received the bulk sample after implantation, and would very much like to thank Anthony Hollingsworth, Anke Wohlers and the MRF for providing me with this material.

Table 8 Parameters of the deuterium implantation conducted at Delphi at the MRF

Sample Surface Temperature	50 ° Celsius
Implantation Time	5 hours
Dose / entire sample	$1*10^{18}$ ions
Flux	$10^{18} – 10^{19}$ m^{-2} s^{-1}
Ion Energy	800 eV
Main Ion	D_3^+

A simulated depth distribution[5] of the radiation damage (simulated by Hollingsworth et al. [257] using Iradina [260]) and deuterium implantation (simulated by myself using SRIM [261]) is shown in Figure 23. Both radiation damaging and implantation are depth dependent processes, and following the simulation, their effects are mostly confined to approximately the first 250 nm of the material. It is noted that the mobility of hydrogen in tungsten is high, such that deuterium likely reaches much deeper parts of the material due to diffusion [258, 262]. Nevertheless, the APT analyses clearly need to focus on specimens obtained directly at or near the material surface.

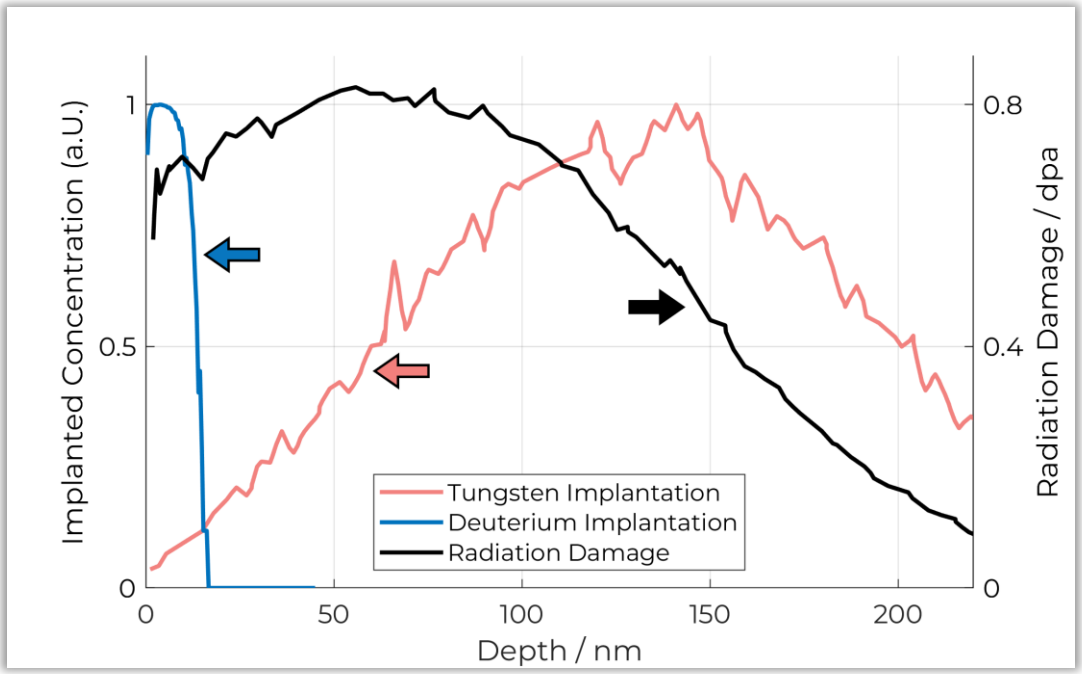

Figure 23: Simulated depth distribution of radiation damage and implantation depth of tungsten (from radiation damaging) and deuterium. Tungsten radiation damage and implantation depth simulations are by Hollingsworth et al. [257], simulated using Iradina.

Since it is expected that the observed trapping is strongly depth dependent and confined near to the surface, it is desirable that the surface is visible in the reconstructed data from an APT specimen, such that the true depth of any observed feature in the dataset can be determined. To achieve this, the surface of the bulk sample was sputter coated with a 5 nm layer of Iridium, using a Leica ACE600 coater (parameters: 80 mA current, $8*10^{-3}$ mbar argon atmosphere). This layer is later visible in the APT experiment to act as surface marker. Subsequently, a protective film of 70 nm carbon was evaporated onto the surface using another instrument of same type, fitted with a carbon thread evaporator. This helps to reduce gallium damage during the following FIB liftout.

APT specimens were prepared from the surface of the material, using the established FIB-liftout method of lifting out a wedge from the surface, sequential 'welding' and sectioning off pieces onto a pre-etched silicon coupon, followed by subsequent sharpening and low energy beam polishing into APT-ready tips [263, 264]. The specimens are prepared such that a thin cap (targeted to 20 nm or less) of the evaporative carbon layer remains on the sample, as seen in Figure 24. This ensures that the APT experiment contains the surface of the material

[5] It is noted that the true number of displacements per atom, or radiation damage in the material may differ from what is predicted by the distribution of displacements as simulated by relatively simplistic Kinchin-Pease model simulations. In the following, the distribution as simulated here is referred to as "simulated damage distribution".

as well as the iridium layer (not visible in SEM image). EBSD was performed prior to some of the liftouts to select grains with a specific orientation relative to the sample surface, and further EBSD analyses (e.g., map) of the material are shown in Appendix D-1.

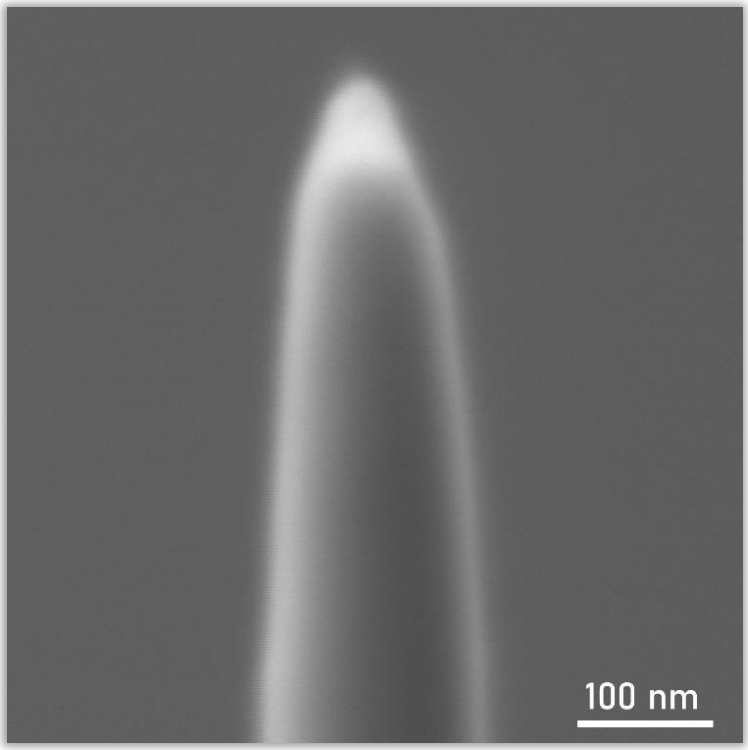

Figure 24: A SEM image of an APT specimen as used for the experiments in this chapter, secondary electron contrast (using a Zeiss SESI Detector, an Everhard-Thornley-Style Detector), 5 keV electron acceleration voltage. The pictures is taken from a 54 degree angle against the tip direction. The protective carbon cap appears bright, tungsten is dark.

The specimens were run in a Cameca LEAP XS 5000 operating in pulsed laser mode, using a constant charge-state-ratio (CSR) constraint to hold the electric field (approximately) constant during the experiment. The target CSR values were selected to achieve field strengths above approx. 28 V/nm, which is the critical voltage above which direct deuterium imaging in laser APT becomes feasible (see Section 3.2). It is noted however that the target CSR was not consistently achieved and held constant throughout all experiments, as will be discussed Section 4.2.3. In some experiments, pulse frequency cycling (introduced in Section 3.1) was applied to obtain additional information and certainty about the various hydrogen- and deuterium signals.

A list of successful APT experiments and parameters is provided in Table 9. The experiments are named W-A to W-G, and the experimental identifiers (“Run Numbers”) are listed in Appendix D-2.

The APT datasets were reconstructed using a calibrated reconstruction method to obtain an approximately accurate reconstruction of the z-axis (depth), as described in [265-267]. To this end, the image compression factors (ICF) were first estimated using the positions of crystallographic pole structures on the desorption map [268]. Then, initial tip radii were chosen such that, along low-index crystallographic planes, the z-lattice spacing as measured in spatial distribution maps (“z-SDM”) resembled the expected crystallographic lattice constant for tungsten.

Selecting an initial tip radius for reconstruction can be seen as equivalent to selecting a field factor k. It is noted that the current samples all carry carbon caps (Figure 24) which are estimated to have an evaporation field below tungsten[6], but the reconstruction parameters are selected to optimise for a correct lattice constant in the tungsten part of the specimen. Therefore, as a side effect, the chosen tip initial tip radii for reconstruction are likely smaller than the actual physical dimensions, and the caps in the reconstructions appear smaller than they are.

Since the material contains only small quantities of elements other than tungsten, association of peaks in the mass-to-charge spectra is straightforward, and no peaks with unknown identities were encountered. Carbon, nitrogen and oxygen were found to form WC, WN and WO-type ions, whose ionic fingerprints partially overlap in the mass-to-charge-state ratio spectrum. Therefore, the composition was determined using MLE deconvolution (and background correction) of the spectra using the AtomProbeLab code by London [150, 269], version 0.2.4.

[6] In theory, the evaporation field of pure carbon is higher than of tungsten [136], however the carbon caps contain a large amount of other elements such as oxygen, therefore the effective field is likely lower.

Table 9: List of successful experiments with relevant APT parameters. Some experiments have additional comments, which are listed in Table 10.

Name	Pulse Frequency	Target Detection Rate	EBSD grain orientation	Target CSR: W^{3+}/W^{2+}	Comment
W-A	Constant 250 kHz	Up to 3.35M ions: 4 % Afterwards: 7 %	-	Unknown, likely 0.1	
W-B	Constant up to 3M ions: 500 kHz, afterwards: 625 kHz	7 %	-	1	
W-C	Cycled 125, 250, 333 kHz switched every 300 000 ions; Constant from ~15M ions: 500 kHz from ~17M ions: 625 kHz	up to 19.5 M ions: 8 %, up to 30 M ions: 12 % afterwards: 15 %	-	2	*1
W-D	Constant up to 2.25M ions: 200 kHz, afterwards: 625 kHz	8 %	-	0.5	
W-E	Cycled 200, 333, 500 kHz switched every 300000 ions	5 %	100	10-13	*2, *3
W-F	Cycled 200, 333, 500 kHz switched every 300000 ions	5 %	100	20-23	*2, *3
W-G	Cycled 200, 333, 500 kHz switched every 300000 ions	3 %	110	3	

Table 10: Additional comments for experiments in Table 9

Number	Comment
*1	Frequency cycling was interrupted due to technical problem at 15M ions, thereafter a constant frequency was used
*2	Constant-CSR control of the laser energy was unstable (the machine-proposed laser energies were oscillating between unreasonably high and low laser energies), therefore laser energies were manually overridden to stabilise the CSR between 10 and 13 or 20 and 23 during run.
*3	These specimens originate from the same grain within the base material

4.2. Results

4.2.1. Reconstructed Datasets and Composition

Figure 25 shows tungsten, iridium, WC/WN/WO ions, and deuterium in the reconstruction of W-A. The ions WC, WN and WO overlap in the mass-to-charge-state ratio spectrum and therefore cannot be shown separately. Reconstruction maps of all other experiments listed in Table 9 are shown in Appendix D-3.

The sputter deposited iridium layer is present in the datasets, marking the surface of the tungsten samples. This means that - provided that the spatial reconstruction is calibrated correctly – the depth of features in the sample can be measured accurately as a distance from the iridium layer. In the following results and analyses, the term “depth” will therefore be used as distance from this iridium layer.

The carbon / nitrogen / oxygen is not distributed uniformly, but rather is clustered. The clusters are likely a by-product of the radiation, and their number density is depth dependant. Further analyses of the clusters (Section 4.2.2) show that the main element in these clusters is nitrogen, with a measured concentration of more than 80 atomic-% within. Similarly, the depth distribution of deuterium, as measured by the peak at m/n=2, is strongly depth dependent.

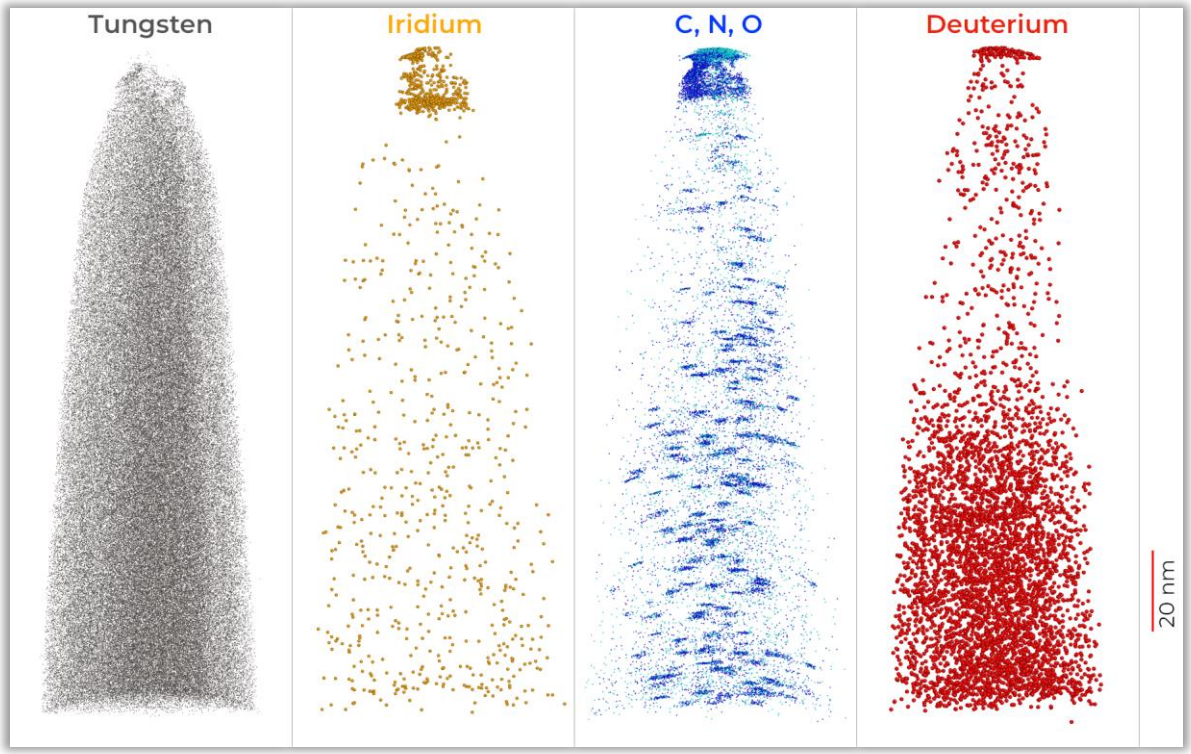

Figure 25: Atom maps of tungsten (only 1% of atoms shown), iridium, carbon-nitrogen-oxygen (from the ions WC, WN and WO, which overlap in the mass-to-charge-state ratio spectrum) and deuterium in the reconstructed W-A.

Unique features in the reconstruction maps were found in two instances. In W-F, boron – a trace element in the material and absent in some of the datasets – was found to be clustered, with one cluster particularly distinct (Figure 26). Possibly this is a decorated dislocation loop induced by irradiation. It is noted that Transmission Electron Microscopy (TEM) analyses on this material by Hollingsworth et al. indicate that dislocation loops are relatively rare, with an estimated density of $7.88*10^{13}$ loops per m^2 of surface area in the radiation-damaged layer [257]. Assuming that every APT specimen incorporates a 50x50 nm of the damaged layer, this translates into 0.197 dislocation loops per specimen, so the observation of only one loop in seven specimens is not a

surprising outcome. There might be a very slight co-segregation of carbon from C^+ and C^{2+} ions in the loop, however this is not entirely clear due to the low concentrations. The cluster structure of the WC, WN, WO appears unaffected.

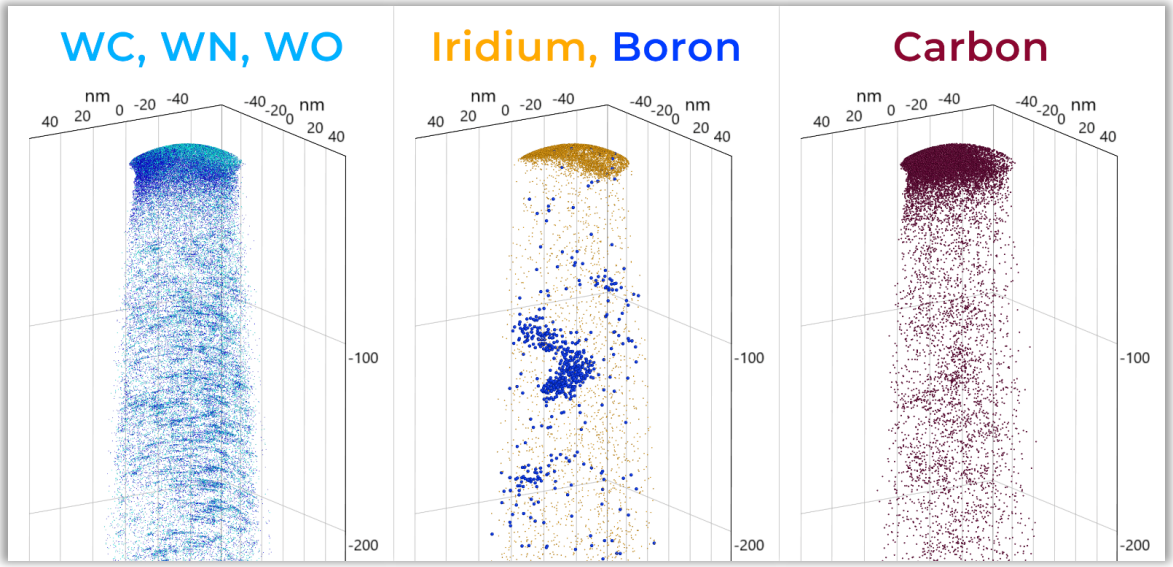

Figure 26: Atom maps of WC, WN and WO ions (overlapped in the mass-to-charge-state ratio spectrum), Iridium and Boron, and Carbon (from C+ and C++ ions, not from WC ions) in the reconstruction W-F

In W-B, the number of WC, WN and WO cluster is much lower than in the other datasets (also see Section 4.2.2). Instead, arod-shaped feature of WC, WN and WO is seen (Figure 27), which could be a dislocation[7]. The distribution of boron in the sample is clearly non-random, but the clustering does not seem to occur around any specific visible feature – boron is not clustered around the linear C,N,O feature. If the features in W-F and W-B both represent dislocations, then it is interesting that their compositions are so clearly different – presumably because W-F contains a radiation-induced loop, while W-B is more likely a "natural", pre-existing dislocation.

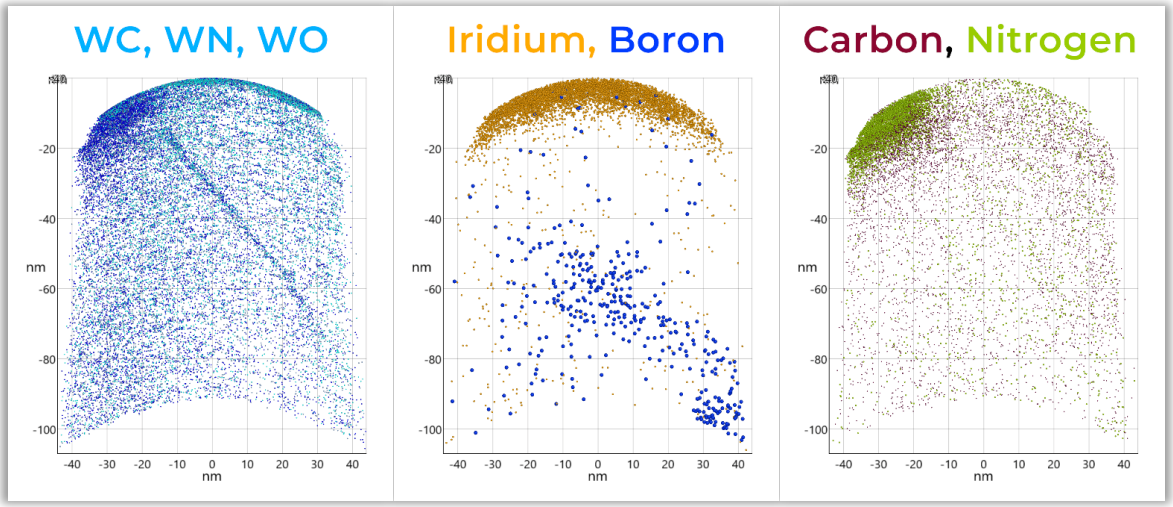

Figure 27: A 25 nm slice of the atom maps of WC, WN and WO ions (overlapped in the mass-to-charge-state ratio spectrum), Iridium and Boron, and Carbon and Nitrogen (from C and N ions, not from WC and WN) in the reconstruction W-B

[7] The pole figure in the desorption map of this dataset (as in all other experiments) shows only one single crystal orientation, meaning that large-angle grain boundaries or triple points can likely can be ruled out as an alternative explanation. However, it cannot be ruled out that the observed feature may not be a dislocation that is part of a low-angle grain boundary, where the dislocation density is so low that only one dislocation is observed in the APT experiment.

The composition of the material as calculated from the spectra, using background correction and MLE-decomposition in AtomProbeLab, over all samples are shown in Table 11. To ensure that contributions from the carbon caps on the tips do not influence the measured composition, detector events with a z-axis component of less than 40 nm (i.e., within the first 40 nm of the tip) were excluded. Apart from Ga and Ir, which are expected due to the sample preparation, amounts of C, N and O are found in all datasets, and trace amounts (0.05 atomic-% or less) of Si and B in some. Nevertheless, the fraction of tungsten is at least 99.7% in all samples, meaning that the purity is relatively high. Appendix D-4 contains additional tables for the global sample compositions including the carbon caps on the surface as well, and confidence intervals for all composition calculations.

Table 11: Composition of the tungsten, as measured from a z-coordinate of above 40 nm (i.e. the first 40nm of the tip are excluded), determined from the APT spectra through deconvolution and composition analysis using AtomProbeLab [269], and equally-weighted mean values and standard deviation. It is noted that the standard deviation assumes that the underlying distribution is gaussian, which may be an oversimplification.

Experiment	C	N	O	Si	Ga	Ir	B	W
	atomic %				*atomic ppm*			
W-A	0	0.07	0.01	0	271	18	-	Balance
W-B	0.06	0.1	0.02	0.01	324	8	22	
W-C	0.01	0.02	0.01	-	481	1	-	
W-D	0.02	0.13	0.02	0	470	22	12	
W-E	0.05	0.05	0	0	813	6	12	
W-F	0.01	0.04	0	0	349	2	3	
W-G	0	0.1	0.01	0	448	6	1	
Mean ±Std Dev	**0.02** ±0.02	**0.07** ±0.04	**0.01** ±0.01	**0** ±0.00	**451** ±165	**9** ±7	**7** ±8	

4.2.2. Clusters in APT datasets

As has been shown in Figure 25, the datasets contain clusters of carbon, nitrogen and oxygen. In order to analyse these, the DBscan cluster algorithm [270] is employed to extract the clusters from the datasets, using the parameters given in Table 12. More details about the cluster search are given in Appendix D-5, and only key results are summarised here.

Table 12: Parameters used for the DBscan cluster algorithm

Parameter	$\mathbf{N_{min}}$	**ε (nm)**	**Solute Species**
Value	15	1.5895	All ions containing C, N, O

Figure 28A shows the depth distribution of clusters identified by the cluster search, where depth is defined as distance from the iridium layer on the sample surface (Section 4.2.1). Since the number of clusters per dataset and depth band is relatively low, the scatter is high. The lines are therefore smoothened to increase readability, using moving average filtering across 5 bins.

It is seen that the density of clusters in all datasets lies within the same order of magnitude, between approx. 0.5 and $2.5*10^{-3}$ clusters per nm^3. Except from W-D, a drop in the cluster concentration with increasing depth is observed within the first ~40 nm below the surface, followed by an increase with depth. In some of the longer datasets (W-G, W-E, W-F and W-B), an additional tail-off in the number of clusters is seen further down in the material. The depth of peak cluster density, excluding the cluster-rich regions near the surface, vary between approximately 65 nm and 130 nm. This roughly corresponds to the simulated depth of peak radiation damage (Figure 23), likely the clusters are a by-product of the ion irradiation.

Figure 28B shows the size distribution of clusters, for improved statistics measured cumulatively across all datasets. The size, taken as the number of carbon/nitrogen/oxygen atoms per cluster, is corrected for an assumed detection efficiency of 80% [246]. The median cluster size is 44 carbon/nitrogen/oxygen atoms, or 55 when corrected for detection efficiency.

Since the N_{min} parameter was set to 15 for all datasets (detection efficiency corrected 18.75), the number of detected clusters at smaller sizes naturally is very small. It noted however that, as technicality of DBSCAN, the assignment of ions to clusters is not deterministic when they could possibly be assigned to two different clusters[8], leading to the detection of clusters of sizes below N_{min}. Therefore, the part of the diagram below approximately 20 atoms/cluster should not be over-interpreted. A curious spike in the number of clusters is seen at 18 to 19 atoms/cluster, however this corresponds exactly to the N_{min} parameter of 15 that is used here (Table 12) after detection efficiency correction, therefore may not be meaningful to the actual properties of the clusters in the material.

Once the clusters are separated, it is possible to apply MLE-deconvolution to analyse their composition. Figure 28C shows the fractions of carbon, nitrogen and oxygen per dataset as calculated globally for all clusters. Only

[8] Using the terminology from [270], the cluster assignment of "reachable" atoms which are reachable from two or more "core" atoms of different clusters is not deterministic.

clusters with a median z-coordinate of 40nm or deeper, and which are smaller than 99th percentile of clusters were considered, to exclude influences from composition changes near the surface or excessively large clusters. It is seen that the fraction of oxygen in the clusters is minor (less than 5 atomic-%, outlier: 8% in W-D), and the clusters mostly consist of nitrogen. In W-B and W-E, a certain fraction of nitrogen (20% or 34%) seems to have been swapped for carbon. The mean cluster composition across all datasets is C : N : O = 12% : 84% : 4%.

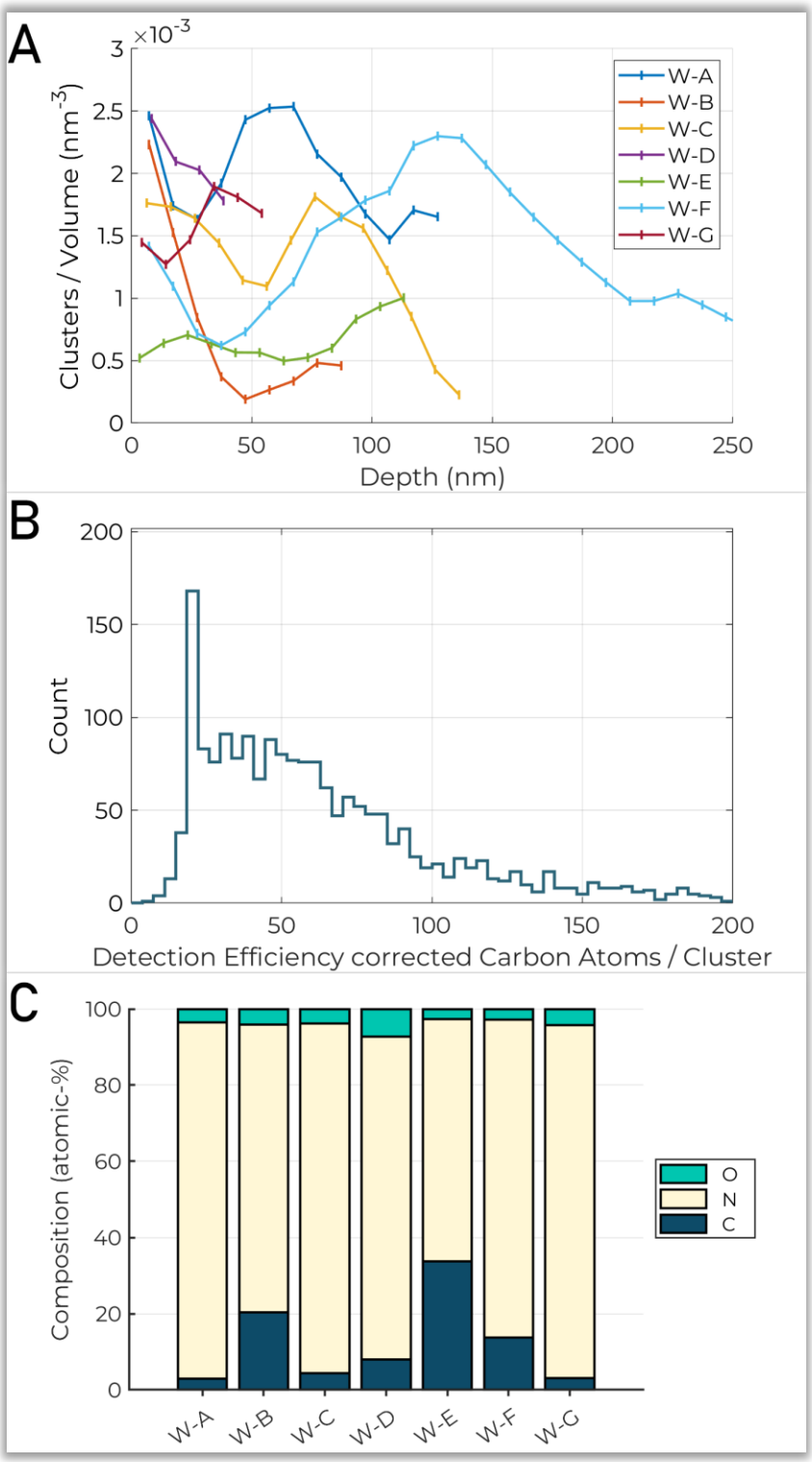

Figure 28: A: Number density of clusters per depth, the lines smoothened through moving average filtering across 5 bins, B: Distribution of cluster size measures as carbon atoms per cluster over all datasets, corrected for assumed detection efficiency of 80%, C: Composition of clusters per dataset, excluding clusters with a reconstructed z-coordinate of less than 40nm and larger than the 99-th size percentile

4.2.3. Consistency of CSR

As shown in Section 3.2, the electric field is critical to the behaviour of contaminant hydrogen, which in turn influences the ability to observe deuterium in the material. Therefore, all of the experiments were run in constant-CSR mode with target field strengths of approximately 30 V/nm or higher. Theoretically, this should ensure (near) constant electric fields during the experiment.

Nevertheless, the electric field is an indirectly controlled parameter during the experiment, which is controlled through a feedback loop measuring a CSR during the experiment and adjusting the laser energy accordingly. Various factors, such as an inaccurate measurement of the CSR during an APT experiment (e.g. due to inaccuracies in live spectrum calibration shifting peaks with voltage) and instabilities in the feedback loop may lead to deviations between target and actual CSR.

Therefore, the electric field strengths and W^{3+}/W^{2+} CSRs throughout the experiments are analysed and shown in Figure 29. The CSR is calculated for each frequency step for those experiments where frequency cycling was performed, and for layers of 300000 ions in all other experiments. The only exception to this is W-C, where the frequency was only cycled during the first section of the experiment: for this case, the CSR is also calculated for layers of 300000 ions. The inset spectra show the hydrogen spectra of the various experiments. To convert between measured CSR and electric field, the CSR-Field curves by Yao et al. [136] were used.

In all experiments, the CSR is relatively constant throughout the runs. However, there are deviations, especially in the beginnings of the experiments. This is mostly because measurement, and therefore control of the electric field, is only possible once evaporation has started, but the electric field may be far off the target value at the initial onset of evaporation, and large adjustments to balance the laser energy are needed. A small glitch is visible in W-F (Figure 29F) around layer 410, where the field strengths briefly dropped below the average value. At this occasion, the field dropped due to an excessively high laser energy. This is a transient issue, and has added an artefact to the deuterium observation, as will be shown in Section 4.2.4 (Figure 30F).

During this study, it became apparent to me that the automatic field control in its current implementation is mostly suited for keeping a CSR constant during an APT experiment where the voltage curve is relatively stable and smooth. It is less efficient when trying to establish a particular field strength coming from a field strength that is far off the target value. In these situations, reaching the desired target using the feedback loop in the control software may be a relatively slow process (requiring several 100000's of ions), and over- or undershoots have been observed, where unreasonably high or low energies were selected. In such instances, improved control was obtained by overriding the feedback loop by manually varying the laser energy such to achieve the desired field strength. The automatic CSR control was only enabled once the CSR was reasonably stable and close to the target.

A major, persistent deviation between target CSR (20-23) and observed CSR (approximately 0.2) occurred in W-F. It is not known what lead to this deviation, which could possibly have been due to a software glitch. Fortunately, the resulting field strength during this experiment (approximately 29.5 V/nm) is still sufficient to enable an acceptable differentiation between contaminant and sample hydrogen (also see the discussion in Section 4.3.1 and Figure 32). In all other experiments, target CSR and observed CSR over time agree well.

It appears that the electric field strength is critical to the separation between the m/n=2 peak for deuterium and the following hump for contaminant H_2. In the runs with field strengths of approx. 32 V/nm or more (Figure 29C, E, G), peak and hump are more distinct than in the runs at lower fields (Figure 29A, B, D, F). Differentiation between contaminant and sample hydrogen is possible with greater certainty in the former experiments.

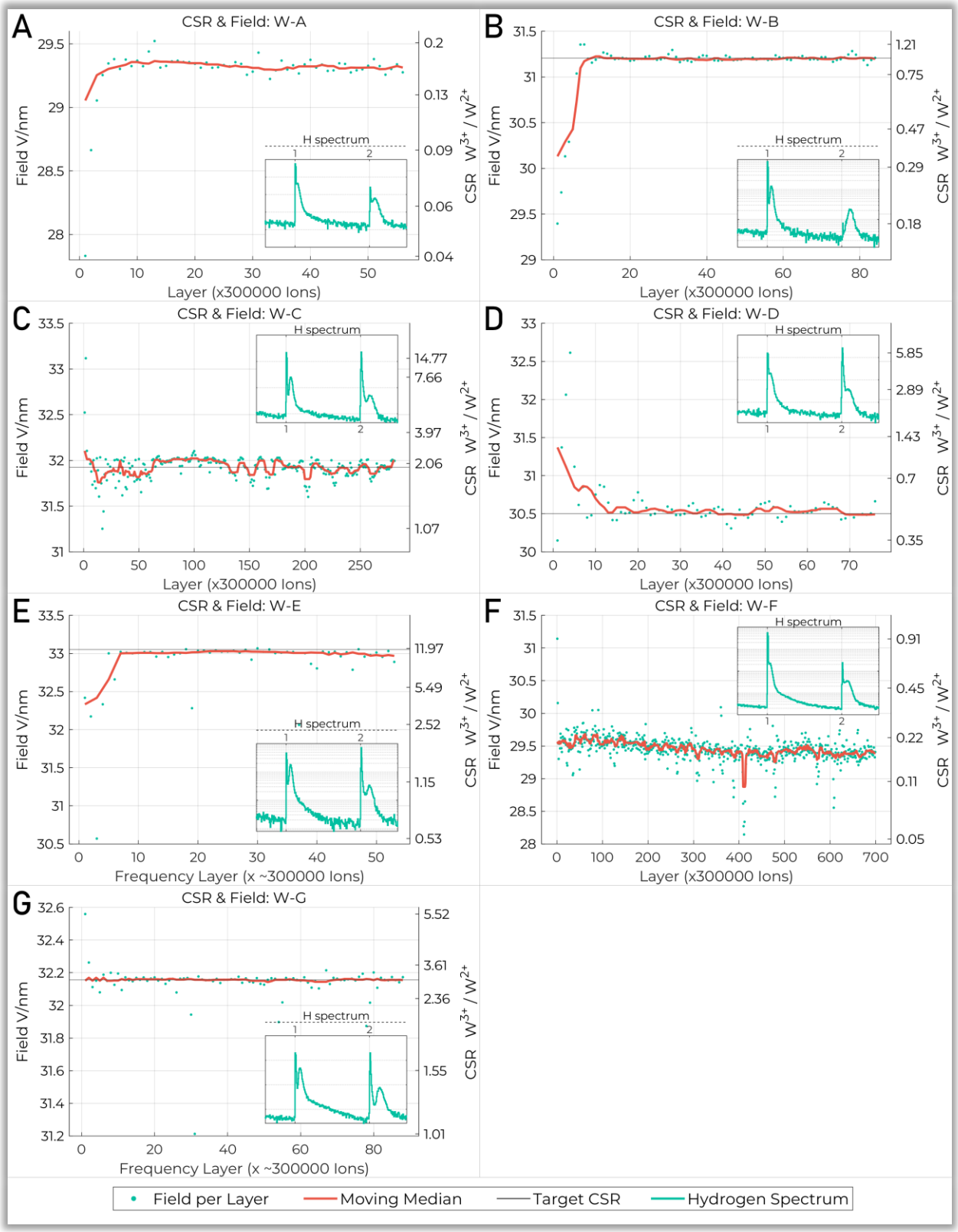

Figure 29: W_3^+/W_2^+ CSR and corresponding electric field throughout the experiments, as calculated per layer. "Layers" are either steps in between frequency changes in those datasets where frequency cycling was used throughout the run (each layer is approx. 300000 ions in these cases), or per layers of 300000 ions. In W-E (Figure E), the actual target CSR varied between 10 and 13, and an intermediate value of 11 was used for the diagram. Inset figures: hydrogen/deuterium spectra of the respective experiments.

4.2.4. Depth Profiles

The depth profiles for deuterium, iridium, carbon/nitrogen/oxygen (plotted as sum signal) and gallium for the seven APT runs are shown in Figure 30. The amounts are in atomic-% as calculated using AtomProbeLab in a line profile type deconvolution of the spectra. An exception to this is deuterium, which is given in ionic-%. The depth axes are aligned such that the iridium layer (surface marker) aligns with a depth of zero. Composition values measured at negative depths, i.e., above the iridium layer have no significance for the analysis of the tungsten. The bin width is 2 nm for all experiments, however since the maximum depth that is reached during the experiment depends on the yield of the APT experiment, the extent of the depth axis varies between experiments. An alternative version of this figure, using the same axis scaling per element for all datasets is given in Appendix D-6.

Firstly, it is seen that the amount of gallium, a contamination from FIB sample preparation, after an initial spike at the start, is low and approximately flat across the samples, with an exception in W-F (Figure 30F). In this sample a wave-like structure is seen, which could be due to gallium implantation during tip sharpening into a depth of up to roughly 30 nm. It is therefore possible that FIB damage has altered this sample near the surface.

The concentration of carbon, nitrogen and oxygen is clearly depth dependent. In W-C and W-F (Figure 30C, F), it is seen that the concentration of these species is elevated to roughly 0.1% at depths of up to approximately 150 nm, then tails off to a bulk concentration below 0.03%. The experiments W-A, W-B, W-E and W-G (Figure 30A, B, E, G), are consistent with this, but only show the elevated concentration near the surface since the runs do not extend sufficiently deep into the material. The line profiles of C, N, O appear rippled due to the clustering in these species. It is noted that the origin of these impurities is unknown, and a short discussion of possible co-implantation is given in Appendix D-7.

The distribution of C, N, O in W-D (Figure 30D) is a special case, going as high at 65.3 atomic-% directly at the surface. This could be consistent with an observation of a phase WX_2 on the material surface, whereas X is one or a combination of C, N and O. MLE decomposition of this layer yields a composition of 29 atomic-% tungsten, 54% oxygen, 9% nitrogen, and less than 3% carbon, indicating that this phase likely is a tungsten oxide with a certain fraction of nitrogen. At this point, it should be noted that phases of the type WO_3, WO_2 and WN_2 are reported in the literature [271, 272], but no WC_2 or any tungsten carbide that is more carbon-rich than WC [273].

Concerning deuterium, complex and varied behaviour is observed across the seven experiments, however, some common observations can still be made. Firstly, an enrichment of deuterium directly behind the surface is observed consistently, depending on the sample up to a depth of 10 to 20 nm. This is followed by a drop in concentration, and another enrichment from between approximately 70 to 180 nm. Based on this, these regions are subsequently referred to as “near-surface” (0-20 nm) and “deep” layer (70-180 nm) and are highlighted in blue and red in the diagrams.

The deuterium distribution in W-F (Figure 30F) further contains two apparent spikes, highlighted by arrows. These are not “real”, but artefacts. In both instances, the feedback-loop controlled laser power briefly veered off course towards an excessively high pulse energy. This led to a brief drop in the electric field, and subsequently a likely evaporation of H_2^+ in the m/n=2 peak.

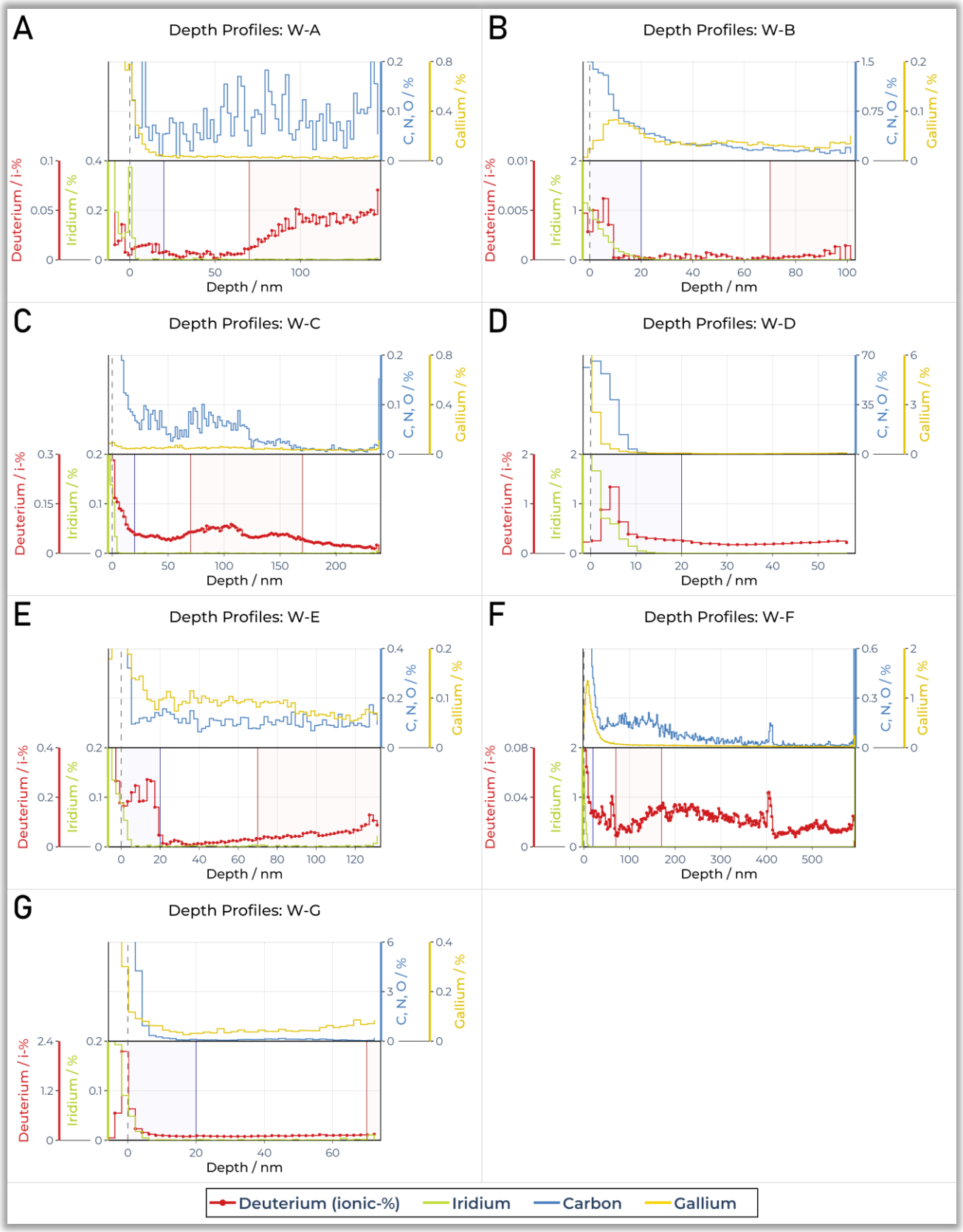

Figure 30: Depth profiles of gallium, carbon-nitrogen-oxygen (summed up), deuterium and iridium in the tungsten specimens. The depth-axes are aligned such that the 0-position aligns with the depth of the iridium layer. The arrows in F indicate artefact spikes, caused by brief incidences of too high laser energies.

There are relatively strong deviations in the absolute deuterium concentrations as observed in these layers between the different samples, especially for the near-surface layer. Figure 31 shows deuterium concentrations in near-surface and deep layers, measured through the 80th-percentiles of concentrations per depth bin[9].

Excluding two outliers, W-D and W-B, the measured concentrations near the surface span a range from approximately 0.015% (W-A, Figure 30B) to 0.25% (W-E, Figure 30E). In the deep layer, the concentrations are from 0.03% (W-F) to 0.08% (W-C), and in the layer in between they are from 0.008% (not detectable in some bins, W-A) to 0.55% (W-C).

W-D is the dataset with the 65.3 atomic-% carbon/nitrogen/oxygen layer on the surface, and the deuterium concentration below this surface layer peaks at 1.3% - much higher than at any other dataset, therefore this dataset is considered an outlier. The other outlier, W-B is the dataset which contains the elongated feature of carbon-nitrogen-oxygen (Figure 27), likely representing a pre-existing dislocation that is open to the tungsten surface. This goes along with a deuterium distribution that is comparable to the other datasets (enrichments in deuterium- and tungsten implantation layer), but the absolute amounts are 0.0003% and 0.0007%, which is considerably lower than in the other datasets and close to the detection limit for these APT experiments (see the hydrogen spectrum in Figure 29B, where the m/n=2 peak is barely above the noise floor).

There seems to be no intra-experiment correlation of the relative amounts of deuterium detected in the layers, i.e. experiments with comparably high amounts of deuterium near the surface do not also feature comparably high amounts of deuterium in the deep layer.

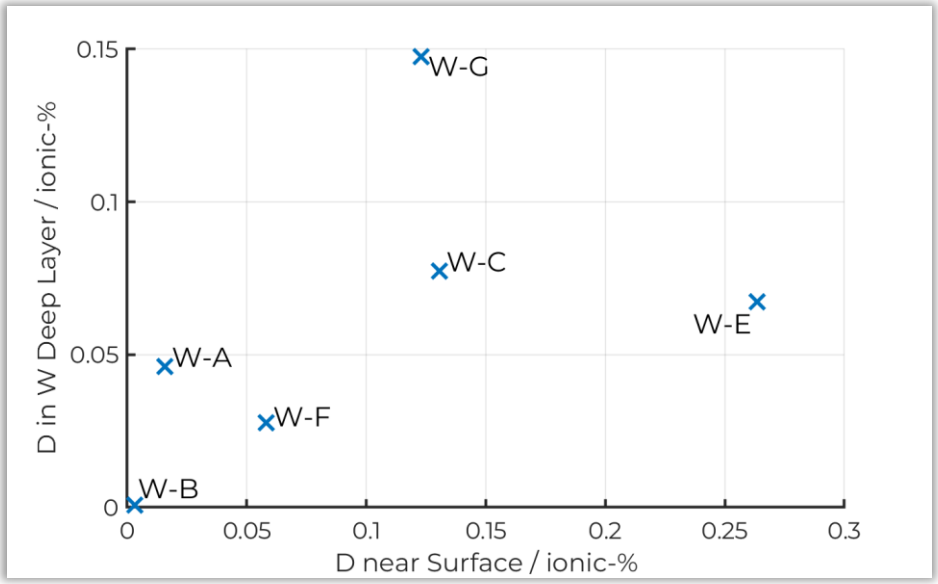

Figure 31: Fractions of deuterium measured in the deuterium-rich layers near the surface and deeper in the material, per dataset. W-D is not extending deep enough to reach the W implantation layer and therefore is missing from the diagram

[9] The purpose of this diagram is to compare the peak concentrations of deuterium which are reached in the respective layers. When peak concentrations as determined from binned depth profiles, binning and random scatter strongly affect the concentration in the bin with highest concentration, because the deuterium ions are finite and ultimately form a discrete, non-continuous distribution in the dataset. This is less of a problem when 80-th percentiles are used instead of peak bin concentrations, therefore I argue that the 80-th percentiles are a better suited proxy for comparing deuterium concentration per depth layer across the samples.

4.3. Discussion

Since this work is both the first application of a new method to image hydrogen in APT and application of APT to deuterium implanted into tungsten, both aspects are treated separately. First, it shall be discussed if and to what extent deuterium (as opposed to contaminant hydrogen) imaging has likely been successful, and the quality of the observations. This does not take into consideration eventual modifications of the deuterium in the material due to sample preparation, which are discussed in the following Section 4.3.2. The observed distribution of deuterium in the material itself is discussed in Section 4.3.3.

4.3.1. Observation of Deuterium

As described in Chapter 3.3, the differentiation between contaminant and sample hydrogen is possible in straight flight path instruments at high electric field strengths above approximately 28.4 V/nm, when a split peak structure emerges, and an ideally contaminant-free deuterium peak is captured. The field in all experiments is on average at 29.5 V/nm or above, and consequently peak-hump structures at m/n=2 from the splitting of contaminant H_2^+ and sample D^+ are observed in all 7 datasets (Figure 29). At least some differentiation therefore is possible for all experiments.

In order for the hydrogen imaging to be free of artefacts, it is however necessary that the CSR is held consistently at high values throughout the runs. Transient drops in the electric field may allow for evaporation of H_2^+, and thereby introduce artefacts into measured "deuterium" concentrations. This is occurring twice in W-F and leads to false spikes in deuterium concentration (Figure 30F), though fortunately these can be spotted easily and isolated. In some experiments (W-A and W-B, see Figure 29A and B), an initial laser power regulation phase in the beginning of the experiments was needed before the fields reached a constant value, but the deviation from the target field is not major. With the exception of the two artefact spikes in W-F (Figure 30F), spurious features in the apparent deuterium distribution due to changes in the electric field during the run are therefore not expected. However, deuterium concentrations measured near the start of experiments (i.e., near the material surface) should be interpreted more cautiously.

One second potential pitfall is that in the current study, the CSR is calculated over an entire layer of atoms. Therefore, the calculation of the electric field cannot account for eventual lateral differences over the specimen apex, but averages across the entire surface visible to the detector. Theoretically, this could lead to unwanted artefacts in the observed deuterium distribution, where the field strength on parts of the surface is low enough to allow for contaminant H_2^+ to evaporate in a peak rather than hump.

It is therefore helpful to invoke frequency cycling as introduced in Chapter 3.1 to obtain more certainty about the reliability of the deuterium signal. The method was applied to four of the seven experiments, and the resulting hydrogen extrapolations are shown in Figure 32. In addition, the extrapolated fractions of deuterium are listed in Table 13.

The trend for the extrapolated m/n=2 detector events (red line) in the run with the lowest electric field, W-F (CSR W^{3+}/W^{2+}: 0.17-0.21), is not perfectly flat but decreases with decreasing time between evaporation events (Figure 32A). This indicates that in W-F the captured "deuterium" signal could contain a small fraction of contaminant H_2. This is not the case for the other three datasets (CSR $W^{3+}/W^{2+} \geq 2$), where the m/n=2

extrapolation is flat. In these runs, the deuterium content measured through the m/n=2 peak should therefore be accurate.

No frequency cycling was conducted in the remaining experiments, however from these results it is concluded that, due to the comparably low CSR of approx. 0.15 in W-A there might be a small fraction of contaminant hydrogen contained in the “deuterium” signal, whilst this is less likely to be the case in the remaining experiments W-B and W-D (CSR 1 and 0.5). I conclude from the observations that the measured deuterium signals are mostly “trustworthy”, but need to be interpreted more carefully in the beginning of the runs and in experiments where the field strength is near 28.4 V.

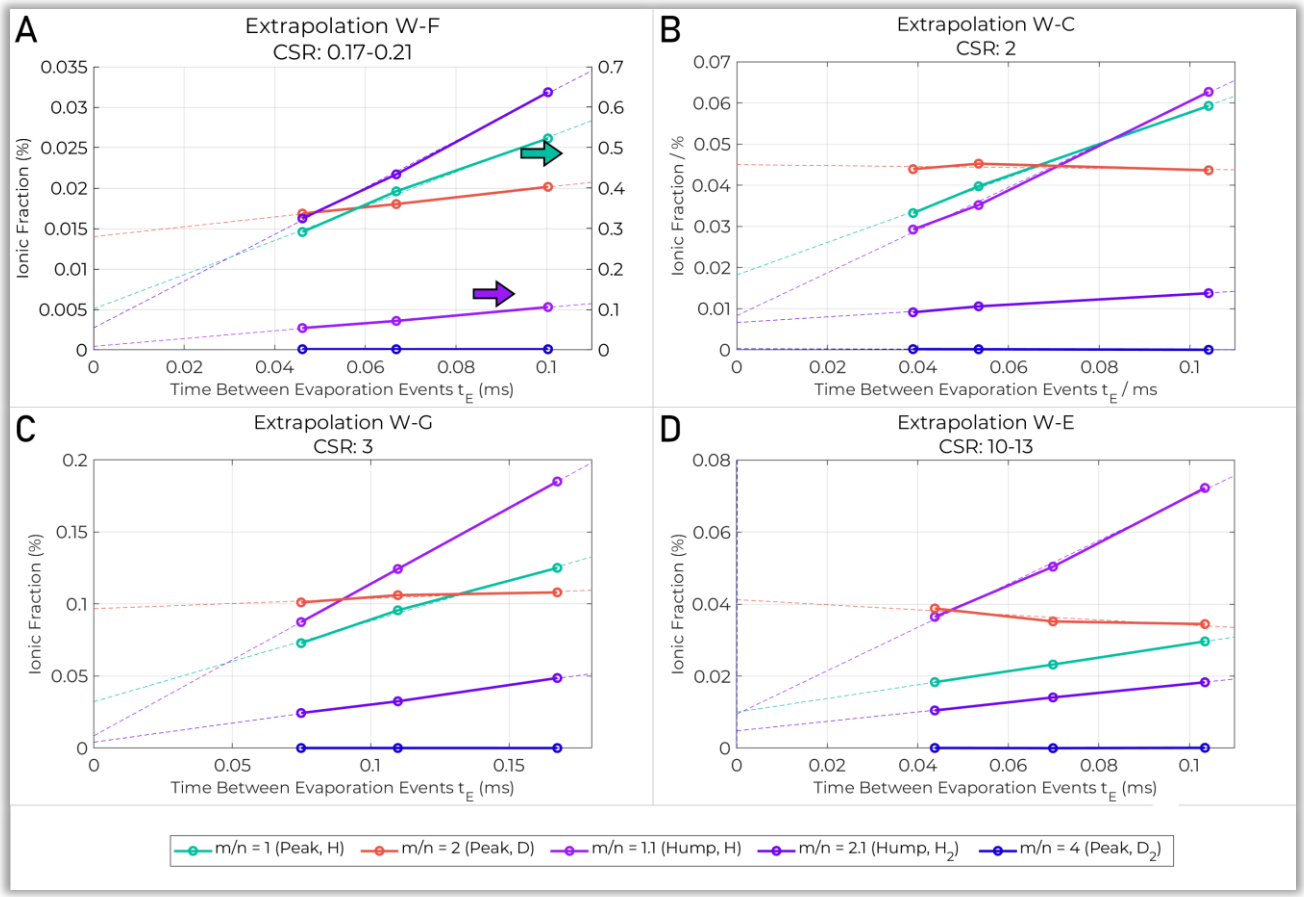

Figure 32: Extrapolation of hydrogen signal to infinitely fast pulse repetition rates in the four experiments where frequency cycling was conducted.It is seen that the ionic fraction of the m/n=2 peak, corresponding to (mostly) deuterium, is near or completely time-independent in all four experiments.

Table 13: Extrapolated fractions of deuterium for infinitely high evaporation rates (y-axis intersections in Figure 32)

	W-F	W-C	W-G	W-E
CSR W+++/W++	0.17-0.21	2	3	10-13
Extrapolated Deuterium Fraction (ionic-%)	0.014	0.045	0.0968	0.0412

4.3.2. Variation between Experiments

The observation that the absolute amounts of deuterium measured in the samples (as described in Section 4.2.4, Figure 31) are so clearly different could be explained in two different ways. One explanation is that the distribution of deuterium in the bulk sample is laterally inhomogeneous such that each APT tip contains different amounts of deuterium. Alternatively, there could be problems with the sample preparation procedure which led to alteration of sample hydrogen concentrations before the APT experiment.

Three mechanisms could possibly lead to a lateral inhomogeneity in the bulk tungsten sample. These are a) an inhomogeneous distribution of the radiation damage and thus trapping sites, b) pre-existing features in the sample, e.g., surface-near dislocations, and c) clustering of deuterium on a length scale greater than the size of APT analysis volume. These options shall be briefly discussed. Inhomogeneous implantation of deuterium is unlikely due to the working mode the Delphi instrument which has been used for implantation.

Option a) is possible because the radiation damage has been introduced through a raster scanned ion beam. If the line distance during scanning is higher than the beam width, it is possible that the radiation damage and therefore retention is inhomogeneous. NanoSIMS, which has not been used in the current study, could potentially help to clarify this, since the result would be deuterium retention in a likely detectable line-pattern on the sample.

In two APT tips, special features which could have influenced the deuterium distribution have been observed: an elongated feature in W-B (likely a dislocation), and a surface layer that is rich in carbon-nitrogen-oxygen (combined 66% atomic-%) in W-D. The presumed dislocation goes along with depressed deuterium contents in the respective dataset, and the surface layer corresponds to higher deuterium contents. This suggests explanation b): sample features influence the deuterium concentration locally, resulting in the respective overall specimen volume containing more or less deuterium than in other datasets. The fact that discrete features were observed in two out of seven APT experiments (three when taking the boron-decorated dislocation loop in W-F into account) also suggests that very likely in all or most samples without such observed “special” features, there still were some of these near the visible APT analysis volume.

Theoretically, it could also be feasible that the hydrogen in the bulk sample clustered, option c), on a length scale greater than the size of an APT analysis volume. This however appears unlikely to me, because most of the observed hydrogen is trapped at vacancies from irradiation, and assuming a uniform distribution of radiation damage, there should be no reason why hydrogen would prefer trapping sites in particular parts of the sample. Clustering of interstitial hydrogen in the lattice is energetically not favoured – depending on distance, the interaction is either negligibly weak or repulsive [68, 69] – so even if for some reason hydrogen is not trapped, it should not cluster just by itself.

FIB influence

In addition to inherent properties of the sample, modification of the hydrogen concentration during APT sample preparation must at least be considered a possible cause for the variations between samples.

Inadvertent pickup of significant amounts of hydrogen during FIB milling of APT tips is a known issue in the preparation of materials with strong tendency to form hydrogen-rich phases (Ti and Zr [194, 274, 275]), and has

to a lesser extent also been observed in steel samples [193]. In recent APT studies, this is commonly mitigated through the use of Cryo-FIB [147, 219], which was not used in the current work due to lack of access. Nevertheless, direct accidental hydrogen incorporation is not applicable in deuterium tracing experiments as here, because the natural abundance of deuterium is too low to achieve incorporation of any detectable amount from an environmental source.

It could also be argued that environmental hydrogen (protium) is incorporated replacing deuterium from any traps in the sample. But this not supported by the frequency cycling experiments (Figure 32), which show a very clear rate dependence of the contaminant signals but not for deuterium, so if deuterium replacement has occurred at all, then the extent of this is minor. It also is noted that the depth distribution of protium (H^+ ions at m/n=1 Da) does not resemble deuterium but is either uniform or slowly increasing throughout the experiments, as would be expected for a contaminant signal. If some deuterium has been displaced from its traps by protium, then it would likewise be expected to follow a similar depth distribution.

A potential valid explanation involving FIB could thus only consist of a loss of deuterium during milling without appreciable replacement by environmental hydrogen. To my knowledge, there is no direct report of hydrogen loss during APT sample preparation in the literature (though design of an according experiment also appears challenging). It has been pointed out by Chang et al. [147] that theoretically, heating of the sample as well as structural damage due to FIB milling could alter the hydrogen distribution. Concerning heating, the temperature increase during FIB sharpening was assumed to be minor for the Ti samples used there [147]. Tungsten has a roughly 10 times higher thermal conductivity than Ti (174 vs 17.3 W/mK [276]) therefore accidental heating may also not be of no concern here.

Importantly, however, it was pointed out to me by Daniel Haley that, at the length scales in APT, “temperature” may not be well defined and instead atomistic effects could be relevant. Temperature is usually defined for ensembles in an equilibrium, but this may oversimplify the interactions between gallium ion impacts and APT specimen, where ballistic effects and interaction between multiple incident ions may be significant. Modelling such phenomena is challenging [277], so potentially more complex mechanisms lead to deuterium escape during FIB milling which are not yet fully understood.

Another potential explanation could be structural ion beam damage, or alterations of deuterium distribution as a consequence of FIB-introduced defects like vacancies. Indeed, as has been mentioned in Section 4.2.4 (Figure 30), a relevant amount of gallium ingress, up to approximately 30 nm, is observed near the tungsten surface in one instance (W-F). Using SRIM [261], Eder et al. simulated average stopping depths for gallium ions in tungsten of approximately 2 to 9 nm for ion acceleration voltages from 2 to 30 kV, which is lower than in most other materials commonly analysed in APT [278] – fortunately, the high capability of tungsten to stop incoming particles likely also works towards limiting depth of FIB damage. Nevertheless, gallium in FIB-prepared APT tips is frequently observed at greater depths than such simulations predict, due to channelling [136, 278, 279], and the current material is no exception to this. Thus, FIB introduced deuterium loss may not be severe, but cannot be ruled out completely.

FIB introduced vacancies may, due to collision cascades, actually extend further into the material than the implanted gallium itself [280]. Langelier et al [280] observed a loss of nitrogen in FIB-prepared Fe-Mn-N steel

samples even beyond the depth of Ga implantation, which could possibly be due to a FIB-related damage effect. They also noted though that for dense materials like their steel samples, collision cascades should not reach significantly further than gallium, meaning it is not guaranteed that this loss indeed is directly related to structural FIB damage. Similar conclusions could apply to the current tungsten material as well – considerable FIB damage may not go significantly deeper than the implanted gallium, but there is no direct proof for this in the data itself.

Lacking a direct and clear marker or imaging method, tracking of vacancies and other FIB-related damage in APT is challenging. Complementary methods such as FIM, which were not applied in this study, could theoretically investigate the depth of FIB damage. An additional difficulty however would be that observed damage likely cannot be distinguished from the pre-existing, tungsten ion radiation induced damage in the material. This, unfortunately, should make an experimental investigation of FIB damage in strongly pre-damaged specimen like in this study impossible, and only simulations could supply this information.

Release over time

Finally, one known difficulty in hydrogen imaging is de-trapping and release from samples over time. In the charging and imaging experiments in steel by Chen et al. [140, 218], great efforts were made to keep the time between hydrogen charging of APT samples and quenching to cryogenic temperatures as short as possible, in the range of 5 minutes or less. On the other hand, imaging of deuterium in steel samples has been successful even if no cooling of samples after exposure (other than during the APT run itself) was conducted at all [193]. Kellogg et al. found in FIM imaging experiments on deuterium implanted tungsten specimen that deuterium was not retained after an unspecified number of “several days” unless trapped at a defect, which in their case was a grain boundary [244]. In general, it appears that escape of hydrogen from APT specimens over time is of concern when hydrogen is not trapped or traps are energetically shallow, but at least some retention is stable over days if traps are sufficiently deep.

For the current material, Thermal Desorption Spectroscopy (TDS) measurements by Hollingsworth et al. [257] on material similar to this study, but without radiation damage (deuterium implanted samples from the same tungsten batch, non-irradiated), show that between day 1 and 14 after implantation the deuterium inventory decreases by approximately 44% – lightly or non-trapped hydrogen escapes. On the other hand, in the same study, the amount of deuterium from radiation-damaged samples after 47 days or more was higher than in the non-damaged sample after 14 days [257], so whilst some deuterium loss over time is occurring, retention of at least some trapped deuterium in the radiation-caused defects in the current sample material is stable over weeks.

In the current study, the times between FIB liftout and APT experiment were of the order of days, and the time between implantation into the bulk sample and beginning of the first liftout was nearly one year (352 days). Any “lightly trapped” deuterium which escapes within a few days of implantation is (nearly) completely gone by the time experiments were run, and only deuterium in sufficiently deep traps is imaged in the APT experiments. A systematic influence of sample age on the imaged deuterium due to de-trapping and release likely exists in the current material, but may not be detectable because the concentration change of the deuterium that is still

retained at the experiment time is too slow. A simplistic calculation of the expected retained fraction of deuterium for different trapping energies is given in Appendix D-8.

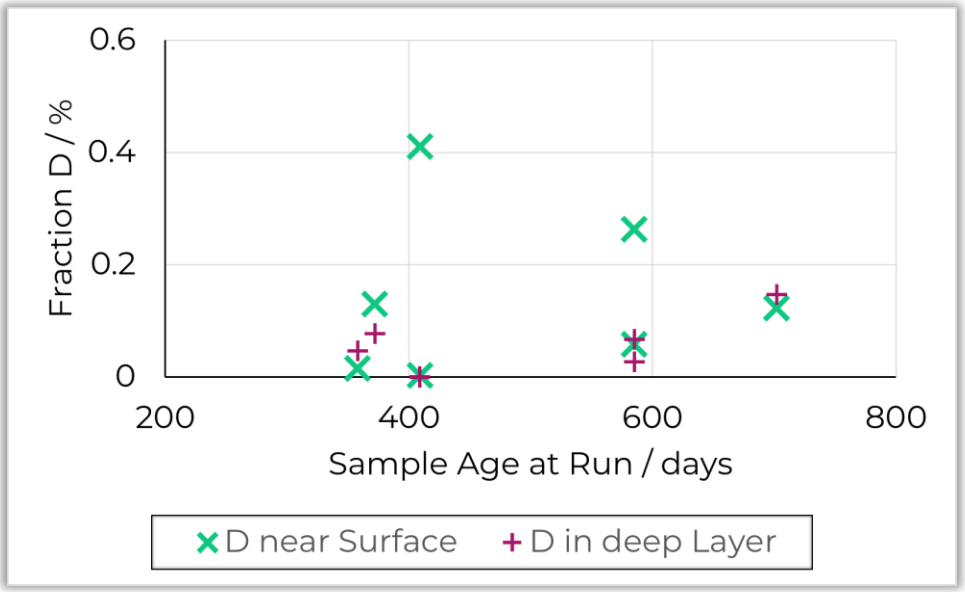

Figure 33: Detected ionic amount of deuterium near sample surface and deep in the material as function of age of the material (as from the day of deuterium implantation) at the time of the APT experiment

Figure 33 shows the ionic fractions of deuterium measured near the surface and in the deep, deuterium-rich layer (also see Figure 31) as function of sample age at the time of the APT experiment, whereby "age" is the time after implantation of deuterium. No trend emerges. If, instead of sample age, the times between beginning of liftout or final sharpening of the APT tip and experiment are taken, no trends are observed either (diagrams in Appendix D-9). Consequently, loss over time is likely not a suitable explanation for the differences between samples, even if the material is known to lose a significant amount of deuterium within days when in a non-irradiated state.

It is noted that, in a similar fashion to hydrogen loss during sample storage time, detrapping can also occur during laser pulses in pulsed-laser APT experiments. This could lead to deuterium loss, or migration inside of the sample. The effect of this shall be estimated. For a theoretical experiment of 25M ions, a 4% evaporation rate and peak width of 4 ns in TOF space (measured at the W^{2+} ions in experiment W-E), the (simplified) assumption is made that the specimen will be at an assumed temperature of 300K [281, 282] for a cumulative time of 2.5 seconds, ignoring any temperature ramps or decays during and after laser pulses. Integrating the differential equation for detrapping from Appendix D-8 with an assumed trap energy of 1 eV, it is found that the fraction of deuterium which is detrapped during the experiment is less than 0.04%. Such a low fraction of deuterium is unlikely to influence the results of the APT experiment to a detectable extent. Given that the trapping energy for hydrogen at a vacancy is likely even higher than 1 eV (1.25 eV, see Table 2), detrapping during the experiment is most likely insignificant in the current study.

As described in Section 1.2.3, the main concerns about hydrogen in tungsten are the build-up of a radioactive tritium inventory and hydrogen embrittlement of the material. For tungsten, increased rates of dislocation nucleation [105, 283], dislocation pinning [284], and hydrogen-enhanced decohesion [285] have been described as relevant embrittlement mechanisms, all of which require that hydrogen diffuses towards a moving crack tip or newly formed defects. The deuterium observed here may however not be able to diffuse towards new

defects, because it likely sits in deep traps from which it cannot escape quickly. Conversely, whilst a potential long-term hydrogen reservoir has been imaged, the relevance of the observed hydrogen to embrittlement may be limited.

4.3.3. Interpretation of Deuterium Distribution

It is observed that the hydrogen in all samples follows a characteristic depth distribution, which sees elevated levels of deuterium directly behind the surface (0-20 nm depth) and at greater depths (70 to 170 nm), with a local minimum in concentration in between. Figure 34 shows the simulated damage profiles (from Figure 23) and measured deuterium concentration (from Figure 30) in direct comparison, with the two deuterium-rich zones highlighted. These two zones approximately match with the simulated depths to which deuterium and tungsten (during irradiation) are implanted into the material. In contrast, no peak in deuterium retention is found at the depth of simulated peak radiation damage.

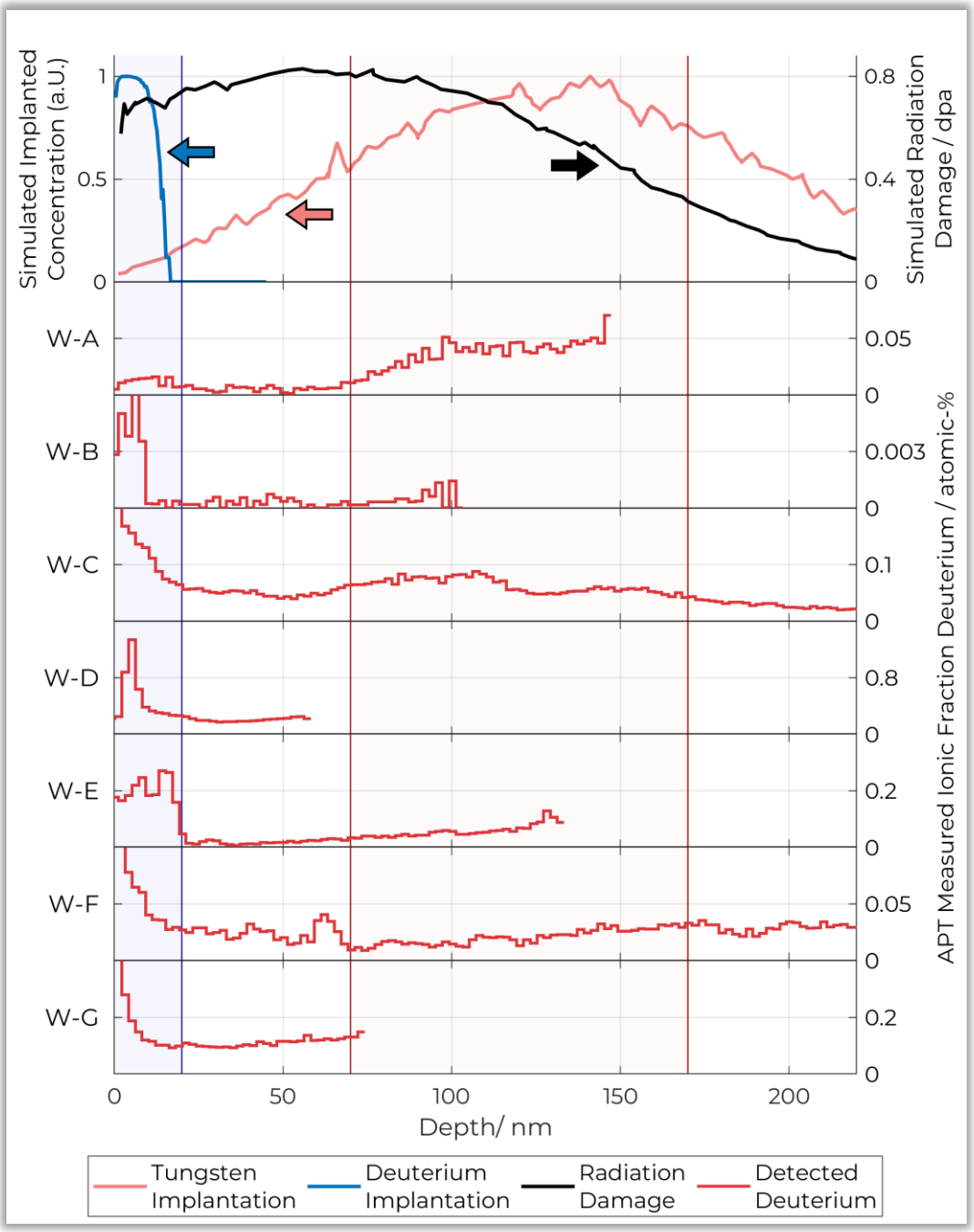

Figure 34: Comparison of simulated depth profiles for radiation damage and deuterium implantation, and deuterium depth profiles from APT experiments

Retention near Surface

Hydrogen-rich layers directly below the surface (here called the deuterium implantation layer) have frequently been observed in hydrogen implanted tungsten [93, 127, 286-291]. Alimov et al. [93, 262] found the concentration of hydrogen directly under the surface to strongly depend on the flux during implantation, however the fluxes in their study were higher by a factor of at least 100 than those used here (more than $5*10^{22}$ vs $1*10^{19}$ ions/m^2s). Under such high fluxes, significant changes to the surface structure such as blister formation occur [262], but this is likely not applicable to the current study, where the flux and total dose are below the threshold for any blistering.

Nevertheless, a thin layer of increased deuterium content at the implantation depth is still found across all samples in this study (20 nm or less, Figure 30), with considerable variation in measured concentration (0.005 to 0.025 ionic-%) between samples. It is noted again that the field strengths (CSRs) did not immediately reach their target values in the beginnings of the APT runs (Figure 29), meaning it could be possible that variations in the field strengths have somehow added measurement errors, partially explaining the large scatter. The fact that the deuterium signal in the extrapolations are nearly constant however (Figure 32) indicates otherwise, meaning that at least a significant fraction of the deuterium observed here likely is “real”.

As mentioned before (Section 4.3.2), non- or lightly trapped deuterium escapes from the current material within days and is not imaged in the APT datasets which were taken almost a year or longer after implantation. The imaged hydrogen in this layer is therefore believed to be trapped, so some mechanism seems to have led to the production of traps in this layer. The nature of a trap generation mechanism in the implantation layer has been considered by several authors, but is not yet fully understood [291, 292].

Firstly, if the implantation energy of deuterium is sufficiently high, the tungsten atoms themselves can be displaced [27, 293], and traps are generated directly during implantation [294]. The current implantation energy of deuterium (800 eV per D_3^+ ion) is below or at the tungsten displacement threshold (assumed to be 940 eV [27, 91] or “above 800 eV” [93]) so this may in parts be a suitable explanation. An alternative mechanism, proposed for low-energy implantations, is that a supersaturation of deuterium in this layer builds up during implantation and leads to mechanical stress until plastic deformation occurs, creating new trapping sites such as dislocations or voids [93, 290, 291]. A mechanism involving accumulation of hydrogen at screw dislocations and subsequent emission of jogs has also been proposed [69].

In W-D, an unusually high deuterium concentration (up to 1.3%) under the surface came alongside a surface oxide with an observed composition of approximately 54 atomic-% oxygen, 9% nitrogen, and less than 3% carbon. It is important to keep in mind that the origin of this oxide is unclear, it could have been present on the sample to begin with or could have formed during or between the radiation- and sample preparation steps. The oxide in the APT analysis volume is below the iridium layer, so it is unlikely that it is due to accidental sample modification during FIB liftout.

Nuclear Reaction Analysis (NRA) studies found that tungsten trioxide surfaces can increase deuterium retention by acting as a diffusion barrier, so potentially such a phenomenon is observed in W-D [295, 296]. In the existing literature, it has been assumed that the diffusion properties in the oxide itself (slower than in pure tungsten) are the reason for this [296], but in current APT study it may be that an additional trapping site at the tungsten-

tungsten oxide interface is observed. To my knowledge, the existence and implications of such a trapping site, which likely is very difficult to observe using the commonly used methods NRA and SIMS, have not yet been considered in existing published work. It is known from theoretical calculations however that single interstitial oxygen atoms can act as a trap for hydrogen, but the trap is weaker than a vacancy [297].

It is also noted that multiple studies – both simulations and experiments – suggest that surface layers of tungsten carbide and nitride can act as diffusion barriers, as well as themselves contain trappings sites and therefore accumulate deuterium, however from the high oxide content in the observed phase this may not be relevant to the current case [298-302].

In W-B, an elongated structure of carbon, oxygen and nitrogen which likely is a pre-existing dislocation that is open to the material surface is observed, but barely any deuterium. Simulations by Bakaev et al. indicate that the hydrogen trapped at screw dislocations is already released at temperatures around 320 to 350 K [69], meaning that such hydrogen likely escaped before the experiment, and that ultrafast "pipe" diffusion of tungsten along the dislocation line is possible [303]. Experimentally, it has been observed that blistering is reduced on mechanically polished surfaces compared to chemically etched surfaces [103, 104], which, following Zayachuk et al., could potentially be due to surface-near dislocations acting as fast transport channels [104]. This could potentially mean that the dislocation in the APT dataset has acted like a "vent" through which hydrogen escapes from the material. It is not entirely clear though why then there seems to be almost no retention in vacancies near the dislocation.

Retention at deeper Layers

Retention of implanted deuterium at defects in ion irradiated layers is frequently reported in the literature, and the current study where deuterium is found in a damaged region is well in line with this [80, 258]. However, in the current work, it is observed that the retained deuterium does not peak in the layer of maximum simulated radiation damage, but slightly deeper, in a layer roughly corresponding to the implantation depth of the tungsten from radiation damaging. This is a surprising detail, and merits further discussion.

Hollingsworth et al. conducted TEM and PAS on samples which were prepared in the same way as the material used here, but radiation damaged with doses from $1*10^{16}$ to $2*10^{18}$ ions/m^2, corresponding to simulated peak damages of 0.0085 to 1.7 dpa [257]. It is known from these analyses that the primary types of trapping defects in the material are single vacancies and clusters of 5 to 7 vacancies. Dislocation loops are rather rare and cannot account for a significant amount of retained hydrogen [257]. In the PAS experiments, it was also found that the radiation damage in this material saturates from approximately 0.425 dpa, but a widening of the layer with the highest level of damage from approximately 100 to 170 nm is observed as the dose increases from 0.0085 to 1.7 (simulated peak) dpa [257].

In the current material, the dose is $1*10^{18}$ ions/m^2, with a simulated peak damage of 0.85 dpa (Figure 23), which is beyond the saturation point observed by Hollingsworth et al. [257]. This means that the simple simulation of damage very likely does not accurately represent the depth distribution of induced trapping sites (vacancies), and could help with interpretation of the APT results: radiation can introduce a high concentration of trapping sites down to at least 170 nm, and saturation of defects and therefore trapping sites has occurred at some depths.

This alone, however, does not explain why the deuterium concentration is not constant up to approximately 170 nm, but instead a local minimum is observed between 20-70 nm in all samples. It may be that the radiation damage at this depth is so high that additional effects come into play, or possibly the carbon/nitrogen/oxygen atoms in this layer interfere with vacancy generation or deuterium trapping. The current APT experiments do not seem to suggest an obvious interpretation.

It could also be feasible that the injected tungsten atoms themselves play some limited role. DFT simulations predict that individual self-interstitial tungsten atoms are only weak hydrogen trapping sites (approx. 0.3 eV), and significant de-trapping should already occur around 152 K within minutes [72, 304]. However, when clustered to loops of self-interstitial atoms, the trap strength is much higher, 0.66 eV or more [304]. This might also be compatible with the experimental observations: in the layer reached by the implanted tungsten, structures of self-interstitials have formed and act as additional trapping sites. It is not known if or to what extent such defects are present in the current material. Potentially, future complementary FIM-APT studies could provide insight into this [240].

Role of Nitride Clusters

Since carbon/nitrogen/oxygen clusters are present in all datasets, the question arises whether traps associated with these clusters are relevant to the retention of deuterium in the material. Trapping of hydrogen at carbides in steel has been observed before using APT [214, 216, 217], therefore such a phenomenon would likely also be detectable in the current data if present. To investigate this, k-th nearest neighbour distributions of deuterium and carbon, nitrogen and oxygen are analysed. As mentioned in Section 4.2.1, carbon, nitrogen and oxygen overlap through WC , WN and WO ions, therefore are treated as the same entity in the following analyses. From the composition calculations (Section 4.2.2 and Appendix D-5), it is known however that most of these C/N/O atoms (at least 63% in all datasets) are nitrogen, and the oxygen concentration is low (less than 8%, unless very close to the surface, Figure 28C).

Figure 35 shows, for all datasets, the distribution of the 5th carbon, nitrogen or oxygen neighbour from each deuterium ion in the reconstructed APT data as well as for randomised spatial distributions of deuterium. Randomised deuterium distributions were obtained by randomly assigning ion positions out of all detector events in the dataset, excluding carbon, nitrogen and oxygen positions, without their replacement. In other words, the carbon, nitrogen, oxygen distributions were not randomised, as this would negate their spatial clustering. In all datasets the first 40 nm of atoms in z-direction were removed to avoid spurious contributions from the carbon caps on the samples.

The observed deuterium-carbon/nitrogen/oxygen distance distributions are either identical to their randomised counterparts (Figure 35B – E, G), or very slightly biased towards lower distances (Figure 35A, F). In all cases, deviations from random distribution are minor, such that there is likely no relevant co-segregation or other feature observed here. This indicates that there are probably no deuterium trapping sites in or on the surface of the carbon/nitrogen/oxygen clusters, or around non-clustered C/N/O species imaged in the current experiments. The positions of deuterium in the dataset with respect to C/N/O seem neutral – neither increased, nor decreased proximity is favoured.

Experiments on tungsten exposure to nitrogen-seeded deuterium plasmas have shown that nitrogen can lead to increased deuterium retention [286, 305, 306]. When the plasma is nitrogen seeded, a small amount of nitrogen accumulates in the tungsten near the surface, and the depth at which most deuterium is retained shifts deeper, presumably deuterium is not retained in, but below this nitrogen-rich layer [286]. From DFT studies, it is known that decoration of a tungsten vacancy with nitrogen however makes it a weaker trapping site for hydrogen, and that presence of nitrogen in the material impedes hydrogen diffusion [307]. This provided an explanation for observations made in the nitrogen-seeded plasma experiments: nitrogen accumulates in tungsten near the surface and expels some hydrogen from this layer by weakening the vacancy trapping sites there, but overall retention still increases because the nitrogen layer acts as a diffusion barrier and impedes hydrogen escape from underlying layers in the material [307]. Carbon, according to DFT simulations, can act in a similar way to nitrogen and decorate vacancies, weakening the trapping sites for hydrogen [308, 309].

It may be that this also applies to the current material. From the line profiles (Figure 30, esp. C, F), it is known that the amount of nitrogen and carbon at depths of up to approx. 130 nm is elevated, and with one exception the number density in carbon/nitrogen/oxygen clusters is found to peak at less than 100 nm in all datasets. The layer of peak simulated radiation damage, which is taken as 20 to 70 nm (Figure 23), overlaps with the comparably nitrogen- and carbon-rich areas, potentially nitrogen and carbon might even have been injected into the material during tungsten irradiation. The concentration of tungsten vacancies and potential other hydrogen trapping sites may be high anywhere up to approximately 170 nm depth, but in the peak damage layer up to 70 nm, an elevated fraction of nitrogen and carbon atoms in this layer are also trapped at the vacancies, weakening these traps for hydrogen.

This could explain why no co-segregation of nitrogen and hydrogen is observed (Figure 35), and why more deuterium is found deeper in the material than in the layer of peak simulated damage, where deeper the fraction of vacancies without carbon/nitrogen decoration might be higher.

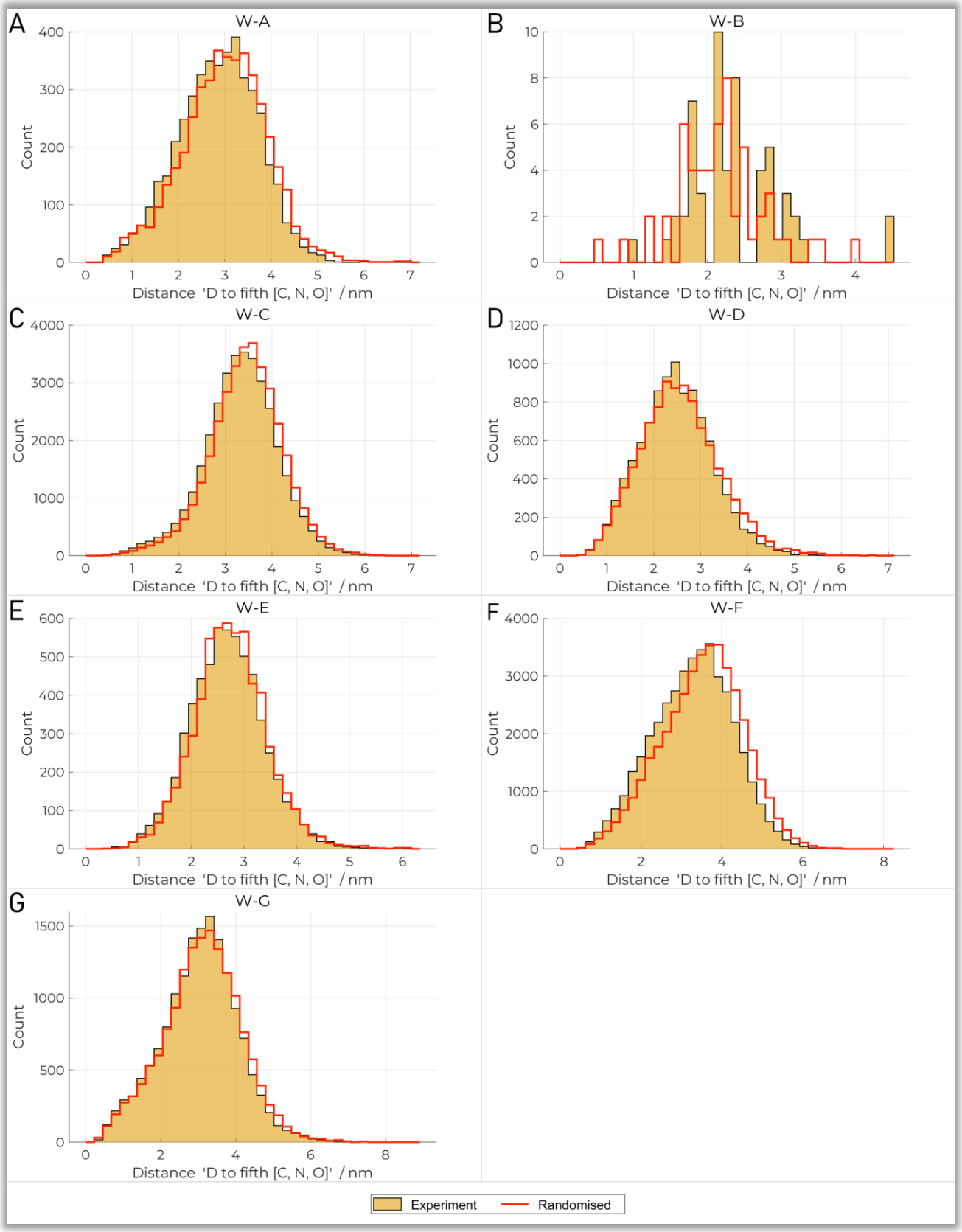

Figure 35 Distance distributions of 5th carbon, oxygen atom from each deuterium atom in the datasets for actual experimental data as well as for randomised deuterium distributions.

4.4. Conclusion

Implanted deuterium in self-radiation damaged tungsten samples has been imaged, using the method based on laser-mode APT at high (and controlled) electric fields. The results show that the method for deuterium imaging in tungsten is definitely feasible. Across all samples, a characteristic depth distribution of the implanted deuterium is observed: the deuterium content is elevated directly behind the tungsten surface in a layer corresponding to the implantation depth, and in a second layer deeper in the material which happens to approximately align with the depth reached by the tungsten ions during radiation damaging. Notably, the layer of highest simulated damage does not align with the maximum deuterium retention. Several possible causes for this have been discussed, but it is not immediately clear to what extent all of these are relevant.

In this chapter, the capabilities of APT for nanometre-resolved imaging of hydrogen are clearly demonstrated. In the context of fusion energy, it is on the other hand not directly clear how the obtained results should be interpreted, and this first application of APT to hydrogen retention in tungsten might give rise to more questions than it answers. Conversely, the study also shows that APT is a useful tool for future research, which might help answering these questions. More studies are needed to clarify why peak deuterium concentration was observed deeper than peak simulated damage, and why the variation in deuterium content measured between APT experiments is so high. I would propose to conduct more experiments on more lightly radiation damaged material which is far from damage saturation, and to couple future APT analyses with NanoSIMS to obtain an overview over eventual inhomogeneities in the hydrogen distribution in the sample.

5. Large-Scale APT data analysis

In this chapter, analyses on a large collection of 848 APT datasets are presented, with special emphasis on investigating contaminant hydrogen. Data from experiments that were undertaken on a Cameca LEAP 3000X HR between 2012 and 2015 at the Oxford Atom Probe Group were exported to build a database, using UI automation. It is shown that a large number of APT experiments can be regarded as a point cloud in which the cityblock distance is a viable method to quantify (dis-) similarity of spectra.

The behaviour of contaminant hydrogen is analysed and correlated with voltage, electric field, and sample base material. To this end, methods are developed that allow applying the necessary analysis steps (determination of hydrogen fraction, sample base material and field strength) quickly on many datasets, without the need for a consideration of individual experiments by a human operator.

5.1. Theory

5.1.1. Data in APT

The primary data collected in APT experiments are the detector coordinates and time-of-flight. A range of processing steps is needed to transform this raw data into mass-to-charge-state ratio spectra and spatially reconstructed APT datasets. Alongside of the detector data, peripheral observables are recorded during the experiment, such as residual gas pressure in the vacuum chamber and specimen base temperature. In the case of the commonly used Cameca LEAP instruments, all data is stored in a proprietary file format by the control software, and their reconstruction software (IVAS or APsuite) is required to read and process these files. No direct and fully automatic method for exporting or analysing batches of many datasets exists at the time.

To overcome this problem, it is possible to employ user interface (UI) automation scripts to indirectly automate IVAS to open raw APT experiment files in IVAS (.rhit, .hits), and export the resulting data into .epos and .csv files. These file formats are open and commonly used in APT, such that the information can both be accessed with a range of existing software, as well as with newly implemented tools. Therefore, .epos and .csv are a suitable base for the automated data analysis as conducted here. To clarify, this method cannot expose the true, unprocessed detector data, but can only access information that has already been processed by (at this time) “black-box” reconstruction procedures in IVAS[10], as is common practice in current APT.

A significant amount of operator input is usually needed in APT to obtain accurate spatial reconstruction of datasets, e.g. for assigning ion identities in the mass-to-charge-state ratio spectrum and selecting reconstruction algorithm parameters. Developing a full automation of this is beyond the scope of the conducted work. Nevertheless, reconstructed spatial information is not required for the research on the material- and field dependence of hydrogen presented here. The UI script does therefore not need to automate a full spatial reconstruction in IVAS, instead it is sufficient to skip or fall back to default values on any reconstruction-related processing steps.

[10] Due to unavoidable use of proprietary file formats and closed software in current commercial atomprobes, it is at this time not possible to avoid several black-box processing steps applied by the software, or to gain further insight into these procedures. This is a longstanding problem in the field of APT.

5.1.2. City Block Distance of APT Spectra

A critical ability for handling a large collection of APT spectra is an effective means of quantifying the similarity of two spectra, to enable search for spectra with certain features or similarities, or to discover groups (clusters) of similar datasets. To achieve this, a method based on the city block distance (also referred to at Manhattan distance, taxicab distance or L_1 distance) [310, 311] is proposed.

From all experiments in the collection, spectra are created, using the same histogram binning for each dataset. The spectra are then normalised such that the counts in every spectrum sum up to the fixed value 1. The entirety of so-obtained spectra is interpreted as a high dimensional point cloud, so every dataset is one data point in the cloud, and each bin corresponds to one dimension. A collection of m spectra with n bins each thereby amounts to a $m * n$ point cloud. The inverse city block distance between spectra can then be used as a measure for similarity: lower distance between two points in the point cloud corresponds to a higher degree of similarity between spectra. This enables the retrieval of spectra by similarity by means of a nearest-neighbour search in the spectral point cloud.

The city block distance between two spectra a and b with n bins is

$$d(a,b) = \sum_{k=1}^{n} \mathrm{abs}(a_k - b_k)$$

Equation 8

where a_k and b_k are the measured intensities of the k-th bin in spectrum a and b. d is scalar.

Usually, the intensities in APT spectra are measured as number of detector events, and hence the sum of all counts per bin in a spectrum is the total count of detector events of an APT dataset. When comparing spectra, it is helpful however to normalise all counts, such that the intensities in all bins of a spectrum sum up to 1, as mentioned above. This effectively makes the distance between two spectra independent of the ion yields of the experiments, such that a distance is only dependent on the spectra shape, but not the ion count.

An example for the city block distance in spectra is provided in Figure 36. The simplistic examples in Figure 36A and B show two normalised spectra each, which in case A are similar and dissimilar in case B. The summed-up differences between intensities per bin, shown as black arrows, amount to the city block distance between the spectra. In the dissimilar case B, the arrows are longer, or their summed-up length is higher, leading to a greater city block distance between spectra than in the similar case A.

The spectra in the collection of archival data used here do not represent a uniform distribution of points in the cloud, as will be shown in Section 5.3.2. Instead, multiple experiments in the past have often been run on the same or similar sample base material, so there are groups of similar datasets in the archival data. The inverse distance of datapoints in the cloud corresponds to similarity, therefore these groups appear as clusters in the point cloud. It is therefore possible to identify the sample base materials present in the archival data by means of cluster search in the point cloud. For a given dataset, it is also possible to infer the sample material based on cluster association in the point cloud.

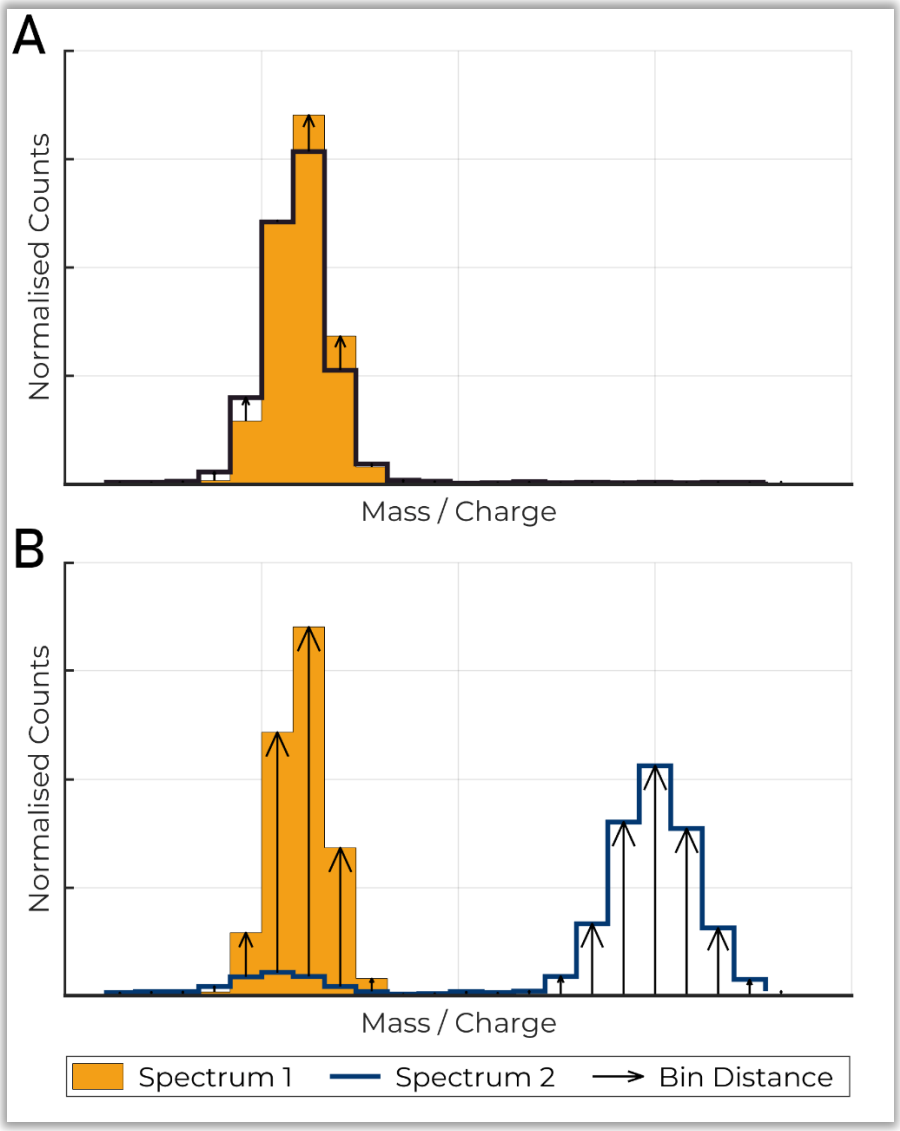

Figure 36: Simplistic example of two APT spectra which are similar (A) or dissimilar B. The cityblock distance between the spectra is the sum of all arrows ("Bin Distances").

5.1.3. Analysis of Hydrogen behaviour

In this work, the statistical dependence of contaminant hydrogen on material, voltage, and electric field across a large body of archival APT data are of interest. In APT, experiments are usually analysed on an experiment-by-experiment base and require input from human operators, which is prohibitive if a large number of experiments is to be re-analysed (see for example the hydrogen analyses in all previous chapters in this thesis). It is therefore necessary that the following steps in the analysis of APT data are automated to not require experiment-by-experiment consideration: measurement of H^+ and H_2^+ fractions, determination of sample base material, and calculation of electric field.

Regarding $H^+$and H_2^+, there exists no ion which could realistically be expected in APT which could overlap with H^+ or H_2^+. This means, in a (theoretical) noise-free APT spectrum, it is possible to reliably and automatically determine the counts of H^+ and H_2^+ by reading the number of counts at the positions where these peaks are expected. For 'real' APT spectra, the accuracy of the determination of H^+, H_2^+ counts hinges only on the background correction. So called "wrap-arounds" are a possible artefact when the pulse frequency is too high,

potentially leading to heavy ions falsely appearing in the low mass-to-charge-state ratio range and interfering with the detected hydrogen signal. However, it is expected that this is very rarely a problem in "good" APT runs, and therefore does not require further consideration. A further theoretical problem arises if the hydrogen peaks incorporate excessively long peak tails which overlap with other peaks at higher mass-to-charge-state ratios, but – especially for the reflectron APT data used here – this is an edge case which does not arise in the current data, and thus does not require further treatment in this study either.

Fortunately, due to the natural weights of all isotopes, there also exist regions in the APT spectrum around the H^+, H_2^+ peaks which are expected to never contain peaks as no ions with a corresponding mass-to-charge-state ratio can exist [148]. Only background noise is observed in these regions, therefore they lend themselves to noise estimation. Time-of-flight-constant (TOF-constant) background fitting using these regions is therefore (almost) universally applicable to all APT spectra. Combination of such a TOF-constant fit with a simple reading of the counts at the expected positions of H^+ or H_2^+ enables automated extraction of H^+ or H_2^+ counts, making the study on hydrogen in many APT experiments viable.

Determination of sample base material is possible based on clusters in the spectra point cloud, as will be shown in Section 5.3.2. This enables material-dependent analyses on the correlation between the measured amount of hydrogen and the voltage applied during the experiment. Also, once the base material of a sample is known, the CSR of the majority ions can usually be extracted easily and automatically as the ratio of two peaks whose position in the spectrum is known. This means that an analysis of hydrogen with respect to voltage in the collection of APT spectra can be easily extended to an analysis of hydrogen with respect to electric field.

5.2. Experimental

5.2.1. Exporting APT Data using UI automation

A user interface (UI) automation script was created to automatically operate the commercial APT software IVAS in order to export data from the proprietary formats into open formats which are useful for the archival data analysis. In IVAS, the files are processed using a "Reconstruction Wizard", which guides the user step-by-step through the reconstruction of the APT data, which can then be saved, and exported afterwards. The script therefore needs to automate Reconstruction Wizard and file export.

The aim of the script is not accurately reconstructing a spatial image from the data, but only exporting it. Hence the script skips or falls back to default values for all processing and calibration steps which are only required for reconstruction but not for data export. As a result, the spatial reconstruction is not constrained with sensible parameters, and the exported spatial reconstruction coordinates are thus meaningless. This is not of concern for the work described here, where no spatial information from the reconstruction is needed (Section 5.1.3). It is also noted that the detector coordinates of events are exported, and in theory allow for reconstruction outside of IVAS, so on the fundamental level the spatial information is not lost, it only is not transformed into reconstruction space. A full list of actions performed by the script is given in Table 14.

Table 14: Actions taken by the UI automation script for IVAS when operating the Reconstruction Wizard

Step in Reconstruction Wizard	Purpose	UI automation script action
1. Setup	Review Experiment data	-
2. Ion Sequence Range Selection	Select part of the raw experiment file to include in reconstruction, select initial voltage for reconstruction, export graphs: voltage, pressure, laser energy etc.	Select everything, export all graphs as .csv format
3. Select Detector Region of Interest (ROI)	Select detector area to include in reconstruction	Leave at pre-selected default
4. Time-of-Flight (TOF) Correction	Apply voltage- and bowl correction to TOF spectrum	Run with default values
5. Mass Calibration	Apply (piecewise) linear correction to m/n-spectrum to match position of clearly identified peaks with their correct locations	Skip (this is corrected during post-processing of the data, outside of IVAS)
6. Ranged-Ion Assignments	Assign peaks in the mass-to-charge-state ratio spectrum to ions for reconstruction	Load a dummy range file containing only one range for H^+ at the m/n-1 peak
7. Reconstruction	Adjust reconstruction parameters	Run with default values (voltage-based reconstruction)

Once the processing in the Reconstruction Wizard is complete, the automation script exports the APT dataset into an epos file [136]. This file along with the csv files of additional sensor data exported in step 2 (Table 14) are copied, then IVAS is reset to its initial state (by deleting a user settings folder which automatically created on IVAS startup), and the reconstruction is re-started with the next raw experiment file. Appendix E-1 provides an overview over all data retrieved per experiment.

The method has been applied to files from APT experiments (.rhit files) which were undertaken between 2012 and 2015 on a Cameca LEAP 3000X HR atom probe. Unlike later generation LEAP instruments, this atom probe does not support changes of pulse frequency and laser energy during experiments, meaning that experiments are at constant pulse rate and laser energy (if laser evaporation is used). Only raw files with a size above 100 MB are selected. This restriction was implemented in an attempt to easily reject “bad” runs where a specimen fractured shortly after start of the experiment, or where the operator stopped the acquisition at an early stage – short runs correspond to small files. In practice, this restriction results in all reconstructed APT runs having at least 6.8M ions. This however also biases the selection of experiments towards high-yielding materials and parameters that typically lead to long runs, i.e. laser assisted evaporation.

5.2.2. Calibration of APT spectra

A crucial step skipped during the reconstruction in IVAS is the calibration of the mass-to-charge-state ratio spectra. Typically, spectrum calibration in APT involves a (piecewise) linear scaling of the mass-to-charge values of the detected ions, such that isotopic fingerprints in the spectra align with their expected positions. The usual procedure is for a human operator to manually identify isotopic fingerprints in the spectrum for this fitting. Here, a semi-automated procedure is applied to the exported data which aims to determine two factors c_{scale} and c_{shift} for each dataset, such that linear calibration of the mass-to-charge state values can be conducted using:

$$m_{\mathrm{cal}} = c_{\mathrm{scale}} * m_{\mathrm{uncal}} + c_{\mathrm{shift}}$$

Equation 9

m_{cal} and m_{uncal} are the (un-) calibrated mass-to-charge state ratios.

To achieve this, datasets which contain clear isotopic fingerprints of one or more out of Ti^{2+}, U^{3+}, Si^{+}, Mo^{2+}, Cr^{2+}, Zr^{2+} and Ga^{+} are identified through manual inspection in a first step. These ions were used because they are commonly found in the archival datasets investigated here, and their fingerprints have characteristic shapes which are easily visually identified by a human operator. It is also attempted to automatically identify the location of the m/n=1 peak in all datasets. Since contaminant H^{+} is observed in nearly every APT experiment, this peak is almost universally present in APT runs and was located successfully in 843 out of the 848 datasets.

In all datasets where the H^{+} peak and at least one other isotopic fingerprint was found (manual inspection), it is possible to calculate how far the (at least 2) observed fingerprints are off from their expected positions, and followingly the correction factors c_{scale} and c_{shift} can be determined. Calculation of this "offset" per fingerprint is implemented through a crosscorrelation of the fingerprint-containing part of the spectrum with a well-calibrated reference spectrum containing the same fingerprint. Once c_{scale} and c_{shift} are known, these spectra can be calibrated. For all datasets where H^{+} but no other fingerprint was identified, only the factor c_{shift} is calculated, such that the m/n=1 peak is at its expected position, and subsequently the scaling factor c_{scale} is determined through an optimisation.

To this end, the assumption is made that for all of these datasets, at least one dataset exists amongst the already corrected ones that at least in parts looks similar, i.e., contains shared isotopic fingerprints. This is an acceptable requirement because spectra in the current collection are typically dominated by ions out of a low number of base materials (as will be shown in Section 5.3.2, Figure 39). For all the spectra where c_{scale} is to be determined through optimisation, this is done by iterating through a range of proto scaling factors c_{scale}, and the scaling factor which minimises the distance to any of the already corrected spectra is selected for c_{scale}.

A more detailed and technical description of the procedure is given in the code, which has been published in [312]. No optimisation was conducted for those 5 datasets where no H^{+} peak was found, instead no scale correction was applied to these datasets (i.e. $c_{\mathrm{scale}} = 1$).

5.2.3. Searching Spectra by Similarity

The distance between respective spectra (Equation 8) is a measure for similarity, therefore distance is a useful mean for searching spectra that are similar to a given input spectrum. Finding the most similar spectra for a given candidate corresponds to computing spectra with lowest distance, i.e., retrieving the nearest neighbours. This is demonstrated using three example spectra from outside the database, for which the most similar spectra from the collection are sought. Appendix E-2 lists run numbers and hash values of these search candidates.

The first example is a Ti^{2+} isotopic fingerprint with a partial Cr^{2+} overlap from a nickel-base superalloy which was analysed at the APT & 3D Nanoanalytics group (P. J. Felfer) in Erlangen, Germany on a Cameca LEAP 4000X HR. This candidate combines two aspects that are likely beneficial for the search for similar neighbours. Firstly, Ti and Cr are common alloying elements in Ni-base superalloys and steels, of which many samples have been previously analysed at the Oxford APT facility, so the number of potentially similar neighbours is high. Secondly, Ti^{2+} and Cr^{2+} are used in the calibration of those spectra where they have been identified, meaning that the calibration of spectra at the locations of Ti^{2+} and Cr^{2+} is particularly good.

The second example is a W^{+}fingerprint from a pure tungsten sample that has been run on a Cameca LEAP 5000 XS. Like for the Ti-Cr case, the number of potentially good matches in the database is high. However, the search candidate was intentionally chosen as a spectrum with relatively few counts (most tungsten in this sample evaporated as W^{2+} and W^{3+}) and a poor peak shape (caused by intentional poor application of the voltage/bowl correction in the IVAS software). This corresponds to an intermediate case where it is expected is that a nearest-neighbour search is more prone to pick up datasets which are a poor match to the search candidate.

The third example is a complex peak overlap of SiO_2^+, Na_4P^{2+}, PO_2^+ and PO_2H^+ ions in a bioactive glass sample, analysed by Ren et al. on a Cameca LEAP 5000 XR [313]. Such material has not been run on the LEAP 3000X HR in the relevant timeframe, so there are no similar samples in the collection of datasets at all. This represents a hard, or impossible, case, where nearest neighbour search can only retrieve “false” leads, i.e., spectra that may look similar, but which are from chemically entirely different materials.

5.2.4. Visualizing Clusters in the Point Cloud

As has been described in Section 5.1.2, it is expected that the point cloud of all spectra in the database contains clusters. This point cloud is very high-dimensional, such that direct visual inspection is not possible. T-distributed stochastic neighbour embedding (t-SNE) is used for visualisation of the high-dimensional point cloud into 2-dimensional space, whilst preserving the spatial relationships as much a possible [314]. This enables an approximate overview over the similarity (distance) relations between the spectra, and in particular makes clusters visible in 2D. In this work, a bin size of 0.1 Da is selected for the t-SNE embedding to reduce computation time and memory usage. This is lower than the bin sizes commonly used in APT spectra (usually in the range 0.001 to 0.01 Da) but is sufficient for the current application.

T-SNE is a visualisation method which works by embedding a high-dimensional dataset into a low-dimensional dimensional space (usually 2D) to enable visual inspection. To this end, a probability distribution based on the point distances in high-dimensional space is computed, then a distribution of points in the low-dimensional space with its own probability distribution is initialised and continuously updated to minimise the divergence of

the probability distributions in high-dimensional and low-dimensional space [314, 315]. The algorithm is not deterministic, but initialisation of points in low-dimensional space and minimisation (via stochastic gradient descend) rely on random number generators [314, 316].

An example for a T-SNE embedding of by van der Maaten et al [314] is given in Figure 37. The dataset contains digitised, hand-written numbers, whereas every number corresponds to an array of grayscale values, one grayscale value per pixel. All number scans have the same number of pixels (28 by 28), so can be seen as a distribution of points in a 784-dimensional point cloud. The T-SNE embedding can embed this into two-dimensional space, shown in the diagram. Similar images – and therefore particular digits – are clustered in the high-dimensional space and remain so in the 2D-embedding.

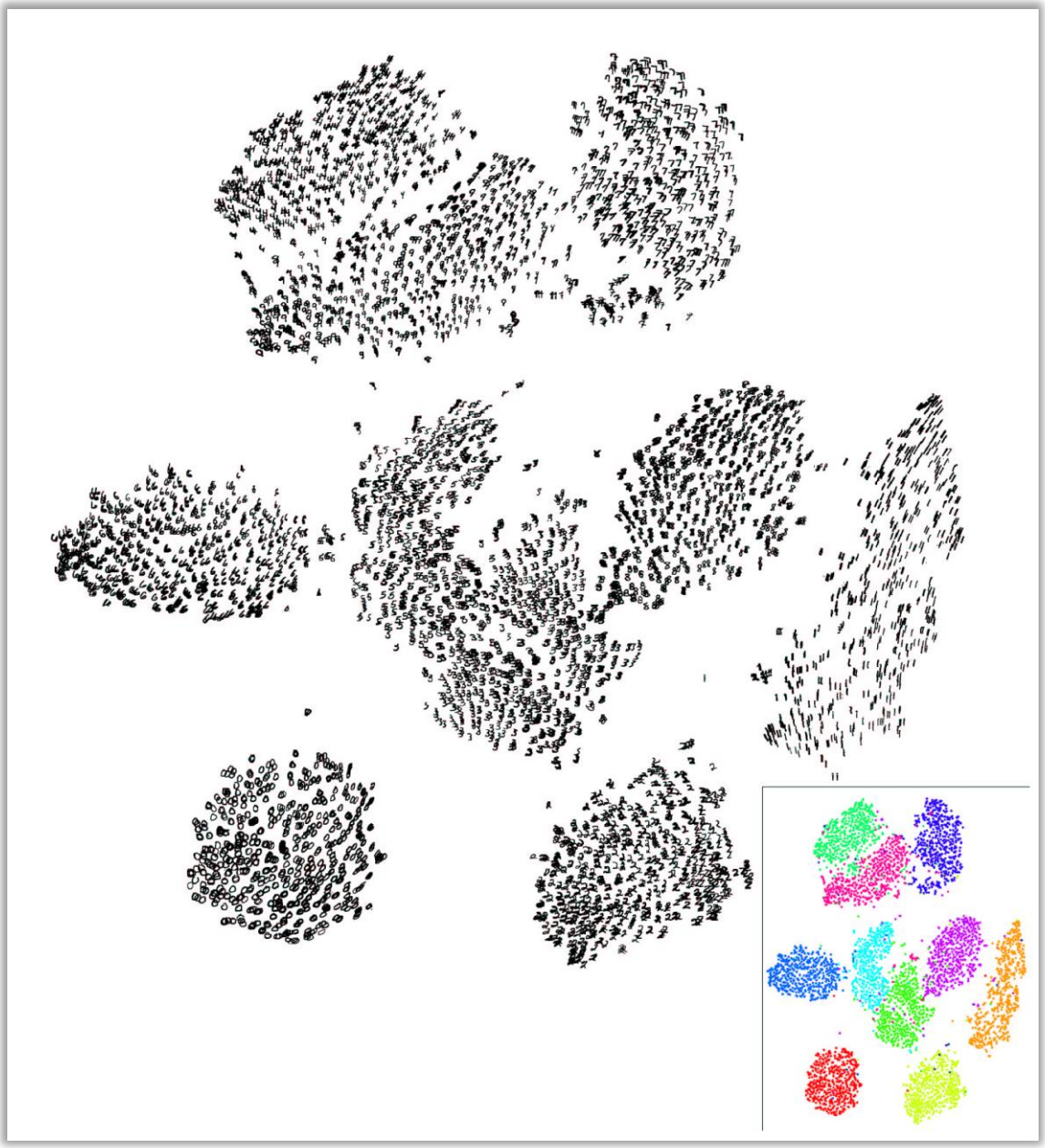

Figure 37: T-SNE embedding of a dataset of digitised, handwritten numbers. It is seen that the different numbers are clustered together. The inset image shows the same datapoints, but coloured according to digit. Diagram taken from [314]. Copyright by L. van der Maaten and G. Hinton, used with permission.

To gather information about the chemistry of APT specimen, isotopic fingerprints of common sample base materials from the Oxford Atom Probe Group (Fe, Ni, Zr, W, Si, Ti, Ga, U) are fitted into the spectra, taking

charge states +1 and +2 into account. If one of these fingerprints accounts for more than a certain fraction of all detector events in the spectra (critical fractions listed in Figure 39, legend), the element is assumed to be the main element of a sample, and this information is included in the t-SNE map by drawing the points in colours and markers specific to the element. This effectively highlights the regions in which particular main elements are found in the t-SNE map.

Generally, visual inspection of t-SNE embeddings is not considered an ideal method for proving the existence of clusters [317]. This is due to human bias when visually inspecting datasets, but t-SNE also can possibly introduce artefacts, such as clusters that are not contained in the original data [315, 318]. To add more confirmation that the clusters on the t-SNE map are not artefacts but "real" [319], the "Ordering Points To Identify the Clustering Structure" algorithm (OPTICS) is applied to the point cloud of spectra (not to the t-SNE coordinates) to create a reachability diagram [320, 321].

OPTICS calculates a so-called reachability distance for every point and orders the list of points in a particular way [320, 322]. The reachability distance is defined as the maximum out of the distance that needs to be travelled to this point and the "core distance" of each point, whereas core distance is the radius around the point within at least MinPoints are found. The algorithm processes the points in a certain order: it travels from point to point, using a queue of yet unprocessed points. Every time when a point is processed, the reachability distances of all yet unprocessed points are re-calculated (using the travel distance from the current point), and the queue of unprocessed points for processing is re-ordered by reachability distance[11] [320, 322].

For the reachability diagram, the reachability distances of all points are plotted in the order in which the algorithm processes the points [320, 322]. Spectra in clusters have low reachability distances, but they are surrounded by distanced points that are not part of the cluster and thus appear as sinks in the reachability plot [320, 321].

5.2.5. Analysis of Hydrogen Behaviour

The ratio of H_2^+ to H^+ is analysed as function of voltage in the collection of spectra. APT experiments are typically undertaken using a constant target detection rate, where the voltage is adjusted in a feedback loop. As the specimen is getting blunter throughout the experiment, resulting in a weaker electric field concentration [323, 324], this usually results in the voltage slowly increasing during the run[12]. So, APT experiments can be seen to scan the contaminant hydrogen across a voltage range.

Every dataset is split into voltage bins of 500V width. For each voltage bin, background correction is conducted, using the universally ion-free regions of the mass-to-charge-state ratio spectrum around hydrogen [148]. Then it is possible to extract the number of H_2^+ and H^+ as background corrected counts at m/n=0.9…1.1 and m/n=1.9…2.1. Bins with less than 50000 total atoms, or less than 500 H_2^+ or H^+ ions are rejected. A side effect of this is the exclusion of all datasets where both H_2^+ and H^+ peaks are missing.

[11] It is noted that the original OPTICS only considers points within a certain maximum distance ε when calculating neighbour distances and processing points, which improves the computational efficiency. The implementation used here is not using this speed-up, thereby the parameter ε is omitted.

[12] Blunting of specimen also leads to increases in the field of view which in turn decreases the electric field required to achieve a certain target detection rate, however this effect is usually outcompeted by the decreasing field concentration.

This provides all data needed to calculate the evolution of the H_2^+/H^+ ratio over voltage for each dataset. Since the base material of the samples can be estimated through association with clusters in the spectra point cloud (Section 5.4.2), it enables drawing diagrams of the fraction of H_2^+, H^+ and the ratio H_2^+/H^+ as function of voltage per base material for many experiments.

As will be demonstrated in Section 5.3.2, the base materials of some of the samples in the collection can be easily identified, including Fe, Si, Ni, Zr and W. For these samples, CSRs of $\mathrm{Fe}^{2+}/\mathrm{Fe}^{+}$, $\mathrm{Si}^{2+}/\mathrm{Si}^{+}$, $\mathrm{Ni}^{2+}/\mathrm{Ni}^{+}$, $\mathrm{Zr}^{3+}/\mathrm{Zr}^{2+}$ and $\mathrm{W}^{3+}/\mathrm{W}^{2+}$ are extracted, respectively, for all voltage bins where the counts of H_2^+ and H^+ were estimated, using counts in the (noise corrected) spectra. Kingham curves as calculated by Yao et al. [136] are used to estimate electric fields from the CSRs. This enables extending the analysis of the voltage dependence of the hydrogen signal to an analysis of electric field dependence.

It is noted that these so-detected CSRs are inaccurate if the respective peaks in the spectra overlap with other ions. However, given that the base material can be determined with good confidence (Section 5.3.2) and that I only draw conclusions from averaged data across many experiments, I argue that the errors that this introduces do not critically influence the results or conclusions.

5.3. Results

5.3.1. Searching Spectra by Similarity

The three example spectra used here to demonstrate nearest-neighbour search and their nearest four neighbours are shown in Figure 38. In the “easy” Ti-Cr overlap case (Figure 38A) all the nearest neighbours indeed look just like the search candidate. The closest neighbour even is a sample from exactly the same alloy (Inconel 718) that was analysed as part of a project in Oxford in 2012 unrelated to the search candidate, which was run in 2016 at the APT group of Erlangen [325]. This means that not only is the appearance of spectra similar, but also the underlying sample composition.

For the “intermediate” case of a W spectrum with few counts and a less well-defined peak shape, all the four nearest neighbours (Figure 38B) are tungsten fingerprints as well. However, none of these corresponds to a sample that is pure tungsten or one of its alloys. All of these samples only contain minor amounts of W, so have small peaks slightly above the noise floor. This may still be regarded as a “correct result” in that searching for a poorly defined fingerprint with few counts and miscalibrated peak shape has yielded more poorly defined fingerprints with few counts.

In the “impossible” case of the bioglass sample (Figure 38C), all the four nearest neighbours are spectra containing Ni and Cu fingerprints from APT runs on materials that have no similarity to bioglass [326]. The similarity – which is not high in these cases – is coincidental and not due to compositional similarities.

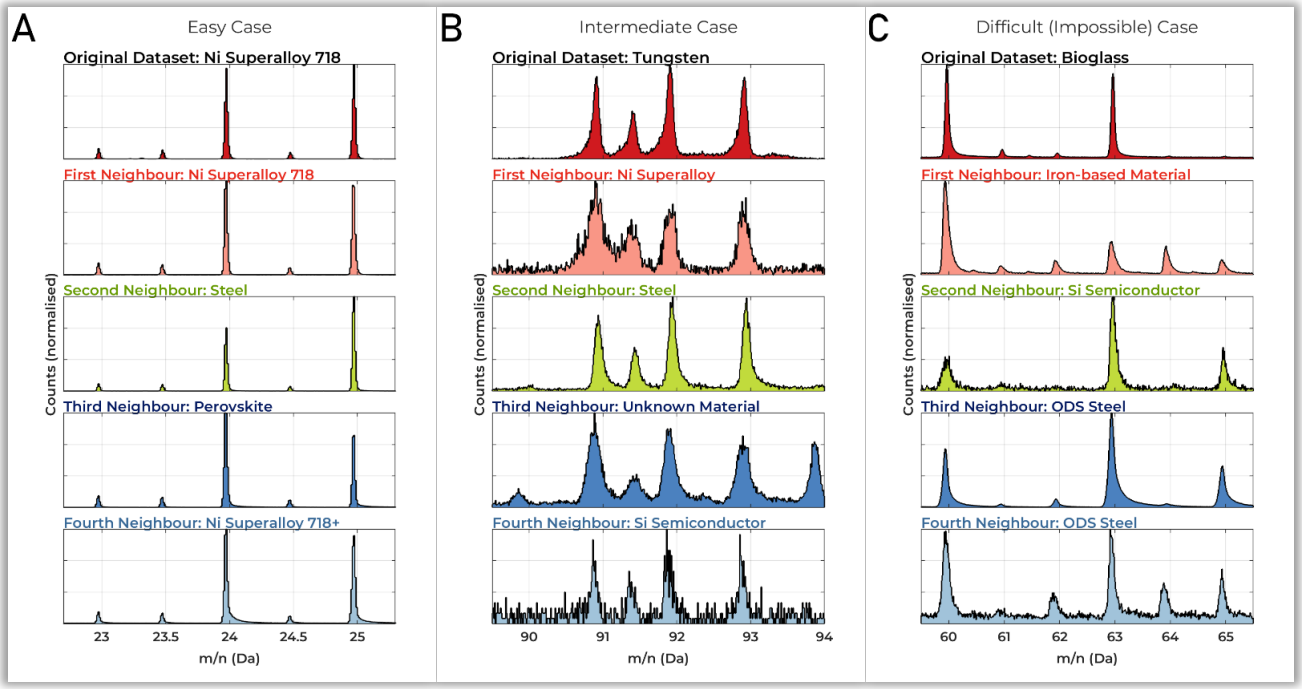

Figure 38: Results of a nearest neighbour search in the spectra point cloud for an easy (A), intermediate (B) and difficult (C) case

5.3.2. Clustering in the Spectra Point Cloud

Figure 39 shows the t-SNE embedding of all spectra in the collection. Datasets where common isotopic fingerprints (Fe, Zr, Si, W, Ni, Ti, Ga, U) fit well (i.e. the +1 and +2 charge states of these ions likely account for more than a critical fraction of counts, see Section 5.2.4) are highlighted in different colours. There are distinct clusters visible, and the clustering appears to occur mainly in line with the chemical sample composition. Close to the centre of the map, a cluster of datasets where none of the fingerprints fits well is found (many “cross” type markers without highlighting). This region of the map contains mostly spectra with very a high noise floor, i.e. arguably unsuccessful experiments, where the spectrum is dominated by this noise floor.

From visual inspection, the large cluster of iron spectra in Figure 39 appears to contain several sub-clusters. Further analyses on the structure of the iron cluster are presented in Appendix E-3.

The OPTICS reachability diagram, using the same markers as the t-SNE diagram is shown in Figure 40. The line clearly has several sinks or valleys, and they correspond to the various base materials. This confirms that the point cloud of spectra indeed contains separable clusters along the sample base material, so the observed clustering on the t-SNE map can be regarded as “real” and not an artefact.

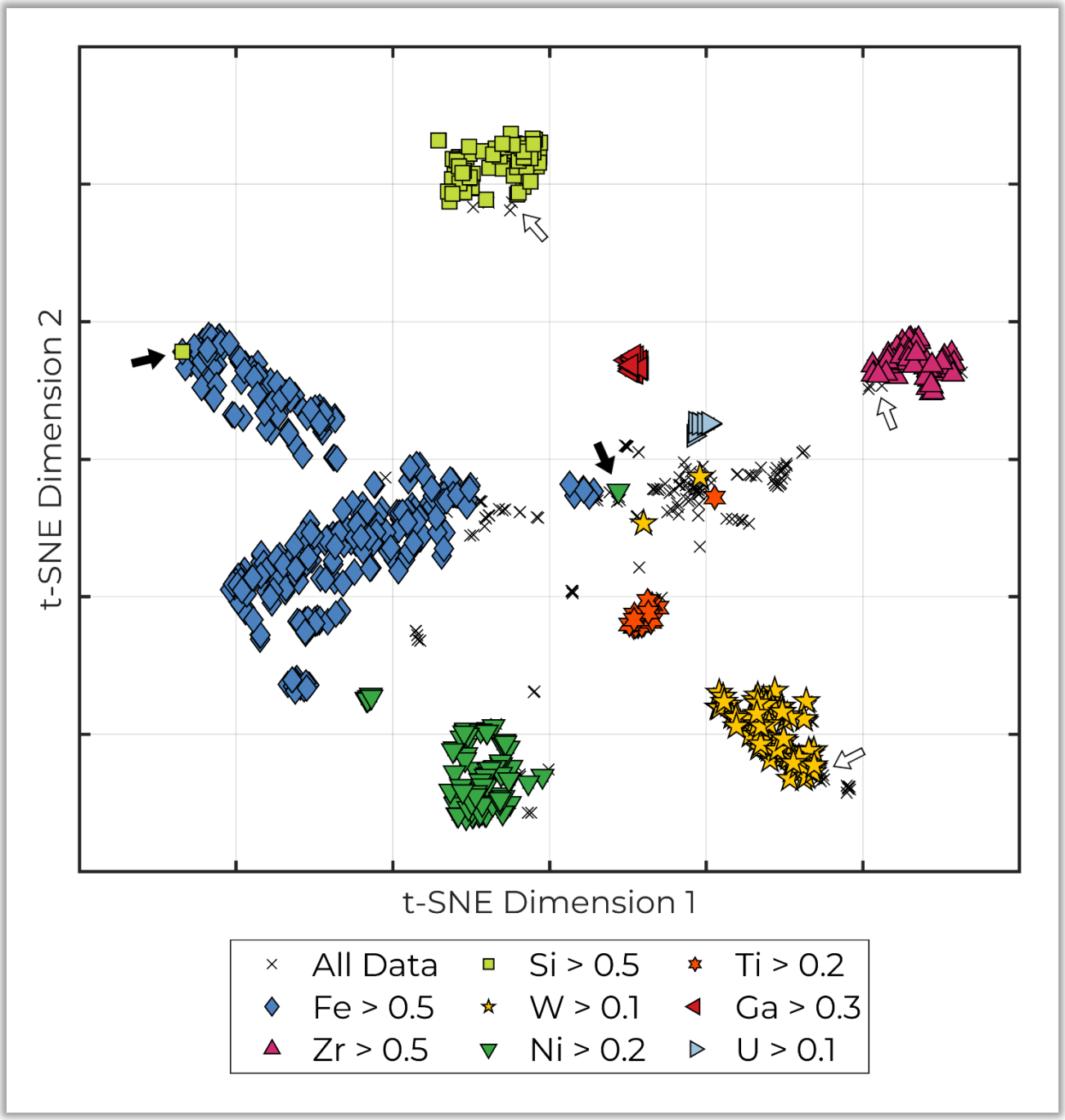

Figure 39: T-SNE embedding of the spectra point cloud. The legend lists the minimum atomic fraction of detector events in the given elemental fingerprints needed for the respective experiments to be considered as having a certain base material. The white arrows indicate some datasets which belong to clusters of materials, but have not been labelled as such by simple fingerprint thresholding. The black arrows indicate datasets which are labelled wrongly by the simple thresholding, i.e., non-fitting marker in a certain cluster.

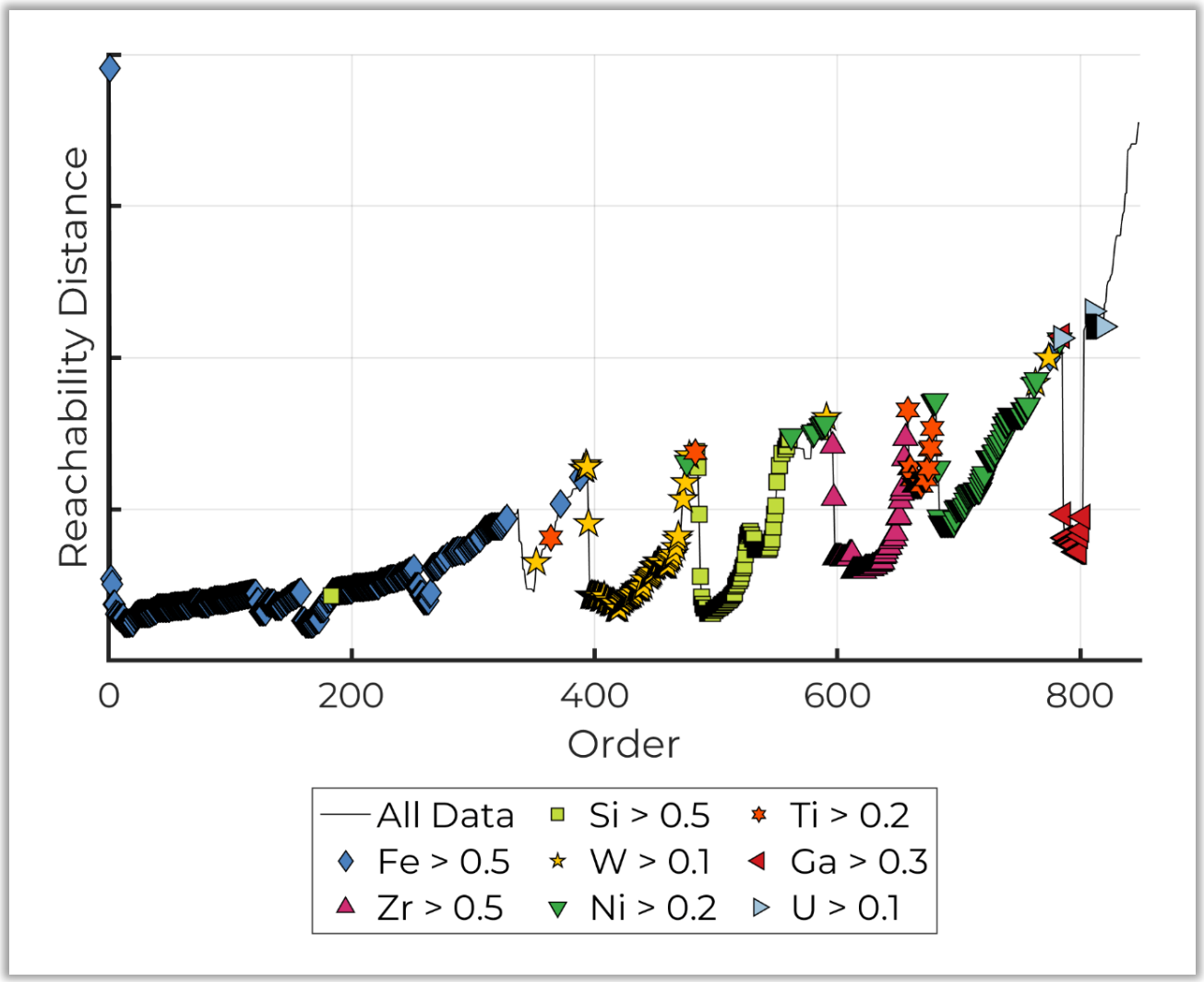

Figure 40: OPTICS reachability plot of the clusters in the spectra point cloud. The legend lists the minimum atomic fraction of detector events in the given elemental fingerprints needed for the respective experiments to be considered as having a certain base material, same as in Figure 39.

5.3.3. Hydrogen Behaviour

The evolution of the measured H_2^+/H^+ values as a function of voltage for the most common materials in the collection is shown in Figure 41, using only laser mode experiments. The underlying curves of the ionic fractions of H_2^+ and H^+ are shown in Figure 42 and Figure 43.

The H_2^+/H^+ ratios in most experiments on iron and nickel based materials are found in a relatively narrow channel around 0.2. However, outliers can extend far away from this value, to below 0.1 and above 1. Similar observations are made in titanium and tungsten, but at lower ratios of approximately 0.1, although it should be noted that the number of titanium datasets (24) is comparably low.

In zirconium, the H_2^+/H^+ ratio usually is slightly higher at approximately 0.2 to 0.3, and increases with voltage throughout the experiment. In a number of Zr experiments, a spike in the H_2^+/H^+ ratio to above the 75th percentile – reflected by the relatively high number of outliers significantly above the 75th percentile – is found at a certain point between 3 and 6 kV. This is not observed in any tungsten experiment, where all curves are rather smooth.

A deviating behaviour of Zr is also observed in the median H_2^+ and H^+ fractions in Figure 42 and Figure 43. The absolute H_2^+ and H^+ fractions increase with voltage in Fe, Ni, Si and W, but the opposite trend is observed in Zr. A similar observation may be made in Ti, but this is unclear due to the high amount of scatter and poor statistics (only 24 experiments). It is also noted that in W, the increase is less pronounced, and the scatter at the lower and upper ends (<4kV and >9 kV) of the voltage range is likely due to poor statistics from the low number of experiments that were run in these voltage ranges.

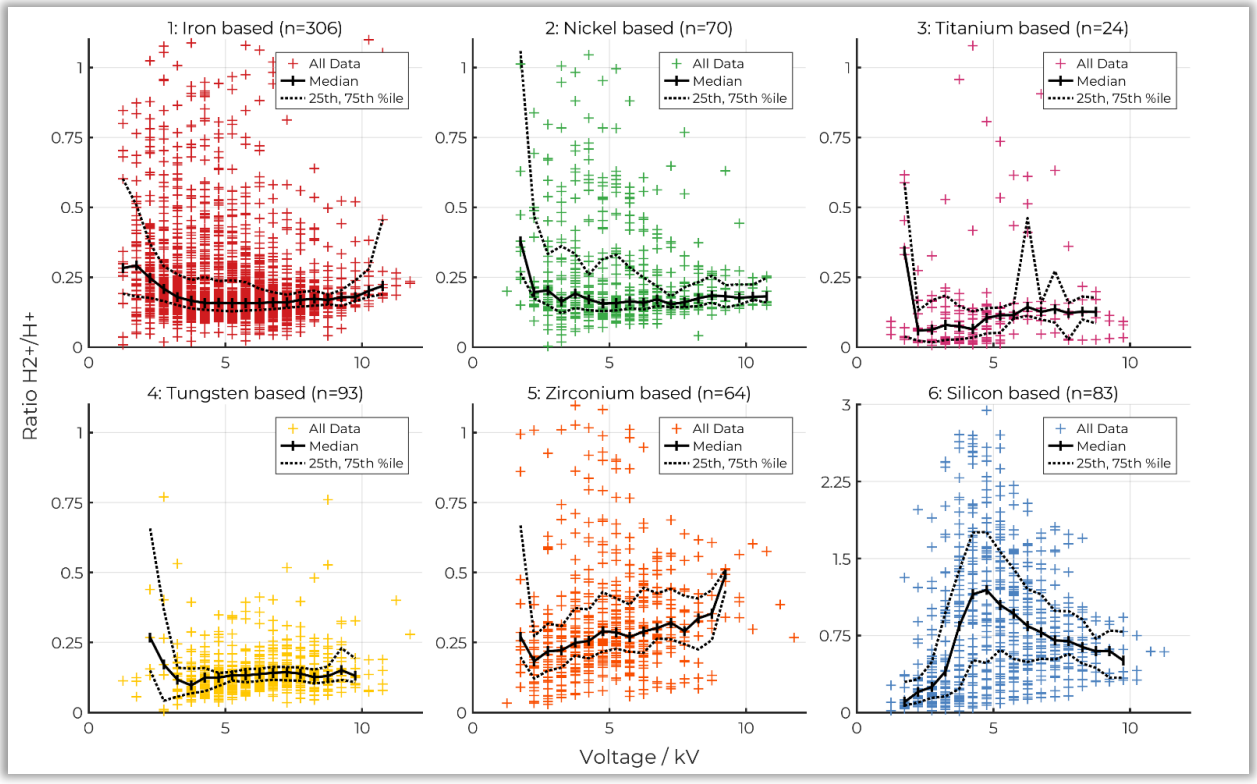

Figure 41: Hydrogen ratio H_2^+/H^+ as function of voltage throughout archival APT experiments, for different base sample materials. Also published in [327] under a CC-BY license.

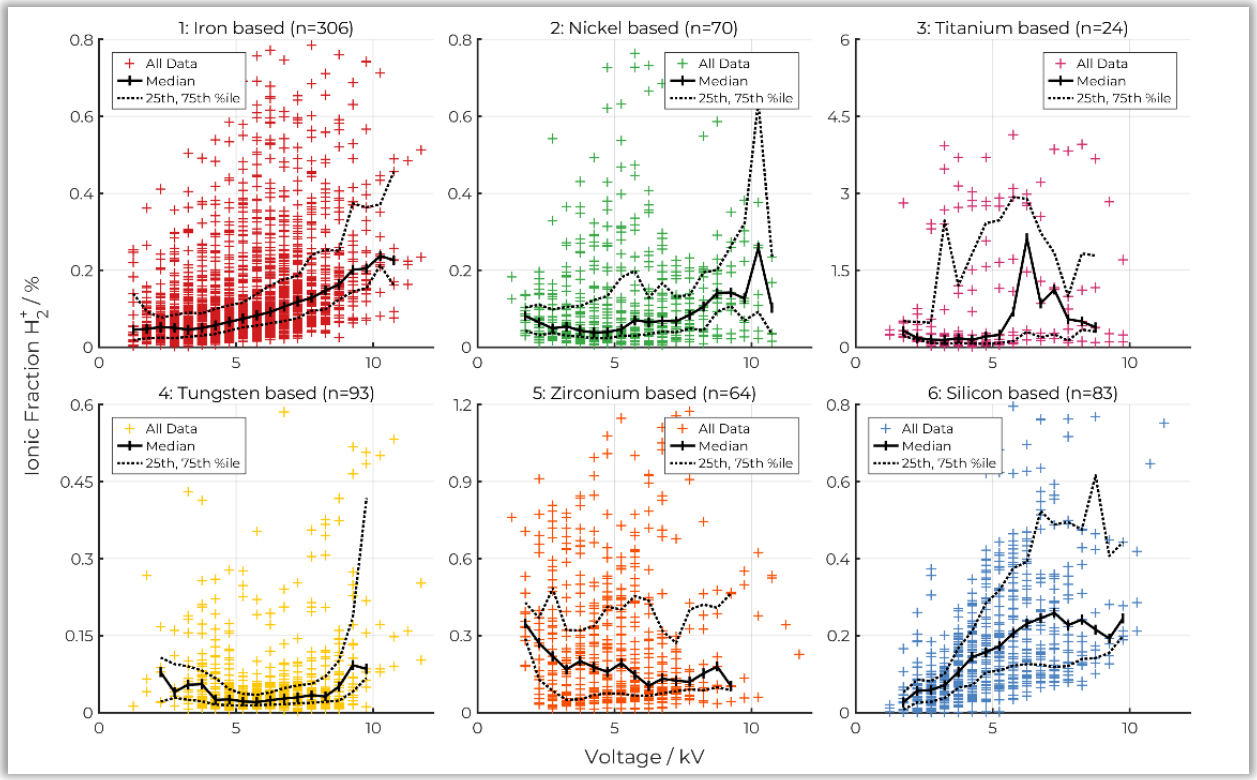

Figure 42: Ionic fraction of H_2^+ as function of voltage throughout archival APT experiments, for different base sample materials. Also published in [327] under a CC-BY license.

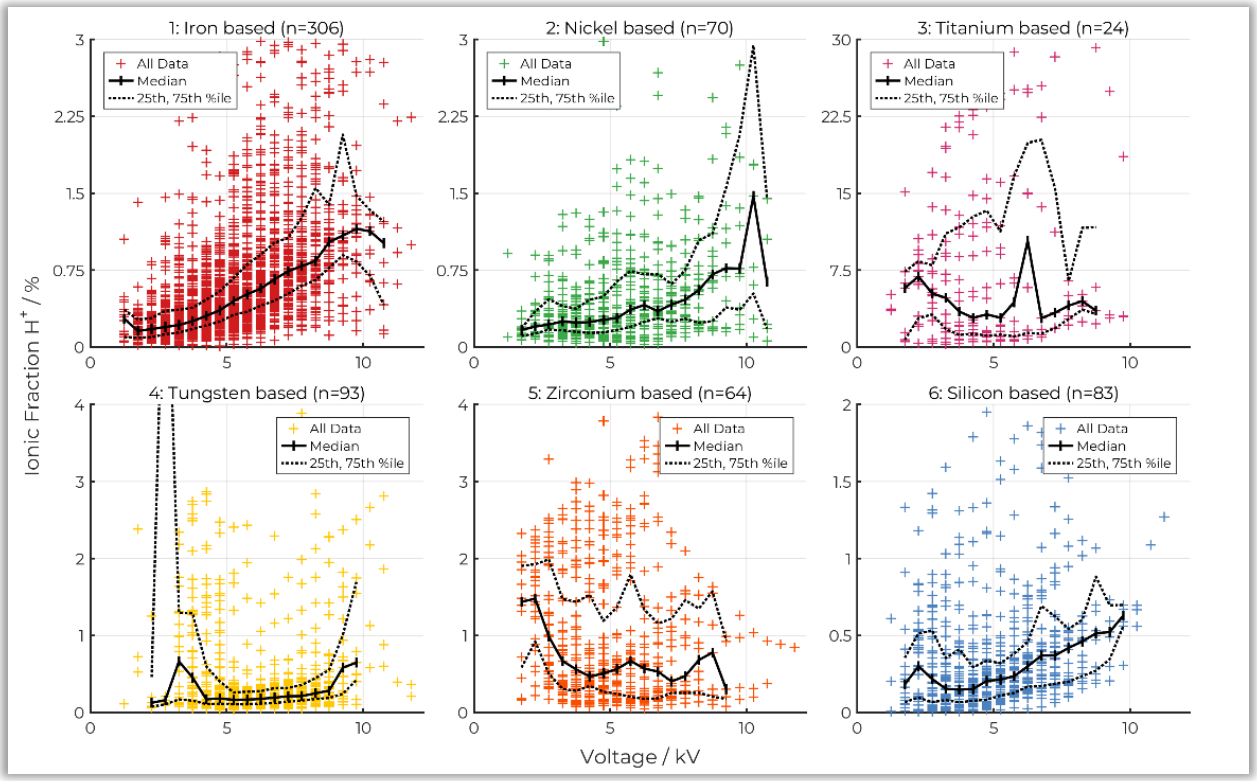

Figure 43: Ionic fraction of H^+ as function of voltage throughout archival APT experiments, for different base sample materials. Also published in [327] under a CC-BY license.

A curious observation is made in silicon. There is a clear maximum in the H_2^+/H^+ ratio at approximately 4-5 kV, which is observed in many experiments as well as in the average ratio across all data points (Figure 41). Upon closer inspection of the curves for H_2^+ and H^+ it is found that this is because of an increase in H_2^+ at this voltage (Figure 42 and Figure 43). H_2^+ and H^+ both increase in silicon as the voltage increases, but the increase of H_2^+ is much stronger at 4-5 kV, while the H^+ increases relatively more at higher voltages.

Figure 44 is a scatter plot of the same experiments and voltage bins as used in Figure 41, but instead of the voltage, the electric field calculated from CSRs is used. Titanium is missing because most of these datasets do not contain the Ti^+ peaks which would be needed for calculating a sensible Ti^{2+}/Ti^+ CSR, or because these peaks are overlapped. Therefore, titanium is excluded. The diagram shows a consistent trend of H_2^+/H^+ decreasing with increasing field strength down to approximately 0.1 to 0.3 across the base materials iron, nickel, and silicon.

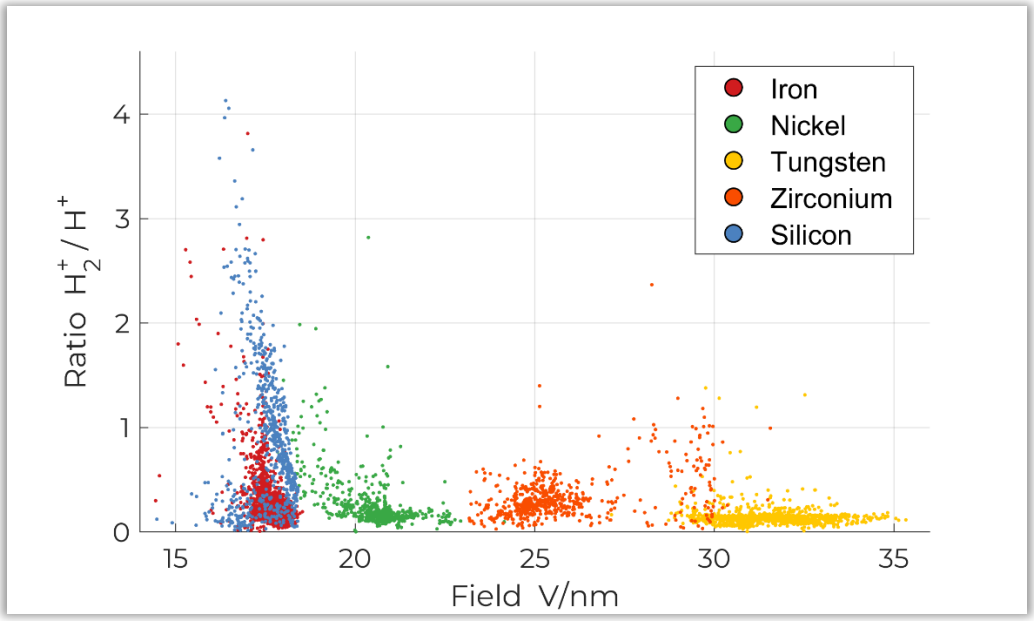

Figure 44: Hydrogen ratio H_2^+/H^+ as function of electric field for archival APT experiments, only laser mode experiments. Also published in [327] under a CC-BY license.

Interestingly, the distribution of the Si data points (Figure 44) appears to be bimodal, due to several data points where a relatively low field is not paired with a high H_2^+/H^+ ratio. Matching up data points from Figure 44 and Figure 41, it appears that the Si data points of low fields and low H_2^+/H^+ ratio in Figure 44 correspond to the data points at the lower voltage range in Figure 41-6 (Silicon), i.e. before the spike in H_2^+/H^+ that is seen in this diagram at 4-5 kV.

On average, the calculated fields for the analysis of tungsten and zirconium are higher than for Si, Fe and Ni, which is in line with the evaporation field for these materials being higher [136]. The ratio of H_2^+/H^+ in tungsten is always low (approximately 0.1), such that it fits and continues with the trend of low H_2^+/H^+ ratios at high fields that is observed in Fe, Ni and Si. Zirconium seems like tungsten in that no clear decrease or increase of H_2^+/H^+ over field is seen, but the absolute values and scatter are higher (approximately 0.2 to 0.3). Unlike Fe, Ni, Si and W, Zr easily forms hydrides during APT sample preparation [171, 194], so it could be possible that the observed behaviour of hydrogen from this material is fundamentally different from the other analysed materials, and no simple relationship with electric field as plotted here is found (also see discussion in Section 5.4.3).

One very interesting observation is that for the current set of experiments, which are all laser mode experiments, no drop to a H_2^+/H^+ ratio of 0 (corresponding to a H_2^+ peak below detection threshold) is observed for any material or field strength. This fits very well with observations made in the experiments in Chapter 3.2, and will be discussed in Section 5.4.3.

5.4. Discussion

5.4.1. Searching Spectra by Similarity

The examples in Figure 38 demonstrate that nearest neighbour search based on city block distance of normalised spectra is feasible to the end goal of retrieving spectra by similarity from a collection. In particular, the fact that the nearest neighbour of an Inconel 718 Ni-superalloy dataset provided by the APT group in Erlangen in the Oxford database is another Inconel 718 specimen from an unrelated project shows how well this method can match fingerprints under good conditions, i.e., where there are well-defined and calibrated spectra.

However, it also becomes clear that there are limits to this. In the case of the poor-quality tungsten fingerprint (Figure 38B), all of the neighbours are similar to the tungsten fingerprint, but none of the data are from tungsten based materials. Instead, the retrieved neighbours are materials which happen to only contain a low amount of tungsten as an alloying element, appearing in rather poorly defined peaks which do not stand well above the noise floor.

Fundamentally, nearest neighbour search retrieves the most similar datasets regardless of the "quality" of a fingerprint. However, if the search candidate is a poorly defined and noisy spectrum, then random noise in the retrieved neighbours seems to be a major marker for their similarity, rather than actual similarity of underlying sample or composition. The method is not immune to noise in spectra, and to the end of finding APT experiments which are similar to a given candidate, a high number of counts is beneficial.

The impossible to match case of the bioglass data demonstrates that (somewhat) similar spectra may also be found if the underlying APT database does not contain any experiment with similar composition (Figure 38C). Nearest neighbour searches cannot guarantee that the composition of the retrieved spectra is even remotely similar. In a laboratory context, this means that additional plausibility checks, such as sample name, are needed to confirm whether a retrieved spectrum actually originates from a similar experiment.

In the work presented here, computation time of nearest neighbour searches it of no concern. This is because computation of nearest neighbour distances on modern hardware is sufficiently fast, such that a brute-force nearest neighbour search is viable (iterate through all datasets, calculate distance to candidate, pick closest datasets). For parameters as used here and on a modern workstation computer (848 datasets, 17999 spectrum bins, Intel Xeon 4114 Dual CPU), nearest neighbour search concludes in less than 0.1 seconds. It was not necessary to use potential methods for the speed-up of the search, such as dimensionality reduction [328] or k-d trees [329].

The presented method of searching for spectra can effectively automate and speed up a process of searching through archival data, which traditionally would require many hours if conducted manually by a human operator. However, the current implementation used here is certainly not efficient in terms of computational complexity, and better optimisation will be needed for application to significantly larger collections of spectra.

5.4.2. Clustering in the Spectra Point Cloud

The t-SNE map (Figure 39) and the OPTICS reachability distances (Figure 40) demonstrate that the spectra point cloud contains clear clusters which are separable by point density. The association of datasets to clusters on the t-SNE map and the OPTICS reachability diagram agrees well with the estimation of sample material, based on

the fitting of isotopic fingerprints. This indicates that sample base material can be seen as the main cause of similarity or clustering in the underlying spectra. Only few cases of outliers are observed where the base material estimated from simple fingerprint fitting does not agree with cluster association, and these cases amount to false positives of the fingerprint fitting method. Two examples are highlighted in Figure 39 with black arrows.

Most clusters do contain datasets that were not identified as having the base material of the other datasets in the clusters (cross markers associated with Fe, Si, Ni, Ti, W, Zr clusters in Figure 39), some of which are highlighted by white arrows in the diagram. This shows that estimation of sample base material based on similarity, i.e., association with certain clusters in the point cloud, is potentially more reliable than a naive estimation based on fitting of fingerprints – the fingerprint-method has produced false negatives by not labelling all datasets in their respective clusters. A cluster-based approach does not rely on fingerprints and fit parameters provided by the operator. In this sense, experiment categorisation based on clusters in the point cloud is an unsupervised machine learning approach, while sample identification based on fingerprints and content thresholds is supervised.

The deeper inspection of the structure internal to the iron cluster in Appendix E-3 provides some insight into which factors other than base element contribute to similarity or cluster structure in the point cloud. These are peak shape, possible alloying elements and, if sufficiently high, the noise floor.

Ranging, the association of peaks in a spectrum to ionic identities, is a fundamental challenge in APT. Much effort and experience are needed for users to obtain reliable results, and in practice ranging often becomes a source of errors and confusion [330]. Automatic tools for ranging for potential ionic identities in a given spectrum have been developed, but these are not yet sufficiently reliable and accurate for ranging arbitrary spectra with only little human input [331-333]. The existing methods usually work by recognising and fitting isotopic fingerprints into a given spectrum [215, 334].

Based on the work presented here, I propose that, on a fundamental level, an alternative approach is possible, where no ranging is needed at all and ionic identities and even sample composition are inferred purely based on similarity in a collection of reference datasets with known composition. A large database of APT spectra with known ground truth (ranging and/or composition) could allow for the training of machine learned models that can characterise APT spectra more accurately than current approaches. This could be of particular use if consistency of analysis is important, e.g., in industrial settings where APT may be applied to a large number of very similar samples, rather than ability to deal with new, completely unknown materials. This however is beyond of the work presented here and will be left for future research.

5.4.3. Hydrogen Behaviour

Figure 41 shows that for Fe, Ni, Ti, and W, the H_2^+/H^+ ratios with increasing voltage often converge into relatively narrow ranges across the analysed archival data. Nevertheless, the number of outliers is significant. This suggests that – in dependence on the material – certain H_2^+/H^+ ratios are likely to be observed under typical experimental conditions (or: conditions commonly chosen in past experiments in the Oxford Atom Probe Tomography Group), but only statistically and not strictly in every experiment.

Figure 44 confirms that in pulsed laser evaporation experiments on Fe, Ni and Si, the H_2^+/H^+ ratio is field dependent. Since the probability of post-ionisation is greater at higher fields, this could indicate that post-ionisation of H_2^+ and subsequent breaking into two H^+ is the underlying cause for this. The observation is well in line with the sub-evaporation threshold experiments in Chapter 3.2, and a more extensive discussion of the potentially underlying post-ionisation is given in Section 3.2.4.

When discussing the electric field, it is very important to keep in mind that the post-ionisation model of Kingham, that was used here to convert CSR values, is only approximately accurate, and there are known materials where it is inaccurate [324, 335]. In addition, the CSR across the detector-visible part of the specimen surface in APT is normally not constant, and my approach which is based on voltage bins simply averages across the entire surface [146, 184]. This means that the absolute values of the electric fields in Figure 44 should not be over-interpreted. In the underlying archival APT experiments, there may be lateral variations of the hydrogen signal across the sample surface to which the current analysis has no sensitivity.

The absolute amounts of H_2^+ and H^+ in Fe, Ni, Si and W usually increase during the experiments with increasing voltages (Figure 42 and Figure 43). Assuming that the amount of "true" sample hydrogen in common Fe, Si, Ni and W samples is low, and that only a low amount of contaminant hydrogen from these materials evaporates in complex molecules (e.g. FeH^+), this indicates that the supply of contaminant H commonly increases throughout experiments on such materials. From the current data, it is not directly obvious which mechanism is underlying this increase. It may be due to changes in field or surface area, which I shall briefly discuss, or other yet unknown factors.

Rigutti et al. [146] studied the amount of detected contaminant hydrogen on multi-layered semiconductors and found that the amount is in negative correlation with the field when different layers, having different evaporation fields, are compared, but positively correlated with the field distribution across the sample surface. Their conclusion is that the relationship between field and hydrogen is complex, and there likely are compounding factors, including sample geometry. I tested whether a field dependence of the hydrogen supply is detectable in the collection of archival data, by plotting the total (ionic) fraction of hydrogen as function of electric field (Figure in Appendix E-4), similar to Figure 44. No clear trend emerges. This result is in confirmation of Rigutti et al., showing that the contaminant hydrogen supply is field-dependent, but also affected by factors beyond the electric field. The observation also holds when I restrict the analysis to datasets from the iron cluster only, which should reduce a potential influence of the sample material.

It can be assumed that higher voltages usually correspond to later stages of an experiment, which in turn corresponds to blunter tips. The surface area of the tip that is visible to the detector is larger on blunt tips (the field of view is wider), so if the supply of contaminant hydrogen per surface area is constant, this could possibly explain the observed increasing amounts of hydrogen with increasing voltage. If this was to be confirmed, it might suggest direct arrival of contaminant hydrogen at the tip from the gas phase during the experiment as the dominant supply mechanism.

Fittingly, a new type of APT instrument with ultra-wide field of view (Cameca Invizo 6000) has recently become available, which can "see" a much larger part of the sample surface, up to the entire specimen including shanks. Early results indicate that the amount of hydrogen detected with this instrument is significantly higher

compared to common atomprobes (e.g. Cameca LEAP 5000 series) [185, 336], however clear conclusions cannot yet be drawn from this very early data. I believe that “seeing” the entire sample surface could provide critical new insights into contaminant hydrogen and its dependence on geometry and other sample features, which can, if at all, only be captured incompletely in current APT instruments.

It is known that Zr and Ti readily form hydrogen-rich phases during sample preparation and APT experimental procedures [139, 147, 194]. The dominant supply route resulting in the detection of hydrogen during the analysis of these materials may differ from that in Fe, Ni, Si, W. It is therefore not particularly unexpected that the trends for hydrogen observed in Fe, Si, Ni and W do not extend to these two elements. Using the terminology from previous chapters, there may be a considerable amount of sample hydrogen (hydrogen contained in the sample) that is observed, as opposed to contaminant hydrogen (contaminant hydrogen arriving at the sample whilst the experiment is running). Also, Zr and Ti have a high tendency to evaporate complex hydride ions (e.g. ZrH^+, ZrH_2^+, TiH_2^+) [139, 171, 184], which the current analysis does not address.

5.5. Conclusion

An analysis on archival APT data, most likely the first of its type in the field, has been conducted. It is shown that the city block distance is suitable to measure (dis-) similarity in APT spectra, and that collections of APT spectra can be interpreted as point clouds. This enables automated search for spectra by similarity. The spectra in the cloud are clustered, mostly (but not exclusively) driven by the chemical composition of the specimen. It is therefore possible, at least approximately, to infer the likely composition of a sample based on neighbouring spectra in the point cloud. Information about the material can be combined with information about the contaminant hydrogen peaks (H^+ and H_2^+), which enables material-dependent large-scale analysis of hydrogen behaviour. The method can discover phenomena which only appear statistically, and which cannot reliably be observed in few targeted experiments.

One important difficulty, and likely main reason why such analyses have not yet been conducted before, is the widespread use of proprietary file formats for storing APT data (.hits, .rhit), which can only be accessed with specialised software (IVAS and APsuite). These packages, at the time that this study was undertaken, do not feature any functionality for automation or statistical cross-experiment analysis, and I circumvented this limitation through UI automation. This, however, is not an ideal approach, firstly because it is not as fast and reliable as direct export, but also because it can only access data which the software allows export of in the first place. It cannot access information which is present in the experimental files, but which is not displayed or made available to the operator by the software, such as fully unprocessed detector data. Introduction of more accessible open formats [337] will likely boost developments in the field.

Overall, I consider the study here presented a first step which explores some fundamental features of large-scale APT data analysis. It is based on only 848 datasets, which is less than 0.1% of the more than 1M APT experiments which I estimate have been conducted to date, and I almost entirely restrict the analysis to mass-to-charge-state ratio spectra. This means the scope for extension of this work in both size and complexity is considerable.

6. Summary and Future Research

Contaminant hydrogen is probably the most commonly observed, yet least understood species in atom probe tomography. It is a dynamic phenomenon, where atoms which are not part of the sample are supplied and evaporated. As such, it depends on a large number of influences and experimental parameter, of which some may not even be known at the time. My work advances our understanding of hydrogen contamination by contributing several new methods and results to the field. Finally, I shall now recapitulate my most important methods and findings, their potential applications, and new questions arising from my work for future research.

First, the behaviour of contaminant hydrogen in APT was studied in Chapter 3, using experiments with cycled frequencies and below evaporation threshold. The cycled rate experiments convincingly demonstrate the time-constant nature of the contaminant hydrogen supply. Through extrapolation of the theoretical hydrogen contant in a contaminant-free, infinitely fast experiment, it is possible to estimate the concentration of sample hydrogen in a specimen. The method is less accurate than the established deuterium tracer method in APT, however its advantages are that it does not require deuterated specimen, or adjustment of APT experiment conditions in order to observe non-overlapped deuterium peaks.

The sub-evaporation threshold experiments allow for a deep investigation of the parameter dependency of contaminant hydrogen. By controlling the voltage in a way to never evaporate the specimen, it is possible to investigate the influence of parameters such as pulse frequency, laser energy or electric field on contaminant hydrogen without an uncertainty arising from a changing tip geometry. My results provide insights into the parameter dependence of contaminant hydrogen, which will be useful for the planning and parameter search in future studies on hydrogen in APT, particularly in laser-assisted evaporation mode.

Both experiments do also lead to new questions. In the cycled frequency experiment, it was observed that the rate of hydrogen detection does not directly change after changes in detection rate or pulse frequency, but requires a short amount of time to equilibrate. This “sluggish” behaviour could possibly be attributed to some sort of reservoir, but the current experiment cannot investigate the nature of such a reservoir, or even highly convincingly proof its existence. This could be investigated further in future experiments, for example by studying the response of hydrogen to single steps in pulse frequency (not cycled) in greater detail.

The main question arising from the sub-evaporation experiment is what the influence of the tip materials is, or whether different materials would lead to different results. Repetitions of similar experiments with different specimen would likely be insightful. One limitation to this however is that the specimen should ideally have a high evaporation field such that no or only little sample material evaporates whilst the field-dependent behaviour of hydrogen is probed. In my opinion, Gold (noble metal, high evaporation field) and Palladium (strongly adsorbs hydrogen) could be some interesting candidates.

One phenomenon which in my opinion has not yet been treated with sufficient effort in modern APT is the H_3^+ molecule. At imaging conditions in modern APT, the concentration of H_3^+ is usually considerably lower than H^+ and H_2^+, meaning it is often overlooked or ignored. Currently, relatively little is known about this ion in APT. I think that cycled frequency- and sub-evaporation threshold experiments provide new methods to study its behaviour. For example, sub-evaporation experiment could be used to find optimal conditions and materials for

H_3^+ emission, then frequency cycling could show if or how the H_3^+ depends on the time between pulses, or by extension on the concentration of H^+ and H_2^+.

I would also add that one potential research area which is not yet getting the attention it deserves is the intermixing between contaminant and sample hydrogen in molecule ions, and the conditions under which it occurs. My thesis clearly demonstrates that contaminant hydrogen behaves fundamentally different from sample hydrogen, because it is not part of the sample, but supplied during the experiment. Nevertheless, mixed molecule ions such as HD^+ or HDO^+ have been reported in APT on deuterated specimen [228], implying that interactions between sample and contaminant exist. Tracer experiments where the abundance of contaminant and sample hydrogen in molecule ions is studied systematically might provide interesting insights into the contaminant-sample interaction.

One direct conclusion from my experiments in Chapter 3 is that deuterium in tungsten can be imaged in APT in laser mode at high electric fields. This has been applied in Chapter 4 to successfully image trapped deuterium in radiation damaged tungsten tips. It is seen that the deuterium follows a characteristic depth distribution, which is due to radiation damaging and deuterium implantation being depth dependent processes.

To further research of fusion reactors, the method will need to be applied to more specimen, which more closely resemble the conditions in a fusion reactor, and finally to “real” samples obtained from future reactors. A word of caution for future however arises from the large scatter observed in my work: If a range of tungsten samples, e.g., from plasma exposure experiments at different doses were to be analysed and compared in a future study, a similar degree of variance between measurements will pose a major challenge. Likely, the number of specimens will need to be high in order to gain relevant insights. Given that the sample preparation is difficult, and yield is low, this may not be feasible. I would therefore suggest using APT in a targeted way on promising samples, e.g., on particular features such as grain boundaries, or on tungsten that has been deuterated just to the point where bubbles should start nucleating.

Finally, Chapter 5 covers a slightly different aspect of APT, the automated analysis of large numbers of past experiments. The most important aspect of this chapter is the introduction of a nearest neighbour distance for APT spectra. This enables a quick and efficient retrieval of spectra by similarity, which in itself should directly have useful applications in APT: For a given observation in a spectrum, such as an unknown peak or unexpected feature, it is now possible to check if and where a similar observation has been made before, in a past experiment. One of the major challenges in APT is the correct interpretation of mass-to-charge spectra, and my approach can directly help this by proving information about past experiments with similar peaks.

There are more analyses, however, which the nearest-neighbour distance enables. A collection of APT spectra can be considered a point cloud, which contains clusters based on spectra similarity. Since similar spectra are usually correlated with similar sample compositions, the clusters can be used to predict the base material of a specimen. This enables material dependent analysis, which in the current work is used to study the voltage-and field dependent behaviour of hydrogen. The most interesting result is the field-dependence of the H_2^+/H^+ ratio across several materials in Figure 44. This observation of an increasing ratio with increasing field also agrees with the observed curves in the sub-evaporation experiments in chapter 3, demonstrating that such a statistical observation across many datasets is experimentally reproducible.

My current analysis does only deal with a small fraction of the available APT data, namely voltage and mass-to-charge spectra. There is more data available which could be used in future research, for example detector coordinates and auxiliary sensor data such as residual gas pressure and temperatures. One particularly interesting research avenue in my opinion might be analysis of detector coordinates, multiplicity counts and patterns therein across many experiments, to the potential end of spotting species which migrate and possibly even react on the surfaces of APT tips.

7. Appendix

Appendix A: Electrochemical Charging Procedure

A charging cell similar to the one described in [220] was used to charge the samples electrochemically. A solution of 0.1 M NaOH (> 97.5%, BDH Laboratory Supplies) and 1 mmol Hexamethylenetetramine (HTMA, > 99.5%, Sigma-Aldrich) in heavy water (D_2O, 99.9%, AlfaAesar) was used as electrolyte [338], A leakless Ag/AgCl electrode (Biochrom/Harvard apparatus) as reference electrode, and a gold wire as counter electrode. To control the potential, a custom Potentiostat was built, and used to charge the tips as a constant half-cell reaction potential of 2.1 V for 30 s. After charging, the samples were cooled in liquid nitrogen and transferred into the atom probe instrument following the cryogenic transfer protocol by Chen et al. [218].

Appendix B: Additional Diagrams for Hydrogen Extrapolation

Appendix B-1: Nominal Composition of Steel Samples

The table shows the nominal composition of the steel used for the experiments in Chapter 3.1.

Component	Mn	Mo	V	C	Nb	Al	Si	N	Fe
Weight-%	1.56	0.51	0.25	0.096	0.056	0.05	0.026	0.004	Balance
Atom-%	1.59	0.3	0.27	0.45	0.034	0.1	0.05	0.02	Balance

Appendix B-2: Identifiers of Extrapolation Experiments

Experiment identifiers and hash values of the experiments used for hydrogen content extrapolation. A documentation of hash values for APT experiments is given in a publication by the IFES technical committee: https://docs.google.com/document/d/e/2PACX-1vQyd3Pc32tS7TjFsiLyjhYlOmqFl_UHPgrkowYIFONIaOYVjmNaiK5HkMIoLurkwP-qzKLLKUXtjU9s/pub

Dataset	Run Number	SHA-256 Hash of raw experiment file	Hash value listed in public experiment list
Evp-Low-Rate	R5111_9237	79c18d6835eb8f3b74943c343168ba4bc08a213bad6cb679eb59e8a4e34c1a75	https://raw.githubusercontent.com/oxfordAPT/hashlist/master/cameca_5000XS.txt
Evp-High-Rate	R5111_9349	e67698d069e67fe40d78f00699fac17d7e185934060037fd756ca57ba529a310	https://raw.githubusercontent.com/oxfordAPT/hashlist/master/cameca_5000XS.txt
Evp-Few-Step	R5083_11341	9907c015b724df8667f5b815369d6abd9f013d723dff971e789a0ffcc526c8d0	https://raw.githubusercontent.com/oxfordAPT/hashlist/master/cameca_5000XR.txt
Freq-Many-Step	R5111_10990	feb460528c22e9b2ec418ea38ae09ec81003c8b8e882b95077a0448228e4ab17	https://raw.githubusercontent.com/oxfordAPT/hashlist/master/cameca_5000XS.txt
Freq-Few-Step	R5111_10989	b4fd2d15d5838cde4a5fee33e34f18a2701a6d1b40ff883ac018e8b46bd18583	https://raw.githubusercontent.com/oxfordAPT/hashlist/master/cameca_5000XS.txt
Freq-High-Rate	R5083_12000	accfb0f4cc1ba430a04fa94e0ec4fd4228ad220f4d7e7fdf50ce4231e2915e1b	https://raw.githubusercontent.com/oxfordAPT/hashlist/master/cameca_5000XR.txt

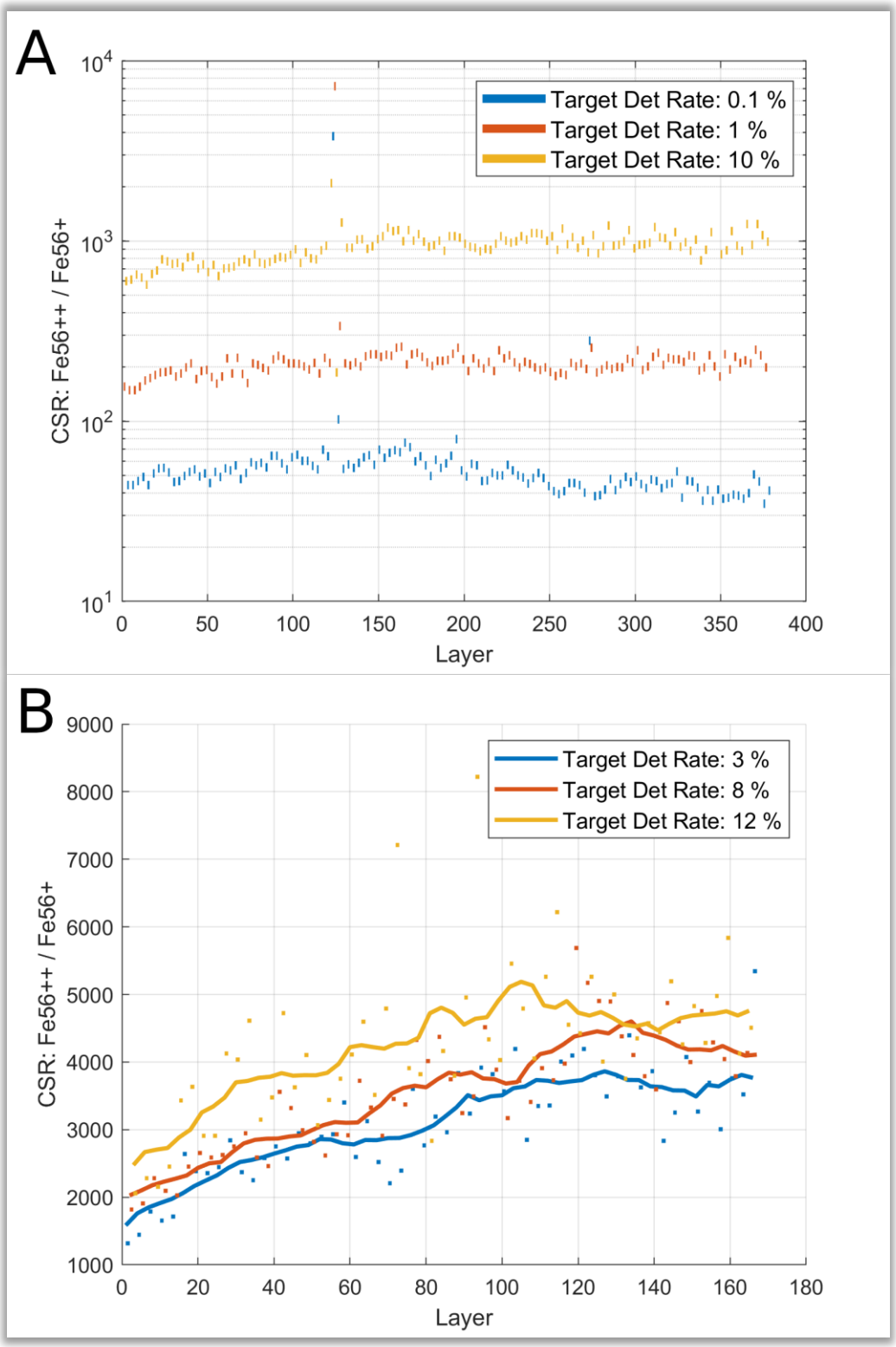

Charge-State ratios (CSR) of the Fe-56 isotope over the layers in the cycled evaporation rate experiments Evp-Low-Rate (A) and Evp-High-Rate(B). For Evp-High-Rate, the moving average across 10 layers for each target detection rate is included. It is seen that the CSR for the different target detection rates in Evp-Low-Rate are very distinct, meanwhile the trend in Evp-High-Rate is less prominent.

Picture and Description also published my previously published paper [141], Supplementary Material.

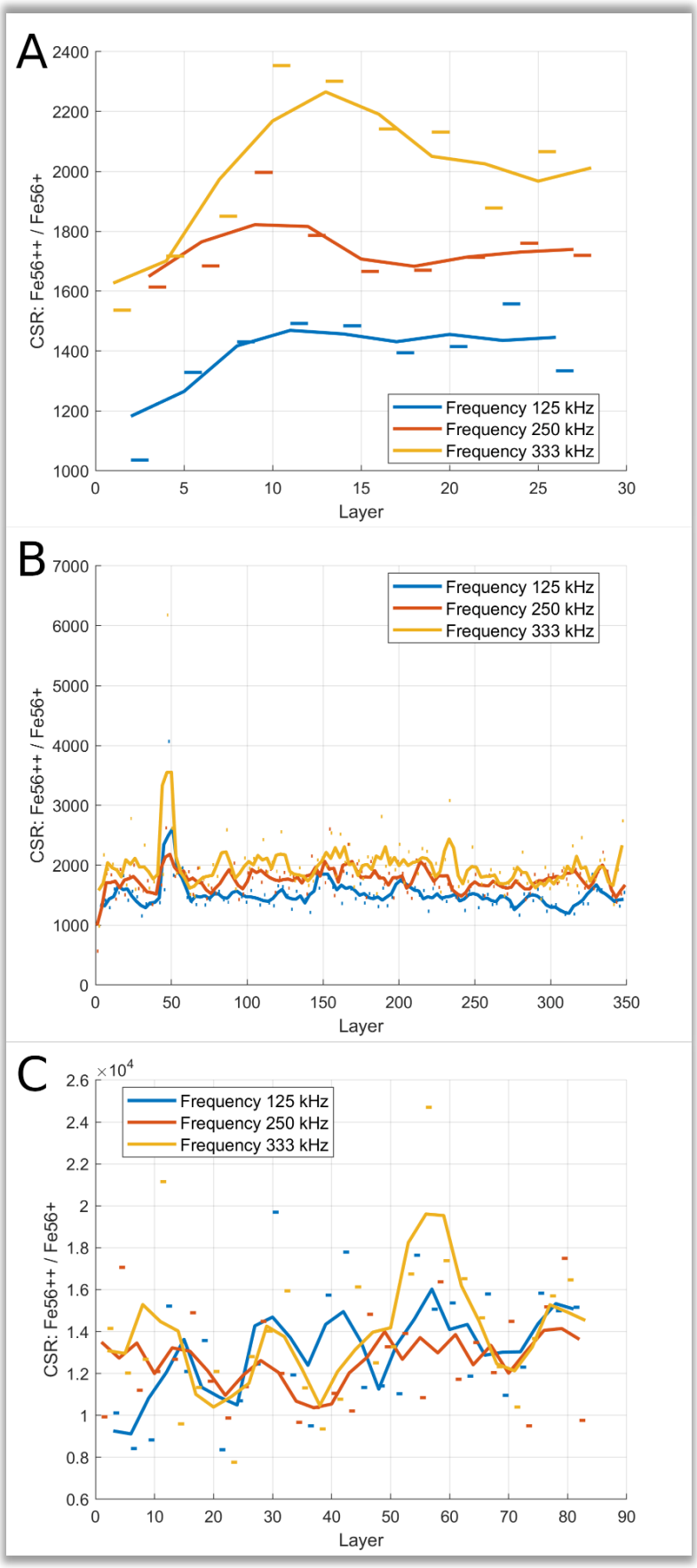

Charge-State ratios (CSR) of the Fe-56 isotope over the layers in the cycled frequency experiments Freq-Few-Step (A), Freq-Many-Step(B) and Freq-High-Rate (C), and moving average CSR across three layers for each frequency. It is seen that the CSR for the different target detection rates in Freq-Few-Step and Freq-Many-Step are slightly different while no such trend is seen in Freq-High-Rate.

Picture and Description also published my previously published paper [141], Supplementary Material.

Appendix B-4: Detected Hydrogen per Layer

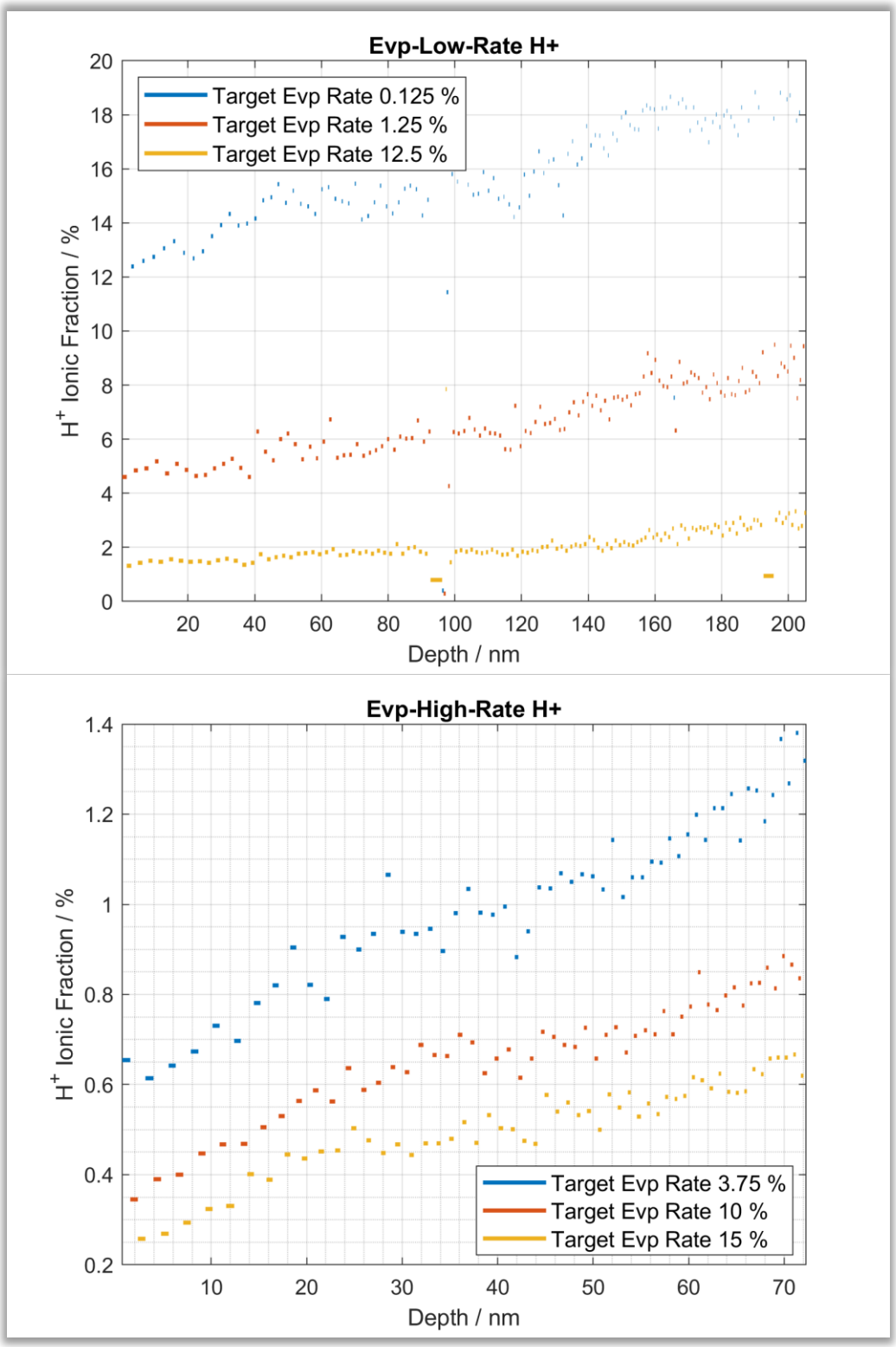

Detected ionic fractions of H^+ throughout the layers in the cycled evaporation rate experiments. It is seen that the amount of H^+ is clearly different for the different target evaporation rates and increases as the experiments progress.

Picture and Description also published my previously published paper [141], Supplementary Material.

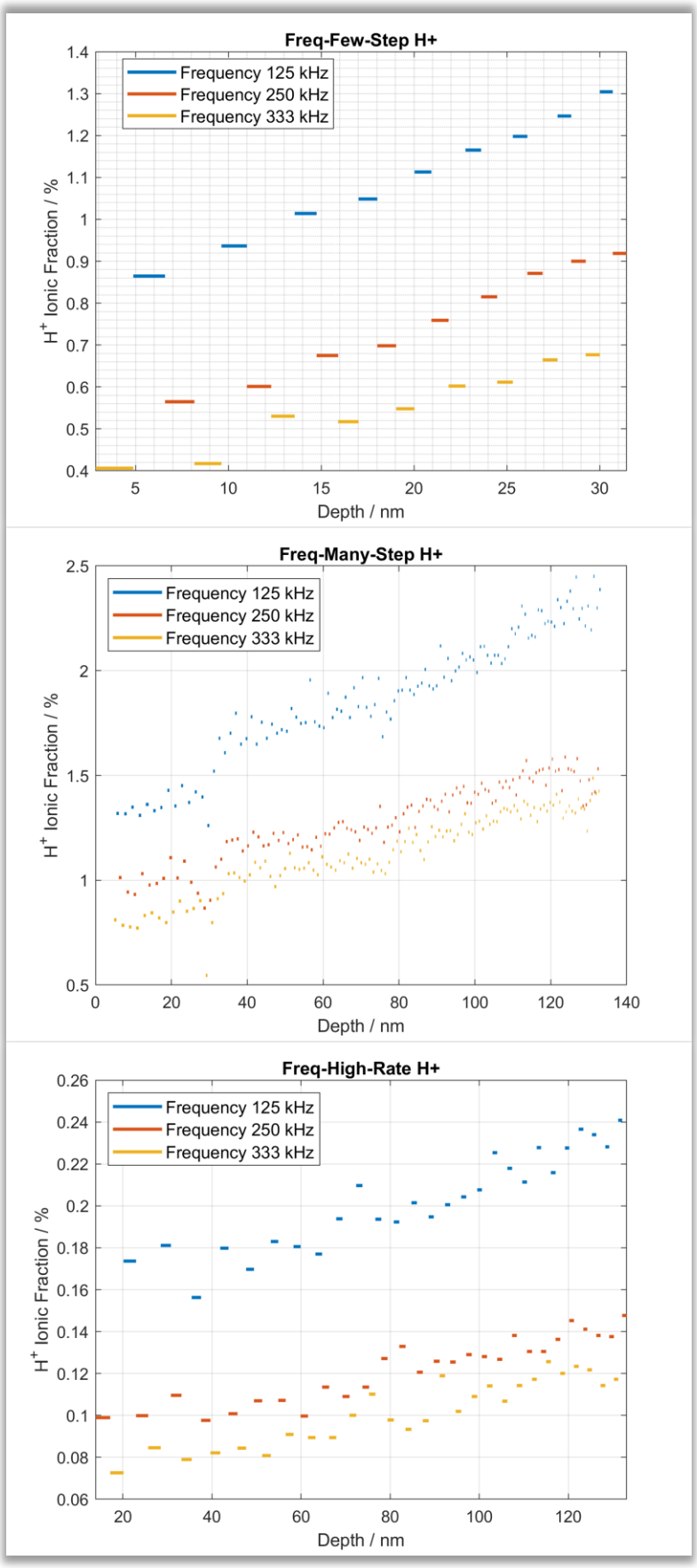

Detected ionic fractions of H^+ throughout the layers in the cycled frequency experiments. It is seen that the amount of H^+ is clearly different for the different frequencies and increase as the experiments progress, similar to the cycled evaporation rate Experiments.

Picture and Description also published my previously published paper [141], Supplementary Material.

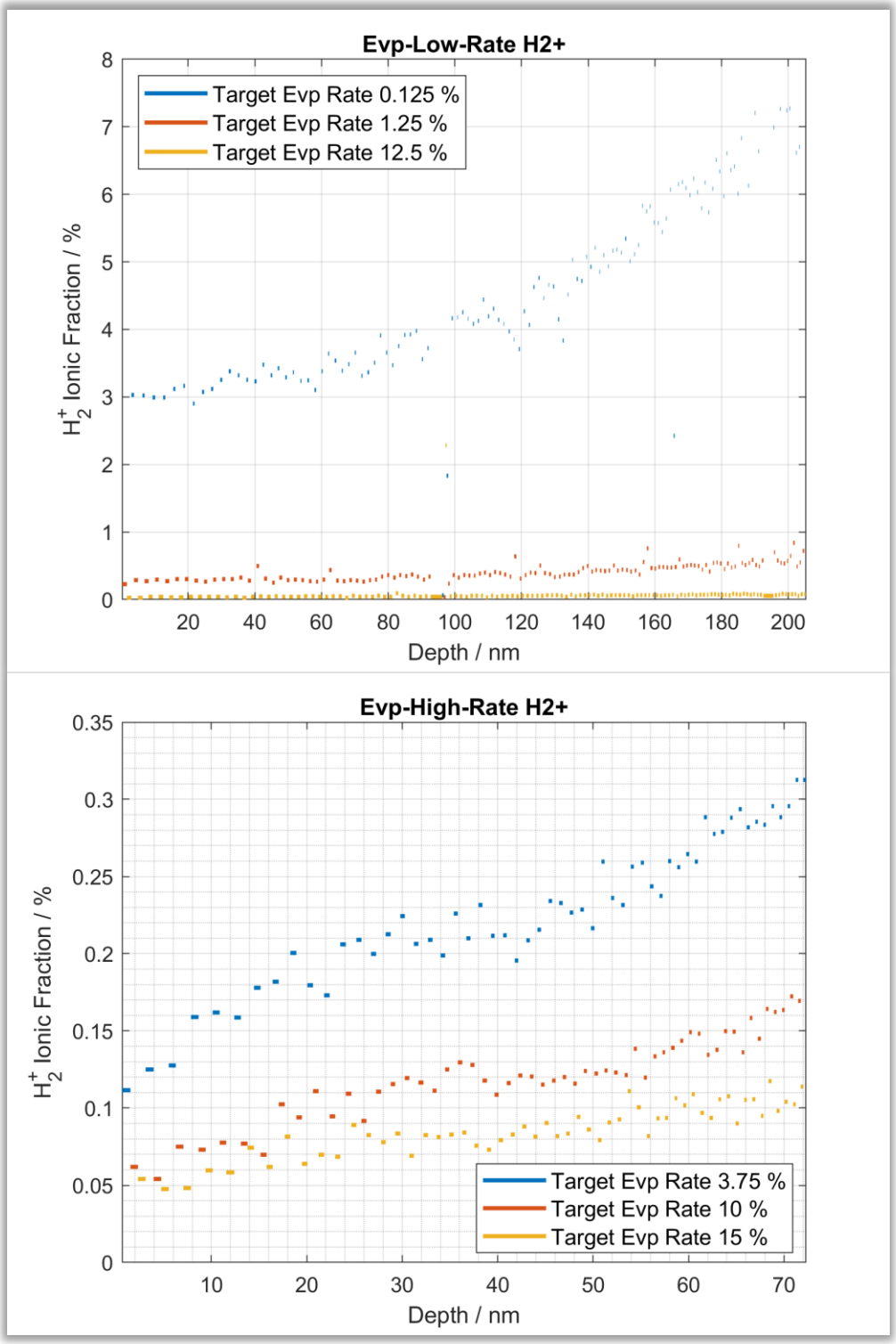

Detected ionic fractions of H_2^+ throughout the layers in the cycled evaporation rate experiments. Similar to the H^+ fractions, the amounts of H_2^+ are different for the different evaporation rates and increase as the experiments progress.

Picture and Description also published my previously published paper [141], Supplementary Material.

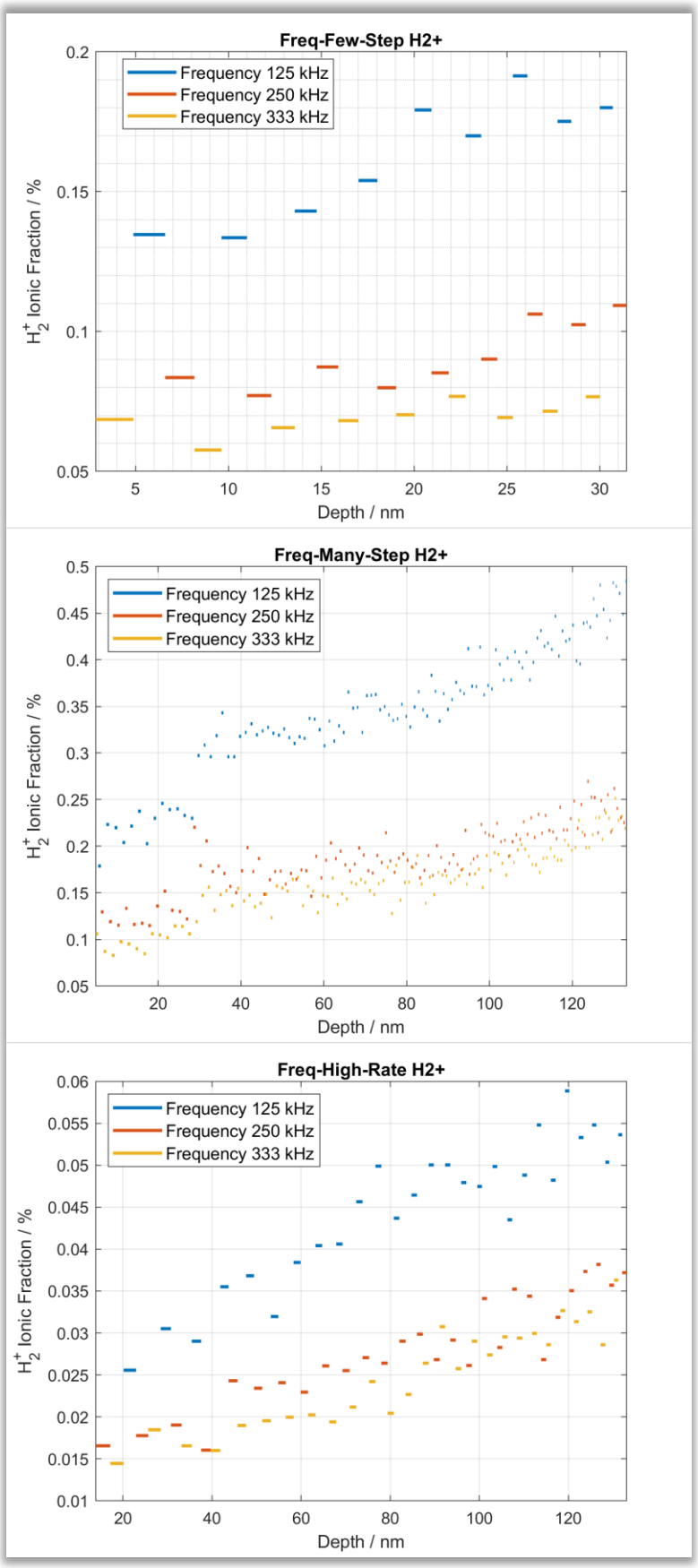

Detected ionic fractions of H_2^+ throughout the layers in the cycled frequency experiments. Similar to the H^+ fractions, the amounts of H^+ are different for the different evaporation rates and increase as the experiments progress.

Picture and Description also published my previously published paper [141], Supplementary Material.

Appendix C: Additional Diagrams for Hydrogen Field Dependence

Appendix C-1: Identifiers of Sub-Evaporation-Threshold Experiments

Experiment identifiers and hash values of sub-evaporation threshold experiments. In many cases, the runs had to be re-started after software crashes during the experiments (see main text, Section 3.1.2), therefore most experiments correspond to more than one run number. All hash values are listed is the public experiment list of the LEAP 5000 XS instrument at the Oxford APT group:
https://raw.githubusercontent.com/oxfordAPT/hashlist/master/cameca_5000XS.txt
A documentation of hash values for APT experiments is given in a publication by the IFES technical committee:
https://docs.google.com/document/d/e/2PACX-1vQyd3Pc32tS7TjFsiLyjhYlOmqFl_UHPgrkowYIFONIaOYVjmNaiK5HkMIoLurkwP-qzKLLKUXtjU9s/pub

Experiment Type	Run Number	Hash Value
Pulsed Voltage, 200 kHz	R5111_23670	005bca0a98dc624ee61b87f85a8d32d36d34e049684fb27fb7fbbefc7edb3c13
	R5111_23838	b2d8b3859b42ce6d2c67755a1a813eb59f05176b155a7757e72f4e7dfd196a7c
Pulsed Voltage, 500 kHz	R5111_23775	208a9d70b4ed301108c14700af23d260a272ab97f891f8fced590d306f69a6ef
	R5111_23839	4306eea531d1f744866980e961a525d2f971dcf465987646d2bf2aa62eb0b5cb
Pulsed Voltage, 25 kHz	R5111_23784	2dd5b45c1441e068e10dd42efdde5678c87d5d9647af00c4a7f857a93b69c4e8
	R5111_23840	a9b1787d312a7a958ad934947713bae1b7ccc516beb06b44ea84a2e013887a0f
Pulsed Laser, 2pJ	R5111_23760	f0c9948c96c32ac612cb723efd0553600ce004440d0bc8cb0143c96c799711a7
	R5111_23761	defa71aeffe2b85dcacdce4b05a7d7e3a63f688f99583d2de8da06d583dc252b
	R5111_23763	be778934c07caded11366cbe8169b1bbeae7b4504ccb4a9b8b27e2df8e3a1a13
	R5111_23764	ce564ed03744be58f598a8583eed8867eb980def6f438f12eab5f2cc0b054ec3
	R5111_23766	dd7de4555f064c294debafce5b7194dae56d1281a821ac2efe6ba79ad9ef3657
	R5111_23767	bfd049d693cb71d69415245910850bf55c8378ccf00ad97d41d64272485bd660
	R5111_23768	bbd95a2779082701326403129c35d0a4a39d6ccbe1a762168bf6d0c173e02eb6
	R5111_23771	c0dcf5ca6cf4fb745b3cb5617efb6700816f957054ff573a2694fd52eb30beb7
	R5111_23773	d1ddf7117331e3b01363512894c7458cc5a0ff9bb942d1a24b24ef6ffbd7e047
Pulsed Laser, 10 pJ	R5111_23747	de97ad1fe2c22ca24e8225a196e4fae3e2f1705f3c5fd1dda73211bc0b730031

Appendix C-2: Conversion Table for Voltage and Field

Conversion for standing (DC) voltage and corresponding pulsed voltage to electric field for the tungsten sample. Values in parentheses () lie above the evaporation threshold of the sample and are only provided for completeness, however no hydrogen spectrum was sampled at these voltages.

DC Voltage (V)	646	896	1146	1396	1646	1896	2146	2396	2646	2896	3046	3146	3296	3546
DC Field (V/nm)	7.7	10.6	13.6	16.6	19.5	22.5	25.5	28.4	31.4	34.4	36.1	37.3	39.1	42.1
Voltage at Pulse (V/nm)	840	1165	1490	1815	2140	2465	2790	3115	3440	3765	3960	4090	*(4285)*	*(4610)*
Field at Pulse (V/nm)	10.0	13.8	17.7	21.5	25.4	29.2	33.1	37.0	40.8	44.7	47.0	48.5	*(50.8)*	*(54.7)*

Appendix C-3: Full Hydrogen Spectra at all Voltages

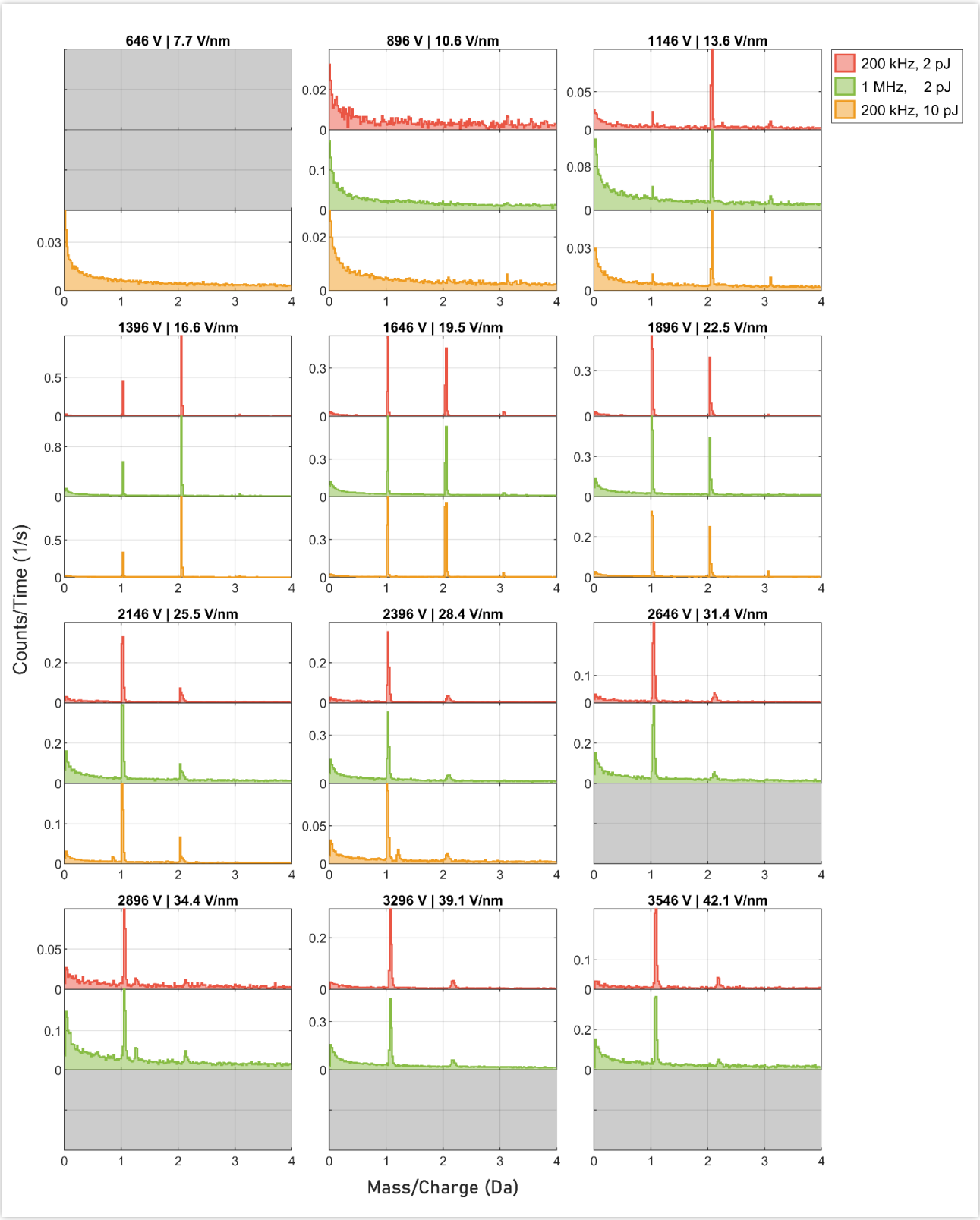

Hydrogen spectrum on tungsten at various field below evaporation threshold in laser mode at 200kHz/2pJ (red), 1 MHz/2pJ (green) and 200kHz/10pJ (yellow). Parameters at which no data was acquired are greyed out. It is seen that the pattern is dependent on the field, however the influence of laser energy and frequency is only minor. The side peaks at 1.2 Da/2986V, 0.8Da/2146V/10pJ and 1.2 Da/2396V/10pJ are likely so-called pulse picking errors, which are a machine artefact where laser pulses occasionally arrive early or late, and no actual feature of the spectra.

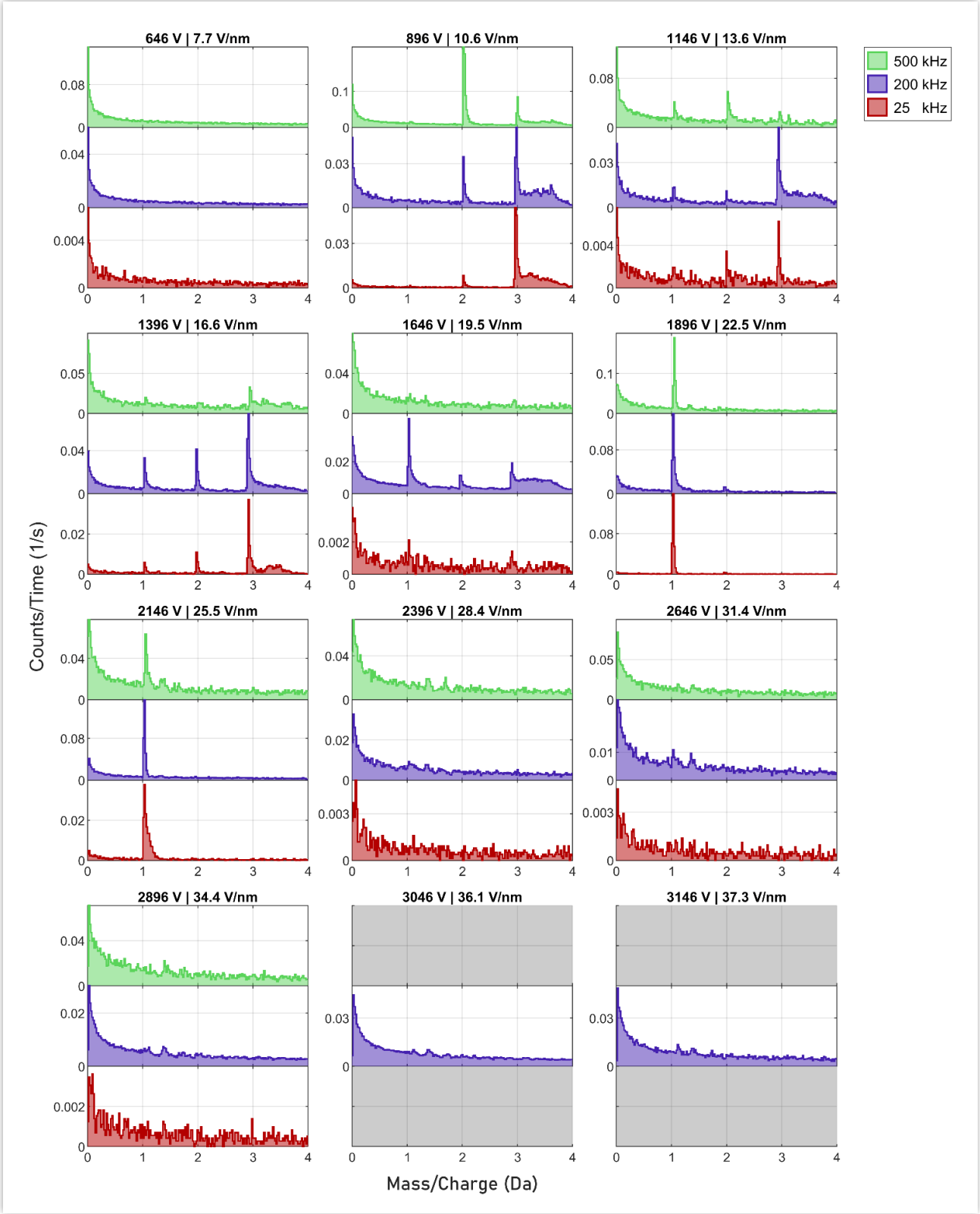

Hydrogen spectrum on tungsten at various fields below evaporation threshold in voltage mode at 500 kHz (green), 200kHz (violet), and 25 kHz (red). Parameters and voltages where no data was acquired are greyed out. The structure of the peaks is dependent on voltage/field and pulse frequency. Above 2396 V/28.4 V/nm, all hydrogen spectra are empty. The “waves” in the spectrum between 1.2 and 1.7 Da, most clearly seen above 2396 V/28.4 V/nm, are believed to be a machine artefact.

Appendix C-4: Transition of H^+ peak

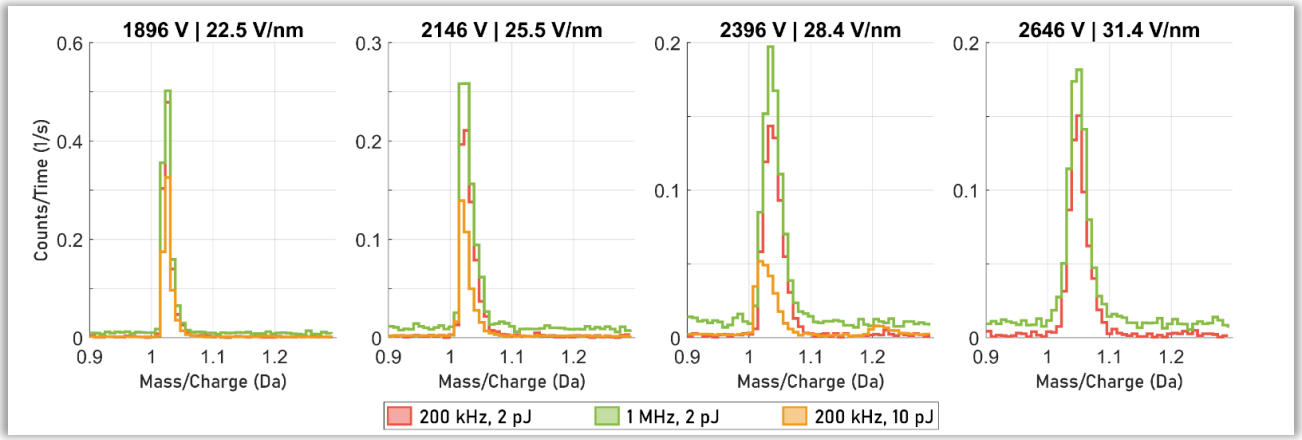

Transition of the H^+ from peak to hump in the sub-evaporation threshold pulsed laser experiments. It is noted that at 2646 V/31.4 V/nm (rightmost tile), no data at 200 kHz/10 pJ was recorded.

Appendix D: Additional Diagrams for Deuterium imaging in Tungsten

Appendix D-1: Grain Selection using EBSD

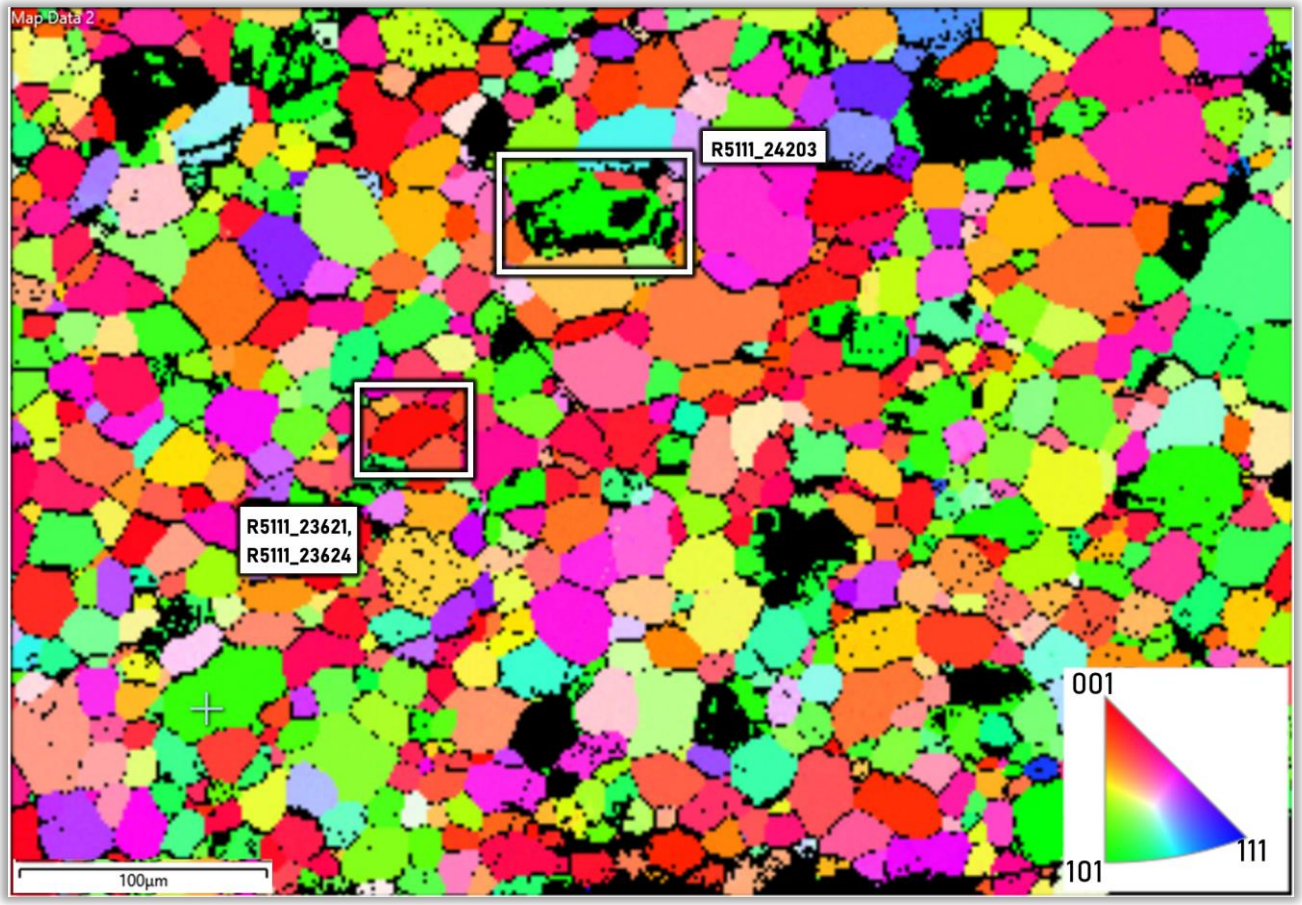

The specimen for the experiments R5111_23621 (W-E), R5111_23624 (W-F) and R5111_24203 (W-G) were prepared from grains which were specifically selected for their grain orientation, using EBSD. The EBSD pattern was acquired using a Zeiss Crossbeam 540 scanning electron microscopy, which is equipped with an Oxford Instruments Nordlys Max EBSD detector. The electron acceleration voltage for acquisition was set to 20 kV.

The Inverse Pole Figure (IPF) Map of the direction perpendicular to the surface of the material is shown in Figure above, and the grains used for the APT samples are highlighted. The specimen in R5111_23621 (W-E) and R5111_23624 (W-F) were lift out from the same grain, which was aligned such that a 110 crystallographic plane was (nearly) parallel to the material surface (EBSD Euler Angles: 354.0°, 3.2°, 18.1°). R5111_24203 (W-G) was lift out from a 100 grain (EBSD Euler Angles: 53.4°, 43.1°, 90.0°).

The EBSD analysis does also allow for some insight into the surface texture of the material. Pole figures, using the unit of multiples of uniform density (MUD) are shown below. It is seen that a preferred grain orientation exists: grains with a 100 plane parallel to the surface are more common than other orientations, and 111 orientations are rare.

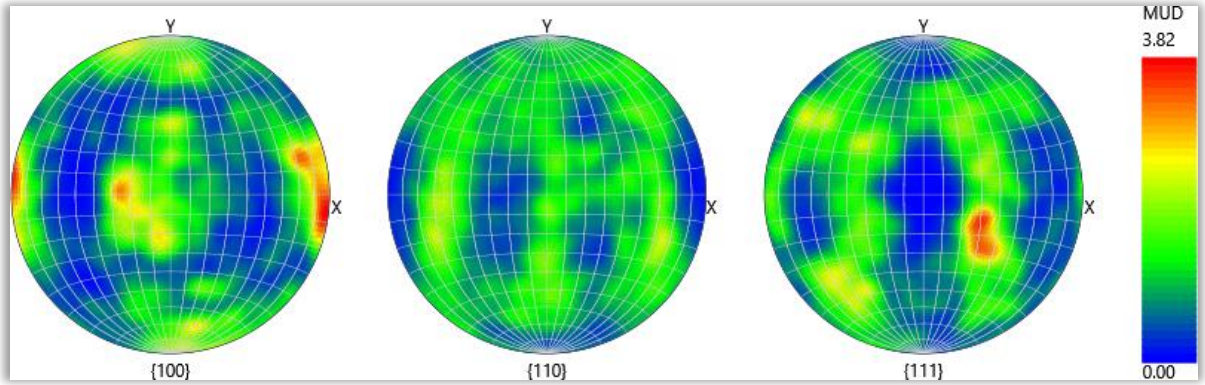

A size distribution of the grains is shown in the figure below. The mean grain size, measured through surface area, is 223 μm^2 and the 5th and 95th percentiles are 38 and 660 μm^2.

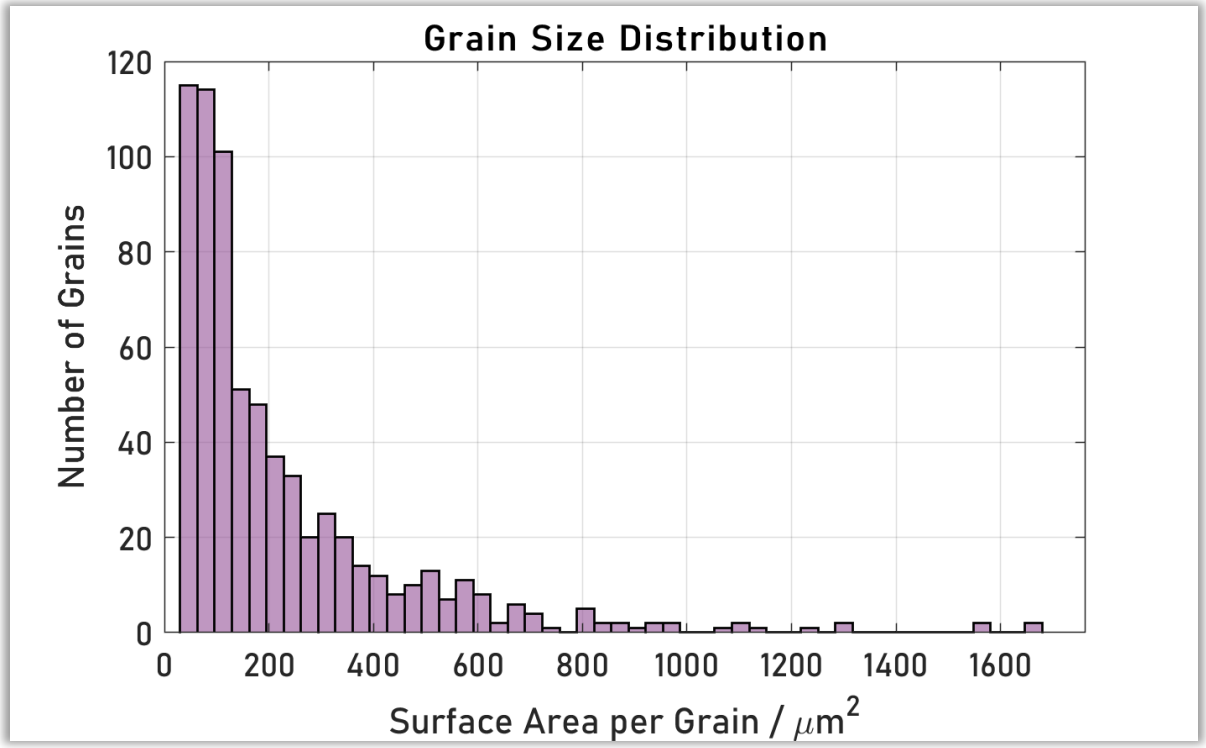

Appendix D-2: Identifiers of implanted Tungsten Experiments

Experiment identifiers and hash values of the datasets used as search candidates. A documentation of hash values for APT experiments is given in a publication by the IFES technical committee:
https://docs.google.com/document/d/e/2PACX-1vQyd3Pc32tS7TjFsiLyjhYlOmqFl_UHPgrkowYIFONIaOYVjmNaiK5HkMIoLurkwP-qzKLLKUXtjU9s/pub

All experiments are listed in the public experiment list of the Cameca LEAP 5000 XS atomprobe at the Oxford Atom Probe Group: https://raw.githubusercontent.com/oxfordAPT/hashlist/master/cameca_5000XS.txt

Dataset	Run Number	SHA-256 Hash of raw experiment file
W-A	R5111_12519	39cd2a42a1862bf8bfd47db663f41a12b8def87a420ff2b2743b85085a3f93b8
W-B	R5111_22841	459f38a27f8a7384d78a9dc5ed71101178212aa1fd3a399ca8be160b69b12f49
W-C	R5111_12575	7e1df47176d8a8fa2d4b5c19ebc466b6a377de0197664296c44875732ba5ea05
W-D	R5111_22837	a0d780912251abd1ffc51732fbaf76fe457da8f9e84b96d33e696a68b1ad8bb2
W-E	R5111_23621	30d1266b05a7e964ac29d662847eb8e161d7938b436acabe72863b96503ea359
W-F	R5111_23624	3ca5a2ba79e112ee60c1acecb2cc31d691d0bb204b123ee3f85adac9eed78292
W-G	R5111_24203	d593112457ff3771dfb892f874e7d35f6674b2a997f246f23b418bfa3d0594ad

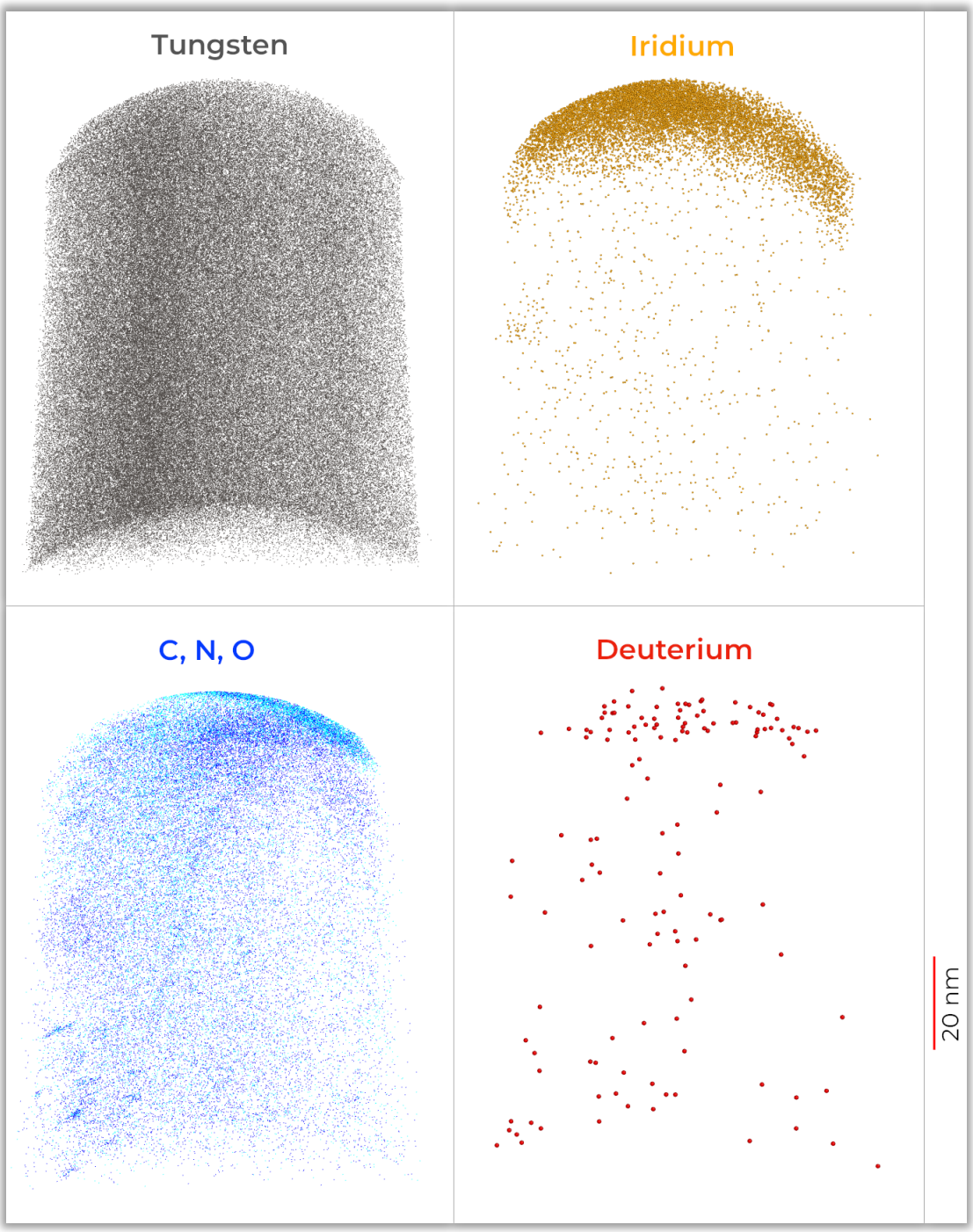

Atom maps of reconstructed dataset R5111_22841 (W-B). Only 1% of W atoms shown.

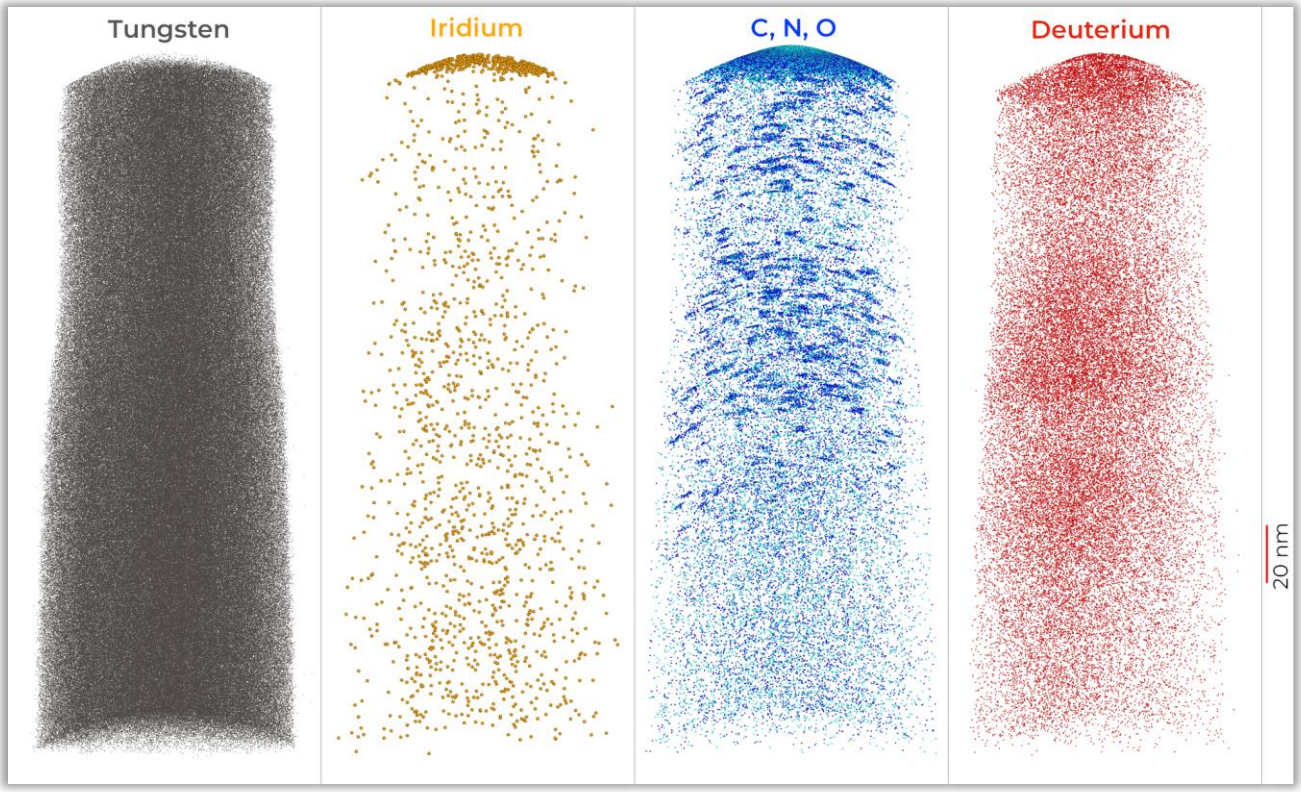

Atom maps of reconstructed dataset R5111_12575 (W-C). Only 1% of W atoms shown.

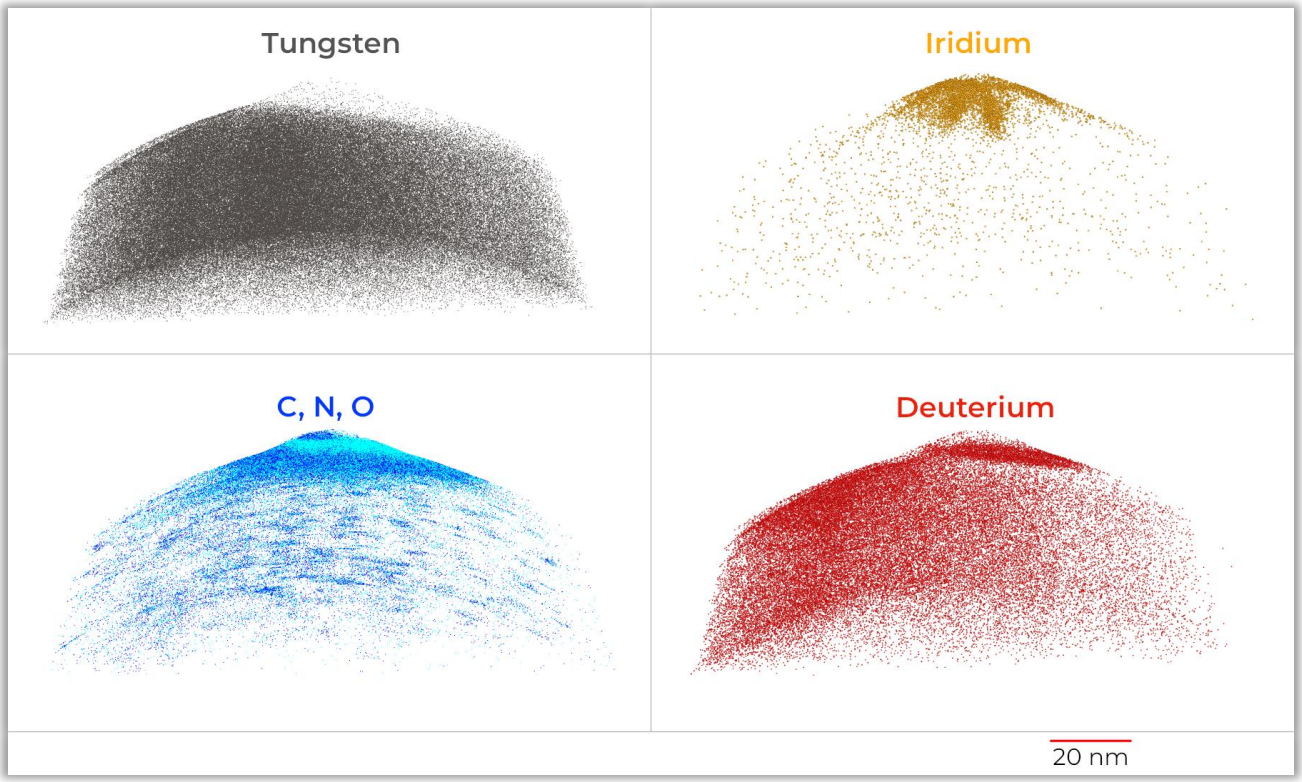

Atom maps of reconstructed dataset R5111_22837 (W-D). Only 1% of W atoms shown.

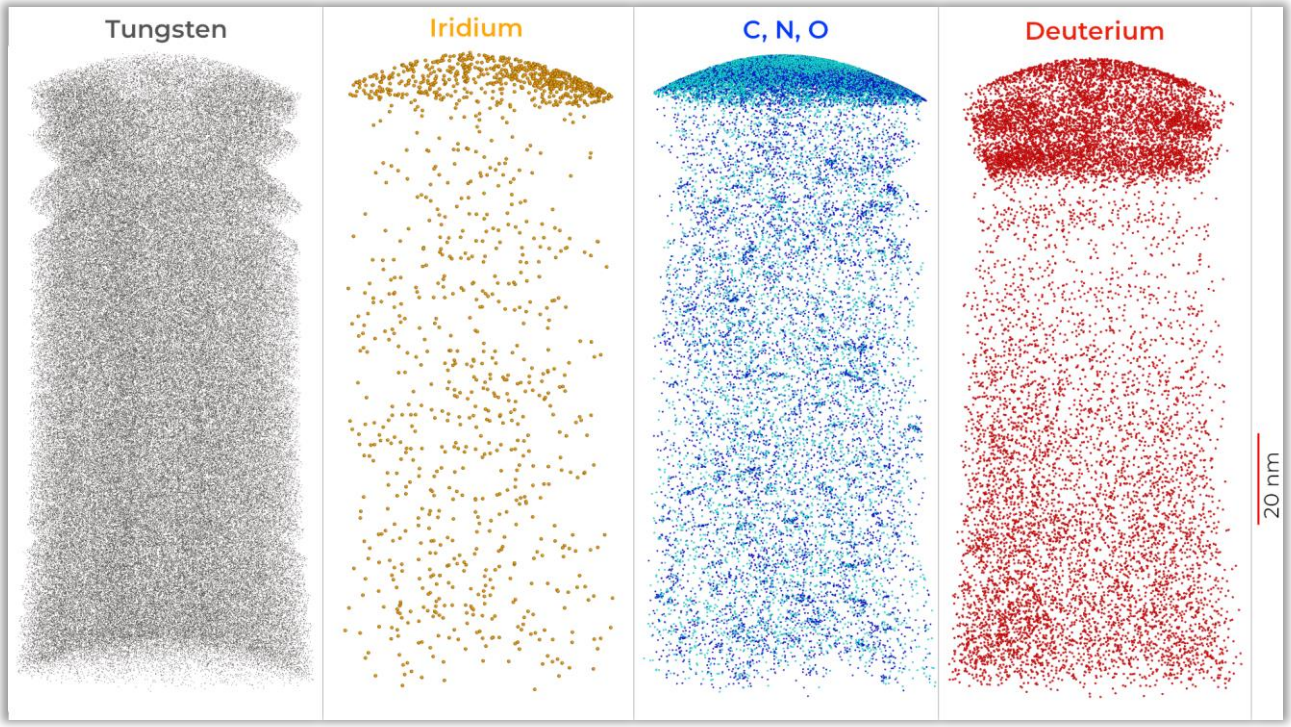

Atom maps of reconstructed dataset R5111_23621 (W-E). Only 1% of W atoms shown.

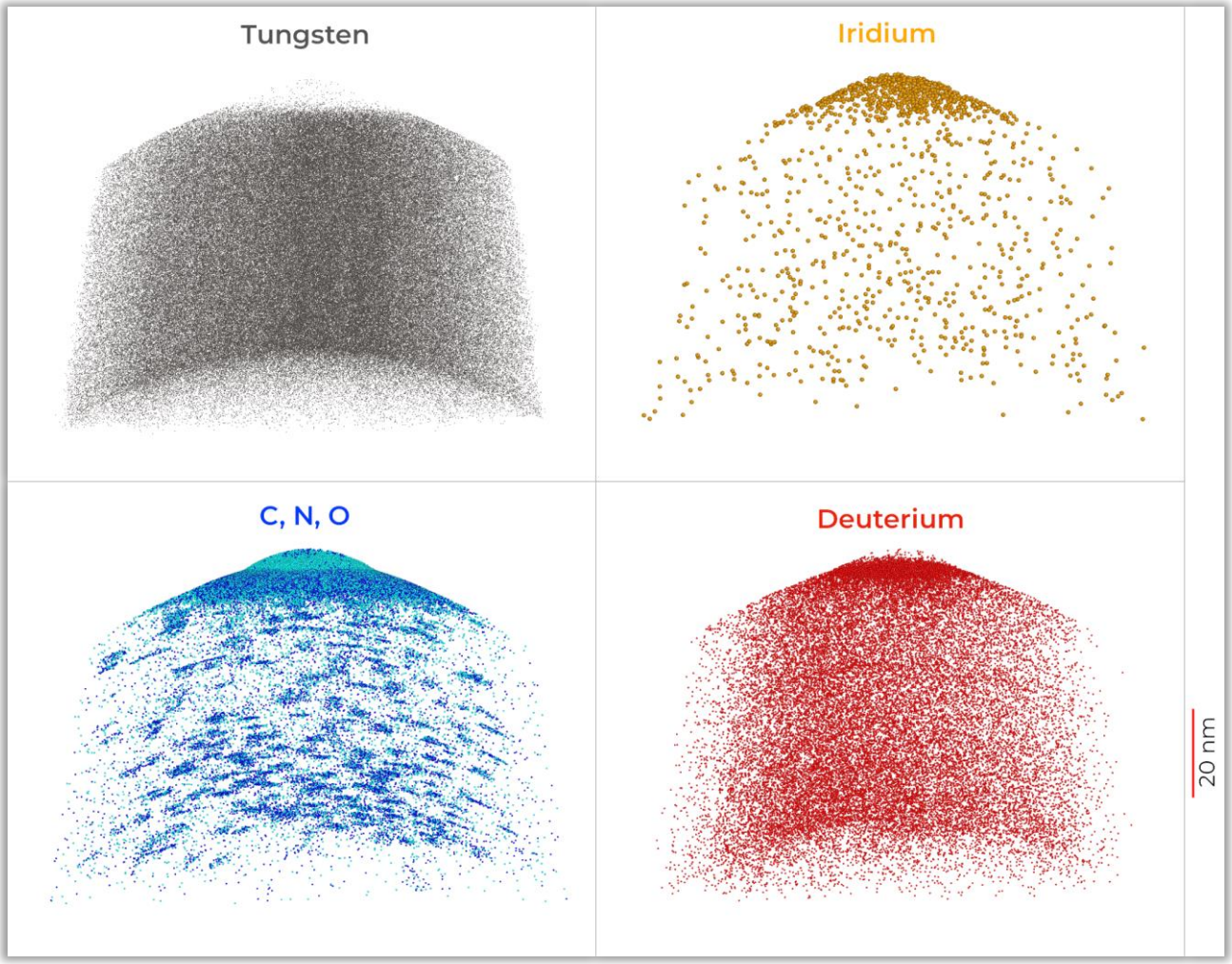

Atom maps of reconstructed dataset R5111_24203 (W-G). Only 1% of W atoms shown.

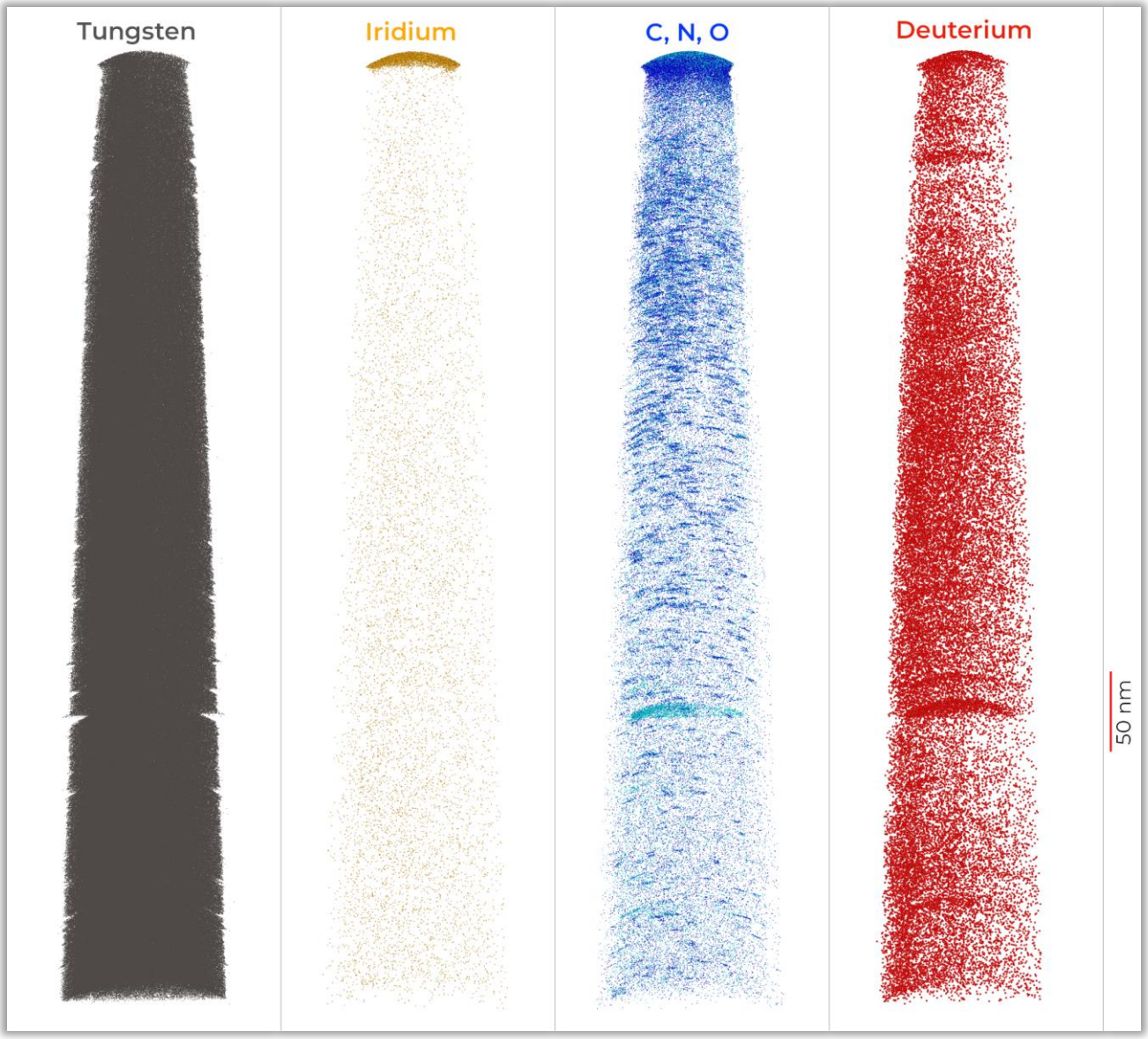

Atom maps of reconstructed dataset R5111_23624 (W-F). Only 1% of W atoms shown.

Appendix D-4: Composition of APT Specimen

Global composition of APT specimen, calculated through MLE decomposition of spectra, for the entire datasets including iridium layers and carbon caps.

Experiment	C	N	O	Si	Ga	Ir	B	W
	atomic %				*atomic ppm*			
R5111_12519	0.02	0.08	0.03	0.02	582	42	-	Balance
R5111_22841	0.13	0.14	0.06	0.05	392	505	17	
R5111_12575	0.02	0.13	0.04	-	490	7	-	
R5111_22837	0.13	0.76	0.7	0.03	695	276	43	
R5111_23621	0.06	0.16	0.07	0	933	40	15	
R5111_23624	0.03	0.04	0.01	0	514	30	3	
R5111_24203	0.04	0.49	0.3	0.02	708	28	8	

95% confidence intervals for global composition of APT specimen, calculated through MLE decomposition of spectra, for the entire datasets including iridium-layers and carbon caps.

	C		N		O		Si		Ga		Ir		B	
	atomic %								*atomic ppm*					
	lower Bound	upper Bound	lower Bound	upper Bound	lower Bound	upper Bound	lower Bound	upper Bound	lower Bound	upper Bound	lower Bound	upper Bound	lower Bound	upper Bound
R511_12519	0.015	0.018	0.074	0.079	0.027	0.03	0.023	0.025	571	592	38	46	0	0
R511_22841	0.128	0.131	0.132	0.141	0.054	0.057	0.042	0.051	384	399	497	513	15	19
R511_12575	0.02	0.021	0.133	0.135	0.034	0.036	0	0	485	495	6	9	0	0
R511_22837	0.131	0.136	0.755	0.765	0.688	0.703	0.026	0.027	685	705	268	283	40	46
R511_23621	0.056	0.059	0.16	0.165	0.067	0.07	0.002	0.002	920	946	36	45	13	18
R511_23624	0.025	0.026	0.041	0.042	0.009	0.009	0.001	0.001	511	517	29	32	2	3
R511_24203	0.043	0.045	0.491	0.497	0.292	0.298	0.018	0.019	698	717	25	31	6	9

95% confidence intervals for global composition of APT specimen, calculated through MLE decomposition of spectra, excluding the first 40nm of all datasets.

	C		N		O		Si		Ga		Ir		B	
	atomic %								*atomic ppm*					
	lower Bound	upper Bound	lower Bound	upper Bound	lower Bound	upper Bound	lower Bound	upper Bound	lower Bound	upper Bound	lower Bound	upper Bound	lower Bound	upper Bound
R511_12519	0.002	0.004	0.066	0.07	0.01	0.012	0	0.001	263	279	15	21	0	0
R511_22841	0.059	0.062	0.098	0.107	0.018	0.021	0.005	0.012	315	332	5	11	20	25
R511_12575	0.006	0.007	0.018	0.019	0.005	0.006	0	0	476	486	0	2	0	0
R511_22837	0.017	0.022	0.128	0.137	0.015	0.024	0	0.002	450	490	14	30	7	17
R511_23621	0.049	0.052	0.044	0.048	0.003	0.005	0.001	0.001	800	828	3	11	9	14
R511_23624	0.006	0.007	0.035	0.036	0.004	0.005	0.001	0.001	346	351	1	3	2	3
R511_24203	0.001	0.004	0.094	0.098	0.008	0.011	0.001	0.001	439	460	4	10	0	3

Appendix D-5: Cluster Search of Carbon, Nitrogen, Oxygen Clusters

The clusters of carbon-nitrogen and oxygen in the tungsten datasets were identified using the DBscan algorithm [270]. DBscan requires two input parameters, N_{min} and ε, which need to be user selected. Atoms are considered "core atoms" of a cluster if in a radius of ε around the atom, there are at least N_{min} other atoms of the type that is considered as "cluster" element (solute atoms). Atoms are considered "reachable" and thereby still belonging to a cluster if the distance between it and a core atom is less than ε. All other atoms are deemed to be outside of clusters.

In the field of APT, there exists no single established method to identify ideal parameters for a given dataset [339-341]. Instead, it is common practice to test different combinations of N_{min} and ε in parameter sweeps [342]. A combination of N_{min} and ε usually is identified based on either visual inspection of the results, or may be spotted as a range of N_{min} and ε where small parameter changes only have little influence on the results, or through comparison with clusters as detected in randomised data [340, 342, 343].

The fundamental requirement for such methods is that, for a given dataset, a global choice of N_{min} and ε exists that produces acceptable results for the entire dataset. This assumption breaks down if the properties of clusters and matrix in the dataset are too inhomogeneous, as is the case for this radiation-damaged material. In the radiation-damaged samples analysed here, the density of clusters as well as distribution of solute in general is clearly depth-dependent. Therefore, no set of cluster search parameters that is appropriate for the entire dataset may exist.

The diagram below illustrates this problem using sample R5111_23624 (W-F). Selection of rather low N_{min} of 5 and high ε of 2.1 nm achieves good detection (potentially even over-detection) of the clusters with low density which are deep in the material (ca. below 400 nm), but clusters in the more dense region (50-250nm depth) to stick together (Figure below, top image). On the other hand, selecting higher N_{min} of 15 and low ε of 1.6 nm achieves better separation of the clusters in the dense area (Figure below, bottom image), however at the cost of missing some of the clusters below 400 nm.

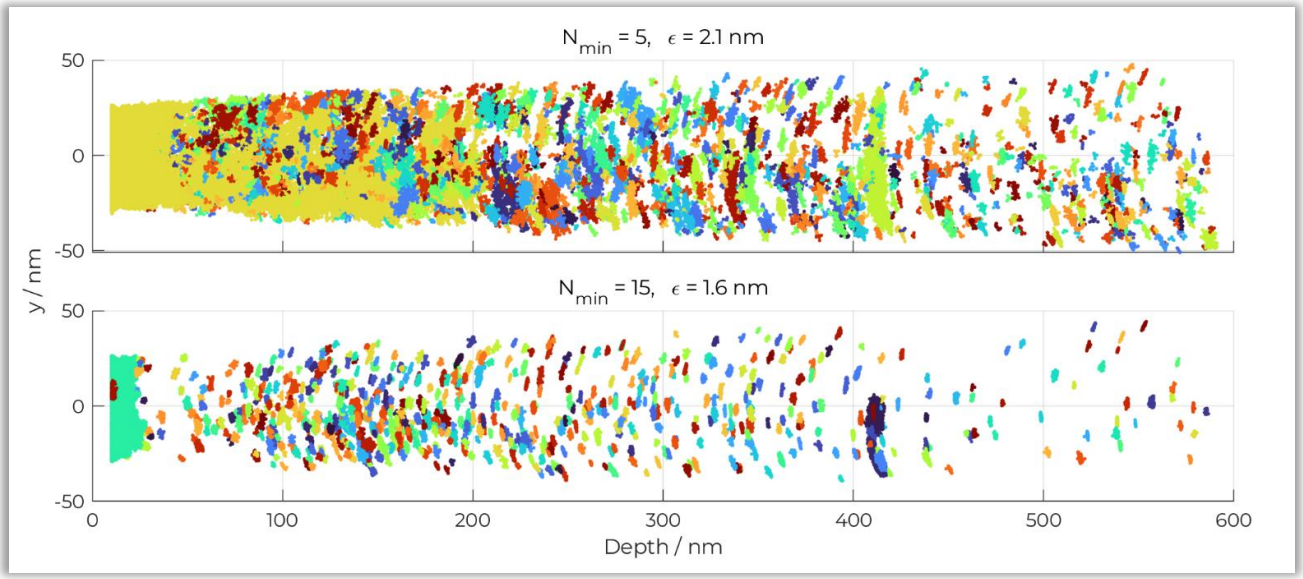

Therefore, instead of searching for DBSCAN parameters which are globally suitable for the entire datasets (which possibly don't exist), an analysis of depth-dependent cluster properties is conducted. To this end, the parameters are selected to optimise for detection and separation of clusters at the depth of peak cluster concentration (such that clusters do not stick together) by visual inspection. It then becomes possible to generate depth profiles of the clusters, whereas the number density of "clusters with respect to the chosen parameters" is determined per depth bin. A set of parameters was found which is appropriate to this task for all datasets, and is listed in Table 12 in the main text. Using these parameters, the depth- and size distributions of the clusters (Figure 28A and B in the main text) can be determined.

It is noted that, since the solute (“clustered species”) is defined carbon, nitrogen and oxygen, the DBscan and therefore all subsequent cluster composition analyses cannot pick up any elements other than these. Since the current material however simply does not contain relevant quantities of any other elements (see composition in Table 11, main text), this limitation is acceptable for the current case and does not need to be rectified through additional analyses of co-clustered species, as in APT would typically be achieved by adding enveloping steps to the cluster search.

Once the clusters have been identified, the global cluster compositions can be calculated using MLE, and the results are shown in Figure 28C in the main text. In addition, it is also possible to conduct MLE decomposition per cluster, which enables an investigation into whether the cluster composition changes with depth (depth is defined as distance from surface iridium layer). In the Figure below, the fractions of carbon and oxygen as calculated by deconvoluting the clustered atoms are shown (non-clustered atoms are not considered). Each marker shows the average composition of clusters in one depth bin, whereby the bin size is such that every bin contains 5 clusters.

The fraction of oxygen (Figure below, A) is elevated to approx. 20 to 50% close to the surface, but swiftly drops with increasing depth, down to approximately 5% or less. At the detected median cluster size of 44 atoms without detection efficiency correction, this corresponds to only 2 detected oxygen atoms per cluster. A trend is not as clearly seen in the distribution of carbon (Figure below, B), however it seems that also in this case, the amount in general drops slightly with increasing depth, down to approximately 20%. The differences in cluster composition between the datasets are relatively large. At depths below 100 nm, the measured fractions range from approximately 40% (R5111_23621, W-E) to below 5% (R5111_12519, W-A). The remaining atoms that make up the clusters are all nitrogen. Likely a relevant fraction of clusters in the material are pure nitrogen clusters without any carbon or oxygen.

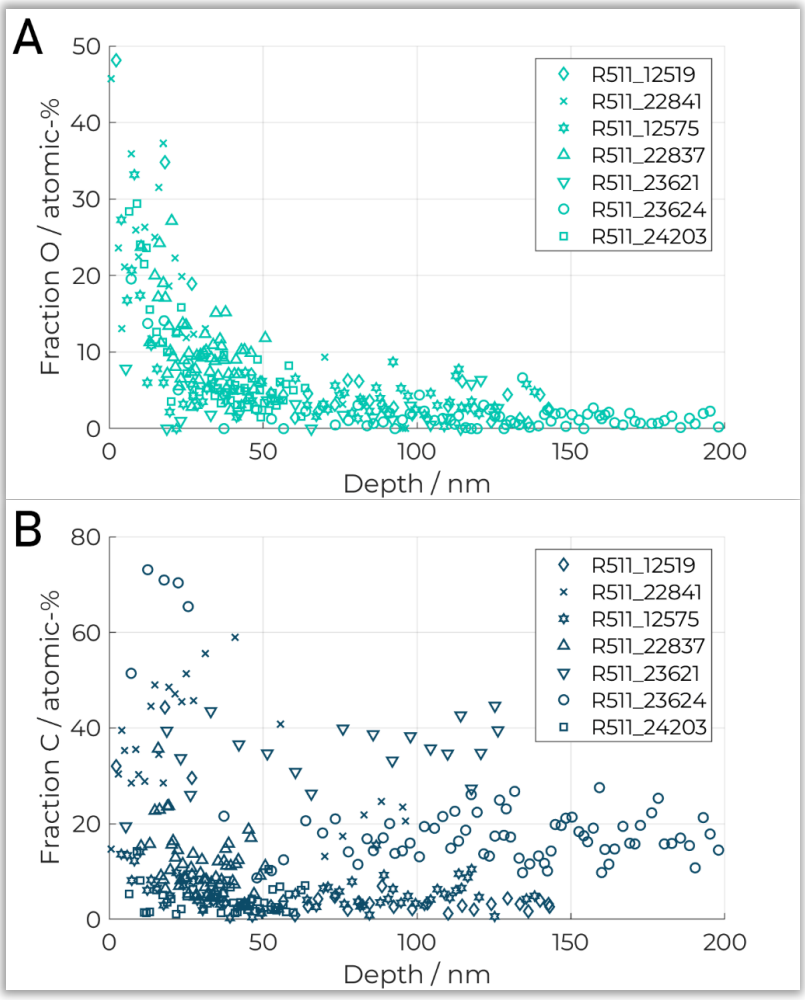

Appendix D-6: Depth Profiles plotted using same Axis Scaling

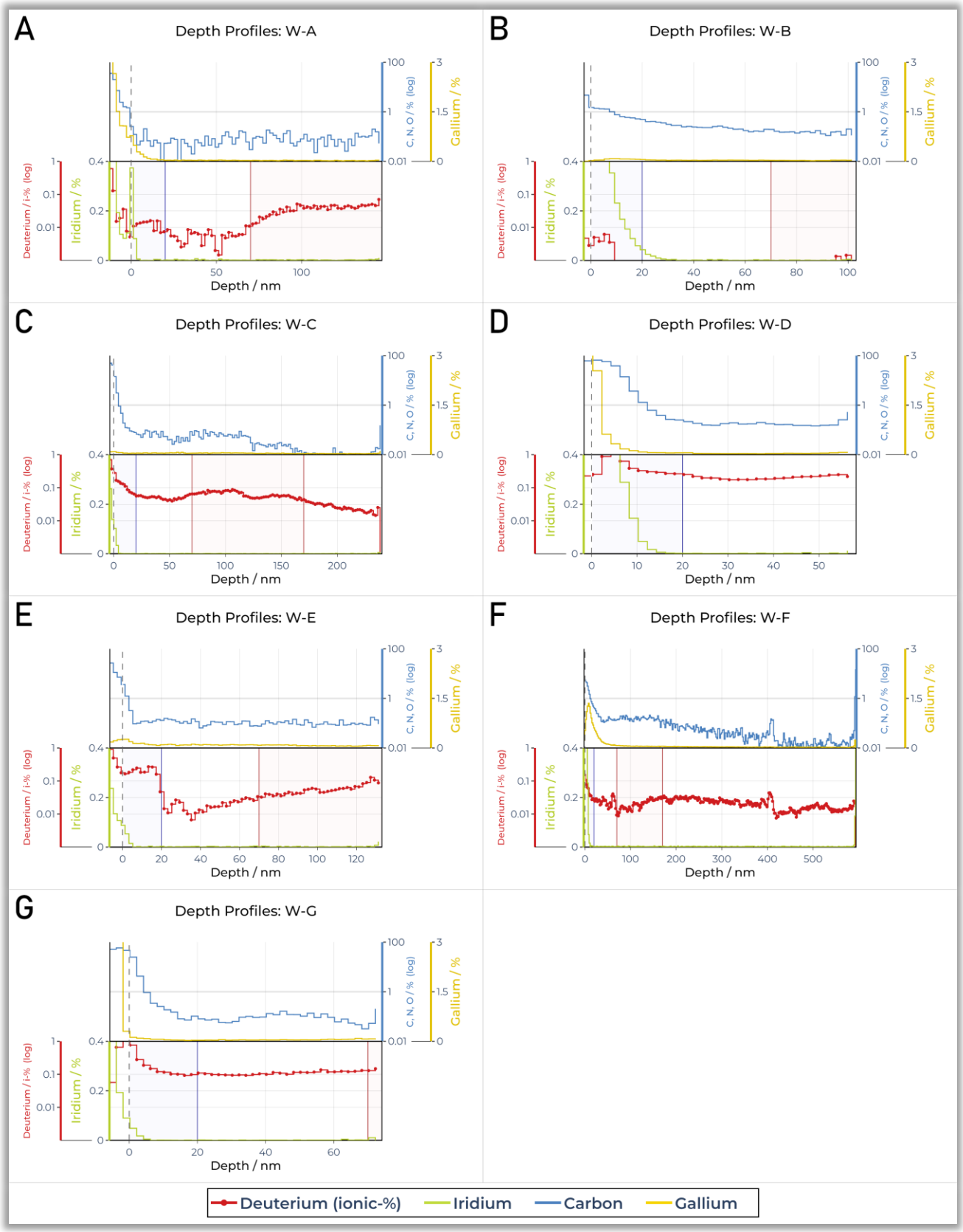

The diagram shows the same depth profiles as Figure 30, using the same axis scaling per species for all experiments. To accommodate the wide ranges, logarithmic scales are used for deuterium and carbon/nitrogen/oxygen.

Appendix D-7: Potential Co-implantation of Carbon or Nitrogen during Irradiation

The tungsten specimens in this work are found to contain impurities of carbon, oxygen and nitrogen, which are clustered in the material. Since no analyses on the material prior to annealing and radiation damaging were conducted, it is not possible to directly determine whether one of these steps has introduced the impurities.

However, as seen in the depth profiles in Figure 30 (in particular Figure 30C and F), their depth distribution is not uniform, but tails off with decreasing depth, reaching a stable (and low) concentration from approximately 200 nm. This roughly aligns with the simulated depth of radiation damage (Figure 23), so it may be speculated that the contamination has actually been introduced during the radiation damaging step. A possible route could be co-implantation, where a contaminant species on the sample surface is injected into the material alongside of the incoming tungsten ions.

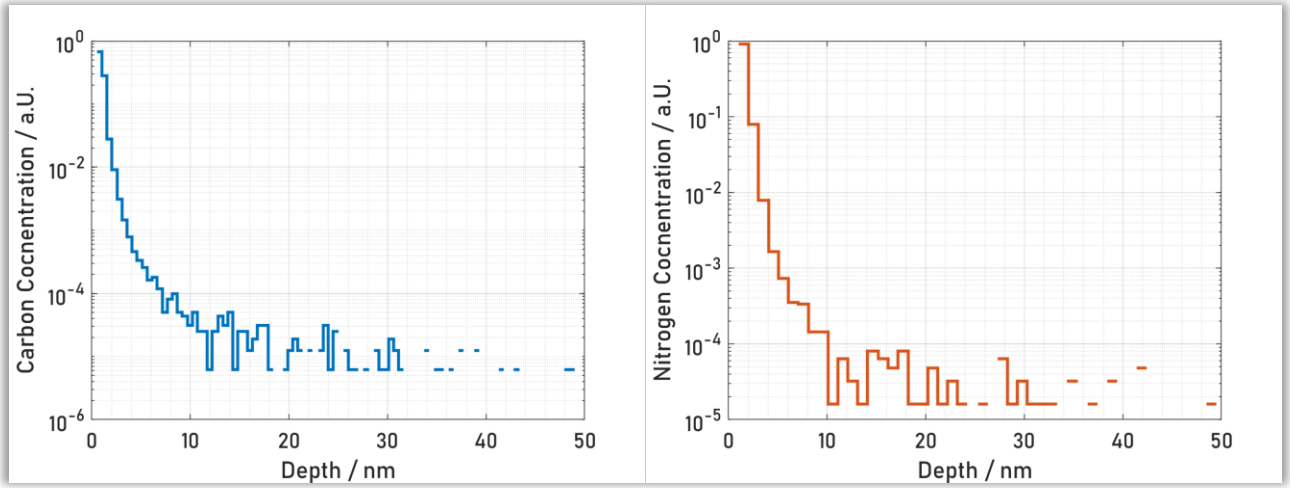

To test this possibility, a simulation using SRIM [261] is conducted. A 1 nm thick layer of carbon or nitrogen is placed on a 50 nm layer of tungsten, and a simulation of 10000 incident tungsten ions with an energy of 2 MeV is conducted. The resulting depth distribution of carbon (blue, left) and nitrogen (orange, right) in the target is shown in the figures above. Missing bins in the diagrams correspond to zero counts.

It is seen that only a very minor fraction of carbon and nitrogen reach further than 10 nm into the tungsten. This does align with the observation of an elevated content of carbon/nitrogen/oxygen within approximately the first 10 nm directly behind the surface (Figure 30), meaning that at least a fraction of these impurities at this depth could indeed be the result of a co-implantation. However, it also shows that injected carbon or nitrogen unlikely reach sufficiently depth to partake in all the observed clusters, which reach down to approximately 200 nm. I conclude that the carbon/nitrogen/oxygen at this depth is therefore more likely to already have existed in the material prior to irradiation, possibly a contamination during annealing.

Nevertheless, even if the origin of the carbon/nitrogen/oxygen clusters is unclear, it may well be possible that the clustering itself is due to the radiation. Carbon clusters in irradiation damaged tungsten have been observed before in a FIM/APT study by Dagan et al [240]. They were attributed to a segregation of tungsten to radiation induced defects, meaning that the clusters act as markers for radiation damage. In the current study, it is found that the depth distribution of clusters (number density in Figure 28A) approximately agrees with the simulated radiation damage depth (Figure 23). The observation of clusters is therefore well in agreement with Dagan et als' observations, and the clustering (of pre-existing species) could indeed be caused by the irradiation.

Appendix D-8: Expected Fraction of Retained Deuterium

In cases where hydrogen release from a material is controlled by de-trapping, and where no re-trapping occurs, the amount of released hydrogen from the sample (making the simplification that all traps have the same trapping energy) can be approximated using a first-order reaction kinetic, where the rate constant is an Arrhenius equation [344-347]:

$$\frac{dA_{released}}{dt} = Z * A_{released}(t) * \exp\left(\frac{-E_a}{R * T}\right)$$

($A \rightarrow$ Released fraction of hydrogen, $Z \rightarrow$ Preexponential factor in Arrhenius equation, $E_a \rightarrow$ Activation energy for detrapping, $R \rightarrow$ Gas constant, $T \rightarrow$ Temperature).

Conversely, the fraction of retained hydrogen in the material is:

$$\frac{dA_{retained}}{dt} = Z * \left(1 - A_{retained}(t)\right) \ * \exp\left(\frac{-E_a}{R * T}\right)$$

This differential equation is numerically integrated for trapping energies E_a of 1.0, 1.1 and 1.2 eV for a timespan of 1 year. Z is set to 10^{13} s^{-1} [348], T is constant 293 K, and the initial concentration of $A_{retained}$ is set to 1. This corresponds to storage of a sample that has been charged with hydrogen to saturation, for one year at room temperature. The results are shown in the diagram below.

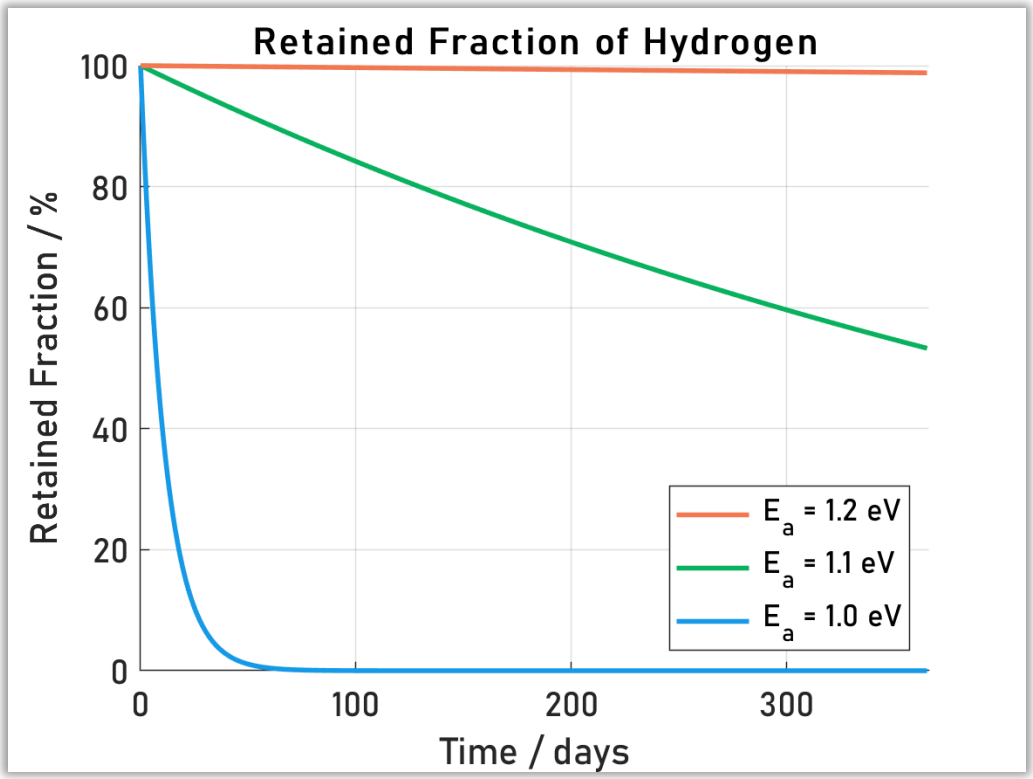

As seen, the influence of the trapping energy is stark. (Almost) zero hydrogen is not de-trapped after one year when the trapping energy is 1.0 eV, but almost no hydrogen is de-trapped when the trapping energy is 1.2 eV. It is important to note that this model is simplistic and does not take re-trapping into account [346], which likely happens to a considerable extent in the radiation-damaged tungsten analysed in Chapter 4. The values in the diagram above therefore rather represent lower bounds for the retained fractions of hydrogen.

It is known from DFT simulations (Table 2) that the trapping energy for a single hydrogen atom at a tungsten vacancy is approximately 1.25 eV [67, 69-72]. From the calculations presented here, it seems likely that at least a fraction of the deuterium in the implanted tungsten sample should not escape within the timeframe in which all experiments have conducted.

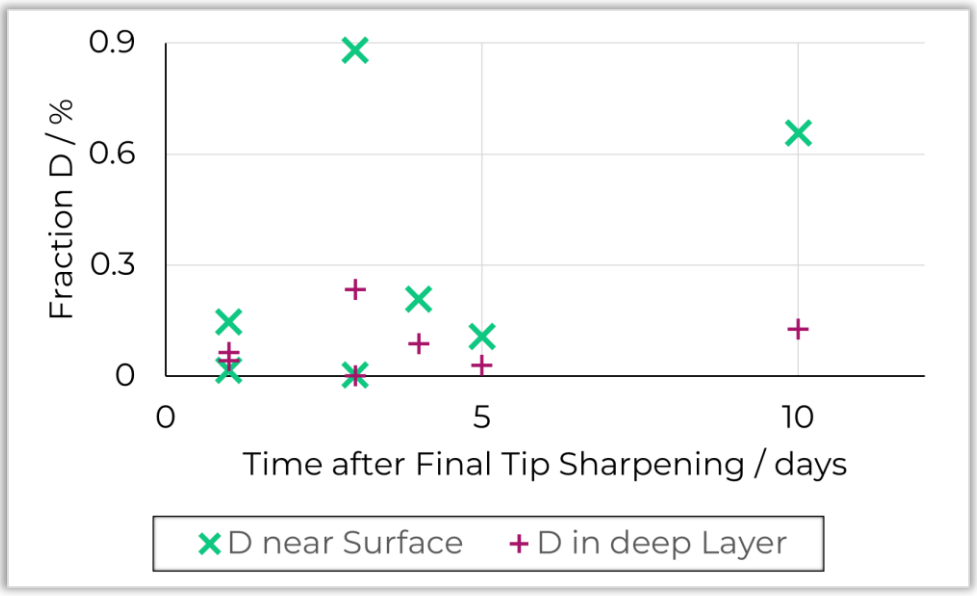

Deuterium content as measured near the sample surface and in the deep, deuterium-rich layer as function of days between final tip sharpening (in FIB) and APT experiment.

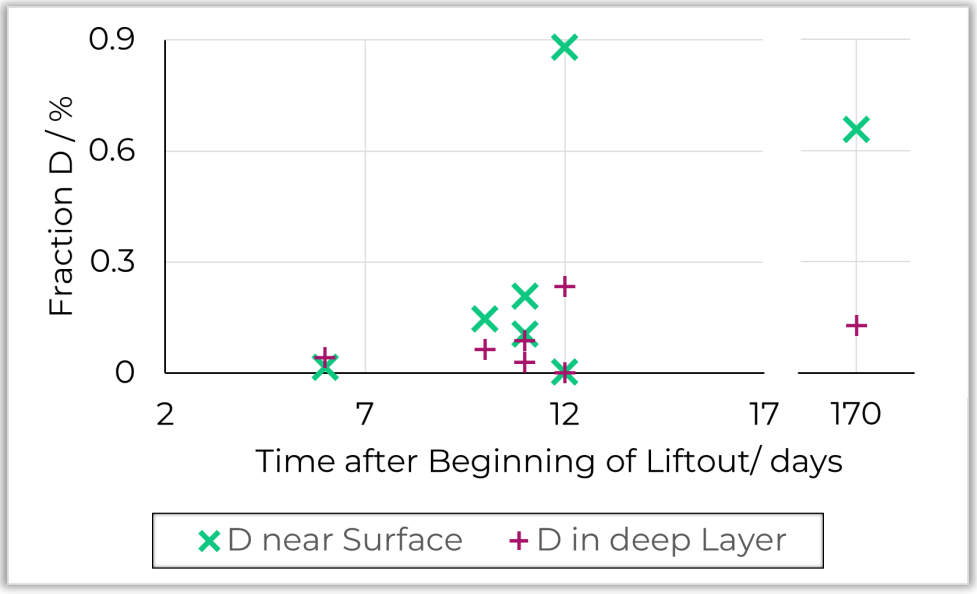

Deuterium content as measured near the sample surface and in the deep, deuterium-rich layer as function of days between beginning of the FIB liftout and APT experiment. Note the broken x-Axis.

Appendix E: Additional Material for APT Data Analysis

Appendix E-1: Available Data

List of all data that is exported by the UI automation script

Data	Comment	Type	Format
x/y/z Reconstruction Coordinates	Useless, as reconstruction is not run with appropriate parameters	Per ion	epos
m/n Ratio	Further processing needed, as mass calibration is skipped		
TOF			
Standing Voltage			
Pulsed Voltage			
x/y Detector Coordinates	Accurate, theoretically enables reconstruction of accurate of x/y/z coordinates		
Detector Event Multiplicity & Pulses Between Detection Events	accurate		
Detection Rate	Can alternatively be calculated from detector event multiplicity	Sampled for intervals throughout experiment	csv
Mass-to-Charge History			
TOF History			
Voltage History			
Pressure			
Specimen Base Temperature			
Laser Position	Only for laser experiments		
Laser Power	Only for laser experiments		

Appendix E-2: Identifiers of Search Candidates

Experiment identifiers and hash values of the datasets used as search candidates. A documentation of hash values for APT experiments is given in a publication by the IFES technical committee:
https://docs.google.com/document/d/e/2PACX-1vQyd3Pc32tS7TjFsiLyjhYlOmqFl_UHPgrkowYIFONIaOYVjmNaiK5HkMIoLurkwP-qzKLLKUXtjU9s/pub

Dataset	Run Number	APT Group	SHA-256 Hash of raw experiment file	Hash value listed in public experiment list
Inconel 718	R56_00545	3D Nanoanalytics, Materials Department, FAU Erlangen-Nuremberg, Germany	5bc338da8e0958a846227f4abcf9b1ad4f3c6182342fe0147f650e9b18c96f77	Not listed at this time
Tungsten	R5111_10114	Oxford Atom Probe Group, Materials Department, University of Oxford, UK	9a14401b87374a3ac47621eedd46a7da239dc158f51d76e3780e5aa2a4bffc60	https://raw.githubusercontent.com/oxfordAPT/hashlist/master/cameca_5000XS.txt
Bioglass	R5083_10591	Oxford Atom Probe Group, Materials Department, University of Oxford, UK	c5a44a2e8c65c8d7241b6b63be340ec35b11979789fbcd5c292970db9c50529e	https://raw.githubusercontent.com/oxfordAPT/hashlist/master/cameca_5000XR.txt

Appendix E-3: Inner Structure of t-SNE of Iron Cluster

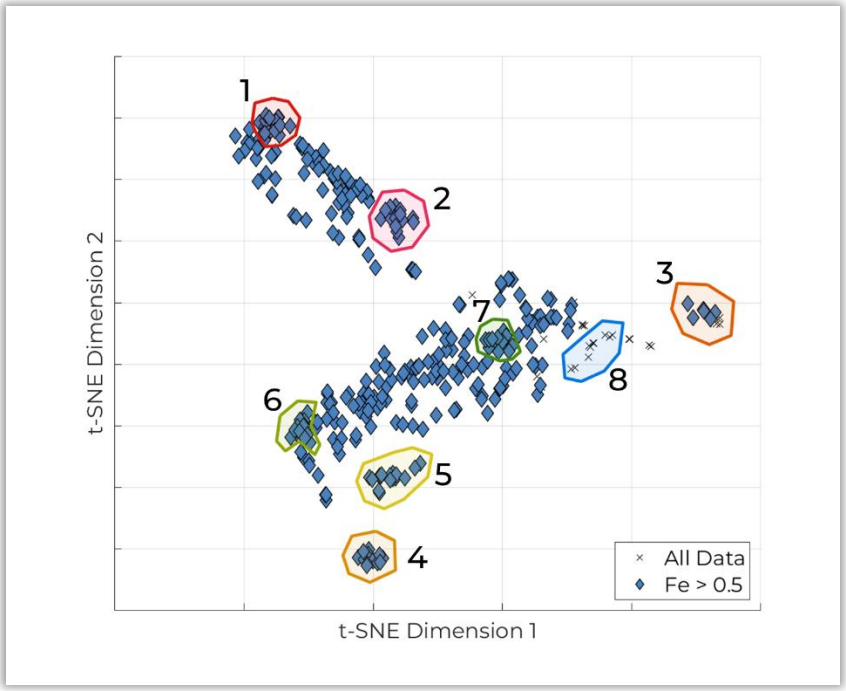

In the t-SNE of the APT point cloud (Figure 39), an apparent structure of sub-clusters is visible. This inner structure appears to be due to the peak shape and the alloying elements, such as Mn, Cr and Ni. This is analysed by comparing the spectra from some Regions of Interest (ROIs) inside of the iron cluster. In above Figure, the Iron cluster form the embedding is shown, and ROIs are highlighted. In below Figure, the spectra around the Fe^{2+} isotopic fingerprints from these 8 ROIs are shown. Whilst the spectra in all ROIs contain an iron fingerprint, all of them also contain combinations of features which are unique to the ROIs and set them apart from spectra in other ROIs

It is noted that the t-SNE coordinates are calculated based on the full spectra and not only the parts around the Fe^{2+} fingerprints. Nevertheless, the region around the Fe^{2+} fingerprint contains most of the largest peaks in APT experiments on typical steels (Fe^{2+}, Cr^{2+}, Mn^{2+}, Ni^{2+}), therefore provides a good clue to understanding the causes of the inner structure in the Fe cluster.

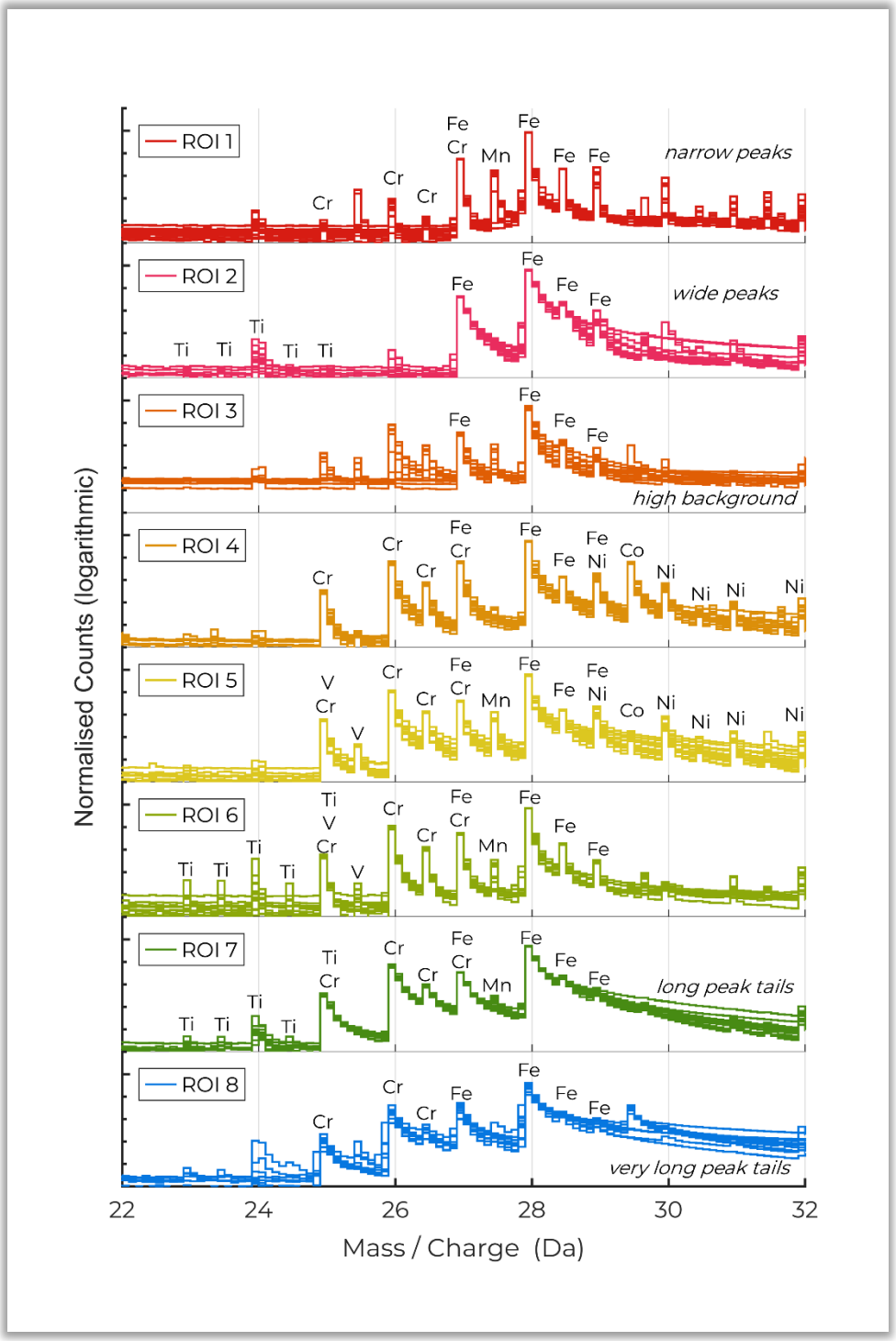
ROI 1
narrow peaks
ROI 2
wide peaks
ROI 3
high background
ROI 4
ROI 5
ROI 6
ROI 7
long peak tails
ROI 8
very long peak tails
Normalised Counts (logarithmic)
22
24
26
28
30
32
Mass / Charge (Da)

Appendix E-4: Field Dependence of Combined H_2^+ and H^+ fraction

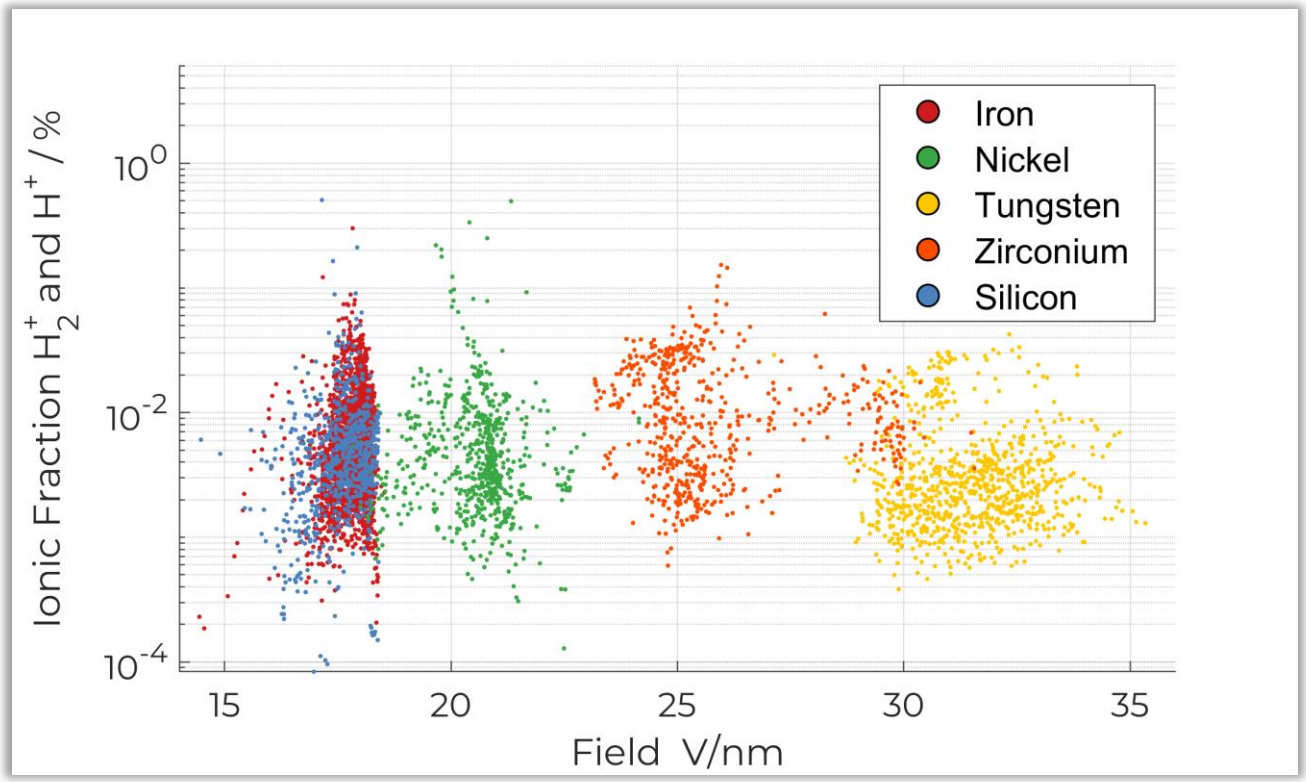

The diagram shows the combined ionic fractions of H_2^+ and H^+ as function of electric field for the datasets in the collection as function of electric field. No clear trend emerges.

8. References

[1] M. L. E. Oliphant, P. Harteck, and E. Rutherford, "Transmutation effects observed with heavy hydrogen," *Proceedings of the Royal Society of London. Series A, Containing Papers of a Mathematical and Physical Character,* vol. 144, no. 853, pp. 692-703, 1934/05/01 1997, doi: 10.1098/rspa.1934.0077.

[2] S. O. Dean, *Search for the ultimate energy source : a history of the U.S. fusion energy program*. 2015.

[3] M. Kikuchi, K. Lackner, and M. Q. Tran, *Fusion Physics*. Vienna: INTERNATIONAL ATOMIC ENERGY AGENCY, 2012.

[4] M. Wang, G. Audi, F. G. Kondev, W. J. Huang, S. Naimi, and X. Xu, "The AME2016 atomic mass evaluation (II). Tables, graphs and references," *Chinese Phys C,* vol. 41, no. 3, p. 030003, Mar 2017, doi: 10.1088/1674-1137/41/3/030003.

[5] G. H. Miley, F. H. Southworth, G. Gerdin, and C. Choi, "Studies of deuterium-fueled Tokamak reactors," *Nuclear Instruments and Methods,* vol. 144, no. 1, pp. 9-16, 1977/07/01 1977, doi: 10.1016/0029-554X(77)90042-8.

[6] R. Aymar, "The ITER reduced cost design," *Fusion Engineering and Design,* vol. 49-50, pp. 13-25, 2000/11/01 2000, doi: 10.1016/S0920-3796(00)00400-2.

[7] F. Romanelli *et al.*, "Fusion Electricity: A roadmap to the realization of fusion energy," 2012.

[8] M. Kikuchi, "A Review of Fusion and Tokamak Research Towards Steady-State Operation: A JAEA Contribution," *Energies,* Review vol. 3, no. 11, pp. 1741-1789, Nov 2010, doi: 10.3390/en3111741.

[9] J. Wesson, "The science of JET," ed, 1999.

[10] G. Federici *et al.*, "Plasma-material interactions in current tokamaks and their implications for next step fusion reactors," *Nuclear Fusion,* vol. 41, no. 12, pp. 1967-2137, Dec 2001, doi: 10.1088/0029-5515/41/12/218.

[11] M. Miyamoto *et al.*, "Systematic investigation of the formation behavior of helium bubbles in tungsten," *Journal of Nuclear Materials,* vol. 463, pp. 333-336, 2015/08/01 2015, doi: 10.1016/j.jnucmat.2014.10.098.

[12] S. I. Krasheninnikov and A. S. Kukushkin, "Physics of ultimate detachment of a tokamak divertor plasma," *Journal of Plasma Physics,* vol. 83, no. 5, p. 155830501, 2017, Art no. 155830501, doi: 10.1017/S0022377817000654.

[13] T. Hirai *et al.*, "Design optimization of the ITER tungsten divertor vertical targets," *Fusion Engineering and Design,* vol. 127, pp. 66-72, Feb 2018, doi: 10.1016/j.fusengdes.2017.12.007.

[14] R. A. Pitts *et al.*, "Physics basis for the first ITER tungsten divertor," *Nuclear Materials and Energy,* vol. 20, p. 100696, Aug 2019, doi: 10.1016/j.nme.2019.100696.

[15] C. Obitz, J. Oijerholm, S. Wikman, and E. Bratu, "Erosion corrosion of CuCrZr specimens exposed for simulated ITER operational conditions," *Nuclear Materials and Energy,* vol. 9, pp. 261-266, Dec 2016, doi: 10.1016/j.nme.2016.05.001.

[16] R. A. Pitts *et al.*, "Physics conclusions in support of ITER W divertor monoblock shaping," *Nuclear Materials and Energy,* vol. 12, pp. 60-74, 2017/08/01 2017, doi: 10.1016/j.nme.2017.03.005.

[17] S. Carli, R. A. Pitts, X. Bonnin, F. Subba, and R. Zanino, "Effect of strike point displacements on the ITER tungsten divertor heat loads," *Nuclear Fusion,* vol. 58, no. 12, p. 126022, Dec 2018, doi: 10.1088/1741-4326/aae43f.

[18] ITER organisation. "Crossection through fusion reactor with separatrix." https://www.iter.org/doc/www/content/com/Lists/Of%20Interest/Attachments/904/pt.3.4363.figures.online.f1.jpg (accessed 21/05/20, 2020).

[19] ITER organisation, "The ITER Tokamak (Poster)," 2016. [Online]. Available: https://www.iter.org/news/publicationcentre/posters.

[20] R. A. Pitts *et al.*, "A full tungsten divertor for ITER: Physics issues and design status," *Journal of Nuclear Materials,* vol. 438, pp. S48-S56, Jul 2013, doi: 10.1016/j.jnucmat.2013.01.008.

[21] J. W. Coenen *et al.*, "Materials for DEMO and reactor applications—boundary conditions and new concepts," *Physica Scripta,* vol. T167, p. 014002, 2015/12/30 2015, doi: 10.1088/0031-8949/2016/t167/014002.

[22] W. M. Haynes, D. R. Lide, and T. J. Bruno, *CRC handbook of chemistry and physics : a ready-reference book of chemical and physical data*, Ninety-fifth ed. (Ebook central). Boca Raton: CRC Press, 2014.

[23] W. G. Guo, L. Cheng, G. De Temmerman, Y. Yuan, and G. H. Lu, "Retarded recrystallization of helium-exposed tungsten," *Nuclear Fusion,* vol. 58, no. 10, p. 106011, Oct 2018, doi: 10.1088/1741-4326/aad2b0.

[24] C. J. M. Denissen, J. Liebe, and M. van Rijswick, "Recrystallisation temperature of tungsten as a function of the heating ramp," *Int J Refract Met H,* vol. 24, no. 4, pp. 321-324, 2006/07/01 2006, doi: 10.1016/j.ijrmhm.2005.10.012.
[25] J. W. Davis, V. R. Barabash, A. Makhankov, L. Plöchl, and K. T. Slattery, "Assessment of tungsten for use in the ITER plasma facing components," *Journal of Nuclear Materials,* vol. 258-263, pp. 308-312, 1998/10/01 1998, doi: 10.1016/s0022-3115(98)00285-2.
[26] X.-X. Zhang, Q.-Z. Yan, C.-T. Yang, T.-N. Wang, M. Xia, and C.-C. Ge, "Recrystallization temperature of tungsten with different deformation degrees," *Rare Metals,* vol. 35, no. 7, pp. 566-570, 2016/07/01 2016, doi: 10.1007/s12598-014-0315-2.
[27] C. H. Skinner *et al.*, "Recent Advances on Hydrogen Retention in ITER's Plasma-Facing Materials: Beryllium, Carbon, and Tungsten," *Fusion Sci Technol,* vol. 54, no. 4, pp. 891-945, 2008/11/01 2008, doi: 10.13182/FST54-891.
[28] M. R. Gilbert and J. C. Sublet, "Neutron-induced transmutation effects in W and W-alloys in a fusion environment," *Nuclear Fusion,* vol. 51, no. 4, p. 043005, 2011/03/23 2011, doi: 10.1088/0029-5515/51/4/043005.
[29] B. S. Li, T. J. Marrow, and D. E. J. Armstrong, "Measuring the brittle-to-ductile transition temperature of tungsten-tantalum alloy using chevron-notched micro-cantilevers," *Scripta Materialia,* vol. 180, pp. 77-82, Apr 2020, doi: 10.1016/j.scriptamat.2020.01.030.
[30] A. Giannattasio and S. G. Roberts, "Strain-rate dependence of the brittle-to-ductile transition temperature in tungsten," *Philos Mag,* vol. 87, no. 16-17, pp. 2589-2598, 2007/06/01 2007, doi: 10.1080/14786430701253197.
[31] B. Lipschultz *et al.*, "Divertor tungsten tile melting and its effect on core plasma performance," *Nuclear Fusion,* vol. 52, no. 12, p. 123002, Dec 2012, doi: 10.1088/0029-5515/52/12/123002.
[32] V. Philipps *et al.*, "Comparison of tokamak behaviour with tungsten and low-Zplasma facing materials," *Plasma Phys Contr F,* vol. 42, no. 12B, pp. B293-B310, 2000/12/01 2000, doi: 10.1088/0741-3335/42/12b/322.
[33] A. Loarte *et al.*, "Progress on the application of ELM control schemes to ITER scenarios from the non-active phase to DT operation," *Nuclear Fusion,* vol. 54, no. 3, p. 033007, 2014/02/20 2014, doi: 10.1088/0029-5515/54/3/033007.
[34] D. N. Hill, "A review of ELMs in divertor tokamaks," *Journal of Nuclear Materials,* vol. 241, pp. 182-198, 1997/02/11 1997, doi: Doi 10.1016/S0022-3115(97)80039-6.
[35] J. Linke *et al.*, "Challenges for plasma-facing components in nuclear fusion," *Matter and Radiation at Extremes,* vol. 4, no. 5, p. 056201, 2019/09/01 2019, doi: 10.1063/1.5090100.
[36] G. Pintsuk, "4.17 - Tungsten as a Plasma-Facing Material," in *Comprehensive Nuclear Materials*, R. J. M. Konings Ed. Oxford: Elsevier, 2012, pp. 551-581.
[37] Z. Zhou, G. Pintsuk, J. Linke, Y. Ma, and M. Rödig, "Performance of the different swaged tungsten grades under transient high heat loads," *Physica Scripta,* vol. T138, p. 014058, Dec 2009, doi: 10.1088/0031-8949/2009/t138/014058.
[38] G. Pintsuk, W. Kuhnlein, J. Linke, and M. Rodig, "Investigation of tungsten and beryllium behaviour under short transient events," *Fusion Engineering and Design,* vol. 82, no. 15-24, pp. 1720-1729, Oct 2007, doi: 10.1016/j.fusengdes.2007.06.030.
[39] Y. Hirooka *et al.*, "Evaluation of Tungsten as a Plasma-Facing Material for Steady-State Magnetic Fusion Devices," *Journal of Nuclear Materials,* vol. 196, pp. 149-158, Dec 1992, doi: Doi 10.1016/S0022-3115(06)80022-X.
[40] T. Hirai, G. Pintsuk, J. Linke, and M. Batilliot, "Cracking failure study of ITER-reference tungsten grade under single pulse thermal shock loads at elevated temperatures," *Journal of Nuclear Materials,* vol. 390-91, pp. 751-754, Jun 15 2009, doi: 10.1016/j.jnucmat.2009.01.313.
[41] M. Wirtz, J. Linke, T. Loewenhoff, G. Pintsuk, and I. Uytdenhouwen, "Transient heat load challenges for plasma-facing materials during long-term operation," *Nuclear Materials and Energy,* vol. 12, pp. 148-155, 2017/08/01 2017, doi: 10.1016/j.nme.2016.12.024.
[42] O. M. Wirtz, "Thermal shock behaviour of different tungsten grades under varying conditions," Aachen, 2012.
[43] G. De Temmerman, T. Hirai, and R. A. Pitts, "The influence of plasma-surface interaction on the performance of tungsten at the performance of tungsten at the ITER divertor vertical targets," *Plasma Phys Contr F,* vol. 60, no. 4, p. 044018, 2018/03/06 2018, doi: 10.1088/1361-6587/aaaf62.

[44] M. Wirtz *et al.*, "Impact of combined hydrogen plasma and transient heat loads on the performance of tungsten as plasma facing material," *Nuclear Fusion,* vol. 55, no. 12, p. 123017, Dec 2015, doi: 10.1088/0029-5515/55/12/123017.
[45] G. De Temmerman *et al.*, "Nanostructuring of molybdenum and tungsten surfaces by low-energy helium ions," *Journal of Vacuum Science & Technology A,* vol. 30, no. 4, p. 041306, 2012/07/01 2012, doi: 10.1116/1.4731196.
[46] B. N. Bazylev, G. Janeschitz, I. S. Landman, and S. E. Pestchanyi, "Erosion of tungsten armor after multiple intense transient events in ITER," *Journal of Nuclear Materials,* vol. 337-339, pp. 766-770, 2005/03/01 2005, doi: 10.1016/j.jnucmat.2004.10.070.
[47] M. J. Norgett, M. T. Robinson, and I. M. Torrens, "A proposed method of calculating displacement dose rates," *Nuclear Engineering and Design,* vol. 33, no. 1, pp. 50-54, 1975/08/01 1975, doi: 10.1016/0029-5493(75)90035-7.
[48] T. Troev, N. Nankov, and T. Yoshiie, "Simulation of displacement cascades in tungsten irradiated by fusion neutrons," *Nucl Instrum Meth B,* vol. 269, no. 6, pp. 566-571, Mar 15 2011, doi: 10.1016/j.nimb.2011.01.010.
[49] X. Yi, M. L. Jenkins, M. A. Kirk, Z. Zhou, and S. G. Roberts, "In-situ TEM studies of 150 keV W+ ion irradiated W and W-alloys: Damage production and microstructural evolution," *Acta Materialia,* vol. 112, pp. 105-120, 2016/06/15 2016, doi: 10.1016/j.actamat.2016.03.051.
[50] A. I. Ryazanov and E. V. Semenov, "Radiation damage formation in fusion structural materials due to elastic and inelastic processes," *Journal of Nuclear Materials,* vol. 417, no. 1-3, pp. 1074-1077, Oct 1 2011, doi: 10.1016/j.jnucmat.2010.12.182.
[51] S. Das, "Recent advances in characterising irradiation damage in tungsten for fusion power," *SN Applied Sciences,* vol. 1, no. 12, p. 1614, 2019/11/15 2019, doi: 10.1007/s42452-019-1591-0.
[52] D. E. J. Armstrong, P. D. Edmondson, and S. G. Roberts, "Effects of sequential tungsten and helium ion implantation on nano-indentation hardness of tungsten," *Applied Physics Letters,* vol. 102, no. 25, p. 251901, 2013/06/24 2013, doi: 10.1063/1.4811825.
[53] D. E. J. Armstrong, X. Yi, E. A. Marquis, and S. G. Roberts, "Hardening of self ion implanted tungsten and tungsten 5-wt% rhenium," *Journal of Nuclear Materials,* vol. 432, no. 1, pp. 428-436, 2013/01/01 2013, doi: 10.1016/j.jnucmat.2012.07.044.
[54] D. E. J. Armstrong, A. J. Wilkinson, and S. G. Roberts, "Mechanical properties of ion-implanted tungsten–5 wt% tantalum," *Physica Scripta,* vol. T145, p. 014076, 2011/12/01 2011, doi: 10.1088/0031-8949/2011/t145/014076.
[55] J. Gibson, D. Armstrong, and S. Roberts, "The micro-mechanical properties of ion irradiated tungsten," *Physica Scripta,* vol. T159, p. 014056, Apr 2014, doi: 10.1088/0031-8949/2014/T159/014056.
[56] P. Vladimirov and S. Bouffard, "Displacement damage and transmutations in metals under neutron and proton irradiation," *Cr Phys,* vol. 9, no. 3-4, pp. 303-322, Apr-May 2008, doi: 10.1016/j.crhy.2008.02.004.
[57] L. R. Greenwood, "Neutron interactions and atomic recoil spectra," United States, 1993. [Online]. Available: https://www.osti.gov/biblio/10111988
[58] L. R. Greenwood and F. A. Garner, "Transmutation of Mo, Re, W, Hf, and V in Various Irradiation Test Facilities and Starfire," *Journal of Nuclear Materials,* vol. 212, pp. 635-639, Sep 1994, doi: Doi 10.1016/0022-3115(94)90136-8.
[59] M. R. Gilbert, J. C. Sublet, and S. L. Dudarev, "Spatial heterogeneity of tungsten transmutation in a fusion device," *Nuclear Fusion,* vol. 57, no. 4, p. 044002, 2017/03/02 2017, doi: 10.1088/1741-4326/aa5e2e.
[60] L. L. Lucas and M. P. Unterweger, "Comprehensive Review and Critical Evaluation of the Half-Life of Tritium," *Journal of research of the National Institute of Standards and Technology,* vol. 105, no. 4, pp. 541-549, 2000, doi: 10.6028/jres.105.043.
[61] D. Murdoch *et al.*, "ITER Design Review: Tritium Issues," *Fusion Sci Technol,* vol. 54, no. 1, pp. 3-8, 2008/07/01 2008, doi: 10.13182/FST08-A1753.
[62] *Décret no 2012-1248 du 9 novembre 2012 autorisant l'Organisation internationale ITER à créer une installation nucléaire de base dénommée «ITER» sur la commune de Saint-Paul-lez-Durance (Bouches-du-Rhône),* Ministère de l'écologie, du développement durable et de l'énergie, DEVP1237370D, 2012.
[63] G. De Temmerman *et al.*, "Efficiency of thermal outgassing for tritium retention measurement and removal in ITER," *Nuclear Materials and Energy,* vol. 12, pp. 267-272, 2017/08/01 2017, doi: 10.1016/j.nme.2016.10.016.

[64] L. M. Giancarli *et al.*, "Overview of the ITER TBM Program," *Fusion Engineering and Design,* vol. 87, no. 5-6, pp. 395-402, Aug 2012, doi: 10.1016/j.fusengdes.2011.11.005.
[65] J. Roth *et al.*, "Tritium inventory in ITER plasma-facing materials and tritium removal procedures," *Plasma Phys Contr F,* vol. 50, no. 10, p. 103001, Oct 2008, doi: 10.1088/0741-3335/50/10/103001.
[66] R. Frauenfelder, "Solution and Diffusion of Hydrogen in Tungsten," *Journal of Vacuum Science and Technology,* vol. 6, no. 3, pp. 388-397, 1969/05/01 1969, doi: 10.1116/1.1492699.
[67] Y.-L. Liu, H.-B. Zhou, and Y. Zhang, "Investigating behaviors of H in a W single crystal by first-principles: From solubility to interaction with vacancy," *Journal of Alloys and Compounds,* vol. 509, no. 33, pp. 8277-8282, 2011/08/18 2011, doi: 10.1016/j.jallcom.2011.03.117.
[68] C. S. Becquart and C. Domain, "A density functional theory assessment of the clustering behaviour of He and H in tungsten," *Journal of Nuclear Materials,* vol. 386-388, pp. 109-111, 2009/04/30 2009, doi: 10.1016/j.jnucmat.2008.12.085.
[69] A. Bakaev, P. Grigorev, D. Terentyev, A. Bakaeva, E. E. Zhurkin, and Y. A. Mastrikov, "Trapping of hydrogen and helium at dislocations in tungsten: anab initiostudy," *Nuclear Fusion,* vol. 57, no. 12, p. 126040, 2017/10/03 2017, doi: 10.1088/1741-4326/aa7965.
[70] D. F. Johnson and E. A. Carter, "Hydrogen in tungsten: Absorption, diffusion, vacancy trapping, and decohesion," *Journal of Materials Research,* vol. 25, no. 2, pp. 315-327, 2010, doi: 10.1557/JMR.2010.0036.
[71] O. V. Ogorodnikova, "Fundamental aspects of deuterium retention in tungsten at high flux plasma exposure," *Journal of Applied Physics,* vol. 118, no. 7, p. 074902, 2015/08/21 2015, doi: 10.1063/1.4928407.
[72] K. Heinola, T. Ahlgren, K. Nordlund, and J. Keinonen, "Hydrogen interaction with point defects in tungsten," *Physical Review B,* vol. 82, no. 9, p. 094102, Oct 2010, doi: 10.1103/PhysRevB.82.094102.
[73] D. Kato, H. Iwakiri, and K. Morishita, "Formation of vacancy clusters in tungsten crystals under hydrogen-rich condition," *Journal of Nuclear Materials,* vol. 417, no. 1, pp. 1115-1118, 2011/10/01 2011, doi: 10.1016/j.jnucmat.2010.12.211.
[74] E. A. Hodille *et al.*, "Simulations of atomic deuterium exposure in self-damaged tungsten," *Nuclear Fusion,* vol. 57, no. 5, p. 056002, 2017/03/14 2017, doi: 10.1088/1741-4326/aa5aa5.
[75] D. Terentyev, V. Dubinko, A. Bakaev, Y. Zayachuk, W. Van Renterghem, and P. Grigorev, "Dislocations mediate hydrogen retention in tungsten," *Nuclear Fusion,* vol. 54, no. 4, p. 042004, 2014/03/21 2014, doi: 10.1088/0029-5515/54/4/042004.
[76] H.-B. Zhou, Y.-L. Liu, S. Jin, Y. Zhang, G. N. Luo, and G.-H. Lu, "Investigating behaviours of hydrogen in a tungsten grain boundary by first principles: from dissolution and diffusion to a trapping mechanism," *Nuclear Fusion,* vol. 50, no. 2, p. 025016, 2010/01/15 2010, doi: 10.1088/0029-5515/50/2/025016.
[77] R. A. Anderl, D. F. Holland, G. R. Longhurst, R. J. Pawelko, C. L. Trybus, and C. H. Sellers, "Deuterium Transport and Trapping in Polycrystalline Tungsten," *Fusion Technology,* vol. 21, no. 2P2, pp. 745-752, 1992/03/01 1992, doi: 10.13182/FST92-A29837.
[78] D. G. Whyte, "On the consequences of neutron induced damage for volumetric fuel retention in plasma facing materials," *Journal of Nuclear Materials,* vol. 390-91, pp. 911-915, Jun 15 2009, doi: 10.1016/j.jnucmat.2009.01.234.
[79] Y. Hatano *et al.*, "Deuterium trapping at defects created with neutron and ion irradiations in tungsten," *Nuclear Fusion,* vol. 53, no. 7, p. 073006, 2013/05/24 2013, doi: 10.1088/0029-5515/53/7/073006.
[80] Y. Hatano *et al.*, "Trapping of hydrogen isotopes in radiation defects formed in tungsten by neutron and ion irradiations," *Journal of Nuclear Materials,* vol. 438, pp. S114-S119, 2013/07/01 2013, doi: 10.1016/j.jnucmat.2013.01.018.
[81] M. Shimada *et al.*, "Irradiation effect on deuterium behaviour in low-dose HFIR neutron-irradiated tungsten," *Nuclear Fusion,* vol. 55, no. 1, p. 013008, 2014/12/01 2015, doi: 10.1088/0029-5515/55/1/013008.
[82] D. Terentyev *et al.*, "Development of irradiation tolerant tungsten alloys for high temperature nuclear applications," *Nuclear Fusion,* vol. 62, no. 8, p. 086035, 2022/06/27 2022, doi: 10.1088/1741-4326/ac75fe.
[83] A. V. Golubeva and D. I. Cherkez, "Hydrogen Retention in Tungsten Alloys Developed for Fusion Facilities (Review)," *Physics of Atomic Nuclei,* vol. 82, no. 7, pp. 996-1004, 2019/12/01 2019, doi: 10.1134/S1063778819070068.

[84] F. Ren, W. Yin, Q. Yu, X. Jia, Z. Zhao, and B. Wang, "Solution and diffusion of hydrogen isotopes in tungsten-rhenium alloy," *Journal of Nuclear Materials,* vol. 491, pp. 206-212, 2017/08/01 2017, doi: 10.1016/j.jnucmat.2017.04.057.

[85] A. V. Golubeva, M. Mayer, J. Roth, V. A. Kurnaev, and O. V. Ogorodnikova, "Deuterium retention in rhenium-doped tungsten," *Journal of Nuclear Materials,* vol. 363, pp. 893-897, Jun 15 2007, doi: 10.1016/j.jnucmat.2007.01.110.

[86] V. K. Alimov *et al.*, "Surface morphology and deuterium retention in tungsten and tungsten–rhenium alloy exposed to low-energy, high flux D plasma," *Journal of Nuclear Materials,* vol. 454, no. 1, pp. 136-141, 2014/11/01 2014, doi: 10.1016/j.jnucmat.2014.07.064.

[87] Y. Hatano *et al.*, "Deuterium retention in W and W-Re alloy irradiated with high energy Fe and W ions: Effects of irradiation temperature," *Nuclear Materials and Energy,* vol. 9, pp. 93-97, 2016/12/01 2016, doi: 10.1016/j.nme.2016.06.016.

[88] F. F. Ma, W. W. Wang, Y. H. Li, H. B. Zhou, and G. H. Lu, "Towards understanding the influence of Re on H dissolution and retention in W by investigating the interaction between dispersed/aggregated-Re and H," *Nuclear Fusion,* vol. 58, no. 9, p. 096026, Sep 2018, doi: 10.1088/1741-4326/aacf48.

[89] M. Ekman, K. Persson, and G. Grimvall, "Phase diagram and lattice instability in tungsten-rhenium alloys," *Journal of Nuclear Materials,* vol. 278, no. 2-3, pp. 273-276, Apr 2000, doi: Doi 10.1016/S0022-3115(99)00241-X.

[90] F.-Y. Yue, Y.-H. Li, H.-B. Zhou, Y. Zhang, and G.-H. Lu, "Insight into the enhancement effect of rhenium-rich precipitation on hydrogen retention in tungsten by investigating the behaviors of hydrogen in tungsten-rhenium sigma phase," *International Journal of Hydrogen Energy,* vol. 44, no. 45, pp. 24880-24894, 2019/09/20 2019, doi: 10.1016/j.ijhydene.2019.07.221.

[91] K. Tokunaga, M. Takayama, T. Muroga, and N. Yoshida, "Depth profile analyses of implanted deuterium in tungsten by secondary ion mass spectrometry," *Journal of Nuclear Materials,* vol. 220-222, pp. 800-804, 1995/04/01 1995, doi: 10.1016/0022-3115(94)00588-5.

[92] C. Linsmeier *et al.*, "Material testing facilities and programs for plasma-facing component testing," *Nuclear Fusion,* vol. 57, no. 9, p. 092012, Sep 2017, doi: 10.1088/1741-4326/aa4feb.

[93] V. K. Alimov and J. Roth, "Hydrogen isotope retention in plasma-facing materials: review of recent experimental results," *Physica Scripta,* vol. T128, pp. 6-13, Mar 2007, doi: 10.1088/0031-8949/2007/t128/002.

[94] S. Lindig *et al.*, "Sub-surface structures of ITER-grade W (Japan) and re-crystallized W after ITER-similar low-energy and high-flux D plasma loadings," *Physica Scripta,* vol. T145, p. 014039, 2011/12/01 2011, doi: 10.1088/0031-8949/2011/t145/014039.

[95] R. A. Causey and T. J. Venhaus, "The Use of Tungsten in Fusion Reactors: A Review of the Hydrogen Retention and Migration Properties," *Physica Scripta,* vol. T94, no. 1, p. 9, 2001, doi: 10.1238/physica.topical.094a00009.

[96] A. A. Haasz, J. W. Davis, M. Poon, and R. G. Macaulay-Newcombe, "Deuterium retention in tungsten for fusion use," *Journal of Nuclear Materials,* vol. 258, pp. 889-895, Oct 1998, doi: Doi 10.1016/S0022-3115(98)00072-5.

[97] R. Causey, K. Wilson, T. Venhaus, and W. R. Wampler, "Tritium retention in tungsten exposed to intense fluxes of 100 eV tritons," *Journal of Nuclear Materials,* vol. 266, pp. 467-471, Mar 1999, doi: Doi 10.1016/S0022-3115(98)00538-8.

[98] J. Roth and K. Schmid, "Hydrogen in tungsten as plasma-facing material," *Physica Scripta,* vol. T145, p. 014031, 2011/12/01 2011, doi: 10.1088/0031-8949/2011/t145/014031.

[99] H. Y. Xu *et al.*, "Enhanced modification of tungsten surface by nanostructure formation during high flux deuterium plasma exposure," *Journal of Nuclear Materials,* vol. 447, no. 1-3, pp. 22-27, Apr 2014, doi: 10.1016/j.jnucmat.2013.12.010.

[100] Y. Z. Jia *et al.*, "Surface morphology and deuterium retention in tungsten exposed to high flux D plasma at high temperatures," *Journal of Nuclear Materials,* vol. 457, pp. 213-219, Feb 2015, doi: 10.1016/j.jnucmat.2014.11.079.

[101] Y. Z. Jia, W. Liu, B. Xu, S. L. Qu, L. Q. Shi, and T. W. Morgan, "Subsurface deuterium bubble formation in W due to low-energy high flux deuterium plasma exposure," *Nuclear Fusion,* vol. 57, no. 3, p. 034003, 2016/12/22 2017, doi: 10.1088/1741-4326/57/3/034003.

[102] L. Buzi *et al.*, "Influence of tungsten microstructure and ion flux on deuterium plasma-induced surface modifications and deuterium retention," *Journal of Nuclear Materials,* vol. 463, pp. 320-324, Aug 2015, doi: 10.1016/j.jnucmat.2014.12.006.

[103] A. Manhard, M. Balden, and U. von Toussaint, "Blister formation on rough and technical tungsten surfaces exposed to deuterium plasma," *Nuclear Fusion,* vol. 57, no. 12, p. 126012, Dec 2017, doi: 10.1088/1741-4326/aa82c8.
[104] Y. Zayachuk, I. Tanyeli, S. Van Boxel, K. Bystrov, T. W. Morgan, and S. G. Roberts, "Combined effects of crystallography, heat treatment and surface polishing on blistering in tungsten exposed to high-flux deuterium plasma," *Nuclear Fusion,* vol. 56, no. 8, p. 086007, 2016/07/14 2016, doi: 10.1088/0029-5515/56/8/086007.
[105] X. Fang *et al.*, "Hydrogen embrittlement of tungsten induced by deuterium plasma: Insights from nanoindentation tests," *Journal of Materials Research,* vol. 33, no. 20, pp. 3530-3536, 2018, doi: 10.1557/jmr.2018.305.
[106] D. Terentyev, A. Bakaeva, T. Pardoen, A. Favache, and E. E. Zhurkin, "Surface hardening induced by high flux plasma in tungsten revealed by nano-indentation," *Journal of Nuclear Materials,* vol. 476, pp. 1-4, Aug 1 2016, doi: 10.1016/j.jnucmat.2016.04.007.
[107] Y. Zayachuk, D. E. J. Armstrong, K. Bystrov, S. Van Boxel, T. Morgan, and S. G. Roberts, "Nanoindentation study of the combined effects of crystallography, heat treatment and exposure to high-flux deuterium plasma in tungsten," *Journal of Nuclear Materials,* vol. 486, pp. 183-190, 2017/04/01 2017, doi: 10.1016/j.jnucmat.2017.01.026.
[108] O. Barrera *et al.*, "Understanding and mitigating hydrogen embrittlement of steels: a review of experimental, modelling and design progress from atomistic to continuum," *Journal of Materials Science,* Review vol. 53, no. 9, pp. 6251-6290, May 2018, doi: 10.1007/s10853-017-1978-5.
[109] C. S. Becquart and C. Domain, "Ab initio calculations about intrinsic point defects and He in W," *Nucl Instrum Meth B,* vol. 255, no. 1, pp. 23-26, Feb 2007, doi: 10.1016/j.nimb.2006.11.006.
[110] X. L. Shu, P. Tao, X. C. Li, and Y. Yu, "Helium diffusion in tungsten: A molecular dynamics study," *Nucl Instrum Meth B,* vol. 303, pp. 84-86, May 15 2013, doi: 10.1016/j.nimb.2012.10.028.
[111] M. J. Baldwin and R. P. Doerner, "Helium induced nanoscopic morphology on tungsten under fusion relevant plasma conditions," *Nuclear Fusion,* vol. 48, no. 3, p. 035001, Mar 2008, doi: 10.1088/0029-5515/48/3/035001.
[112] J. Amano and D. N. Seidman, "Diffusivity of 3He atoms in perfect tungsten crystals," *Journal of Applied Physics,* vol. 56, no. 4, pp. 983-992, 1984/08/15 1984, doi: 10.1063/1.334039.
[113] H. B. Zhou, Y. L. Liu, Y. Zhang, S. Jin, and G. H. Lu, "First-principles investigation of energetics and site preference of He in a W grain boundary," *Nucl Instrum Meth B,* vol. 267, no. 18, pp. 3189-3192, Sep 15 2009, doi: 10.1016/j.nimb.2009.06.067.
[114] X. C. Li, Y. N. Liu, Y. Yu, G. N. Luo, X. L. Shu, and G. H. Lu, "Helium defects interactions and mechanism of helium bubble growth in tungsten: A molecular dynamics simulation," *Journal of Nuclear Materials,* vol. 451, no. 1-3, pp. 356-360, Aug 2014, doi: 10.1016/j.jnucmat.2014.04.022.
[115] D. Perez, T. Vogel, and B. P. Uberuaga, "Diffusion and transformation kinetics of small helium clusters in bulk tungsten," *Physical Review B,* vol. 90, no. 1, p. 014102, Jul 11 2014, doi: 10.1103/PhysRevB.90.014102.
[116] E. V. Kornelsen and A. A. Vangorkum, "A Study of Bubble Nucleation in Tungsten Using Thermal-Desorption Spectrometry - Clusters of 2 to 100 Helium-Atoms," *Journal of Nuclear Materials,* vol. 92, no. 1, pp. 79-88, 1980/08/01 1980, doi: Doi 10.1016/0022-3115(80)90144-0.
[117] D. Nishijima, M. Y. Ye, N. Ohno, and S. Takamura, "Formation mechanism of bubbles and holes on tungsten surface with low-energy and high-flux helium plasma irradiation in NAGDIS-II," *Journal of Nuclear Materials,* vol. 329-333, pp. 1029-1033, 2004/08/01 2004, doi: 10.1016/j.jnucmat.2004.04.129.
[118] M. Thompson *et al.*, "Observation of a helium ion energy threshold for retention in tungsten exposed to hydrogen/helium mixture plasma," *Nuclear Fusion,* vol. 56, no. 10, p. 104002, Oct 2016, doi: 10.1088/0029-5515/56/10/104002.
[119] S. I. Krasheninnikov, "Viscoelastic model of tungsten 'fuzz' growth," *Physica Scripta,* vol. T145, p. 014040, Dec 2011, doi: 10.1088/0031-8949/2011/T145/014040.
[120] T. J. Petty, M. J. Baldwin, M. I. Hasan, R. P. Doerner, and J. W. Bradley, "Tungsten 'fuzz' growth re-examined: the dependence on ion fluence in non-erosive and erosive helium plasma," *Nuclear Fusion,* vol. 55, no. 9, p. 093033, Sep 2015, doi: 10.1088/0029-5515/55/9/093033.
[121] G. M. Wright *et al.*, "Tungsten nano-tendril growth in the Alcator C-Mod divertor," *Nuclear Fusion,* vol. 52, no. 4, p. 042003, 2012/03/29 2012, doi: 10.1088/0029-5515/52/4/042003.

[122] S. Kajita, W. Sakaguchi, N. Ohno, N. Yoshida, and T. Saeki, "Formation process of tungsten nanostructure by the exposure to helium plasma under fusion relevant plasma conditions," *Nuclear Fusion,* vol. 49, no. 9, p. 095005, Sep 2009, doi: 10.1088/0029-5515/49/9/095005.
[123] S. Takamura, N. Ohno, D. Nishijima, and S. Kajita, "Formation of Nanostructured Tungsten with Arborescent Shape due to Helium Plasma Irradiation," *Plasma and Fusion Research,* vol. 1, pp. 051-051, 2006, doi: 10.1585/pfr.1.051.
[124] Y. Noiri, S. Kajita, and N. Ohno, "Nanostructure growth by helium plasma irradiation to tungsten in sputtering regime," *Journal of Nuclear Materials,* vol. 463, pp. 285-288, Aug 2015, doi: 10.1016/j.jnucmat.2015.01.036.
[125] M. J. Baldwin, R. P. Doerner, D. Nishijima, K. Tokunaga, and Y. Ueda, "The effects of high fluence mixed-species (deuterium, helium, beryllium) plasma interactions with tungsten," *Journal of Nuclear Materials,* vol. 390-391, pp. 886-890, 2009/06/15 2009, doi: 10.1016/j.jnucmat.2009.01.247.
[126] M. Miyamoto *et al.*, "Observations of suppressed retention and blistering for tungsten exposed to deuterium–helium mixture plasmas," *Nuclear Fusion,* vol. 49, no. 6, p. 065035, 2009/05/26 2009, doi: 10.1088/0029-5515/49/6/065035.
[127] M. J. Baldwin, R. P. Doerner, W. R. Wampler, D. Nishijima, T. Lynch, and M. Miyamoto, "Effect of He on D retention in W exposed to low-energy, high-fluence (D, He, Ar) mixture plasmas," *Nuclear Fusion,* vol. 51, no. 10, p. 103021, 2011/08/31 2011, doi: 10.1088/0029-5515/51/10/103021.
[128] M. A. Cusentino, "Discovering Key Unknowns for Tungsten-Hydrogen-Helium Plasma Material Interactions Using Molecular Dynamics," 2018.
[129] C. S. Corr *et al.*, "Mechanical properties of tungsten following rhenium ion and helium plasma exposure," *Nuclear Materials and Energy,* vol. 12, pp. 1336-1341, Aug 2017, doi: 10.1016/j.nme.2017.04.012.
[130] E. Bernard, R. Sakamoto, N. Yoshida, and H. Yamada, "Temperature impact on W surface exposed to He plasma in LHD and its consequences for the material properties," *Journal of Nuclear Materials,* vol. 463, pp. 316-319, Aug 2015, doi: 10.1016/j.jnucmat.2014.11.041.
[131] Z. X. Zhang, E. Hasenhuetl, K. Yabuuchi, and A. Kimura, "Evaluation of helium effect on ion-irradiation hardening in pure tungsten by nano-indentation method," *Nuclear Materials and Energy,* vol. 9, pp. 539-546, Dec 2016, doi: 10.1016/j.nme.2016.06.010.
[132] S. Cui *et al.*, "Thermal conductivity reduction of tungsten plasma facing material due to helium plasma irradiation in PISCES using the improved 3-omega method," *Journal of Nuclear Materials,* vol. 486, pp. 267-273, Apr 2017, doi: 10.1016/j.jnucmat.2017.01.023.
[133] S. Kajita, G. De Temmerman, T. Morgan, S. van Eden, T. de Kruif, and N. Ohno, "Thermal response of nanostructured tungsten," *Nuclear Fusion,* vol. 54, no. 3, p. 033005, Mar 2014, doi: 10.1088/0029-5515/54/3/033005.
[134] L. Buzi *et al.*, "Response of tungsten surfaces to helium and hydrogen plasma exposure under ITER relevant steady state and repetitive transient conditions," *Nuclear Fusion,* vol. 57, no. 12, p. 126009, Dec 2017, doi: 10.1088/1741-4326/aa81e4.
[135] S. Markelj *et al.*, "Deuterium retention in tungsten simultaneously damaged by high energy W ions and loaded by D atoms," *Nuclear Materials and Energy,* vol. 12, pp. 169-174, Aug 2017, doi: 10.1016/j.nme.2016.11.010.
[136] B. Gault, M. P. Moody, J. M. Cairney, and S. P. Ringer, *Atom probe microscopy*. Springer Science & Business Media, 2012.
[137] T. F. Kelly and M. K. Miller, "Atom probe tomography," *Review of Scientific Instruments,* vol. 78, no. 3, p. 031101, 2007/03/01 2007, doi: 10.1063/1.2709758.
[138] G. L. Kellogg, "Pulsed laser stimulated field desorption of hydrogen from molybdenum," *The Journal of Chemical Physics,* vol. 74, no. 2, pp. 1479-1487, 1981/01/15 1981, doi: 10.1063/1.441162.
[139] I. Mouton *et al.*, "Quantification Challenges for Atom Probe Tomography of Hydrogen and Deuterium in Zircaloy-4," *Microscopy and Microanalysis,* vol. 25, no. 2, pp. 481-488, 2019, doi: 10.1017/S143192761801615X.
[140] Y.-S. Chen *et al.*, "Atom Probe Tomography for the Observation of Hydrogen in Materials: A Review," *Microscopy and Microanalysis,* p. ozac005, 2022, doi: 10.1093/micmic/ozac005.
[141] M. S. Meier, M. E. Jones, P. J. Felfer, M. P. Moody, and D. Haley, "Extending Estimating Hydrogen Content in Atom Probe Tomography Experiments Where H2 Molecule Formation Occurs," *Microscopy and Microanalysis,* pp. 1-14, 2021, doi: 10.1017/S1431927621012332.

[142] G. Sundell, M. Thuvander, and H. O. Andren, "Hydrogen analysis in APT: Methods to control adsorption and dissociation of H-2," *Ultramicroscopy,* Article; Proceedings Paper vol. 132, pp. 285-289, Sep 2013, doi: 10.1016/j.ultramic.2013.01.007.
[143] R. P. Kolli, "Controlling residual hydrogen gas in mass spectra during pulsed laser atom probe tomography," *Advanced Structural and Chemical Imaging,* vol. 3, no. 1, p. 10, 2017/02/22 2017, doi: 10.1186/s40679-017-0043-4.
[144] S. H. Yoo, S. H. Kim, E. Woods, B. Gault, M. Todorova, and J. Neugebauer, "Origins of the hydrogen signal in atom probe tomography: case studies of alkali and noble metals," *New Journal of Physics,* vol. 24, no. 1, p. 013008, Jan 1 2022, doi: 10.1088/1367-2630/ac40cd.
[145] L. Rousseau, J.-B. Maillet, L. Stephenson, B. Gervais, B. Gault, and F. Vurpillot, "Mysterious Field Evaporation Behavior of Hydrogen in Aluminium Based Material Analyzed with Atom Probe Tomography," *Microscopy and Microanalysis,* vol. 28, no. S1, pp. 690-691, 2022, doi: 10.1017/S1431927622003233.
[146] L. Rigutti *et al.*, "Surface Microscopy of Atomic and Molecular Hydrogen from Field-Evaporating Semiconductors," *The Journal of Physical Chemistry C,* vol. 125, no. 31, pp. 17078-17087, 2021/08/12 2021, doi: 10.1021/acs.jpcc.1c04778.
[147] Y. H. Chang *et al.*, "Characterizing solute hydrogen and hydrides in pure and alloyed titanium at the atomic scale," *Acta Materialia,* Article vol. 150, pp. 273-280, May 2018, doi: 10.1016/j.actamat.2018.02.064.
[148] D. Haley, A. J. London, and M. P. Moody, "Processing APT Spectral Backgrounds for Improved Quantification," *Microscopy and Microanalysis,* vol. 26, no. 5, pp. 964-977, 2020, doi: 10.1017/S1431927620024290.
[149] K. J. Coakley and N. A. Sanford, "Learning Atom Probe Tomography time-of-flight peaks for mass-to-charge ratio spectrometry," *Ultramicroscopy,* vol. 237, p. 113521, 2022/07/01 2022, doi: 10.1016/j.ultramic.2022.113521.
[150] A. J. London, D. Haley, and M. P. Moody, "Single-Ion Deconvolution of Mass Peak Overlaps for Atom Probe Microscopy," *Microscopy and Microanalysis,* Article vol. 23, no. 2, pp. 300-306, Apr 2017, doi: 10.1017/s1431927616012782.
[151] A. A. Pisarev, "1 - Hydrogen adsorption on the surface of metals," in *Gaseous Hydrogen Embrittlement of Materials in Energy Technologies*, vol. 1, R. P. Gangloff and B. P. Somerday Eds.: Woodhead Publishing, 2012, pp. 3-26.
[152] K. Christmann, "Some general aspects of hydrogen chemisorption on metal surfaces," *Progress in Surface Science,* vol. 48, no. 1, pp. 15-26, 1995/01/01 1995, doi: 10.1016/0079-6816(95)93412-Z.
[153] S. Liu, J. Liu, X. Liu, J.-X. Shang, R. Yu, and J. Shui, "Non-classical hydrogen storage mechanisms other than chemisorption and physisorption," *Applied Physics Reviews,* vol. 9, no. 2, p. 021315, 2022/06/01 2022, doi: 10.1063/5.0088529.
[154] Y. H. Kim, Y. Zhao, A. J. Williamson, M. J. Heben, and S. B. Zhang, "Nondissociative adsorption of H2 molecules in light-element-doped fullerenes," *Physical review letters,* vol. 96 1, p. 016102, 2006.
[155] S. Burkart, N. Blessing, and G. Ganteför, "Indication of a size-dependent transition from molecular to dissociative chemisorption on clusters," *Physical Review B,* vol. 60, no. 23, pp. 15639-15642, Dec 1999, doi: 10.1103/PhysRevB.60.15639.
[156] P. Ferrin, S. Kandoi, A. U. Nilekar, and M. Mavrikakis, "Hydrogen adsorption, absorption and diffusion on and in transition metal surfaces: A DFT study," *Surface Science,* vol. 606, no. 7, pp. 679-689, 2012/04/01 2012, doi: 10.1016/j.susc.2011.12.017.
[157] J. Greeley and M. Mavrikakis, "Surface and Subsurface Hydrogen: Adsorption Properties on Transition Metals and Near-Surface Alloys," *The Journal of Physical Chemistry B,* vol. 109, no. 8, pp. 3460-3471, 2005/03/01 2005, doi: 10.1021/jp046540q.
[158] R. Kirchheim and A. Pundt, "25 - Hydrogen in Metals," in *Physical Metallurgy (Fifth Edition)*, D. E. Laughlin and K. Hono Eds. Oxford: Elsevier, 2014, pp. 2597-2705.
[159] T. T. Tsong and E. W. Müller, "Field Adsorption of Inert-Gas Atoms on Field Ion Emitter Surfaces," *Physical Review Letters,* vol. 25, no. 14, pp. 911-913, May 5 1970, doi: 10.1103/PhysRevLett.25.911.
[160] R. G. Forbes, "On charged-surface models and the origin of field adsorption," *Surface Science,* vol. 223, no. 1, pp. 326-352, 1989/12/01 1989, doi: 10.1016/0039-6028(89)90741-3.
[161] R. G. Forbes, "Further comments on field adsorption," *Surface Science,* vol. 246, no. 1, pp. 386-389, 1991/04/03 1991, doi: 10.1016/0039-6028(91)90441-T.

[162] R. L. C. Wang, H. J. Kreuzer, and R. G. Forbes, "Field adsorption of helium and neon on metals: an integrated theory," *Surface Science,* vol. 350, no. 1, pp. 183-205, 1996/04/20 1996, doi: 10.1016/0039-6028(96)80062-8.
[163] W. Drachsel and J. H. Block, "Isotopic effects in field desorption of hydrogen from tungsten," *Surface Science,* vol. 246, no. 1, pp. 141-149, 1991/04/03 1991, doi: 10.1016/0039-6028(91)90405-H.
[164] G. L. Kellogg and T. T. Tsong, "Pulsed-Laser Atom-Probe Field-Ion Microscopy," *Journal of Applied Physics,* Article vol. 51, no. 2, pp. 1184-1193, 1980, doi: 10.1063/1.327686.
[165] C. F. Ai and T. T. Tsong, "A study of the temperature dependence of a surface catalyzed and field enhanced formation of H3 and NH3 on metal surfaces," *The Journal of Chemical Physics,* vol. 81, no. 6, pp. 2845-2854, 1984/09/15 1984, doi: 10.1063/1.447958.
[166] T. T. Tsong, T. J. Kinkus, and S. B. McLane, "Pulsed-laser stimulated field desorption of gas molecules and field evaporation of metal atoms," *The Journal of Chemical Physics,* vol. 78, no. 12, pp. 7497-7498, 1983/06/15 1983, doi: 10.1063/1.444707.
[167] T. T. Tsong and T. J. Kinkus, "Energy distributions of pulsed-laser field-desorbed gaseous ions and field-evaporated metal ions: A direct time-of-flight measurement," *Physical Review B,* vol. 29, no. 2, pp. 529-542, Jan 15 1984, doi: 10.1103/PhysRevB.29.529.
[168] M. Hellsing and B. Hellsing, "Field adsorption and desorption of hydrogen on W(110) — an atom-probe study," *Surface Science,* vol. 176, no. 1, pp. 249-260, 1986/10/02 1986, doi: 10.1016/0039-6028(86)90174-3.
[169] T. T. Tsong, T. J. Kinkus, and C. F. Ai, "Field induced and surface catalyzed formation of novel ions : A pulsed-laser time-of-flight atom-probe study," *The Journal of Chemical Physics,* vol. 78, no. 7, pp. 4763-4775, 1983/04/01 1983, doi: 10.1063/1.445276.
[170] S. Chen, R. Murakami, K. Araki, and M. Owari, "Quantitative Analysis of Residual Hydrogen on Platinum Surface by Atom Probe," *e-Journal of Surface Science and Nanotechnology,* vol. 18, pp. 127-132, 2020, doi: 10.1380/ejssnt.2020.127.
[171] M. E. Jones *et al.*, "Improving the Quantification of Deuterium in Zirconium Alloy Atom Probe Tomography Data Using Existing Analysis Methods," *Microscopy and Microanalysis,* pp. 1-10, 2021, doi: 10.1017/S1431927621012848.
[172] D. Haley, I. McCarroll, P. A. J. Bagot, J. M. Cairney, and M. P. Moody, "A Gas-Phase Reaction Cell for Modern Atom Probe Systems," *Microscopy and Microanalysis,* vol. 25, no. 2, pp. 410-417, 2019, doi: 10.1017/S1431927618016240.
[173] D. R. Kingham, "The post-ionization of field evaporated ions: A theoretical explanation of multiple charge states," *Surface Science,* vol. 116, no. 2, pp. 273-301, 1982/04/02 1982, doi: 10.1016/0039-6028(82)90434-4.
[174] N. Ernst, J. H. Block, H. J. Kreuzer, and X. Ye, "Thermal field desorption spectroscopy of chemisorbed hydrogen for a single step site," *Physical Review Letters,* Article vol. 71, no. 6, pp. 891-894, 1993, doi: 10.1103/PhysRevLett.71.891.
[175] T. C. Clements and E. W. Müller, "Occurrence of H3+ in the Field Ionization of Hydrogen," *The Journal of Chemical Physics,* vol. 37, no. 11, pp. 2684-2687, 1962/12/01 1962, doi: 10.1063/1.1733072.
[176] R. E. Christoffersen, "Configuration-Interaction Study of the Ground State of the H3+ Molecule," *The Journal of Chemical Physics,* vol. 41, no. 4, pp. 960-971, 1964/08/15 1964, doi: 10.1063/1.1726039.
[177] M. J. Gaillard *et al.*, "Experimental determination of the structure of H3+," *Physical Review A,* vol. 17, no. 6, pp. 1797-1803, Jun 1978, doi: 10.1103/PhysRevA.17.1797.
[178] E. Herbst, E. Herbst, S. Miller, T. Oka, and J. K. G. Watson, "The astrochemistry of H3+," *Philosophical Transactions of the Royal Society of London. Series A: Mathematical, Physical and Engineering Sciences,* vol. 358, no. 1774, pp. 2523-2534, 2000/09/15 2000, doi: 10.1098/rsta.2000.0665.
[179] T. Utsumi, "Surface Studies Using Ion Energy-Distribution of Field Ionized Gases on Metal-Surfaces," *Jpn J Appl Phys,* vol. 13, no. S2, pp. 47-50, 1974/01/01 1974, doi: 10.7567/JJAPS.2S2.47.
[180] N. Ernst and J. H. Block, "Temperature programmed field desorption of protonated hydrogen from rhodium and tungsten," *Surface Science,* vol. 126, no. 1, pp. 397-404, 1983/03/02 1983, doi: 10.1016/0039-6028(83)90734-3.
[181] M. C. Reckzügel, W. Drachsel, and J. H. Block, "Field desorption of H3 and field dissociation of H+3," *Applied Surface Science,* vol. 76-77, pp. 108-114, 1994/03/02 1994, doi: 10.1016/0169-4332(94)90330-1.

[182] M. C. Reckzügel, W. Drachsel, and J. H. Block, "Structure of H3+ in high electric fields with implications for the structure of adsorbed H3," *The Journal of Chemical Physics,* Article vol. 102, no. 19, pp. 7708-7713, 1995, doi: 10.1063/1.469022.
[183] X. Ye, H. J. Kreuzer, and D. R. Salahub, "Theory of field adsorption of hydrogen," *Applied Surface Science,* vol. 67, no. 1, pp. 1-8, 1993/04/02 1993, doi: 10.1016/0169-4332(93)90285-J.
[184] Y. H. Chang *et al.*, "Quantification of solute deuterium in titanium deuteride by atom probe tomography with both laser pulsing and high-voltage pulsing: influence of the surface electric field," *New Journal of Physics,* vol. 21, no. 5, p. 053025, 2019/05/22 2019, doi: 10.1088/1367-2630/ab1c3b.
[185] F. Vurpillot, L. Rousseau, J.-B. Maillet, and B. Gault, "Is it possible to remove the degeneracy of hydrogen signal in the APT analysis of Al based materials?," presented at the APT&M 2022, Nanjing, China, 2022. [Online]. Available: https://youtu.be/WJbPoROpMqY?t=9075.
[186] T. T. Tsong and Y. Liou, "Cluster-ion formation in pulsed-laser-stimulated field desorption of condensed materials," *Physical Review B,* vol. 32, no. 7, pp. 4340-4357, Oct 1985, doi: 10.1103/PhysRevB.32.4340.
[187] Z. M. Stepień and T. T. Tsong, "Formation of metal hydride ions in low-temperature field evaporation," *Surface Science,* vol. 409, no. 1, pp. 57-68, 1998/06/20 1998, doi: 10.1016/S0039-6028(98)00200-3.
[188] E. W. Müller, S. Nakamura, O. Nishikawa, and S. B. McLane, "Gas-Surface Interactions and Field-Ion Microscopy of Nonrefractory Metals," *Journal of Applied Physics,* vol. 36, no. 8, pp. 2496-2503, 1965/08/01 1965, doi: 10.1063/1.1714519.
[189] O. Nishikawa, T. Yoshimura, and M. Shibata, "Atom-probe study of hydrogen physisorption on Al and Cu," *Surface Science,* vol. 124, no. 2, pp. 440-450, 1983/01/02 1983, doi: 10.1016/0039-6028(83)90802-6.
[190] O. Nishikawa, "Reduced evaporation field by the field induced dipoles of physisorbed He, Ne and H2," *Surface Science,* vol. 131, no. 2, pp. 239-244, 1983/09/01 1983, doi: 10.1016/0039-6028(83)90274-1.
[191] M. Wada, R. Uemori, and O. Nishikawa, "Effect of hydrogen on the evaporation field of metals," *Surface Science,* vol. 134, no. 1, pp. 17-29, 1983/11/01 1983, doi: 10.1016/0039-6028(83)90309-6.
[192] P. Felfer *et al.*, "An Atom Probe with Ultra-Low Hydrogen Background," *Microscopy and Microanalysis,* pp. 1-9, 2021, doi: 10.1017/S1431927621013702.
[193] A. J. Breen *et al.*, "Solute hydrogen and deuterium observed at the near atomic scale in high-strength steel," *Acta Materialia,* vol. 188, pp. 108-120, 2020/04/15 2020, doi: 10.1016/j.actamat.2020.02.004.
[194] R. Ding and I. P. Jones, "In situ hydride formation in titanium during focused ion milling," *Journal of Electron Microscopy,* vol. 60, no. 1, pp. 1-9, 2011, doi: 10.1093/jmicro/dfq066.
[195] B. Arroyo, L. Andrea, J. A. Álvarez, S. Cicero, and R. Lacalle, "Analysis of Samples Cleaning Methods Prior to Hydrogen Content Determination in Steel," *Metals*, vol. 10, no. 6*,* doi: 10.3390/met10060723.
[196] G. Schimo-Aichhorn *et al.*, "Hydrogen Insertion into Complex-Phase High-Strength Steel during Atmospheric Corrosion at Low Relative Humidity," *Metals*, vol. 12, no. 4*,* doi: 10.3390/met12040624.
[197] Y. Chang *et al.*, "Ti and its alloys as examples of cryogenic focused ion beam milling of environmentally-sensitive materials," *Nature Communications,* vol. 10, no. 1, p. 942, 2019/02/26 2019, doi: 10.1038/s41467-019-08752-7.
[198] I. Mouton *et al.*, "Hydride growth mechanism in zircaloy-4: Investigation of the partitioning of alloying elements," *Materialia,* vol. 15, p. 101006, 2021/03/01 2021, doi: 10.1016/j.mtla.2021.101006.
[199] D. Banerjee, C. G. Shelton, B. Ralph, and J. C. Williams, "A resolution of the interface phase problem in titanium alloys," *Acta Metallurgica,* vol. 36, no. 1, pp. 125-141, 1988/01/01 1988, doi: 10.1016/0001-6160(88)90033-8.
[200] I. E. McCarroll *et al.*, "The effect of hydrogen on the early stages of oxidation of a magnesium alloy," *Corros Sci,* vol. 165, p. 108391, Apr 1 2020, doi: 10.1016/j.corsci.2010.108391.
[201] R. A. Karnesky Jr, N. C. Bartelt, D. Huang, N. E. Teslich Jr, and M. Kumar, "Imaging and quantification of hydrogen isotope trapping," Sandia National Laboratories (SNL), Albuquerque, NM, and Livermore, CA …, 2012.
[202] Y.-S. Chen, "Characterisation of hydrogen trapping in steel by atom probe tomography," University of Oxford, 2017.
[203] D. G. Brandon, "Gas Impact, Field Etching, and Field Deformation," in *Field-Ion Microscopy*, J. J. Hren and S. Ranganathan Eds. Boston, MA: Springer US, 1968, pp. 53-68.
[204] M. J. Southon, "Field Emission and Field Ionization," in *Field-Ion Microscopy*, J. J. Hren and S. Ranganathan Eds. Boston, MA: Springer US, 1968, pp. 6-27.
[205] H. O. Andrén and U. Rolander, "Field dependence of hydrogen adsorption," *Surface Science,* vol. 266, no. 1, pp. 76-80, 1992/04/15 1992, doi: 10.1016/0039-6028(92)91001-R.

[206] Y. J. Kim and D. N. Seidman, "Atom-Probe Tomographic Analyses of Hydrogen Interstitial Atoms in Ultrahigh Purity Niobium," *Microscopy and Microanalysis,* Article vol. 21, no. 3, pp. 535-543, Jun 2015, doi: 10.1017/s143192761500032x.
[207] J. Meija *et al.*, "Isotopic compositions of the elements 2013 (IUPAC Technical Report)," *Pure Appl Chem,* vol. 88, no. 3, pp. 293-306, Mar 2016, doi: 10.1515/pac-2015-0503.
[208] A. T. Macrander and D. N. Seidman, "Hydrogen adsorption on (110) tungsten at 30 k: an atom-probe field-ion microscope study," *Surface Science,* vol. 147, no. 2, pp. 451-465, 1984/11/03 1984, doi: 10.1016/0039-6028(84)90466-7.
[209] Z. M. Stępień, "Interaction of hydrogen with tantalum surface in a high electric field," *Vacuum,* vol. 54, no. 1, pp. 257-262, 1999/07/01 1999, doi: 10.1016/S0042-207X(98)00474-6.
[210] E. J. Kautz, S. V. Lambeets, J. Royer, D. E. Perea, S. S. Harilal, and A. Devaraj, "Compositional partitioning during early stages of oxidation of a uranium-molybdenum alloy," *Scripta Materialia,* vol. 212, p. 114528, 2022/04/15 2022, doi: 10.1016/j.scriptamat.2022.114528.
[211] Y. Shimizu *et al.*, "Crystallite distribution analysis based on hydrogen content in thin-film nanocrystalline silicon solar cells by atom probe tomography," *Applied Physics Express,* vol. 14, no. 1, p. 016501, 2020/12/16 2021, doi: 10.35848/1882-0786/abd13f.
[212] H. Sepehri-Amin, T. Ohkubo, T. Nishiuchi, S. Hirosawa, and K. Hono, "Quantitative laser atom probe analyses of hydrogenation-disproportionated Nd-Fe-B powders," *Ultramicroscopy,* Article; Proceedings Paper vol. 111, no. 6, pp. 615-618, May 2011, doi: 10.1016/j.ultramic.2010.11.015.
[213] J. R. de Laeter *et al.*, "Atomic weights of the elements. Review 2000 (IUPAC Technical Report)," vol. 75, no. 6, pp. 683-800, 2003, doi: doi:10.1351/pac200375060683.
[214] J. Takahashi, K. Kawakami, Y. Kobayashi, and T. Tarui, "The first direct observation of hydrogen trapping sites in TiC precipitation-hardening steel through atom probe tomography," *Scripta Materialia,* Article vol. 63, no. 3, pp. 261-264, Aug 2010, doi: 10.1016/j.scriptamat.2010.03.012.
[215] A. J. London, "Quantifying Uncertainty from Mass-Peak Overlaps in Atom Probe Microscopy," *Microscopy and Microanalysis,* vol. 25, no. 2, pp. 378-388, 2019, doi: 10.1017/S1431927618016276.
[216] J. Takahashi, K. Kawakami, and T. Tarui, "Direct observation of hydrogen-trapping sites in vanadium carbide precipitation steel by atom probe tomography," *Scripta Materialia,* Article vol. 67, no. 2, pp. 213-216, Jul 2012, doi: 10.1016/j.scriptamat.2012.04.022.
[217] Y.-S. Chen *et al.*, "Direct observation of individual hydrogen atoms at trapping sites in a ferritic steel," *Science,* Article vol. 355, no. 6330, pp. 1196-1199, Mar 2017, doi: 10.1126/science.aal2418.
[218] Y. S. Chen, P. A. J. Bagot, M. P. Moody, and D. Haley, "Observing hydrogen in steel using cryogenic atom probe tomography: A simplified approach," *International Journal of Hydrogen Energy,* vol. 44, no. 60, pp. 32280-32291, Dec 6 2019, doi: 10.1016/j.ijhydene.2019.09.232.
[219] Y. S. Chen *et al.*, "Observation of hydrogen trapping at dislocations, grain boundaries, and precipitates," *Science,* Article vol. 367, no. 6474, pp. 171-+, Jan 2020, doi: 10.1126/science.aaz0122.
[220] D. Haley, S. V. Merzlikin, P. Choi, and D. Raabe, "Atom probe tomography observation of hydrogen in high-Mn steel and silver charged via an electrolytic route," *International Journal of Hydrogen Energy,* Article vol. 39, no. 23, pp. 12221-12229, Aug 2014, doi: 10.1016/j.ijhydene.2014.05.169.
[221] J. Takahashi, K. Kawakami, and Y. Kobayashi, "Origin of hydrogen trapping site in vanadium carbide precipitation strengthening steel," *Acta Materialia,* Article vol. 153, pp. 193-204, Jul 2018, doi: 10.1016/j.actamat.2018.05.003.
[222] P. Kesten, A. Pundt, G. Schmitz, M. Weisheit, H. U. Krebs, and R. Kirchheim, "H- and D distribution in metallic multilayers studied by 3-dimensional atom probe analysis and secondary ion mass spectrometry," *Journal of Alloys and Compounds,* Article; Proceedings Paper vol. 330, pp. 225-228, Jan 2002, doi: 10.1016/s0925-8388(01)01596-1.
[223] R. Gemma, T. Al-Kassab, R. Kirchheim, and A. Pundt, "APT analyses of deuterium-loaded Fe/V multi-layered films," *Ultramicroscopy,* Article; Proceedings Paper vol. 109, no. 5, pp. 631-636, Apr 2009, doi: 10.1016/j.ultramic.2008.11.005.
[224] R. Gemma, T. Al-Kassab, R. Kirchheim, and A. Pundt, "Analysis of deuterium in V-Fe5at.% film by atom probe tomography (APT)," *Journal of Alloys and Compounds,* Article; Proceedings Paper vol. 509, pp. S872-S876, Sep 2011, doi: 10.1016/j.jallcom.2010.11.122.
[225] R. Gemma, T. Al-Kassab, R. Kirchheim, and A. Pundt, "Visualization of deuterium dead layer by atom probe tomography," *Scripta Materialia,* Article vol. 67, no. 11, pp. 903-906, Dec 2012, doi: 10.1016/j.scriptamat.2012.08.025.

[226] I. E. McCarroll, Y.-C. Lin, A. Rosenthal, H.-W. Yen, and J. M. Cairney, "Hydrogen trapping at dislocations, carbides, copper precipitates and grain boundaries in a dual precipitating low-carbon martensitic steel," *Scripta Materialia,* vol. 221, p. 114934, 2022/12/01 2022, doi: 10.1016/j.scriptamat.2022.114934.
[227] R. Gemma, T. Al-Kassab, and A. Pundt, "Deuterium Distribution in Fe/V Multi-Layered Films," *Molecules,* Article vol. 27, no. 22, 2022, Art no. 7848, doi: 10.3390/molecules27227848.
[228] D. Haley, P. A. J. Bagot, and M. P. Moody, "Atom Probe Analysis of Ex Situ Gas-Charged Stable Hydrides," *Microscopy and Microanalysis,* vol. 23, no. 2, pp. 307-313, 2017, doi: 10.1017/S1431927616012630.
[229] T. Li *et al.*, "Atomic-scale insights into surface species of electrocatalysts in three dimensions," *Nature Catalysis,* vol. 1, no. 4, pp. 300-305, 2018/04/01 2018, doi: 10.1038/s41929-018-0043-3.
[230] D. Tweddle, P. Hamer, Z. Shen, V. P. Markevich, M. P. Moody, and P. R. Wilshaw, "Direct observation of hydrogen at defects in multicrystalline silicon," *Progress in Photovoltaics: Research and Applications,* vol. n/a, no. n/a, 2019/08/07 2019, doi: 10.1002/pip.3184.
[231] Y. F. Shi *et al.*, "Towards accurate atom scale characterisation of hydrogen passivation of interfaces in TOPCon architectures," *Solar Energy Materials and Solar Cells,* vol. 246, p. 111915, Oct 1 2022, doi: 10.1016/j.solmat.2022.111915.
[232] Y. Li, F. Ma, F. Yue, Q. Ren, H. Zhou, and G. Lu, "Radiation-induced precipitation of transmutation elements rhenium/osmium and their effects on hydrogen behavior in tungsten," *Progress in Natural Science: Materials International,* vol. 29, no. 3, pp. 285-294, 2019/06/01 2019, doi: 10.1016/j.pnsc.2019.03.014.
[233] Y. Ueda *et al.*, "Simultaneous irradiation effects of hydrogen and helium ions on tungsten," *Journal of Nuclear Materials,* vol. 386-388, pp. 725-728, 2009/04/30 2009, doi: 10.1016/j.jnucmat.2008.12.300.
[234] B. Tyburska-Püschel and V. K. Alimov, "On the reduction of deuterium retention in damaged Re-doped W," *Nuclear Fusion,* vol. 53, no. 12, p. 123021, 2013/11/25 2013, doi: 10.1088/0029-5515/53/12/123021.
[235] H. Xie, K. Xu, G.-H. Lu, T. Yu, and F. Yin, "Trapping of hydrogen and helium at an {110}<111> edge dislocation in tungsten," *Journal of Nuclear Materials,* vol. 484, pp. 270-275, 2017/02/01 2017, doi: 10.1016/j.jnucmat.2016.12.014.
[236] Y. L. Liu, Y. Zhang, H. B. Zhou, G. H. Lu, F. Liu, and G. N. Luo, "Vacancy trapping mechanism for hydrogen bubble formation in metal," *Physical Review B,* Article vol. 79, no. 17, p. 4, May 2009, Art no. 172103, doi: 10.1103/PhysRevB.79.172103.
[237] A. Wagner and D. N. Seidman, "Range Profiles of 300- and 475-eV 4He+ Ions and the Diffusivity of 4He in Tungsten," *Physical Review Letters,* vol. 42, no. 8, pp. 515-518, Feb 19 1979, doi: 10.1103/PhysRevLett.42.515.
[238] R. Herschitz and D. N. Seidman, "An atomic resolution study of radiation-induced precipitation and solute segregation effects in a neutron-irradiated W-25 at.% Re alloy," *Acta Metallurgica,* vol. 32, no. 8, pp. 1155-1171, 1984/08/01 1984, doi: 10.1016/0001-6160(84)90122-6.
[239] A. Xu *et al.*, "Ion-irradiation-induced clustering in W–Re and W–Re–Os alloys: A comparative study using atom probe tomography and nanoindentation measurements," *Acta Materialia,* vol. 87, pp. 121-127, 2015/04/01 2015, doi: 10.1016/j.actamat.2014.12.049.
[240] M. Dagan *et al.*, "Imaging of radiation damage using complementary field ion microscopy and atom probe tomography," *Ultramicroscopy,* vol. 159 Pt 2, pp. 387-94, Dec 2015, doi: 10.1016/j.ultramic.2015.02.017.
[241] M. J. Lloyd *et al.*, "Decoration of voids with rhenium and osmium transmutation products in neutron irradiated single crystal tungsten," *Scripta Materialia,* vol. 173, pp. 96-100, 2019/12/01 2019, doi: 10.1016/j.scriptamat.2019.07.036.
[242] M. J. Lloyd *et al.*, "Radiation-induced segregation in W-Re: from kinetic Monte Carlo simulations to atom probe tomography experiments," *The European Physical Journal B,* vol. 92, no. 10, p. 241, 2019/10/21 2019, doi: 10.1140/epjb/e2019-100244-y.
[243] A. Xu *et al.*, "Ion-irradiation induced clustering in W-Re-Ta, W-Re and W-Ta alloys: An atom probe tomography and nanoindentation study," *Acta Materialia,* vol. 124, pp. 71-78, Feb 1 2017, doi: 10.1016/j.actamat.2016.10.050.
[244] G. L. Kellogg and J. K. G. Panitz, "A Direct observation of the Trapping of Deuterium Ions at a Grain Boundary in Tungsten," *Applied Physics Letters,* Article vol. 37, no. 7, pp. 625-627, 1980, doi: 10.1063/1.91999.
[245] Jonathan Bennett & AutoIT Team. "AutoIT. www.autoitscript.com." https://www.autoitscript.com/site/ (accessed 12/6/19.

[246] T. J. Prosa, B. P. Geiser, D. Lawrence, D. Olson, and D. J. Larson, "Developing detection efficiency standards for atom probe tomography," in *SPIE NanoScience + Engineering*, 2014, vol. 9173, doi: 10.1117/12.2062211.
[247] M. A. Liu, P. E. J. Rivera-Diaz-del-Castillo, J. I. Barraza-Fierro, H. Castaneda, and A. Srivastava, "Microstructural influence on hydrogen permeation and trapping in steels," *Mater Design,* vol. 167, p. 107605, Apr 5 2019, doi: 10.1016/j.matdes.2019.107605.
[248] T. T. Tsong, "Measurement of the field evaporation rate of several transition metals," *Journal of Physics F: Metal Physics,* vol. 8, no. 7, pp. 1349-1352, Jul 1978, doi: 10.1088/0305-4608/8/7/008.
[249] C. M. C. De Castilho and D. R. Kingham, "Calculations of field ionization in the field ion microscope," *Surface Science,* Article vol. 173, no. 1, pp. 75-96, 1986, doi: 10.1016/0039-6028(86)90108-1.
[250] D. W. Saxey, "Correlated ion analysis and the interpretation of atom probe mass spectra," *Ultramicroscopy,* vol. 111, no. 6, pp. 473-479, 2011/05/01 2011, doi: 10.1016/j.ultramic.2010.11.021.
[251] F. Meisenkothen, E. B. Steel, T. J. Prosa, K. T. Henry, and R. Prakash Kolli, "Effects of detector dead-time on quantitative analyses involving boron and multi-hit detection events in atom probe tomography," *Ultramicroscopy,* vol. 159 Pt 1, pp. 101-11, Dec 2015, doi: 10.1016/j.ultramic.2015.07.009.
[252] T. J. Prosa and E. Oltman, "Study of LEAP® 5000 Deadtime and Precision via Silicon Pre-Sharpened-Microtip™ Standard Specimens," *Microscopy and Microanalysis,* vol. 28, no. 4, pp. 1019-1037, 2022, doi: 10.1017/S143192762101206X.
[253] E. W. Müller, "Das Feldionenmikroskop," *Zeitschrift für Physik,* vol. 131, no. 1, pp. 136-142, 1951/03/01 1951, doi: 10.1007/BF01329651.
[254] T. F. Kelly, "Kinetic-Energy Discrimination for Atom Probe Tomography: Review Article," *Microscopy and Microanalysis,* vol. 17, no. 1, pp. 1-14, 2011, doi: 10.1017/S1431927610094468.
[255] C. Bacchi *et al.*, "Development of an Energy-Sensitive Detector for the Atom Probe Tomography," *Microscopy and Microanalysis,* vol. 28, no. 4, pp. 1076-1091, 2022, doi: 10.1017/S1431927621012708.
[256] J. Suttle, T. Kelly, and R. McDermott, "A superconducting ion detection scheme for atom probe tomography," in *APS March Meeting Abstracts*, 2016, vol. 2016, p. Y7. 003.
[257] A. Hollingsworth *et al.*, "Comparative study of deuterium retention and vacancy content of self-ion irradiated tungsten," *Journal of Nuclear Materials,* vol. 558, p. 153373, 2022/01/01 2022, doi: 10.1016/j.jnucmat.2021.153373.
[258] W. R. Wampler and R. P. Doerner, "Deuterium retention in tungsten from exposure to plasma," *Physica Scripta,* Article; Proceedings Paper vol. T138, p. 8, Dec 2009, Art no. 014037, doi: 10.1088/0031-8949/2009/t138/014037.
[259] Y. Zayachuk and A. Hollingsworth, "(Personal Communication)," ed.
[260] J. P. Crocombette and C. Van Wambeke, "Quick calculation of damage for ion irradiation: implementation in Iradina and comparisons to SRIM," *Epj Nucl Sci Technol,* 10.1051/epjn/2019003 vol. 5, May 15 2019, doi: 10.1051/epjn/2019003.
[261] J. F. Ziegler, M. D. Ziegler, and J. P. Biersack, "SRIM - The stopping and range of ions in matter (2010)," *Nucl Instrum Meth B,* vol. 268, no. 11-12, pp. 1818-1823, Jun 2010, doi: 10.1016/j.nimb.2010.02.091.
[262] V. K. Alimov, J. Roth, and M. Mayer, "Depth distribution of deuterium in single- and polycrystalline tungsten up to depths of several micrometers," *Journal of Nuclear Materials,* vol. 337-339, pp. 619-623, 2005/03/01 2005, doi: 10.1016/j.jnucmat.2004.10.082.
[263] K. Thompson, D. Lawrence, D. J. Larson, J. D. Olson, T. F. Kelly, and B. Gorman, "In situ site-specific specimen preparation for atom probe tomography," *Ultramicroscopy,* vol. 107, no. 2-3, pp. 131-9, Feb-Mar 2007, doi: 10.1016/j.ultramic.2006.06.008.
[264] M. K. Miller, K. F. Russell, K. Thompson, R. Alvis, and D. J. Larson, "Review of Atom Probe FIB-Based Specimen Preparation Methods," *Microscopy and Microanalysis,* vol. 13, no. 6, pp. 428-436, 2007, doi: 10.1017/S1431927607070845.
[265] B. Gault, F. de Geuser, L. T. Stephenson, M. P. Moody, B. C. Muddle, and S. P. Ringer, "Estimation of the Reconstruction Parameters for Atom Probe Tomography," *Microscopy and Microanalysis,* vol. 14, no. 4, pp. 296-305, 2008, doi: 10.1017/S1431927608080690.
[266] B. P. Geiser, T. F. Kelly, D. J. Larson, J. Schneir, and J. P. Roberts, "Spatial Distribution Maps for Atom Probe Tomography," *Microscopy and Microanalysis,* vol. 13, no. 6, pp. 437-447, 2007, doi: 10.1017/S1431927607070948.
[267] M. P. Moody, B. Gault, L. T. Stephenson, D. Haley, and S. P. Ringer, "Qualification of the tomographic reconstruction in atom probe by advanced spatial distribution map techniques," *Ultramicroscopy,* vol. 109, no. 7, pp. 815-824, 2009/06/01 2009, doi: 10.1016/j.ultramic.2009.03.016.

[268] B. Gault *et al.*, "Advances in the calibration of atom probe tomographic reconstruction," *Journal of Applied Physics,* vol. 105, no. 3, p. 034913, 2009/02/01 2009, doi: 10.1063/1.3068197.
[269] *AtomProbeLab*. (2016). [Online]. Available: https://sourceforge.net/projects/atomprobelab/
[270] M. Ester, H.-P. Kriegel, J. r. Sander, and X. Xu, "A Density-Based Algorithm for Discovering Clusters in Large Spatial Databases with Noise," presented at the Proceedings of the Second International Conference on Knowledge Discovery and Data Mining, 1996.
[271] Y. Shimony and L. Ben-Dor, "Phase change of WO2," *Journal of Materials Science Letters,* vol. 2, no. 7, pp. 353-354, 1983/07/01 1983, doi: 10.1007/BF00726327.
[272] H. A. Wriedt, "The N-W (nitrogen-tungsten) system," *Bulletin of Alloy Phase Diagrams,* vol. 10, no. 4, pp. 358-367, 1989/08/01 1989, doi: 10.1007/BF02877592.
[273] A. S. Kurlov and A. I. Gusev, "Phase equilibria in the W–C system and tungsten carbides," *Russian Chemical Reviews,* vol. 75, no. 7, pp. 617-636, 2006/07/31 2006, doi: 10.1070/RC2006v075n07ABEH003606.
[274] F. Yan *et al.*, "Atomic-scale investigation of hydrogen distribution in a TiMo alloy," *Scripta Materialia,* vol. 162, pp. 321-325, 2019/03/15 2019, doi: 10.1016/j.scriptamat.2018.11.040.
[275] G. J. C. Carpenter, J. A. Jackman, J. P. McCaffrey, and R. Alani, "In Situ Hydride Formation in Zirconium and Titanium during Ion Milling," *Microscopy and Microanalysis,* vol. 1, no. 4, pp. 175-184, 1995, doi: 10.1017/S1431927695111757.
[276] F. Cardarelli, *Materials Handbook : A Concise Desktop Reference*. London, UNITED KINGDOM: Springer London, Limited, 2008.
[277] X. Gu, Z. Fan, and H. Bao, "Thermal conductivity prediction by atomistic simulation methods: Recent advances and detailed comparison," *Journal of Applied Physics,* vol. 130, no. 21, p. 210902, 2021, doi: 10.1063/5.0069175.
[278] K. Eder, V. Bhatia, J. Qu, B. Van Leer, M. Dutka, and J. M. Cairney, "A multi-ion plasma FIB study: Determining ion implantation depths of Xe, N, O and Ar in tungsten via atom probe tomography," *Ultramicroscopy,* vol. 228, p. 113334, 2021/09/01 2021, doi: 10.1016/j.ultramic.2021.113334.
[279] P. J. Felfer, T. Alam, S. P. Ringer, and J. M. Cairney, "A reproducible method for damage-free site-specific preparation of atom probe tips from interfaces," *Microscopy Research and Technique,* vol. 75, no. 4, pp. 484-491, 2012/04/01 2012, doi: 10.1002/jemt.21081.
[280] B. Langelier, H. P. Van Landeghem, G. A. Botton, and H. S. Zurob, "Interface Segregation and Nitrogen Measurement in Fe–Mn–N Steel by Atom Probe Tomography," *Microscopy and Microanalysis,* vol. 23, no. 2, pp. 385-395, 2017, doi: 10.1017/S1431927617000150.
[281] H. F. Liu and T. T. Tsong, "Numerical calculation of the temperature evolution and profile of the field ion emitter in the pulsed-laser time-of-flight atom probe," *Review of Scientific Instruments,* vol. 55, no. 11, pp. 1779-1784, 1984, doi: 10.1063/1.1137658.
[282] A. Vella, "On the interaction of an ultra-fast laser with a nanometric tip by laser assisted atom probe tomography: A review," *Ultramicroscopy,* vol. 132, pp. 5-18, 2013/09/01 2013, doi: 10.1016/j.ultramic.2013.05.016.
[283] X. Fang *et al.*, "Plastic deformation of tungsten due to deuterium plasma exposure: Insights from micro-compression tests," *Scripta Materialia,* vol. 162, pp. 132-135, 2019/03/15 2019, doi: 10.1016/j.scriptamat.2018.10.052.
[284] Y. Li *et al.*, "Three mechanisms of hydrogen-induced dislocation pinning in tungsten," *Nuclear Fusion,* vol. 60, no. 8, p. 086015, 2020/07/15 2020, doi: 10.1088/1741-4326/ab98a4.
[285] H. Cao and S. Wang, "The effect of hydrogen on dislocation motion and cracking in tungsten foil," *Corros Sci,* vol. 207, p. 110547, 2022/10/01/ 2022, doi: https://doi.org/10.1016/j.corsci.2022.110547.
[286] O. V. Ogorodnikova *et al.*, "Effect of nitrogen seeding into deuterium plasma on deuterium retention in tungsten," *Physica Scripta,* vol. T145, no. T145, p. 014034, Dec 2011, doi: 10.1088/0031-8949/2011/T145/014034.
[287] J. D. Zhang *et al.*, "Formation of bubbles and blisters in hydrogen ion implanted polycrystalline tungsten," *Radiation Effects and Defects in Solids,* vol. 173, no. 11-12, pp. 1027-1036, 2018/12/02 2018, doi: 10.1080/10420150.2018.1531411.
[288] M. Poon, A. A. Haasz, J. W. Davis, and R. G. Macaulay-Newcombe, "Impurity effects and temperature in single crystal dependence of D retention tungsten," *Journal of Nuclear Materials,* vol. 313, pp. 199-203, Mar 2003, doi: 10.1016/S0022-3115(02)01445-9.
[289] C. N. Taylor and M. Shimada, "First GD-OES results on various deuterium ion fluences implanted in tungsten," *Nuclear Materials and Energy,* vol. 16, pp. 29-33, Aug 2018, doi: 10.1016/j.nme.2018.06.006.

[290] M. Rieth, R. Doerner, A. Hasegawa, Y. Ueda, and M. Wirtz, "Behavior of tungsten under irradiation and plasma interaction," *Journal of Nuclear Materials,* vol. 519, pp. 334-368, Jun 2019, doi: 10.1016/j.jnucmat.2019.03.035.
[291] L. Gao *et al.*, "Deuterium supersaturation in low-energy plasma-loaded tungsten surfaces," *Nuclear Fusion,* vol. 57, no. 1, p. 016026, 2016/11/11 2017, doi: 10.1088/0029-5515/57/1/016026.
[292] Y.-G. Li, Q.-R. Zheng, L.-M. Wei, C.-G. Zhang, and Z. Zeng, "A review of surface damage/microstructures and their effects on hydrogen/helium retention in tungsten," *Tungsten,* vol. 2, no. 1, pp. 34-71, 2020/03/01 2020, doi: 10.1007/s42864-020-00042-w.
[293] A. A. Haasz, M. Poon, and J. W. Davis, "The effect of ion damage on deuterium trapping in tungsten," *Journal of Nuclear Materials,* vol. 266, pp. 520-525, Mar 1999, doi: Doi 10.1016/S0022-3115(98)00586-8.
[294] M. Fukumoto *et al.*, "Deuterium trapping in tungsten damaged by high-energy hydrogen ion irradiation," *Journal of Nuclear Materials,* vol. 390-391, pp. 572-575, 2009/06/15 2009, doi: 10.1016/j.jnucmat.2009.01.107.
[295] A. Dunand, M. Minissale, J. B. Faure, L. Gallais, T. Angot, and R. Bisson, "Surface oxygen versus native oxide on tungsten: contrasting effects on deuterium retention and release," *Nuclear Fusion,* vol. 62, no. 5, p. 054002, May 1 2022, doi: 10.1088/1741-4326/ac583a.
[296] K. Kremer, M. Brucker, W. Jacob, and T. Schwarz-Selinger, "Influence of thin surface oxide films on hydrogen isotope release from ion-irradiated tungsten," *Nuclear Materials and Energy,* vol. 30, p. 101137, Mar 2022, doi: 10.1016/j.nme.2022.101137.
[297] X.-S. Kong *et al.*, "The role of impurity oxygen in hydrogen bubble nucleation in tungsten," *Journal of Nuclear Materials,* vol. 433, no. 1, pp. 357-363, 2013/02/01 2013, doi: 10.1016/j.jnucmat.2012.10.024.
[298] V. Tiron, I. L. Velicu, C. Porosnicu, I. Burducea, P. Dinca, and P. Malinsky, "Tungsten nitride coatings obtained by HiPIMS as plasma facing materials for fusion applications," *Applied Surface Science,* vol. 416, pp. 878-884, Sep 15 2017, doi: 10.1016/j.apsusc.2017.04.183.
[299] L. Gao *et al.*, "Interaction of deuterium plasma with sputter-deposited tungsten nitride films," *Nuclear Fusion,* vol. 56, no. 1, p. 016004, Jan 1 2016, doi: 10.1088/0029-5515/56/1/016004.
[300] X. B. Ye and B. C. Pan, "The mechanism on retention of hydrogen in three representative tungsten nitride compounds in nuclear fusion reactors," *Journal of Nuclear Materials,* vol. 544, p. 152687, Feb 2021, doi: 10.1016/j.jnucmat.2020.152687.
[301] X. D. Ou, L. Q. Shi, K. Sato, Q. Xu, and Y. X. Wang, "Effect of carbon on hydrogen behaviour in tungsten: first-principle calculations," *Nuclear Fusion,* vol. 52, no. 12, p. 123003, Dec 2012, doi: 10.1088/0029-5515/52/12/123003.
[302] H. Kimura, Y. Nishikawa, T. Nakahata, M. Oyaidzu, Y. Oya, and K. Okuno, "Chemical behavior of energetic deuterium implanted into tungsten carbide," *Fusion Engineering and Design,* vol. 81, no. 1-7, pp. 295-299, Feb 2006, doi: 10.1016/j.fusengdes.2005.09.024.
[303] P. Grigorev, T. D. Swinburne, and J. R. Kermode, "Hybrid quantum/classical study of hydrogen-decorated screw dislocations in tungsten: Ultrafast pipe diffusion, core reconstruction, and effects on glide mechanism," *Physical Review Materials,* vol. 4, no. 2, p. 023601, Feb 12 2020, doi: 10.1103/PhysRevMaterials.4.023601.
[304] A. De Backer *et al.*, "Multiscale modelling of the interaction of hydrogen with interstitial defects and dislocations in BCC tungsten," *Nuclear Fusion,* vol. 58, no. 1, p. 016006, 2017/11/06 2018, doi: 10.1088/1741-4326/aa8e0c.
[305] M. Oberkofler *et al.*, "First nitrogen-seeding experiments in JET with the ITER-like Wall," *Journal of Nuclear Materials,* vol. 438, pp. S258-S261, Jul 2013, doi: 10.1016/j.jnucmat.2013.01.041.
[306] H. T. Lee, M. Ishida, Y. Ohtsuka, and Y. Ueda, "The influence of nitrogen on deuterium permeation through tungsten," *Physica Scripta,* vol. T159, no. T159, p. 014021, Apr 2014, doi: 10.1088/0031-8949/2014/T159/014021.
[307] S. Wang *et al.*, "Effects of nitrogen on hydrogen retention in tungsten: First-principles calculations," *Journal of Nuclear Materials,* vol. 459, pp. 143-149, Apr 2015, doi: 10.1016/j.jnucmat.2015.01.025.
[308] L. Yang and B. D. Wirth, "Carbon clustering and effect on hydrogen trapping in tungsten: A first-principles study," *Computational Materials Science,* vol. 184, p. 109932, Nov 2020, doi: 10.1016/j.commatsci.2020.109932.
[309] S. Jin, Y. L. Liu, H. B. Zhou, Y. Zhang, and G. H. Lu, "First-principles investigation on the effect of carbon on hydrogen trapping in tungsten," *Journal of Nuclear Materials,* vol. 415, no. 1, pp. S709-S712, Aug 1 2011, doi: 10.1016/j.jnucmat.2010.10.043.

[310] S. Craw, "Manhattan Distance," in *Encyclopedia of Machine Learning*, C. Sammut and G. I. Webb Eds. Boston, MA: Springer US, 2010, pp. 639-639.
[311] P. Willett, J. M. Barnard, and G. M. Downs, "Chemical Similarity Searching," *Journal of Chemical Information and Computer Sciences,* vol. 38, no. 6, pp. 983-996, 1998/11/23 1998, doi: 10.1021/ci9800211.
[312] M. S. Meier. "APTmap." https://github.com/MartinMega/APTmap (accessed 20 Apr 2023.
[313] Y. Ren, H. Autefage, J. R. Jones, M. M. Stevens, P. A. J. Bagot, and M. P. Moody, "Developing Atom Probe Tomography to Characterize Sr-Loaded Bioactive Glass for Bone Scaffolding," *Microscopy and Microanalysis,* pp. 1-11, 2021, doi: 10.1017/S1431927621012976.
[314] L. van der Maaten and G. Hinton, "Visualizing Data using t-SNE," *J. Mach. Learn. Res.,* Article vol. 9, pp. 2579-2605, Nov 2008.
[315] M. Wattenberg, F. Viégas, and I. Johnson, "How to Use t-SNE Effectively," *Distill,* vol. 1, no. 10, 2016, doi: 10.23915/distill.00002.
[316] The Mathworks Inc., *Statistics and Machine Learning Toolbox User's Guide (R2021b)*, 2021. [Online]. Available: https://uk.mathworks.com/help/releases/R2021b/pdf_doc/stats/stats.pdf.
[317] J. M. Lewis, "Finding a better k: A psychophysical investigation of clustering," in *Proceedings of the Annual Meeting of the Cognitive Science Society*, 2009, vol. 31, no. 31.
[318] D. Kobak and P. Berens, "The art of using t-SNE for single-cell transcriptomics," *Nature Communications,* vol. 10, no. 1, p. 5416, 2019/11/28 2019, doi: 10.1038/s41467-019-13056-x.
[319] C. Hennig, "What are the true clusters?," *Pattern Recognition Letters,* vol. 64, pp. 53-62, 2015/10/15 2015, doi: 10.1016/j.patrec.2015.04.009.
[320] M. Ankerst, M. M. Breunig, H.-P. Kriegel, and J. Sander, "OPTICS: ordering points to identify the clustering structure," presented at the Proceedings of the 1999 ACM SIGMOD international conference on Management of data, Philadelphia, Pennsylvania, USA, 1999.
[321] E. Schubert and M. Gertz, "Improving the Cluster Structure Extracted from OPTICS Plots," in *LWDA*, 2018, pp. 318-329.
[322] M. Daszykowski, B. Walczak, and D. L. Massart, "Looking for Natural Patterns in Analytical Data. 2. Tracing Local Density with OPTICS," *Journal of Chemical Information and Computer Sciences,* vol. 42, no. 3, pp. 500-507, 2002/05/01 2002, doi: 10.1021/ci010384s.
[323] Y. Suchorski, W. A. Schmidt, N. Ernst, J. H. Block, and H. J. Kreuzer, "Electrostatic Fields above Individual Atoms," *Progress in Surface Science,* vol. 48, no. 1-4, pp. 121-134, Jan-Apr 1995, doi: Doi 10.1016/0079-6816(95)93420-C.
[324] B. Gault *et al.*, "Behavior of molecules and molecular ions near a field emitter," *New Journal of Physics,* vol. 18, no. 3, p. 033031, Mar 18 2016, doi: 10.1088/1367-2630/18/3/033031.
[325] M. Pröbstle *et al.*, "Superior creep strength of a nickel-based superalloy produced by selective laser melting," *Materials Science and Engineering: A,* vol. 674, pp. 299-307, 2016/09/30 2016, doi: 10.1016/j.msea.2016.07.061.
[326] G. Yeli, M. A. Auger, K. Wilford, G. D. W. Smith, P. A. J. Bagot, and M. P. Moody, "Sequential nucleation of phases in a 17-4PH steel: Microstructural characterisation and mechanical properties," *Acta Materialia,* vol. 125, pp. 38-49, Feb 15 2017, doi: 10.1016/j.actamat.2016.11.052.
[327] M. S. Meier, P. A. J. Bagot, M. P. Moody, and D. Haley, "Large-Scale Atom Probe Tomography Data Mining: Methods and Application to Inform Hydrogen Behavior," *Microscopy and Microanalysis,* p. ozad027, 2023, doi: 10.1093/micmic/ozad027.
[328] S. R. Broderick, A. Bryden, S. K. Suram, and K. Rajan, "Data mining for isotope discrimination in atom probe tomography," *Ultramicroscopy,* vol. 132, pp. 121-8, Sep 2013, doi: 10.1016/j.ultramic.2013.02.001.
[329] J. L. Bentley, "MULTIDIMENSIONAL BINARY SEARCH TREES USED FOR ASSOCIATIVE SEARCHING," *COMMUNICATIONS OF THE ACM,* vol. 18, no. 9, pp. 509-517, 1975, doi: 10.1145/361002.361007.
[330] D. Haley, P. Choi, and D. Raabe, "Guided mass spectrum labelling in atom probe tomography," *Ultramicroscopy,* vol. 159 Pt 2, pp. 338-45, Dec 2015, doi: 10.1016/j.ultramic.2015.03.005.
[331] L. J. Johnson, M. Thuvander, K. Stiller, M. Oden, and L. Hultman, "Blind deconvolution of time-of-flight mass spectra from atom probe tomography," *Ultramicroscopy,* vol. 132, pp. 60-4, Sep 2013, doi: 10.1016/j.ultramic.2013.03.015.
[332] F. Meisenkothen, D. V. Samarov, I. Kalish, and E. B. Steel, "Exploring the accuracy of isotopic analyses in atom probe mass spectrometry," *Ultramicroscopy,* vol. 216, p. 113018, 2020/09/01 2020, doi: 10.1016/j.ultramic.2020.113018.

[333] F. Vurpillot, C. Hatzoglou, B. Radiguet, G. Da Costa, F. Delaroche, and F. Danoix, "Enhancing Element Identification by Expectation–Maximization Method in Atom Probe Tomography," *Microscopy and Microanalysis,* vol. 25, no. 2, pp. 367-377, 2019, doi: 10.1017/S1431927619000138.
[334] D. J. Larson, T. J. Prosa, R. M. Ulfig, B. P. Geiser, T. F. Kelly, and P. S. C. J. Humphreys, *Local Electrode Atom Probe Tomography: A User's Guide*. Springer New York, 2013.
[335] D. K. Schreiber, A. N. Chiaramonti, L. M. Gordon, and K. Kruska, "Applicability of post-ionization theory to laser-assisted field evaporation of magnetite," *Applied Physics Letters,* vol. 105, no. 24, p. 244106, 2014/12/15 2014, doi: 10.1063/1.4904802.
[336] L. Tegg, A. J. Breen, T. Sato, and J. M. Cairney, "Characterisation of a new ultrawide field-of-view atom probe microscope using a model Al-Mg-Si alloy," presented at the APT&M 2022, Nanjing, China, 2022. [Online]. Available: https://youtu.be/twlWhoy0wg4?t=554
[337] M. Kühbach *et al.*, "Community-Driven Methods for Open and Reproducible Software Tools for Analyzing Datasets from Atom Probe Microscopy," *Microscopy and Microanalysis,* pp. 1-16, 2021, doi: 10.1017/S1431927621012241.
[338] F. M. Al-Faqeer, K. G. Weil, and H. W. Pickering, "Analysis of hydrogen absorption under competitive adsorption conditions - Effect of hexamethylenetetramine," *J Electrochem Soc,* Article vol. 150, no. 5, pp. B211-B216, May 2003, doi: 10.1149/1.1562594.
[339] D. Vaumousse, A. Cerezo, and P. J. Warren, "A procedure for quantification of precipitate microstructures from three-dimensional atom probe data," *Ultramicroscopy,* vol. 95, no. 1-4, pp. 215-21, May-Jun 2003, doi: 10.1016/s0304-3991(02)00319-4.
[340] Y. Dong *et al.*, "Atom Probe Tomography Interlaboratory Study on Clustering Analysis in Experimental Data Using the Maximum Separation Distance Approach," *Microscopy and Microanalysis,* vol. 25, no. 2, pp. 356-366, 2019, doi: 10.1017/S1431927618015581.
[341] L. T. Stephenson, M. P. Moody, P. V. Liddicoat, and S. P. Ringer, "New Techniques for the Analysis of Fine-Scaled Clustering Phenomena within Atom Probe Tomography (APT) Data," *Microscopy and Microanalysis,* vol. 13, no. 6, pp. 448-463, 2007, doi: 10.1017/S1431927607070900.
[342] C. A. Williams, D. Haley, E. A. Marquis, G. D. Smith, and M. P. Moody, "Defining clusters in APT reconstructions of ODS steels," *Ultramicroscopy,* vol. 132, pp. 271-8, Sep 2013, doi: 10.1016/j.ultramic.2012.12.011.
[343] A. Cerezo and L. Davin, "Aspects of the observation of clusters in the 3-dimensional atom probe," *Surface and Interface Analysis,* vol. 39, no. 2-3, pp. 184-188, 2007/02/01 2007, doi: 10.1002/sia.2486.
[344] R. L. Blaine and H. E. Kissinger, "Homer Kissinger and the Kissinger equation," *Thermochimica Acta,* vol. 540, pp. 1-6, 2012/07/20 2012, doi: 10.1016/j.tca.2012.04.008.
[345] F.-G. Wei, M. Enomoto, and K. Tsuzaki, "Applicability of the Kissinger's formula and comparison with the McNabb–Foster model in simulation of thermal desorption spectrum," *Computational Materials Science,* vol. 51, no. 1, pp. 322-330, 2012/01/01 2012, doi: 10.1016/j.commatsci.2011.07.009.
[346] L. Cheng, M. Enomoto, and F. G. Wei, "Further Assessment of the Kissinger Formula in Simulation of Thermal Desorption Spectrum of Hydrogen," *Isij International,* Article vol. 53, no. 2, pp. 250-256, 2013, doi: 10.2355/isijinternational.53.250.
[347] H. E. Kissinger, "REACTION KINETICS IN DIFFERENTIAL THERMAL ANALYSIS," *Analytical Chemistry,* Article vol. 29, no. 11, pp. 1702-1706, 1957, doi: 10.1021/ac60131a045.
[348] A. H. M. Krom and A. Bakker, "Hydrogen trapping models in steel," *Metallurgical and Materials Transactions B,* vol. 31, no. 6, pp. 1475-1482, 2000/12/01 2000, doi: 10.1007/s11663-000-0032-0.